

**FINAL REPORT  
12 DECEMBER 1974**

**ULTRAVIOLET AND VISIBLE SCATTERED LIGHT EFFECTS  
ON THE OPTICAL PERFORMANCE OF THE  
LARGE SPACE TELESCOPE (LST)**

Author: William B. Wetherell  
Computer  
Programmers: Ira M. Egdall (GASPR)  
Christopher M. King (MISCAT)

Prepared for  
GEORGE C. MARSHALL SPACE FLIGHT CENTER  
NATIONAL AERONAUTICS AND SPACE ADMINISTRATION  
MARSHALL SPACE FLIGHT CENTER, ALABAMA 35812

Under contract NAS8-30639

**Itek**

**Optical Systems Division**

ITEK CORPORATION • 10 MAGUIRE ROAD • LEXINGTON, MASSACHUSETTS 02173



## CONTENTS

1. Introduction . . . . .	1-1
2. Summary and Conclusions . . . . .	2-1
2.1 Ripple Analysis . . . . .	2-1
2.2 Wide Angle Scatter Analysis . . . . .	2-3
2.3 Effects of Mirror Surface Coatings . . . . .	2-5
2.4 Future Experimental Measurements Program . . . . .	2-5
2.5 General Conclusions . . . . .	2-6
3. Statement of Work . . . . .	3-1
3.1 Background . . . . .	3-1
3.2 Scope of Work . . . . .	3-1
4. Ripple Analysis. . . . .	4-1
4.1 Computer Programs . . . . .	4-2
4.2 Rotationally Symmetric Cosine Phase Gratings . . . . .	4-9
4.3 Zonal Ridges . . . . .	4-36
4.4 Rotationally Symmetric "Random" Wavefronts . . . . .	4-43
4.5 Effects of Apodization in the Presence of Wavefront Error . . . . .	4-52
4.6 "Waffle" Wavefront Due to Cell Structure of Mirror Substrate . . . . .	4-56
4.7 Anglo-Australian Telescope Primary Mirror . . . . .	4-61
4.8 Simulated LST Wavefronts . . . . .	4-91
4.9 Statistical Models for Ripple and Figure Error . . . . .	4-100
5. Wide Angle Scatter Analysis . . . . .	5-1
5.1 Beckman Model for Surface Scattering . . . . .	5-1
5.2 Data From the Literature . . . . .	5-3
5.3 Scatter Coefficient Model Based on Empirical Data . . . . .	5-9
5.4 Image Irradiance Due to Scattering . . . . .	5-23
5.5 Starlight Scattered From Primary Mirror . . . . .	5-25
6. Effects of Mirror Surface Coatings . . . . .	6-1
7. Future Experimental Measurements Program . . . . .	7-1
7.1 Measurement of Scattered Light . . . . .	7-1
7.2 Surface Irregularity Measurements . . . . .	7-6
8. References . . . . .	8-1
Appendix A — Translation of Schwesinger's Paper . . . . .	A-1
Appendix B — Surface Roughness Measurements Techniques. . . . .	B-1
Appendix C — Perfect Lens PSF Overlays. . . . .	C-1

## FIGURES

1-1	Present Status of Information . . . . .	1-3
4-1	Flow Charts for Deterministic and Statistical Computer Program Models. . . . .	4-3
4-2	Examples of Output Plots for OPD, Relative Intensity and Encircled Energy, MTF, MTF Degradation Function, and *Autocorrelation Function . . . . .	4-10
4-3	Effective Object Radiance for a Tenth Magnitude and the Wavefront Error Shown in Fig. 4-2 . . . . .	4-12
4-4	MTF Accuracy at Low $\nu_n$ for GASPR. . . . .	4-13
4-5	MTF Accuracy at High $\nu_n$ for GASPR . . . . .	4-14
4-6	PSF's for Single Cosine Phase Gratings of Different Spatial Frequency. . . . .	4-17
4-7	PSF's for Single Cosine Phase Gratings of Different Phase Amplitude . . . . .	4-19
4-8	Effects of Varying Phase Angle $\phi$ . . . . .	4-20
4-9	PSF Without Central Obstruction . . . . .	4-21
4-10	PSF for Central Obstruction Alone . . . . .	4-22
4-11	PSF for Central Obstruction With Cosine Phase Grating . . . . .	4-23
4-12	MTF With and Without Obstruction . . . . .	4-24
4-13	*Autocorrelation Function With and Without Obstruction . . . . .	4-25
4-14	OPD Waveforms for Phase Gratings . . . . .	4-26
4-15	PSF's for Combination High and Low Spatial Frequency Waveforms . . . . .	4-27
4-16	OPD Waveform; $b_1 = 18$ , $b_2 = 25$ , $a_1 = a_2 = 0.02$ , $\phi_1 = 0$ , $\phi_2 = \pi$ . . . . .	4-28
4-17	PSF's for Two-Cosine Phase Gratings of Waveform of Fig. 4-16 . . . . .	4-29
4-18	OPD Waveforms for Multiple Spatial Frequencies . . . . .	4-31
4-19	PSF's for Multiple Spatial Frequencies . . . . .	4-32
4-20	MTF's for Multiple Spatial Frequencies . . . . .	4-33
4-21	Single Ridge of Width 0.1 . . . . .	4-38
4-22	Single Ridge of Width 0.02S . . . . .	4-39
4-23	OPD Waveforms for Edge Roll-Off . . . . .	4-40
4-24	PSF's for Edge Roll-Off . . . . .	4-41
4-25	MTF's for Edge Roll-Off . . . . .	4-42
4-26	OPD Waveforms, Random Wavefronts of Different Correlation Lengths. . . . .	4-44
4-27	PSF's, Random Wavefronts of Different Correlation Lengths. . . . .	4-45
4-28	MTF's, Random Wavefronts of Different Correlation Lengths . . . . .	4-46
4-29	*Autocorrelation Functions, Random Wavefronts of Different Correlation Lengths . . . . .	4-47
4-30	OPD Waveforms, Random Wavefronts Generated With Different Smoothing Functions . . . . .	4-49
4-31	PSF's, Random Wavefronts Generated With Different Smoothing Functions . . . . .	4-50
4-32	*Autocorrelation Functions, Random Wavefronts Generated With Different Smoothing Functions . . . . .	4-51



4-33	Apodization of a Perfect Lens . . . . .	4-53
4-34	Apodization in the Presence of a Cosine Phase Grating; $a = 0.0707$ , $b = 12$ . . . . .	4-54
4-35	Apodization in the Presence of a Very Small Random Wavefront Error; $w = 0.005$ . . . . .	4-55
4-36	PSF for Perfect Lens . . . . .	4-58
4-37	PSF for a 0.50-Radian Waffle Wavefront Error . . . . .	4-58
4-38	PSF for 0.50-Radian Waffle Wavefront Error Plus 0.32 Central Obstruction . . . . .	4-59
4-39	MTF for Example of Fig. 4-38 . . . . .	4-59
4-40	Coarse Wavefront Data at $\lambda = 578$ nm . . . . .	4-63
4-41	Arrangement of Wavefront Profiles on Anglo-Australian Telescope 154-Inch Primary Mirror . . . . .	4-64
4-42	Radial Wavefront Profiles for Anglo-Australian Telescope 154-Inch Primary Mirror . . . . .	4-65
4-43	Wavefront Map: Interpolated From Data Grid . . . . .	4-68
4-44	Point Spread Function at $\lambda = 578$ nm. . . . .	4-69
4-45	Point Spread Function at $\lambda = 325$ nm. . . . .	4-70
4-46	Point Spread Function at $\lambda = 121.5$ nm . . . . .	4-71
4-47	Wavefront Profiles for Radii 5A, 9, and for Averaged Over Zones Case, as Used in GASPR . . . . .	4-73
4-48	PSF's for Radius 5A. . . . .	4-74
4-49	MTF's for Radius 5A . . . . .	4-75
4-50	PSF's for Radius 9 . . . . .	4-76
4-51	MTF's for Radius 9 . . . . .	4-77
4-52	PSF's, Wavefront Error Averaged Over Zones. . . . .	4-78
4-53	MTF's, Wavefront Error Averaged Over Zones. . . . .	4-79
4-54	*Autocorrelation Functions for Radii 5A, 9, and Averaged Over Zones Wavefronts . . . . .	4-80
4-55	Amplitude Spectrum for Wavefront Profile Averaged Over Zones. . . . .	4-84
4-56	Amplitude Spectrum for Radius 5A . . . . .	4-86
4-57	$\Delta DE$ for Radius 5A; Plotted as $\sqrt{\Delta DE}$ for Direct Comparison to Amplitude Spectrum Plot . . . . .	4-86
4-58	Amplitude Spectrum for Radius 9 . . . . .	4-87
4-59	$\Delta DE$ for Radius 9; Plotted as $\sqrt{\Delta DE}$ for Direct Comparison to Amplitude Spectrum Plot . . . . .	4-87
4-60	Effective Radiance Plots for Radius 5A . . . . .	4-88
4-61	Effective Radiance Plots for Radius 9 . . . . .	4-90
4-62	OPD Waveform and *Autocorrelation Function for Simulated LST, $\lambda = 325$ nm. . . . .	4-93
4-63	PSF's for Simulated LST . . . . .	4-94
4-64	MTF's for Simulated LST. . . . .	4-95
4-65	Effective Radiance Plots for 3.0- and 2.4-Meter Telescopes at $\lambda = 632.8$ nm . . . . .	4-96
4-66	Effective Radiance Plots for 3.0- and 2.4-Meter Telescopes at $\lambda = 325$ nm . . . . .	4-97
4-67	Effective Radiance Plots for 3.0- and 2.4-Meter Telescopes at $\lambda = 121.5$ nm . . . . .	4-98
4-68	MTF Plots for 3.0- and 2.4-Meter Telescopes at Three Wavelengths With Spatial Frequency in Cycles/Arc-Second . . . . .	4-99
4-69	Pupil Displacement Coordinates for Computing Autocorrelation Function of OPD Function Over Pupil of Telescope. . . . .	4-105
4-70	Five Autocorrelation Functions for Two-Dimensional, Gaussian, Smoothed Random Wavefronts of 0.3 Correlation Length; Generated by Random Number Generator With Five Different Seeds . . . . .	4-108
4-71	Standard Deviation Curves for the Five Autocorrelation Functions of Fig. 4-70 . . . . .	4-109

4-72	Average of Five Autocorrelation Functions of Fig. 4-70, Compared to Gaussian Autocorrelation Functions . . . . .	4-110
4-73	Autocorrelation Functions for Two-Dimensional, Gaussian, Smoothed Random Wavefronts of Varying Correlation Length . . . . .	4-111
4-74	Five *Autocorrelation Functions Having Same Correlation Length (0.10) and Smoothing Function (Square) But Different Seeds . . . . .	4-113
4-75	*Autocorrelation Function for Rotationally Symmetric, Random Wavefront of Correlation Length 0.1 . . . . .	4-114
4-76	Autocorrelation Function for "Patrick" 48-Inch-Aperture, f/2.5 Parabolic Primary . . . . .	4-115
4-77	Autocorrelation Function for 12-Inch Spherical Mirror . . . . .	4-115
4-78	Variance From the Statistical Mean in MTF Calculations . . . . .	4-117
5-1	Beckman Theory Scatter Curves for Different Correlation Lengths, Compared to King-Kormendy and University of Arizona Data . . . . .	5-4
5-2	Surface Brightness, in Magnitude Per Square Second, in the Image of a Star of Magnitude Zero . . . . .	5-5
5-3	Brightness Profile of a 0-Magnitude Star . . . . .	5-6
5-4	Scatter as a Function of Surface Roughness Normal Incidence; Corrected for Best Fit Background . . . . .	5-8
5-5	Photograph, TV Scan, and Autocovariance Function for a 29 Å RMS Polished Potassium Chloride Surface . . . . .	5-10
5-6	Height and Slope Distribution Functions for the Same Potassium Chloride Surface . . . . .	5-10
5-7	Photograph of Feco Fringe, TV Scanning Camera Trace, and Autocovariance Function for an 8 Å RMS Roughness Polished Cer-Vit Surface . . . . .	5-11
5-8	Height and Slope Distribution Functions for the Same Cer-Vit Surface . . . . .	5-12
5-9	Autocorrelation Data for Sample E-1 . . . . .	5-13
5-10	Effect of Dust on BRDF of Metal Mirror . . . . .	5-14
5-11	General Form of Empirical Scatter Coefficient $\rho_s(\alpha)$ . . . . .	5-15
5-12	Variation of $\rho_s(\alpha)$ With Roll-Off Angle . . . . .	5-18
5-13	Variation of $\rho_s(\alpha)$ With Wavelength and Slope s . . . . .	5-19
5-14	Heinisch Infrared Data <sup>26</sup> Scaled to 514.5 nm and Compared to University of Arizona Data . . . . .	5-20
5-15	Cassegrain Configuration for Scatter Calculation. . . . .	5-24
5-16	Star Profile Model of Eq. 96 Compared to King-Kormendy Star Profiles. . . . .	5-27
5-17	Variation of Star Profile as a Function of Scatter Constant . . . . .	5-29
5-18	Variation of Star Profile as a Function of Wavelength . . . . .	5-30
5-19	Variation of Star Profile With Number of Mirrors . . . . .	5-31
5-20	Telescope Model for Computing Vignetting Factor When Star is Off-Axis and Angle $\alpha$ . . . . .	5-33
5-21	Vignetting Pattern . . . . .	5-34
5-22	Star Matrix and Starfield Boundary for Calculating Contribution of Each Star to Scattered Starlight Background . . . . .	5-35
6-1	Effect of Surface Roughness on Aluminum Reflectivity. . . . .	6-3
7-1	Basic Center of Curvature Scatter Measurement Experiment . . . . .	7-3
7-2	Filter for Producing Gaussian Intensity Distribution . . . . .	7-3
7-3	Techniques for Producing Gaussian Pinholes . . . . .	7-5

## TABLES

4-1	Accuracy of the Encircled Energy Function at Simpson's Rule Radii for Different PSF Sampling Increments . . . . .	4-8
4-2	Relative Intensities for Cosine Phase Gratings of the Same Phase Amplitude and Different Spatial Frequencies . . . . .	4-16
4-3	Displaced Energy for Single Cosine Phase Gratings for Spatial Frequencies of 12 and 27 Cycles Per Radius . . . . .	4-16
4-4	Relative Intensity and Energy Distribution for PSF of Cosine Phase Grating. . . . .	4-18
4-5	Variation of Sideband Internal Structure With Phase Angle $\phi$ . . . . .	4-20
4-6	Some Quantities Affected by Varying Correlation Length . . . . .	4-43
4-7	Some Quantities Affected by Varying the Smoothing Function . . . . .	4-48
4-8	Relative Heights for Diffraction Spikes . . . . .	4-57
4-9	Estimated Diffraction Spike Heights for LST . . . . .	4-57
4-10	Wavefront Error Profiles for A.A.T. 154-Inch Diameter Primary Mirror, Measured Along Radii 18 Degrees Apart . . . . .	4-66
4-11	RMS Wavefront Error for the Rotationally Symmetric Wavefronts Generated From the A.A.T. Data . . . . .	4-72
4-12	$\Delta DE$ for the A.A.T. Radius Profiles 5A and 9, and for a Perfect Lens With a Central Obstruction $\epsilon = 0.324$ . . . . .	4-85
4-13	Inputs to Generate Simulated LST Wavefronts . . . . .	4-92
4-14	Spatial Frequency at Which MTF = 0.10 for 2.4-Meter and 3.0-Meter Simulated LST's . . . . .	4-100
4-15	Zed Integrals for the Two-Dimensional Autocorrelation Functions Used in Generating Fig. 4-73. . . . .	4-112
5-1	Scatter Data From University of Arizona Measurements . . . . .	5-7
5-2	Variation of Total Scattered Light With Roll-Off Angle . . . . .	5-22
5-3	Variation of Total Scattered Light With Wavelength and Surface Roughness . . . . .	5-22
5-4	Variation of RMS Deviation of Wavefront, $\sigma_w$ , With Wavelength. . . . .	5-22
5-5	Stellar Population Density at Galactic Equator . . . . .	5-37
5-6	$T$ as a Function of $\rho_s$ and $\alpha_0$ at Galactic Equator . . . . .	5-37
5-7	$T$ as a Function of $L$ at Galactic Equator . . . . .	5-38
5-8	$T$ as a Function of Wavelength at Galactic Equator. . . . .	5-38
7-1	Period $d$ of Phase Grating Associated With Scatter Angle $\alpha$ and Wavelength $\lambda$ . . . . .	7-7



Itek 74-9507-1

## 1. INTRODUCTION

This is the final report on National Aeronautics and Space Administration contract number NAS8-30639 to study the effects on image quality of scattering due to irregularities in the optical surfaces of the Large Space Telescope (LST). The objective of the study is to build a complete model for the point spread function (PSF) of an astronomical telescope, one which is complete enough to show the manner in which figure error, ripple, and surface microstructure in the optical surfaces degrade image quality. The underlying purposes are to develop tools for use in analyzing how well the surfaces of the primary and secondary mirrors of the LST should be finished to assure adequate performance in the visible and ultraviolet wavelength ranges, and to evaluate the relative importance of figure error, ripple, and surface microstructure in degrading image quality.

Image quality requirements for the LST are more stringent than those of any earlier telescope. The absence of any intervening atmosphere means that the PSF will be defined by factors internal to the telescope, including aberrations, manufacturing errors in the optical surfaces, and pointing stability, rather than atmospheric turbulence. The absence of any intervening atmosphere also allows operation at wavelengths down to perhaps 100 nanometers, which makes it more desirable to minimize optical surface irregularities, due to their more critical effect at the shorter wavelengths. The very large aperture diameter of the LST primary mirror makes it difficult and very costly to achieve the nearly ideal surface finish desired to obtain the highest level of performance at the shortest wavelengths involved. It is therefore important to have a means of modeling the telescope's image quality in the presence of mirror surface irregularities, so that quantitative estimates can be made of the degree to which a given amount and type of mirror surface irregularity will reduce image quality.

There is a considerable body of data as to the relationship between image quality and optical surface figure error. Most of this data has been developed for application to aerial reconnaissance and related areas of imagery, where the objects are of low contrast, and the desire is to resolve fine detail in a continuous tone image. In recent years, there have also been a number of studies on the influence of surface microstructure on scattering at angles greater than 1 degree, largely as a result of developments in the fields of high energy lasers and laser communication systems. But there has been very little study of ripple or surface irregularities of characteristic lateral dimensions between those of figure error and microstructure. These affect the point spread function and scattering at angles between a few Airy radii and 1 degree, a region of interest to astronomers. A more complete evaluation of the effects of ripple will be the principal focus of this study. We will build a model for the PSF which includes quantitative estimates of the degradation due to ripple, based on presently available data.

Fig. 1-1 represents our knowledge of the complete point spread function, as of the early stages of this study, scaled to a 3.0-meter aperture diameter. The perfect lens diffraction pattern and its envelope are well known, with the envelope being an inverse cubic function of its

radius. Knowledge of degradations in the PSE is confined to two extremes. At the inner extreme, the diffraction pattern for degraded lenses can be calculated out to a few Airy radii before the accuracy limitations of the two-dimensional Fourier transform routines involved are reached. [The programs involved use a wavefront (real or modeled) as an input, but define it with a grid of sample points too widely spaced to show the effects of anything except figure error.] At the outer extreme, scattering from mirror samples has been measured at angles greater than 1 degree, as represented by the three curves in the lower right corner of the figure. The only measured data between these two extremes of which we are aware are the two star profiles of King and Kormendy. It is difficult to evaluate their applicability to the LST, since they were measured from silver halide photographs taken with ground based telescopes.

In this study, we pursue two paths to fill in the gap between 10 Airy radii and 1 degree. The first, to which we devote the major effort, is to develop an improved computer program capable of calculating the PSF out to 300 Airy radii or more, using a rotationally symmetric wavefront containing very fine irregularities. The second is to develop a wide angle scatter function model which will permit extrapolation of data measured at angles greater than 1 degree in to angles of a few arc-seconds. We will attempt to justify these models on the basis of data available from the literature and data obtained from other workers in the field. (In this latter regard, we have been particularly fortunate in obtaining high resolution measurements of surface irregularities in the 154-inch primary mirror for the Anglo-Australian Telescope.) We will also recommend measurements where we feel the present data gives insufficient backing to the model.

The text of this report is divided into seven sections, including this introduction. Section 2 summarizes the report and gives conclusions. Section 3 reproduces the technical portion of the statement of work. Sections 4, 5, and 6 correspond roughly to phases Ia, Ic, and Ib, respectively, of the statement of work. Section 7 corresponds to phase II, part 2 of the statement of work. Results of the data survey of phase II, part 1 have been incorporated into the other sections, where pertinent. Two of the more significant reports gathered in that survey are included as appendices A and B.

Section 4 discusses the ripple analysis. The core of this analysis is a computer program for computing the point spread function for a rotationally symmetric wavefront defined by 512 points spread along a radius. This was developed from an existing Itek program, which was modified to increase its accuracy, and to allow modeling of a wide variety of wavefront error patterns. It allows computation of the PSF out to about 300 Airy radii, or 16 arc-seconds for the 3-meter LST at its test wavelength. Section 4 presents a basic discussion of image formation in the presence of ripple as a foundation for our discussion of scattering by wavefront irregularities. These results are used in examining the effects of random wavefront error on the PSF, and in analyzing statistical models for image degradation based on wavefront autocollimation models. The computer program is used in an extensive analysis of ripple in the 154-inch (3.91-meter) aperture primary mirror for the Anglo-Australian Telescope. From the latter data and the study of random wavefronts, we build a model wavefront for the LST. We also use a separate computer program to look at the specific problem of the corrugated, or "waffle" wavefront error which can arise from the cellular structure of the lightweighted mirror structure.

Section 5 describes the wide angle scatter analysis. It opens with a brief description of the most common model presently used to describe scattering by random surface irregularities. Recent mirror scatter measurements are used to demonstrate that this model is not applicable to scattering from optical surfaces. An empirical model for mirror scatter is developed, based on results from the University of Arizona. This is then compared to results from other experiments, and its wavelength scaling properties are defined on the basis of the phase grating diffraction theory described in Section 4. This scatter function model is used in developing a star profile model. The latter is used in turn in a computer program for calculating the effective back-

ground radiance contribution from starlight scattered from the primary mirror of the telescope. Results computed with the latter are discussed.

Section 6 discusses the effects of mirror surface coatings on scatter from the mirrors. This section is brief, since there is little quantitative data to indicate that there is any significant effect, except in portions of the ultraviolet where surface plasmon coupling occurs. There is insufficient data to evaluate the plasmon effects, but studies currently in progress will produce new data in 1975.

Section 7 gives some recommendations for future experimental programs to measure scattering and surface irregularities. Scattering measurements are discussed in terms of two specific measurement techniques we feel are worth pursuing. Surface irregularity measurements are discussed in terms of the type of data required, since a number of possible measurements are possible, and no one technique can measure the entire range of data required.

The two computer programs developed during this study are described in operating manuals submitted separately. Brief descriptions are included in Sections 4.1 and 5.5.2.

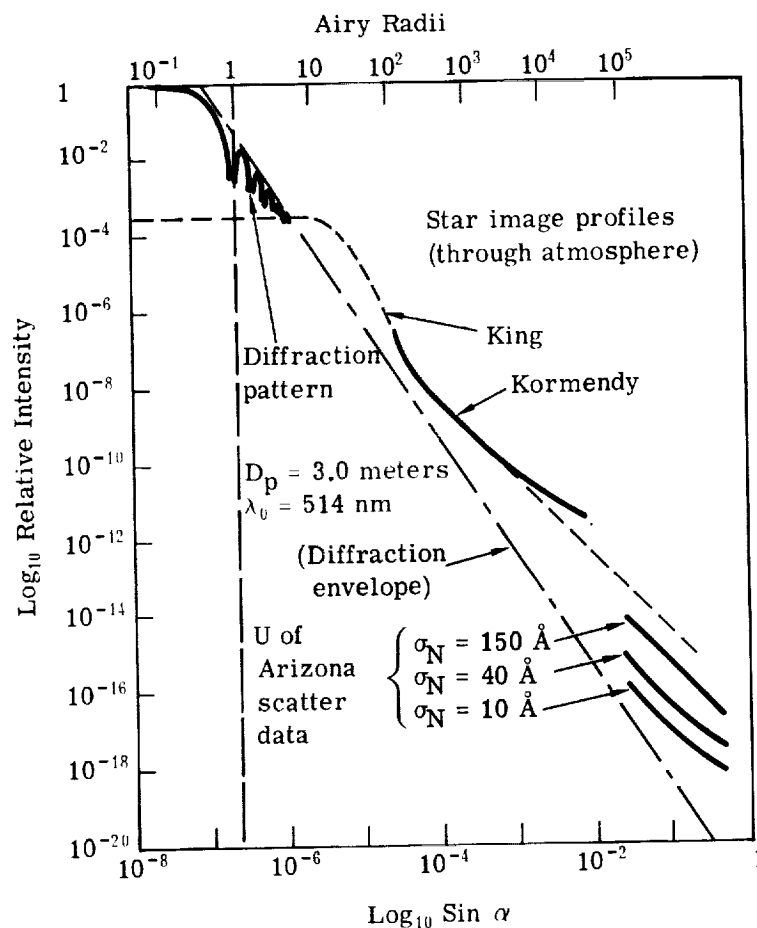


Fig. 1-1 — Present status of information





## 2. SUMMARY AND CONCLUSIONS

This section of the report summarizes the main text of the report, and gives the conclusions drawn from the study. The material is presented in roughly the same order as in the main text. Where a figure or table will aid in summarizing, it will be identified by number, rather than be reproduced.

### 2.1 RIPPLE ANALYSIS

The computer program GASPR is a modified form of an existing Itek program for computing PSF's from specific, rotationally symmetric wavefronts. The accuracy of the program was increased by changing from a 96- to a 512-point Gaussian quadrature in solving the Hankle transform. It is capable of computing the PSF out to more than 300 Airy radii. Input options were expanded to include 3rd, 5th, and 7th order spherical aberration, defocus and a central obstruction, the original options, plus random wavefront error, sums of cosine phase gratings, sums of zonal ridges and Gaussian apodization. The exact forms are defined by Eqs. 3 through 10. Arbitrary (or real) wavefronts can be input by defining OPD values at evenly spaced radii. Outputs include the PSF and encircled energy plots of the original program, plus effective radiance, MTF, MTF degradation function, and \*Autocorrelation† function plots. Accuracy of the PSF is within round-off error for a perfect lens. Accuracy of the other outputs depends on the radius increment and truncation radius used in defining the PSF (see Table 4-1 and Figs. 4-4 and 4-5). A program listing and writeup have been supplied to the customer separately.

Any wavefront can be represented as a spectrum of cosine phase gratings of different spatial frequency, phase amplitude, phase angle, and orientation. In principle, the diffraction from such a wavefront can be represented as the summation of the diffracted wavefronts produced by the component phase gratings. In practice, interactions between phase gratings of different spatial frequency and the higher order sidebands of single spatial frequency components make this very difficult unless the phase amplitudes of the various components are very small, less than about 0.04 wavelength. The presence of figure error or a central obstruction will spread out energy in the phase grating sidebands even at those low levels of wavefront error. These effects are demonstrated by a series of examples using rotationally symmetric phase gratings, which may be found in Section 4.2.

The interactions mentioned above make it difficult to build a simple model for scattering based on a one-to-one correspondence between a spectrum of cosine phase gratings and the scatter function. However, this type of model makes it possible to draw two conclusions which

---

† An asterisk is used in "\* Autocorrelation function" to indicate that this is an approximation to the true wavefront autocorrelation function, as discussed in connection with Eq. 14, in Section 4.1.2.

are very useful in scaling scatter function with wavelength, when the individual spatial frequency components have small phase amplitudes. First, the scatter angle  $\alpha$  is related to the spatial frequency component of period  $d$  by the grating equation  $\sin \alpha = \lambda/d$ . Thus, changing the wavelength will change the angle at which the light is scattered such that

$$\sin \alpha_2 = (\lambda_2/\lambda_1) \sin \alpha_1$$

The energy diffracted by the spatial frequency component is proportional to the square of the phase amplitude, and thus is proportional to  $(\lambda_1/\lambda_2)^2$ . The solid angle into which the light is scattered is proportional to  $(\alpha_2/\alpha_1)^2$ . Therefore, the relative intensity scales as

$$I(\alpha_2, \lambda_2) = (\lambda_1/\lambda_2)^4 I(\alpha_1, \lambda_1)$$

The above conclusion has important consequences in defining a scatter function model, as is discussed in Sections 2.4.2 and 5.3. Among the most interesting experimental consequences is the implication that scatter measurements made at, say, 1 degree with 10.6-micrometer radiation can be scaled to give visible light scattering at a few arc-minutes (see Fig. 5-14 for an example).

The random wavefront model was used to investigate the relative effects on the PSF of three wavefronts having the same net rms wavefront error and different correlation lengths, i.e., a different balance between figure error and ripple. The more significant results are shown in Table 4-6, Fig. 4-27 (PSF's and encircled energies) and Fig. 4-28 (MTF's). Neither Strehl definition nor high spatial frequency MTF (which determines continuous tone resolution limits) are strongly affected by the shift in spatial frequency content. Encircled energy and the PSF are very strongly degraded by the increase in high spatial frequency content (ripple). Thus reducing ripple to a minimum is important for experiments requiring the diameter containing a given encircled energy to be minimized.

A substantial amount of data has been provided to us by Grubb Parsons concerning the surface quality of the 154-inch (3.91-meter) aperture primary mirror for the Anglo-Australian Telescope. This consists of 20 radius profiles taken at 1-inch increments. An extensive analysis has been performed on this data, and is presented in Section 4.7. This includes some coarse resolution two-dimensional analyses, plus use of individual radius profiles to define rotationally symmetric wavefronts for use in GASPR. We have performed spatial frequency analyses of two profiles and compared the resulting amplitude density functions to displaced energy functions (in effect, scatter functions) computed from GASPR outputs (Figs. 4-56 through 4-59). The wavefront error data has also been scaled to give performance at 325 and 121.5 nanometers in the ultraviolet.

A number of observations can be drawn from the data on the A.A.T. primary. First, there is a considerable amount of ripple in the mirror with periods on the order of a few inches, in spite of the fact that the final polishing was done with a full aperture flexible lap. Second, there is a net truly rotational component to the wavefront error, as determined by zonal averaging, and some visual evidence that there may be somewhat higher elliptical ridges. (None of these ridges seem to remain intact around the entire circumference, however.) Third, the Fourier transforms of individual profiles show evidence of peaks in the spatial frequency spectrum.

The two profiles selected for closest study were radius 5A, chosen for its large high spatial frequency component and lack of low spatial frequency irregularities, and radius 9, chosen for a good mix of high and low spatial frequency components. Examination of the amplitude spectra and displaced energy functions for these two cases illustrates a point made above: when only high spatial frequency components of low phase amplitude are present, there is a fairly close one-to-

one correspondence between features of the scatter function and the spatial frequency spectrum of the wavefront irregularities. (Compare Figs. 4-56 and 4-57 for radius 5A.) When large phase amplitude, low spatial frequency components are present, this relationship tends to break down, due to interactions between components. (Compare Figs. 4-58 and 4-59 for radius 9.)

PSF and MTF data for the ultraviolet wavelengths show how much image quality degradation results from the figure error and ripple in this mirror. (It was never intended to operate at those wavelengths, nor in turbulence-free outer space.) This gives some indication of what might be expected from the LST, except in that the A.A.T. primary, with a wavefront error of 0.12 wavelength rms at 578 nanometers, has about twice the wavefront error that is expected for the complete LST, which is to have a wavefront error of 0.06 wave rms at 633 nanometers. (Some consideration is being given to relaxing that tolerance.)

To simulate the LST performance, we have taken an analytic model of the zonally averaged wavefront for the A.A.T. telescope, added a higher spatial frequency random component, to simulate surface roughness, and scaled the rms wavefront error to match the projected values at 632.8, 325, and 121.5 nanometers. The results are given in Section 4.8. These represent the best performance model for the LST which can be generated at present, based on the original performance specifications. Data is presented for both the 3.0- and 2.4-meter aperture diameters currently being considered (see Figs. 4-62 through 4-68).

Three additional tasks were performed as part of the ripple analysis. The first of these tasks was a study of the effects of apodization in the presence of wavefront error. This is frequently recommended as a technique for improving image quality, and it works well when no aberrations are present (Fig. 4-33). But apodization affects only the pupil diffraction, and does not reduce diffraction due to wavefront error at all (Fig. 4-34). Apodization may prove a valuable technique for suppressing the diffraction pattern and bringing out the scatter function when measuring the latter at very small scatter angles. We recommend its incorporation into the scatter experiment discussed in Section 7.

The second added task was to examine the effects of a waffle-like surface deformation pattern in the primary mirror which might result from elastic deformation of the front plate of the lightweighted mirror during polishing or due to gravity release. In effect, this would emboss the square or hexagonal structure of the mirror substrate core on the reflecting surface of the mirror. The results of the study are shown in Fig. 4-37 and Tables 4-8 and 4-9. The values quoted for the LST in Table 4-9 are based on a very simple model for the surface deformations, and may therefore be pessimistic. In monochromatic light, the image defects take the form of a set of eight false star images set in a square centered on the main image. (In white light, they will form eight spectra extending radially outward from the central image.) The monochromatic images will be substantially brighter than the diffraction pattern ring structure, and may reach to within 6 to 10 stellar magnitudes of the central image, depending on the wavelength. Clearly, this is a problem which should be given more detailed consideration.

Finally, we looked at statistical models for the effects of ripple. This investigation was confined largely to examining the validity of earlier statistical models based on a Gaussian autocorrelation function. Our study indicates that the Gaussian model for the autocorrelation function is faulty on formal mathematical grounds, and a very poor approximation for real mirrors from a practical point of view. Practically speaking, the surface irregularities of a real mirror cover too large a spatial frequency range to be well represented by a Gaussian autocorrelation function. We were not able to define a more suitable model in the time we could devote to this topic. That will have to wait for a future effort.

## 2.2 WIDE ANGLE SCATTER ANALYSIS

This study opened with an examination of the Beckmann model for scattering by random surface irregularities, based on the Gaussian autocorrelation function (see Fig. 5-1). The Beck-

mann model has to be rejected for the reasons cited in the section above: the surface irregularities contain too broad a range of spatial frequencies to be represented by a Gaussian autocorrelation function. The star profiles of King and Kormendy (Figs. 5-2 and 5-3) and the scatter measurements of the University of Arizona (Fig. 5-4) indicate that the real scatter function will have a very long straight section (in log-log plots), which is incompatible with Gaussian theory. Autocorrelation measurements by Michelson Laboratory confirm that the autocorrelation function is non-Gaussian (Figs. 5-5 and 5-7).

We have generated an empirical model for the scatter function based on these observations. This model assumes the scatter function to have a fixed slope over most angles—that is, scatter is proportional to the  $(\text{angle})^{-s}$ , where  $s$  is a constant. The final form of the scatter function is shown by Eq. 70 and Figs. 5-12 and 5-13. It includes provision for wavelength scaling of the type discussed above. As a test of the model, we have scaled scatter data measured at 10.6 micrometers to 515 nanometers for comparison to University of Arizona data (see Fig. 5-14). The results appear to be compatible with each other and with the model.

This scatter model has been applied to image illumination calculations for a Cassegrain telescope to examine how the scatter functions of mirrors add. The results indicate that the form of addition is a function of the slope of the scatter function and the axial beam diameters of the mirrors involved. If  $s = 2.0$ , the scatter functions may be added directly, with only a correction factor for the specular reflectivity of mirrors further along the train of optics. That is, if there are  $n$  mirrors of specular reflectivity  $\rho$ , and the slope  $s = 2.0$ , then the total scatter coefficient will equal  $n\rho^{n-1}$  times the scatter coefficient of a single mirror.

This scatter function, with  $s = 2.0$ , has been used to generate an equation for the star profile, including the effects of diffraction. The result, Eq. 96, has been used to match the inverse square curve of King (see Fig. 5-16). The indicated scatter coefficient  $\rho_s(\alpha_1, \lambda_1) = 0.085$  is large, when compared to Arizona data at the same angle and wavelength ( $\sin \mu_1 = 0.10$ ,  $\lambda_1 = 514.5$  nm). King and Kormendy's data is for a telescope with five optical surfaces. When this is considered, the results make the King and Kormendy star profiles appear fully compatible with mirror scattering at angles above 10 to 20 arc-seconds.

The MISCAT computer program was developed using the above star profile model, with adaptations to account for off-axis vignetting in the telescope tube, to calculate the contributions of field stars to the effective background radiance through scattering from the primary mirror. The model used for the computation sets up a rectangular grid of star profiles based on stellar population statistics, with each star profile weighted by a vignetting factor which is a function of their angle off the axis of the telescope. Where each star profile intersects the axis of the telescope, its relative intensity is added to that of all the other stars. The process is repeated for all the stellar populations at each magnitude included in the run. The total sum gives the effective background radiance contributed by the stars in the portion of the sky whose population statistics have been used.

This program was used with stellar population statistics for the galactic equator (see Table 5-5), telescope parameters appropriate for the LST, and a variety of scatter coefficients. The results are shown in Tables 5-6 through 5-8. This data indicates that telescope tube length will have no appreciable effect on the background radiance contribution due to scattered starlight, but that both the scatter coefficient and the wavelength will have an effect. In evaluating these results, keep in mind that the darkest sky background expected in the visible spectrum is on the order of 23.5 magnitudes per arc-second squared. The only data point that matches or exceeds this value is for a wavelength of 121.5 nanometers and a scatter coefficient of 0.1. The latter is much larger than is expected for the LST, at least with clean mirrors. We conclude from these results that scattered starlight can be kept to tolerable levels without superpolishing the mirror,

for the worst possible star backgrounds. For this reason, we have not made calculations for the galactic poles, as called out in the statement of work.

### 2.3 EFFECTS OF MIRROR SURFACE COATINGS

There is insufficient data to specify the effects of surface coatings on the scatter function quantitatively, and we therefore could not include them in the scatter function model. Qualitatively, it is the feeling of workers in the field that the effects are negligible, where the only coatings are the aluminum reflective layer and a protective coating of  $\text{MgF}_2$ . There may be an exception to this at wavelengths in the ultraviolet where surface plasmon effects cause absorption and re-emission of some light. It has been demonstrated that roughening the optical surface will increase the efficiency of plasmon coupling (see Fig. 6-1). This surface was roughened by crystallization in an undercoating, however, and this is not considered representative of the roughness characteristics of polished optical surfaces. Current thinking is that the problem is less severe than implied by Fig. 6-1, but again, there is insufficient quantitative data. Michelson Laboratory is involved in an experimental program to measure ultraviolet scattering from aluminized mirrors, and better answers should be available in the near future.

### 2.4 FUTURE EXPERIMENTAL MEASUREMENTS PROGRAM

The wide angle scatter function model discussed above is based on a linear extrapolation of scatter measurements made at angles greater than 1 degree. This extrapolation involves an assumption as to the nature and size of surface irregularities in the ripple domain, and there is no concrete proof that this assumption is correct. It is important that scatter measurements be made at angles within the range of 1 arc-second to 1 degree to confirm or refute the validity of the scatter function model. It is also important to make direct measurements of the mirror surface irregularities associated with scatter at these angles to better understand the scatter mechanism.

Only two techniques seem to offer the hope of adequate scatter measurements. One is the center of curvature scatter measurements experiment described in Section 7.1.1. Coupling this with the illumination apodization technique described in Section 4.5 should make it possible to measure scattering successfully down to angles of a few Airy disk diameters. The second technique is to make measurements at a number of wavelengths from the same sample, and scale them to the shortest measured wavelength by the technique described above. This would not only serve to give narrow angle measurements of scattering at short wavelengths, but would also serve to check the validity of the scatter function model, and to check for instrumentation errors in regions where the scaled scatter functions overlap.

A variety of experimental techniques can be useful in measuring surface irregularities, but no one will cover the range of measurements we think is required. To cover all scales of surface irregularities which can effect scattering in the visible and ultraviolet requires measurements with lateral resolutions ranging from tens of centimeters to fractions of a micrometer. We have three recommendations tied to what should be measured and not how to measure it. First, data is lacking at lateral resolutions ranging from tens of centimeters to millimeters on LST-size mirrors. This lack should be remedied. Second, the surface irregularity measurements should be Fourier transformed, to give an amplitude spectrum or power spectrum of the surface irregularities. This is needed to relate the surface measurements to the angles at which light is scattered. Third, when rms deviation measurements are made for surface irregularities which are to be compared to measured scatter functions, care should be taken that the spatial frequency bandpass used in the rms summation correspond to the range of angles over which the scatter measurements are made.

## 2.5 GENERAL CONCLUSIONS

This study has produced no startling new revelations concerning scattering and the requirements for a smooth surface on the mirrors in the LST, nor were any such revelations expected. In general, the study has given a better understanding of scattering at small angles and how scattering relates to irregularities on the mirror surfaces. The principal purposes of the program were to develop analytical models for scattering due to ripple and microstructure, and to indicate directions for future experimental work, if any is needed. In this, the study has been successful. Beyond this, several general conclusions can be stated concerning ripple effects and wide angle scattering.

We have shown ripple to be a significant problem where there is a need to minimize the diameter containing, say, 95 to 98 percent of the light in the image of a point source. Ripple which will degrade an image in this respect may not significantly degrade the peak intensity of the image. Ripple of significant magnitude can be present even when the mirror is polished with a full aperture, flexible lap of a type we would expect to reduce ripple. These levels of ripple will not be detected by the usual interferometric tests for figure error. We therefore feel that more attention should be devoted to developing techniques for measuring ripple quantitatively, and for controlling ripple in the fabrication process.

Wide angle scattering, as far as it contributes to the effective background radiance through scattering of light from field stars, appears to be less of a problem than previously thought. If our model for the scatter function is correct, then scattering of the light from field stars by the primary mirror should be no problem with a normally finished mirror. This conclusion should be qualified in three aspects, however. First, the scatter function model upon which this conclusion is based involves an extrapolation of existing data which should be confirmed by experimental measurements. Second, the effects of surface plasmon coupling on scattering in the ultraviolet is still largely unknown, and may have a bearing on whether or not a superpolished surface is needed. Third, insufficient attention has been given to scattering from surface contaminants, and some measurements of such scattering should be made with whatever apparatus is used to confirm the nature of small angle scattering.

### 3. STATEMENT OF WORK

This statement of work is abstracted from the request for proposal, and describes only the technical work to be performed. Discussion of details of the procedures for reporting results has been omitted.

#### 3.1 BACKGROUND

With the near diffraction limited, very narrow angular images that are to be achieved in the LST, it has become increasingly important to determine what effects scattered light from optical surfaces will have on the ultimate performance of the LST for various types of astronomical observations. The purpose of this study is to develop an analytical model of the optical performance of a telescope, such as LST, in the presence of scattered light and to determine a meaningful measurements program to establish credibility of the analytical model in order to determine what performance can be expected for the LST and what specifications must be placed on the LST optics.

#### 3.2 SCOPE OF WORK

The contractor will supply the necessary manpower and resources to accomplish a study on ultraviolet and visible scattered light effects on the optical performance of the LST. The study will be divided into two phases. The Phase I effort will be to develop an analytical model to describe the effects of optical surface scatter on the point spread function (PSF) and the modulation transfer function (MTF) of the LST OTA optics. The Phase II effort will be aimed at verification of the analytical model. This effort will consist of two parts. First, a survey will be made to obtain pertinent experimental data on existing telescope optics in an attempt to establish credibility with the developed analytical model. The second part will be to determine and recommend an experimental measurements program that needs to be performed in order to obtain optical surface scatter data that is needed to completely establish credibility in the analytical model. Details of the tasks to be covered in Phases I and II are described below.

##### Phase I—Development of Analytical Model

The contractor will develop an analytical model that will predict both the PSF and MTF for optical surfaces that produce both wavefront errors and scattered light. While limited analytical models already exist, the purpose of this study will be to carry the analysis much further to include the following points:

- a. The effect of both surface finish (smoothness) and mirror figure must be considered. The high spatial frequency components of the surface amplitude function will affect the near angle (less than 1 arc-second) scatter thus degrading the PSF and MTF. The analytical model should include the effects of all spatial frequencies in the optical surface. Interferometric mirror figure

measurements are in effect low spatial frequency band-pass filters and thus in no way record what type scatter is present due to high spatial frequencies in the optical surface. One problem to be addressed in the LST program is how to specify both surface smoothness and wavefront error. At what point does it cease to make sense to reduce the mirror figure error because the surface finish dominates the shape of the PSF? Or what PSF or MTF can one expect for a mirror with a given figure error and surface finish?

In addition, the analysis must consider the combined effect and individual contributions of all optical elements in the LST (OTA).

b. The effects of an overcoating of aluminum plus  $\text{MgF}_2$  or  $\text{LiF}$  on the surface finish and thus optical image performance will be included in the analytical model.

c. The effects of wide angle scattering by field stars on producing an artificial background sky brightness will be considered. This should be done using actual star counts for two regions of the celestial sphere (the galactic poles and the galactic center) and over the entire spectral regime that LST will be used (900 nm to 1 mm) at a sufficient number of wavelengths to describe the system characteristics.

#### Phase II—Verification of the Analytical Model

Part 1. A survey will be made to obtain all available data pertinent to this problem. Emphasis in this task will be placed on establishing credibility in the analytical model and predicting the LST performance with today's state of the art.

Part 2. Based on the analysis and survey of available data, the contractor shall determine and recommend an experimental measurements program that should be conducted to obtain all the data necessary to allow NASA to predict with confidence the optical performance of the LST. The performance of the measurements program will not be a part of this study.



#### 4. RIPPLE ANALYSIS

"Ripple" refers to optical surface irregularities having characteristic lateral dimensions in the range between those of figure error and surface microstructure. There are no sharp boundaries between figure error, ripple, and surface microstructure. In fact, the three categories of surface irregularities exist largely as conversational conveniences, since they all degrade the image through the same diffraction process. The three categories arise from differences in the test procedures used to measure each, and the fact that the characteristic lateral dimensions of optical surface irregularities determine the "scatter" angle at which light is diffracted. Of more significance for this study, the mathematical techniques used to analyze diffraction by surface irregularities depend on their characteristic lateral dimensions.

Figure error is usually measured interferometrically, and is usually specified completely, including its variation in two dimensions. Typically, the two-dimensional wavefront is represented by a 20- by 20-point square grid in data reduction and in calculating the resultant modulation transfer function (MTF) and point spread function (PSF). In special cases, a much larger grid can be used (see Section 4.6). But this can be done only if fast Fourier transform techniques are used in calculating the MTF and PSF. These techniques reduce the accuracy of the calculations somewhat, and place restrictions on the sampling intervals used in defining the MTF and PSF. While these limitations are completely acceptable in defining the MTF, they do not allow adequate quantitative determination of the effects of higher spatial frequency ripple on the PSF.

For our purposes, we consider figure error to include those surface irregularities with spatial frequencies up to about 5 cycles per pupil radius, the limitation set by a 20- by 20-point sample grid. This study considers figure error only in a few specific cases.

Surface microstructure is too fine-scale for deterministic analysis, and must be treated statistically. It is the source of wide angle scattering, and will be treated in Section 5. For the present, we note only that the characteristic lateral dimensions of microstructure range from less than 1 wavelength to perhaps 1 millimeter.

The characteristic lateral dimensions associated with ripple, then, range from 1 millimeter up to, in the case of the LST, about 30 centimeters. The number of sample points required to define ripple adequately in two dimensions, and the number of calculations required to convert this data into a PSF at the desired level of accuracy, makes two-dimensional ripple analysis unattainable. In general, therefore, we will examine only rotationally symmetric ripple. This allows the two-dimensional Fourier transform to be reduced to a one-dimensional Hankel transform, making accurate calculations of the PSF possible in a fraction of the time required for comparable two-dimensional PSF's. These rotationally symmetric wavefronts are not identical to what will be found in real telescopes, but they do allow examination of the magnitude of the image degradation caused by high spatial frequency ripple.

The analysis of ripple will be deterministic, rather than statistical: that is, specific wavefronts will be analyzed rather than statistical models. These may be analytic, defined by equa-

tions, or random, defined with the aid of a random number generator. All will be rotationally symmetric except for a special case in Section 4.6.

Section 4.1 gives description of the programs used in the ripple analysis. Sections 4.2 through 4.5 will discuss the rotationally symmetric waveforms analyzed, and will rely heavily on output plots from the computer program GASPR. Section 4.6 discusses one specific two-dimensional waveform, the "waffle" wavefront resulting from a square-celled lightweighted mirror substrate. Section 4.7 gives an extensive analysis of the 154-inch diameter primary mirror built for the Anglo-Australian Telescope. Section 4.8 describes a model for the LST wavefront, based on the types of surface irregularities encountered in the 154-inch mirror, scaled to the rms wavefront error values currently expected for the LST. Section 4.9 closes the deterministic analysis with conclusions drawn from the above, and a discussion of the validity of various models for the autocorrelation function.

Please note that in the following sections all values pertaining to the heights of surface irregularities refer to the heights on the wavefront, unless otherwise specified. These are, of course, twice the height of the corresponding mirror surface irregularities.

Also note that a set of perfect lens PSF curves is included in Appendix C in the form of overlay transparencies. These may be superimposed on the PSF plots in Section 4 to show differences between the perfect and modified PSF's under discussion.

#### 4.1 COMPUTER PROGRAMS

Fig. 4-1 is a flow chart representing the basic computational techniques used in a number of Itek computer programs for calculating MTF's and PSF's. The core of the computation routine is represented by the four boxes at the bottom of the flow chart, showing the relationships between the complex pupil function, the complex amplitude image, the point spread function, and the optical transfer function. It should be noted that this is a very generalized chart, and that the detailed computation routines used in different programs are quite different, and not necessarily interchangeable.

The various programs can be divided into two classes, deterministic and statistical. The one statistical program we use currently is PORO, which uses an MTF degradation function of the form

$$T_{\omega} = e^{-\{(2\pi\omega)^2 [1 - \Phi_{11}(\nu_n)]\}} \quad (1)$$

to define the image degradation due to a statistical wavefront error of  $\omega$  wavelengths rms. Here  $\nu_n$  is the normalized spatial frequency, and  $\Phi_{11}$  is the autocorrelation function model for the wavefront. Currently, a Gaussian autocorrelation function of the form

$$\Phi_{11}(\nu_n) = e^{-(2N_H^2 \nu_n^2)} \quad (2)$$

is used, where  $N_H$  is the reciprocal of the autocorrelation length for the wavefront. This program was used in connection with the discussion of autocorrelation functions in Section 4.9.

All of the deterministic programs available at Itek start with a specific wavefront deformation map, convert this into a complex pupil function, and compute the OTF (or MTF) and PSF from that. The programs differ in the form and source of the wavefront deformation map. FRED and FITSCAN use interferograms from real wavefronts to compute the wavefront deformation maps. FRAP-2D uses third order aberrations and a random number generator to produce a two-dimensional synthetic wavefront deformation map. GASP generates a rotationally symmetric

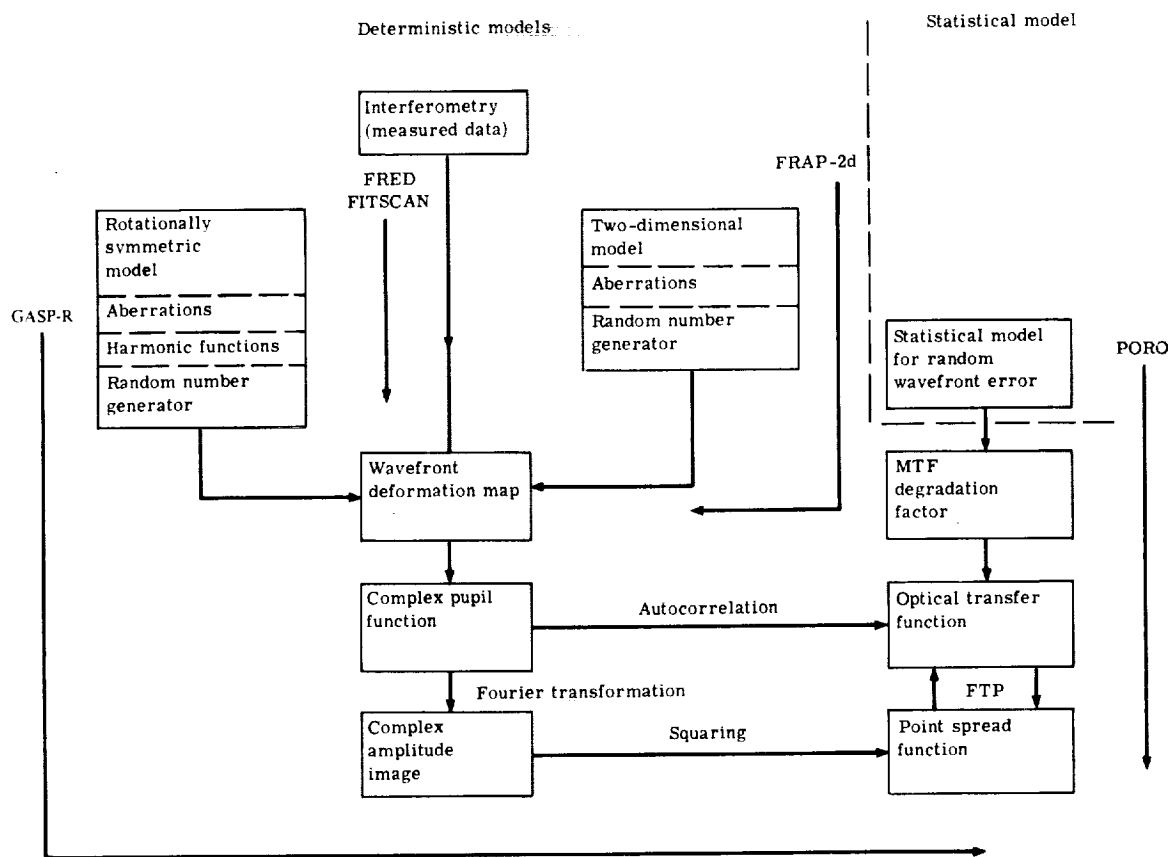


Fig. 4-1 — Flow charts for deterministic and statistical computer program models

REPRODUCIBILITY OF THE  
ORIGINAL PAGE IS POOR

wavefront map using rotationally symmetric third, fifth, and seventh order aberrations. The two-dimensional programs are used to a limited extent in connection with Sections 4.6, 4.7, and 4.9 of this report. The main computer program used in this study is GASPR, revised version of GASP, having increased accuracy and a substantially larger number of input and output options.

GASP and GASPR both use Hankel transforms (Fourier-Bessel transforms) to compute the PSF from the rotationally symmetric complex pupil function. GASP uses 96-point Gaussian quadrature for the Fourier integration, with the wavefront being defined by 96 points along one pupil radius. With GASP, the PSF can be computed out to about 46 Airy radii. Beyond that, spurious oscillations are produced, due to the limited number of sampling points. In GASPR, the number of sample points was increased to 512, to extend the range over which an accurate PSF can be calculated. Linear extrapolation from the 96-point case led us to expect the limit on radius to be about 250 Airy radii, but in fact useful results can be obtained to at least 300 Airy radii. The ultimate limit has not been determined.

GASPR was created for this study program, and a complete description will be provided separately. A description of its input and output options will be given here, along with some discussion as to its accuracy, for the benefit of readers who only wish to know enough to interpret the results presented in the next few sections of the report.

#### 4.1.1 Input Options

The user of GASPR may define the form of the wavefront he wishes to analyze through the choice of a number of input options. They are as follows:

1. Central obstruction—A circular central obscuration may be included, defined by its normalized diameter  $\epsilon$ .
2. Seidel aberrations—3rd, 5th, and 7th order spherical aberration and defocus may be included. (The nonrotationally symmetric Seidel aberrations are, of course, excluded.) These aberrations are specified in terms of the optical path difference (OPD) at the edge of the pupil.
3. Analytic OPD functions—Two basic OPD functions have been added, the cosine phase grating  $C_i$  and the Gaussian cross section ridge  $G_j$ :

$$C_i = a_i \cos(2\pi b_i \rho + \phi_i) \quad (3)$$

and

$$G_j = h_j \exp [-(\rho - \rho_{oj})^2/w_j^2] \quad (4)$$

where  $a_i$  = phase amplitude (OPD amplitude) in wavelengths  
 $b_i$  = spatial frequency in cycles per pupil radius  
 $\phi_i$  = phase angle in radians  
 $\rho$  = normalized pupil radius  
 $\rho_{oj}$  = normalized pupil radius at which  $G_j$  reaches maximum  
 $h_j$  = phase height (OPD height) of ridge in wavelengths, and  
 $w_j$  = half-width at which  $G_j = h_j/e$ .

G can also be used to generate edge roll-off by setting  $\rho_o$  to a value greater than 1.0, and selecting  $w$  and  $h$  appropriately.

More complex analytic OPD functions can be generated by using combinations of  $C_i$  and  $G_j$ . The possible combinations available are defined by Eq. 5:

$$\text{OPD}(\rho) = \sum_{\ell=1}^p \left[ \left( \sum_{k=1}^0 G_k \right) \times \sum_{\substack{i=1 \\ j=1}}^{m,n} (C_i + G_j) \right] \quad (5)$$

The maximum value for  $m, n$ , and  $0$  is 10, and for  $p$  is 8.

4. "Random" wavefront—Values of OPD along a radius are defined with the aid of a random number generator and one of four smoothing functions. The user defines the wavefront in terms of its rms wavefront error  $\omega$ , the correlation width  $c$ , the type of smoothing function (Gaussian, square, triangular, or linear exponential), and the seed. The seed is a number determining where in the random number table the generation process begins. It permits the same wavefront to be regenerated exactly. The smoothing functions are of the form

$$\text{Gaussian } S_c(r) = \exp [-r^2/(c/2)^2] \quad (6)$$

$$\text{Square } S_c(r) = \begin{cases} 1, & r \leq c/2 \\ 0, & r > c/2 \end{cases} \quad (7)$$

$$\text{Triangular } S_c(r) = \begin{cases} 1 - |r|/c, & r \leq c \\ 0, & r > c \end{cases} \quad (8)$$

$$\text{Linear exponential } S_c(r) = \exp [-|r|/(c/2)] \quad (9)$$

The random numbers are generated at equally spaced increments of 0.006 in normalized radius units, and smoothed with the above functions. A parabolic interpolation routine is then used to define the OPD at the 512 unevenly spaced points used in the Gaussian quadrature integration technique.

5. Measured wavefront profile—Any set of measured data (or an arbitrarily chosen set of numbers) can be entered at equally spaced radius increments. A parabolic interpolation routine will be used to determine the values of this wavefront at the 512 sample points, as described above.

6. Apodization—One apodization function is available. This defines a pupil transmittance function  $A$ , in which the effective transmittance falls off as a Gaussian function of the pupil radius  $\rho$ :

$$A(\rho) = \exp (-k\rho^2) \quad (10)$$

where  $\rho(1/e) = k^{-1/2}$

7. Any combination of input options 1 through 6 may be used, except that a random wavefront cannot be used at the same time as a measured wavefront.

#### 4.1.2 Output Options

GASPR computes the PSF from the specified wavefront, using a Hankel transform. In turn, a Hankel transform of this PSF is used to generate the MTF. A series of other outputs, both printed and plotted, is available:

1. OPD—The input waveform may be plotted, showing OPD as a function of the normalized pupil radius. No printout of this function is available. (The rms wavefront error  $\omega$  is always printed out.)

2. PSF—Two forms of the point spread function are available. In one,  $\log_{10}$  of the relative intensity is plotted as a function of the image radius, specified in Airy radii units (one Airy radius =  $1.22 \lambda/D_p$ , where  $D_p$  is the entrance pupil diameter). In the other, the effective object radiance in magnitudes per square arc-second is plotted as a function of radius in arc-seconds. These two outputs are available both as plots and as printouts.

The normalization technique used for the PSF should be understood. Two steps are involved, in the case of the  $\log_{10}$  relative intensity output. First, the PSF is normalized so that the total energy in the PSF equals unity, including that part of the PSF beyond the radius at which the output is truncated. This is equivalent to normalizing the MTF to 1.0 at zero spatial frequency, and is done to distinguish between changes in effective transmittance and changes in the image spread when a central obstruction or apodization is present. Second, the PSF is multiplied by a constant which will make the PSF equal to unity at radius zero when there is no central obstruction and no wavefront error. Thus the actual value of the relative intensity at radius zero is equal to the Strehl definition  $\mathcal{D}$ . For a perfect lens with a central obstruction,  $\mathcal{D} = (1 - \epsilon^2)$ .

For the effective radiance plot, the relative intensity  $I^*(r)$  is converted to effective radiance  $\mathcal{M}_V(r)$  magnitudes per square arc-second using the equation

$$\mathcal{M}_V(r) = 26.84 + m_V - 5 \log_{10} D_p + 5 \log_{10} \lambda - 2.5 \log_{10} I^*(r) \quad (11)$$

where  $m_V$  = magnitude of star

$D_p$  = aperture diameter in meters

$\lambda$  = wavelength in meters.

$m_V$  is normally specified in visual magnitudes, although other types of magnitudes can be used (see Section 5.5.1 for derivation). Note only that  $\mathcal{M}_V(r)$  will be in whatever type of units are used for  $m_V$ . The user must specify  $m_V$ ,  $D_p$ , and  $\lambda$ . The top of the effective radiance scale will be set to the nearest integer smaller than the value of  $\mathcal{M}_V(r)$  defined by the first five terms of Eq. 11.  $I^*(r)$  incorporates the normalization to the Strehl definition. Thus  $\mathcal{M}_V(0)$  should represent the true peak effective radiance of the stellar image.

The effective radiance plot option is included to allow direct comparison of performance at different wavelengths. It should be noted that the computation does not take into consideration variations in spectral type for the star. Thus, for a comparison with a real star, the user must adjust the value of  $m_V$  at each wavelength appropriately.

3. Encircled energy (EE)—The encircled energy is printed out and plotted every time the PSF is printed out and plotted. It is calculated by integrating the PSF function after it has been normalized to unit energy. The encircled energy plot appears on the same graphs as the  $\log_{10}$  relative intensity and effective radiance functions, and can neither be deleted nor plotted separately. The integration technique used is Simpson's rule. The accuracy of the results will be discussed in Section 4.1.3.

4. EE(perf) - EE—This output is available in printout only. This function will be referred to as the displaced energy,  $DE(r)$ . A positive value indicates that a fraction  $DE(r)$  of the total energy in the PSF has been displaced outward beyond radius  $r$ . A negative value indicates an inward displacement (as, for example, with an apodized lens). Since the comparison is made to EE(perf), the encircled energy for a perfect lens with no central obstruction, the energy displacement caused by a central obstruction can also be evaluated.

$DE(r)$  can be used to calculate both where the displaced energy comes from and where it goes to the function.  $\Delta DE = DE(r_1) - DE(r_2)$ ,  $r_1 < r_2$  indicates the difference in energy content in the PSF between  $r_1$  and  $r_2$  for the test case as compared to the perfect, unobstructed lens. A nega-

tive value indicates a net loss in energy, and a positive value indicates a net gain, compared to the perfect case. Although this function is not printed out or plotted, hand calculations will be used in some of the analysis in subsequent sections.

5. MTF—The modulation transfer function  $T(\nu_n)$  is plotted as a function of the normalized spatial frequency  $\nu_n = \nu/\nu_0$ , where  $\nu_0 = D_p/\lambda$  cycles per radian, or  $\nu_0 = 1/\lambda F$  cycles per unit length,  $F$  being the focal ratio. Both plotted and printed outputs are available.

The MTF is calculated by taking a Hankel transform of the PSF function generated above. Since the PSF is truncated, it does not represent all the energy in the PSF. To minimize the errors in the MTF due to this truncation, the value of  $T(0)$  has been set equal to the encircled energy at the truncation radius. The magnitude of the residual error is discussed in Section 4.1.3.

6. MTF degradation function  $T_\omega$ —The MTF degradation function is calculated by the equation

$$T_\omega(\nu_n) = T(\nu_n)/T_I(\nu_n), \quad (12)$$

where  $T_I(\nu_n)$  is the perfect lens MTF given by

$$T_I(\nu_n) = \frac{2}{\pi} [\arccos \nu_n - \nu_n \sin(\arccos \nu_n)] \quad (13)$$

When a central obstruction is present, the analytic equation for the MTF of an obscured perfect lens is substituted for  $T_I$ . Both printed and plotted outputs are available. This function will always be plotted and printed out when the MTF is calculated and printed out. (The plot can be suppressed.)

7. \*Autocorrelation function  $\Phi_{11}(\nu_n)$ —The \*Autocorrelation function is computed by inverting Eq. 1. Thus

$$\Phi_{11}(\nu_n) = 1 + [1/T_\omega(\nu_n)]/(2\pi\omega)^2 \quad (14)$$

This function is automatically calculated whenever MTF is calculated. Both printout and plot are provided, but the plot may be suppressed.

Strictly speaking, this function is not the true autocorrelation function for the wavefront. Eq. 1 was derived for small random wavefront errors having Gaussian height distributions (but not necessarily a Gaussian autocorrelation function). It does not apply rigorously to any deterministic wavefronts which do not exhibit Gaussian characteristics. Also, for large wavefront errors, both the MTF and  $T_\omega$  can have negative values, indicating spurious resolution; under these conditions, Eq. 1 is totally inapplicable. Results obtained in this study, however, indicate that Eq. 1 may have some application to other than Gaussian random wavefronts, when the wavefront error is small, although  $\Phi_{11}(\nu_n)$  may have a form which cannot be defined analytically with any great ease. This property allows examination of the properties of the autocorrelation near zero  $\nu_n$ , even though mathematical rigor is not maintained. To distinguish it from the true autocorrelation function in later discussions, this function is termed the \*Autocorrelation function.

8. Zed integral—The zed function is computed by the integral

$$\text{Zed} = \int_0^1 \Phi_{11}(\nu_n) T_I(\nu_n) \nu_n d\nu_n \quad (15)$$

It is contended by some that this function should always equal zero, if the mean value of the wavefront error is zero and  $\Phi_{11}(\nu_n)$  is the true autocorrelation function. (See Section 4.9 for further discussion.) If true, a very small value for zed may be taken as an indication of the validity of using the \*Autocorrelation function.

Figs. 4-2 and 4-3 show examples of the output plots. Fig. 4-2 shows the array of five plots which would normally be used for optical analysis. Fig. 4-3 shows the effective radiance function for the same wavefront. All plots are for a 12-cycle-per-radius cosine waveform of phase amplitude 0.08 wavelength. For the effective radiance plot,  $m_v = 0$ ,  $D_p = 3.0$  meters, and  $\lambda = 325$  nanometers.

#### 4.1.3 Accuracy of Computer Programs

The accuracy of the results calculated with GASPR can be evaluated by computing the PSF, MTF, and encircled energy for a perfect lens with no obstruction and no wavefront error. The correct answers for these examples can be defined by well-known analytic equations. In fact, since these functions are built into EE(perf) - EE and  $T_\omega$ , the encircled energy and MTF accuracy may be evaluated internally.

Itek has a separate computer program, SPRE, which computes the PSF using an analytic equation. (It is used to evaluate the effects of central obstructions and annular ring obstructions on the PSF.) A comparison of results between SPRE and GASPR shows the latter to be accurate to within 1 in the sixth significant figure, which is essentially round-off error.

Encircled energy is computed from the calculated values for the PSF using a Simpson's rule integration. Simpson's rule requires an odd number of points: e.g., the values of the PSF at  $r_A = 0, 0.1, 0.2, 0.3$ , and  $0.4$  are used to calculate EE at radius  $0.4$ . To calculate EE at radius  $0.3$ , in this example, it is necessary to extrapolate between the values calculated by Simpson's rule at  $r_A = 0.2$  and  $0.4$ , using a modified integration technique. Thus, the greatest accuracy is attained at the Simpson's rule points. The oscillation in accuracy between odd and even points is most noticeable within the central maximum, where the encircled energy is changing most rapidly. At the Simpson's rule points, the accuracy depends on the increment between sample points. Outside the central maximum, the accuracy at Simpson's rule points remains constant at the values indicated in Table 4-1. The accuracy at non-Simpson's rule points approaches this level well outside the central core.

Table 4-1 — Accuracy of the Encircled Energy Function at Simpson's Rule Radii for Different PSF Sampling Increments

Radius Increment	Error in Perfect Lens EE
0.20	-0.0017
0.10	-0.000093
0.05	-0.0000057

In computing the MTF, there are two forms of error. One is an error at low spatial frequencies due to truncation of the PSF. The other is an error at high spatial frequencies due to PSF sampling point increments. The magnitude of these errors is shown in Figs. 4-4 and 4-5, which plot the MTF degradation function  $T_\omega$  versus normalized spatial frequency  $\nu_n$  for test case perfect lenses. In Fig. 4-4, both scales have been greatly expanded to show the magnitude of the error. This graphically illustrates why  $T(0)$  should be set equal to the encircled energy at the truncation radius. Much larger errors are present at high spatial frequencies, due to the finite sampling increments, as shown in Fig. 4-5.



The errors in the MTF affect the accuracy of both  $T_\omega$  and  $\Phi_{11}$  fairly strongly, particularly when the rms wavefront error is small. This may be seen by comparing the MTF degradation and \*Autocorrelation curves in Fig. 4-2 to Fig. 4-5. The sampling increment used was 0.10, and the high frequency behavior of both  $T_\omega$  and  $\Phi_{11}$  shows a strong correlation to Fig. 4-5. (It should be noted that in the case of a rotationally symmetric wavefront error, both of these functions will have a value of 1.0 at  $\nu_n$ , so the rise in value is not due solely to the sampling increment error.)

The positive value of these errors in the MTF will have a particularly strong effect on  $\Phi_{11}$  when  $\omega$  is very small. As a result, the zed integral will be positive for small wavefront errors. For large wavefront errors, zed is driven negative. (More about this in Section 4.9.)

In general, most curves shown in this report use a radius increment of 0.1 Airy radii and truncate the PSF at 100 Airy radii. Truncation at 50 Airy radii is used in a limited number of cases. Their accuracy may be judged accordingly.

These accuracy estimates are made for the perfect lens case. There is no way of rigorously determining the accuracy of the program when wavefront error is present, since no calculation routine of higher known accuracy is available at present.

## 4.2 ROTATIONALLY SYMMETRIC COSINE PHASE GRATINGS

Cosine phase gratings are rotationally symmetric wavefront errors of the form of Eq. 3, which we rewrite here:

$$\text{OPD} = a \cos (2 b\rho + \phi) \quad (3)$$

Fourier analysis states that any waveform can be expressed in terms of a spectrum of sinusoidal functions of appropriate amplitude, frequency, and phase angle. In this sense, consideration of the behavior of cosine phase gratings containing only a few harmonics gives some understanding of the behavior to be expected of high spatial frequency ripple.

The analysis given here was performed entirely with the GASPR computer program. We have not done extensive theoretical analysis to try and derive analytic equations for some of the simpler cases. Comparison of our results to earlier work done by Ratcliffe<sup>1\*</sup> and Barakat<sup>2</sup> leads to some interesting suppositions, however, and allows us to state some equations empirically which agree well with our computer derived results.

Ratcliffe's treatise<sup>1</sup> gives a very clear exposition of the properties of a linear sinusoidal phase grating in diffracting a plane wavefront, both being of infinite extent. Ratcliffe defines the phase grating by its phase amplitude in radians,  $\Delta\phi = 2\pi a$ , where  $a$  is the phase amplitude in wavelengths, and by its period  $d$ , in units of length. When  $\Delta\phi \ll 1.0$ , the only significant amounts of diffracted energy appear in its first order sidebands, defined by the diffraction angle  $\sin \alpha = \pm\lambda/d$ . (The wavefront is assumed to be normally incident on the phase grating.) The complex amplitude of each sideband is  $i\Delta\phi/2 = i\pi a$ , and its intensity is  $\pi^2 a^2$ . The net reduction in intensity of the undiffracted wavefront is  $1 - 2\pi^2 a^2$ .

In the more general case where  $\Delta\phi > 1.0$ , a series of sidebands is generated, with the diffraction angles defined by the standard grating equation for normal incidence,

$$\sin \alpha_n = \pm n\lambda/d \quad (16)$$

The complex amplitude  $A_n$  of each sideband of order  $n$  is given by

---

\* References are listed in Section 8.

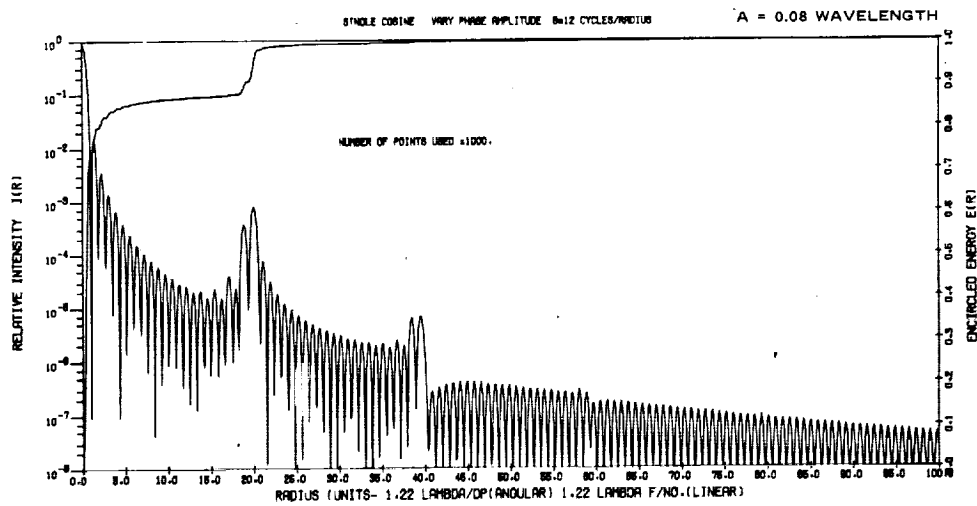
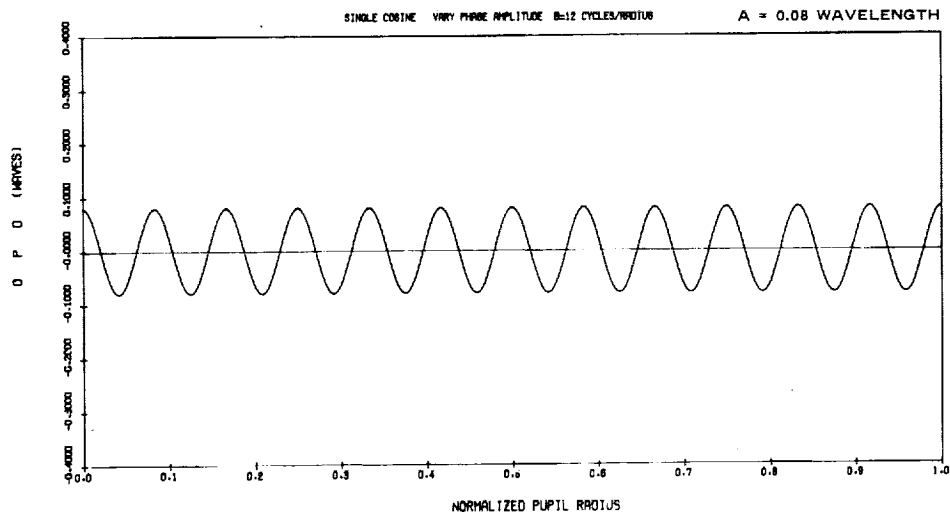


Fig. 4-2 — Examples of output plots for OPD, relative intensity and encircled energy, MTF, MTF degradation function, and \* Autocorrelation function

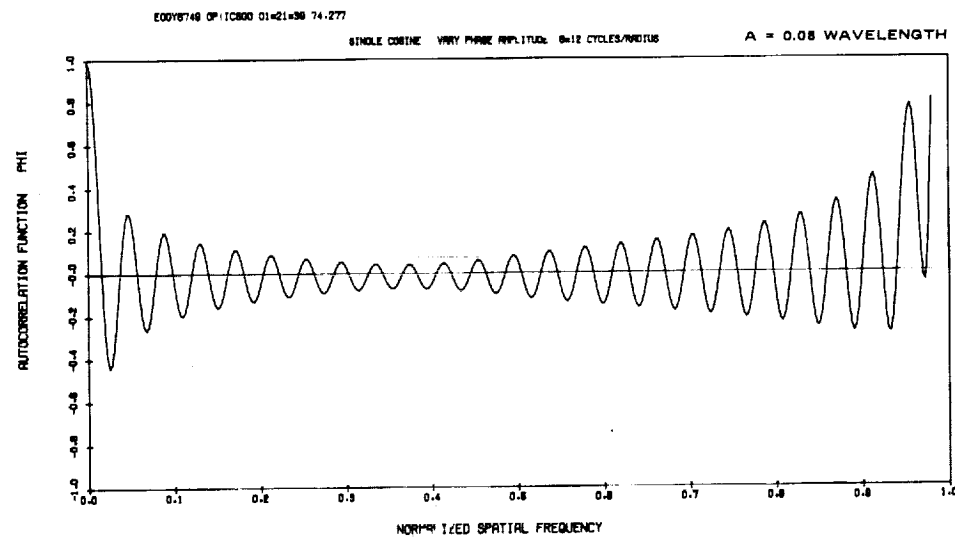
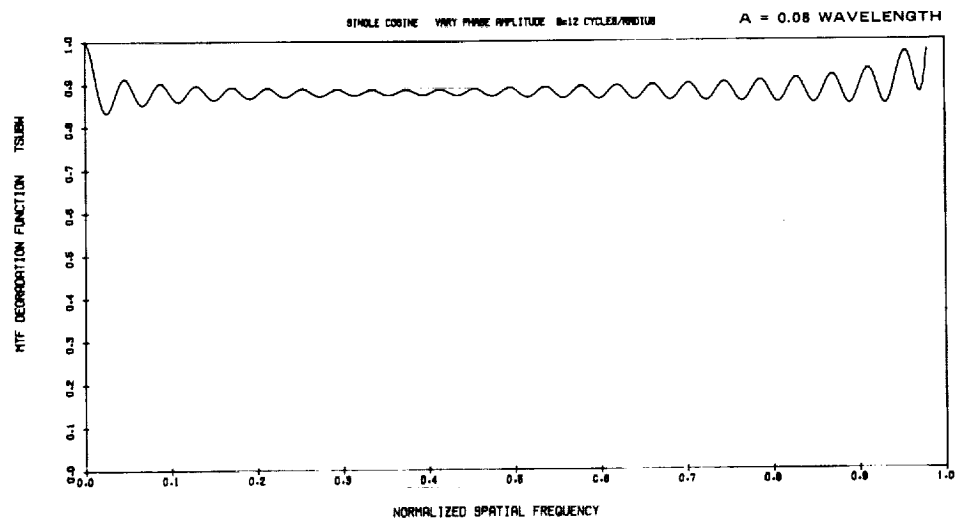
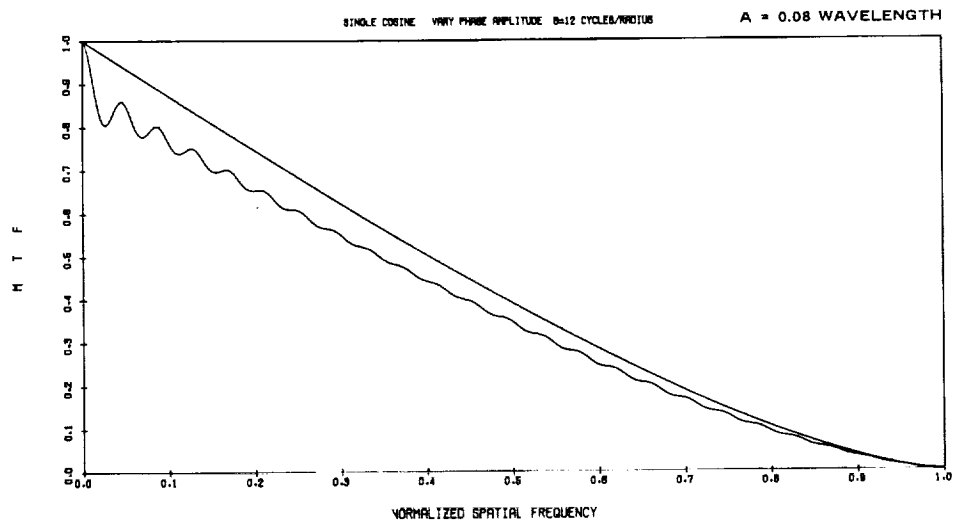


Fig. 4-2 — Continued

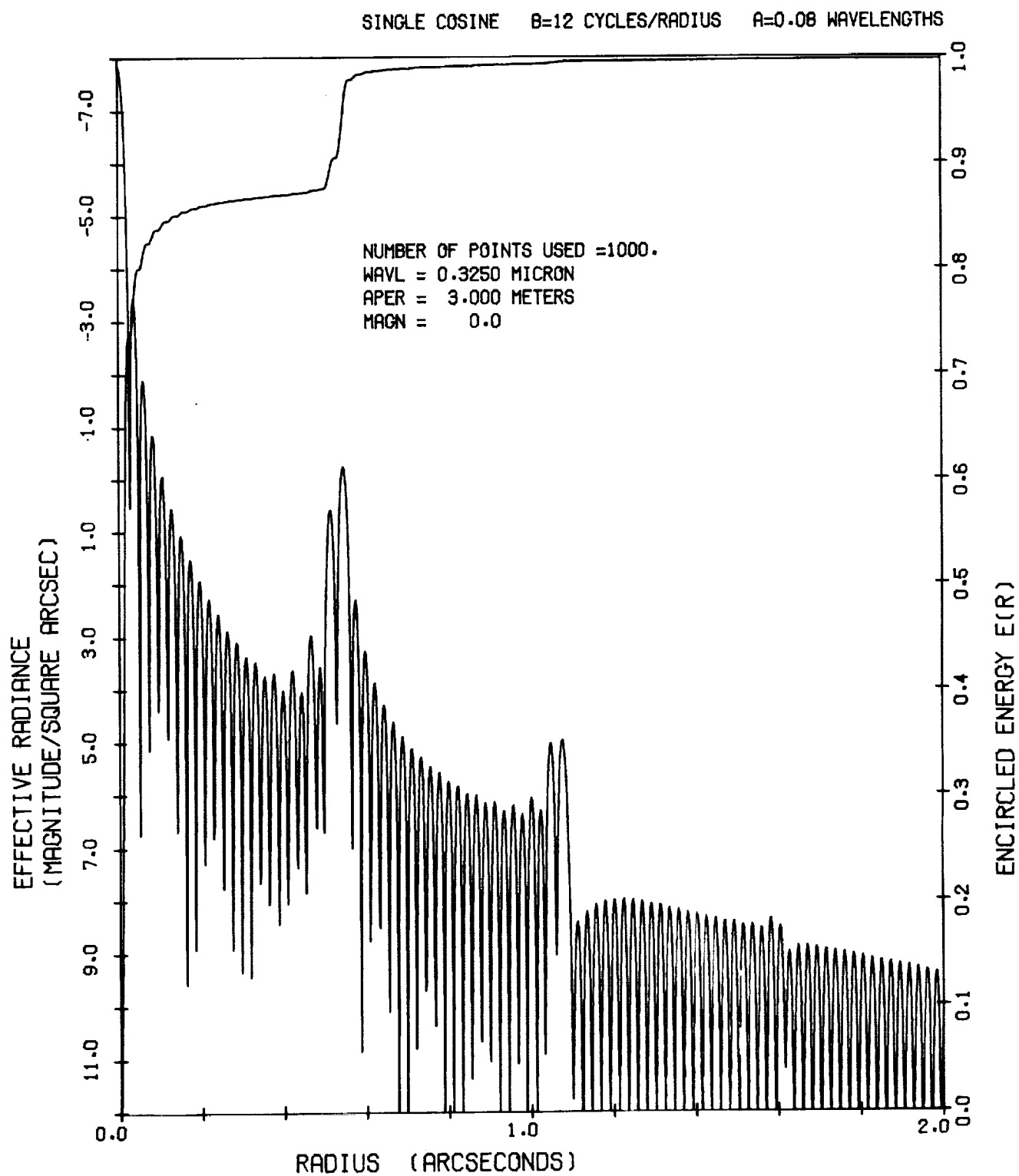


Fig. 4-3 — Effective object radiance for a tenth magnitude and the wavefront error shown in Fig. 4-2

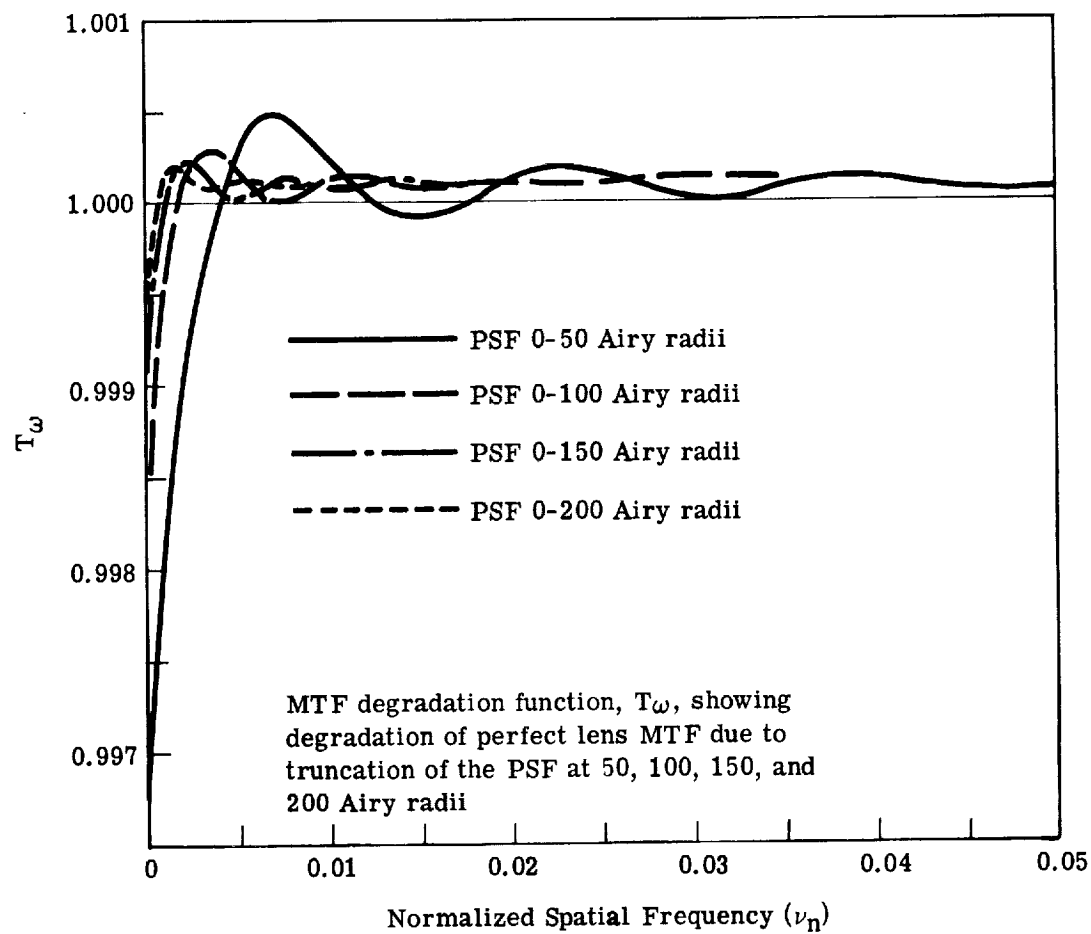


Fig. 4-4 — MTF accuracy at low  $\nu_n$  for GASPR

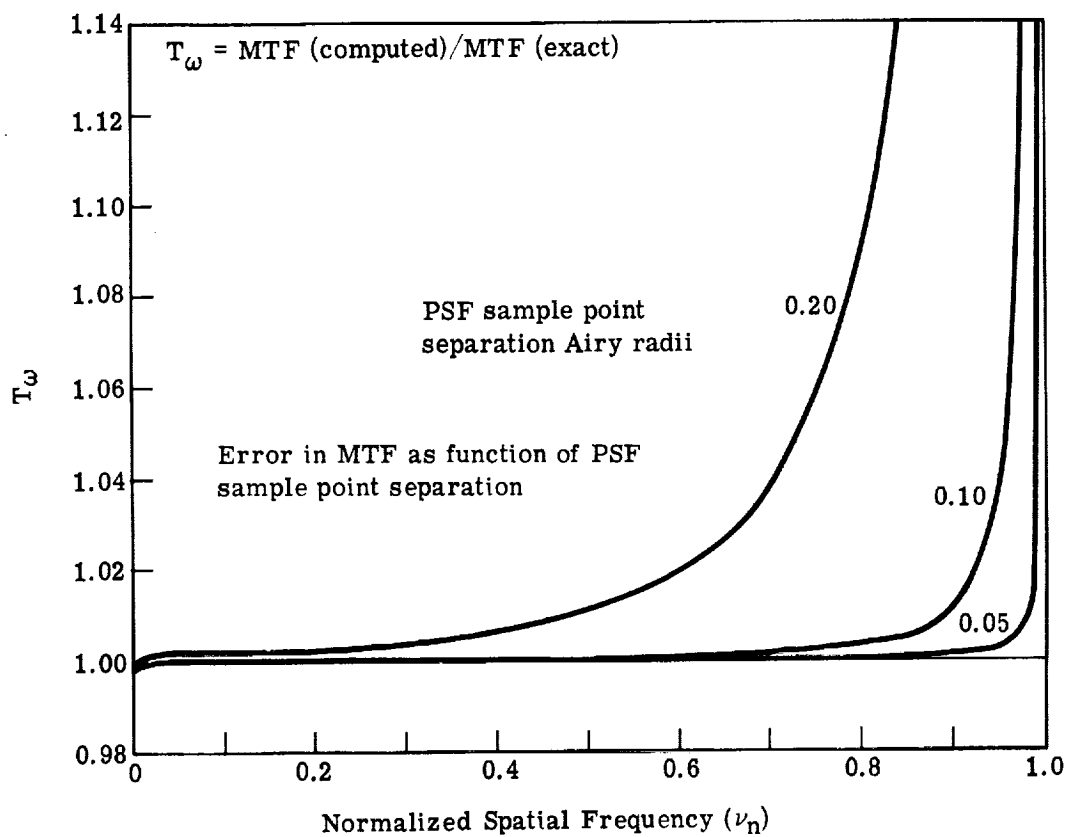


Fig. 4-5 — MTF accuracy at high  $\nu_n$  for GASPR

$$A_n = (i)^n J_n(\Delta\phi) = (i)^n J_n(2\pi a), \quad (17)$$

$J_n$  being the  $n$ th order Bessel function of the first kind, and  $n = 0$  corresponding to the undeviated wavefront.

Barakat<sup>2</sup> considered the case of a single rotationally symmetric cosine phase grating and computed the resulting MTF. Although he did not discuss the PSF extensively, he did derive an equation for the Strehl definition. In our terminology,

$$\mathcal{D} = [J_0(2\pi a)]^2 \quad (18)$$

Note that this is equal to  $A_0^2$ . This leads one to suppose that the rest of Eq. 17 might have some application to the rotationally symmetric case.

The rotationally symmetric cosine phase grating diffracts light into a series of sidebands which can be defined by Eq. 16. The diffracted light is not traveling as two plane waves, however. Rather it is traveling in directions defined by the shells of cones whose apex half-angles are defined by  $\alpha_n$ . If we assume that each order contains the same energy as is diffracted into the corresponding order for a linear phase grating, then the fractional displaced energy  $\Delta DE_n$  is given by

$$\Delta DE_n = 2[J_n(2\pi a)]^2 \quad (19)$$

To compute the relative intensity, one would presumably divide by the circumference of the cone of order  $n$ ,  $2\pi r_n$ , with the radius  $r_n$  expressed in some appropriate units. An empirical solution to this will be given below.

Further examination of the properties of rotationally symmetric cosine phase gratings will be done in terms of specific examples, keyed to GASPR outputs. These will cover single spatial frequencies, combinations of two spatial frequencies, and multiple spatial frequencies.

#### 4.2.1 Single Spatial Frequency

In Eq. 3 there are three variables, spatial frequency  $b$ , phase amplitude  $a$ , and the phase angle  $\phi$ . In addition, the pupil may have a central obstruction of differing diameter ratio  $\epsilon$ . We will consider the effects of varying all four quantities. First, however, it is useful to rewrite Eq. 16 in terms of  $b$ .  $b$  is given in cycles per radius. Thus  $d = D_p/2b$ , and

$$\sin \alpha_n = \pm 2nb\lambda/D_p \quad (20)$$

The radius of the sideband can then be written in terms of Airy radii  $1.22\lambda/D_p$  or in terms of the unit  $\lambda/D_p$ , which is sometimes termed a Rayl:

$$r_{An} = 1.64nb \text{ (Airy units)} \quad (21)$$

$$r_{Rn} = 2.0nb \text{ (Rayls)} \quad (22)$$

##### 4.2.1.1 Variation of Spatial Frequency

Fig. 4-6 shows the PSF plots for three cosine phase gratings of different spatial frequencies.  $a = 0.02$  wavelength and  $\phi = 0$  in all three cases.  $b = 12, 27$ , and  $39$  cycles per radius, respectively, from top to bottom in the figure. The first order sideband is clearly defined, and the second order sideband can be seen weakly. A close comparison with a perfect lens PSF would show a slight increase in the relative intensity in the region between the two harmonics, and a reduction in relative intensity outside that region.

The peak intensity of the first order sideband can be approximated fairly well by the equation

$$I^*(b) = \pi a^2 / 2b = \pi a^2 / 1.22 r_{Am} = \pi a^2 / r_{Rm} \quad (23)$$

where the asterisk indicates that this is the relative intensity, normalized to the value at  $r = 0$  for a perfect lens. Table 4-2 compares results.

Table 4-2 — Relative Intensities for Cosine Phase Gratings of the Same Phase Amplitude and Different Spatial Frequencies

b	$I^*$ (computer)	$I^*$ (Eq. 23)
12	$5.35 \times 10^{-5}$	$5.24 \times 10^{-5}$
27	$2.34 \times 10^{-5}$	$2.33 \times 10^{-5}$
39	$1.63 \times 10^{-5}$	$1.61 \times 10^{-5}$

Expanding the Bessel function of Eq. 19 for  $n = 1$  and comparing the results to Eq. 23 shows the latter to be similar to the first term in the expansion. One can speculate that a more general form of Eq. 23 can be written:

$$I_n^*(b) = [J_n(2\pi a)]^2 / 2\pi mb, n = 1, 2, 3, \dots \quad (24)$$

In effect, Eq. 24 states that the relative intensity in the  $n$ th order sideband equals the total energy in that sideband (Eq. 19) divided by the sideband "circumference" measured in Rayls. The validity of this equation will be tested in the next section.

Examination of the displaced energy function  $EE(perf) - EE$  indicates that energy is displaced outward from the center of the PSF and inward from beyond the second order sideband. Table 4-3 lists data for the first two cases. (The second harmonic for  $b = 39$  is outside 100 Airy radii.)

Table 4-3 — Displaced Energy for Single Cosine Phase Gratings for Spatial Frequencies of 12 and 27 Cycles Per Radius

b	12	27
Radius for maximum outward displacement, $r_1$	13.4	28.2
$DE(r_1)$	0.007641	0.007719
Radius for maximum inward displacement, $r_2$	39.6	88.8
$DE(r_2)$	-0.000140	-0.000118
Total DE	0.007781	0.007837
Strehl definition, $\mathcal{D}$	0.992128	0.992128
$1 - \mathcal{D}$	0.007872	0.007872

Thus, Strehl definition is an excellent definition of total displaced energy in this case for small wavefront error.



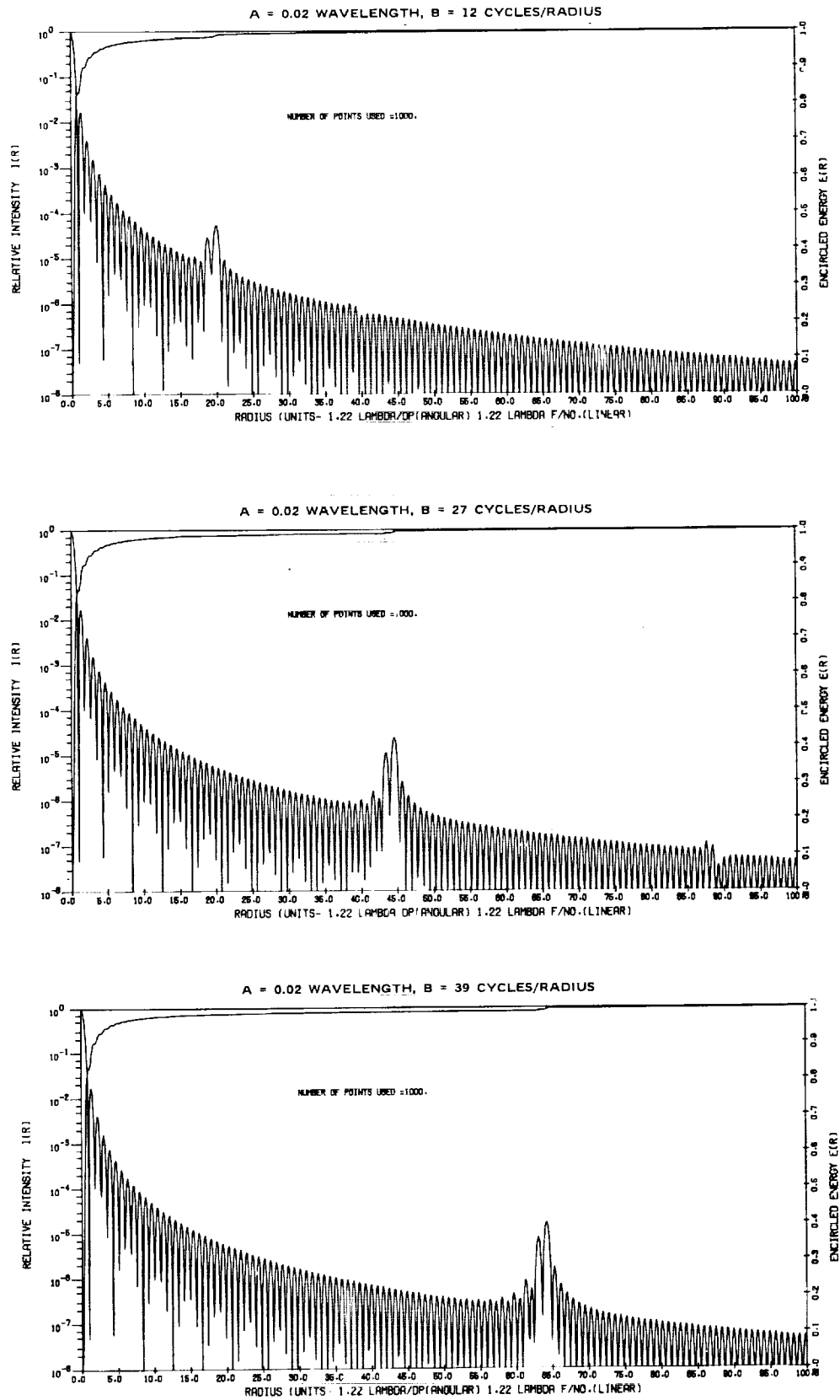


Fig. 4-6 — PSF's for single cosine phase gratings of different spatial frequency

#### 4.2.1.2 Variation of Phase Amplitude

Fig. 4-7 shows three PSF's for cosine phase gratings of different phase amplitudes. Coupled with Figs. 4-2 and 4-6a, they complete a series of five cases in which the phase amplitude  $a = 0.02, 0.04, 0.08, 0.16$ , and  $0.38274$  wavelengths. The last value was selected because it reduces the Strehl definition to zero, in accordance with Eq. 18. All five examples have the same spatial frequency,  $b = 12$  cycles per radius, and phase angle,  $\phi = 0$ .

Fig. 4-7c, for which  $a = 0.38274$ , presents a good test for the validity of Eq. 19, for  $\Delta DE_n$ , and 24, for  $I_n^*$ . Table 4-4 summarizes the calculations. The values for  $I_n^*$  agree quite well.

Table 4-4 — Relative Intensity and Energy Distribution for  
PSF of Cosine Phase Gratings ( $a = 0.38274$ ,  $b = 12$ )

$n$	$I_n^*$ (computer)	$I_n^*$ (Eq. 24)	$\Delta DE_n$ (Eq. 19)
1	$3.60 \times 10^{-3}$	$3.56 \times 10^{-3}$	53.7%
2	$1.25 \times 10^{-3}$	$1.24 \times 10^{-3}$	37.3%
3	$1.75 \times 10^{-4}$	$1.75 \times 10^{-4}$	7.9%
4	$1.36 \times 10^{-5}$	$1.39 \times 10^{-5}$	0.84%
5	$8.07 \times 10^{-7}$	$7.13 \times 10^{-7}$	0.054%

A comparison of the values for  $\Delta DE_n$  to the encircled energy curve in Fig. 4-7c also shows good agreement.

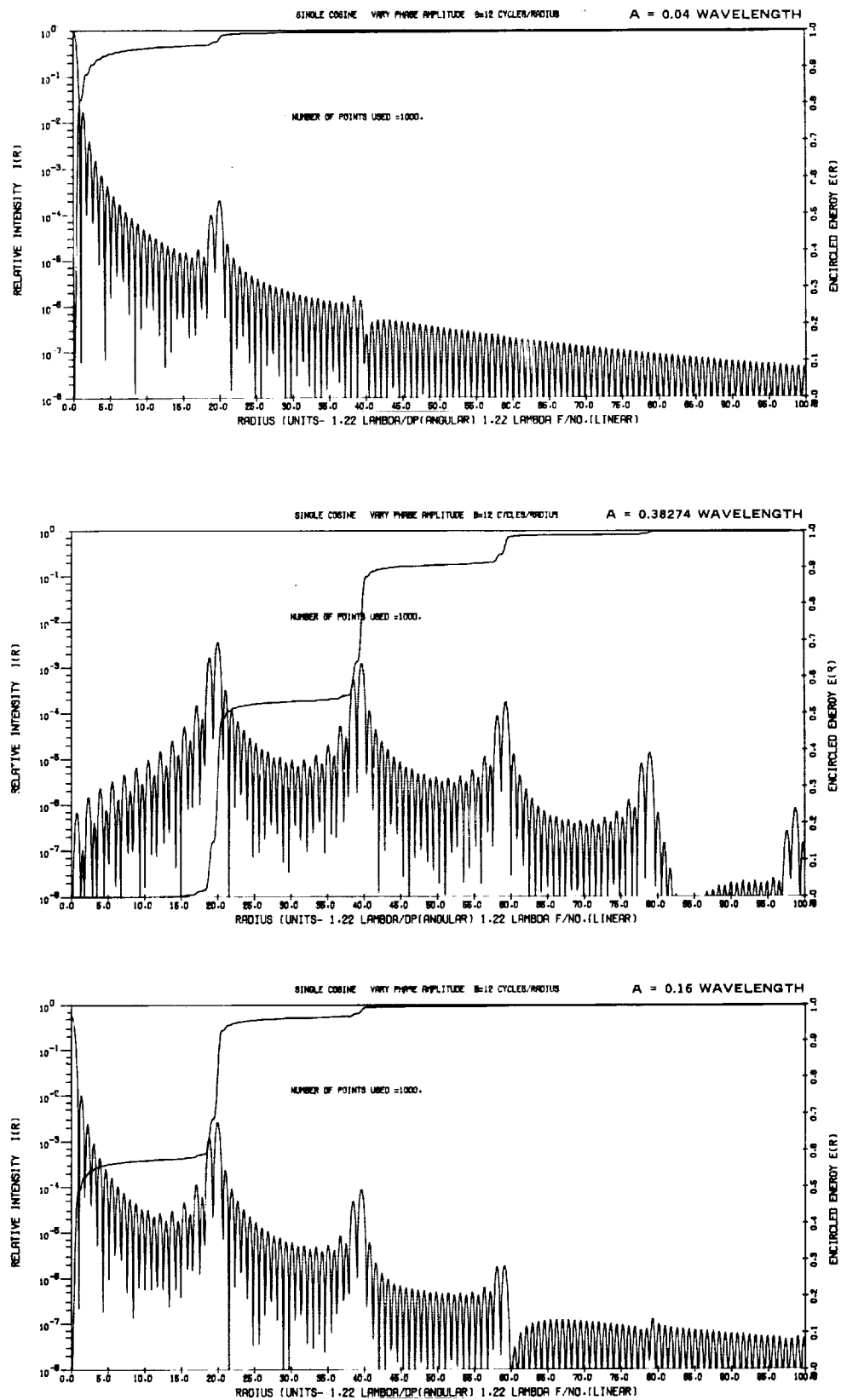


Fig. 4-7 — PSF's for single cosine phase gratings of different phase amplitude

#### 4.2.1.3 Variation of Phase Angle

Changing the phase angle  $\phi$  varies the internal structure of the sideband and alters its maximum relative intensity. No change is made in the general distribution of energy, however Fig. 4-8 shows the changes in internal structure of the first sideband for  $\phi = 0, \pi/4, \pi/2$ , and  $3\pi/4$ . Values of  $\phi$  differing by  $\pi$  produce identical PSF's. Numerical data is presented in Table 4-5. This data, and other data not presented, indicates that the exact position of the maxima within the sideband can be calculated by the equation

$$r_{An} = 1.64nb + \text{constant} \quad (25)$$

where the values of the constant associated with each phase angle are given in the Table 4-5.

Table 4-5 — Variation of Sideband Internal Structure With Phase Angle  $\phi$   
( $a = 0.02$ ,  $b = 20$  cycles per radius)

$\phi$	$r_A$	$I_1^*(r_A)$	Constant
0	33.1	$3.19 \times 10^{-5}$	+0.3
$\pi/4$	32.2	$2.46 \times 10^{-5}$	-0.6
	33.4	$2.44 \times 10^{-5}$	+0.6
$\pi/2$	32.5	$3.38 \times 10^{-5}$	-0.3
$3\pi/4$	32.8	$3.55 \times 10^{-5}$	0

$A = 0.02$  WAVELENGTH,  $B = 20$  CYCLES/RADIUS,

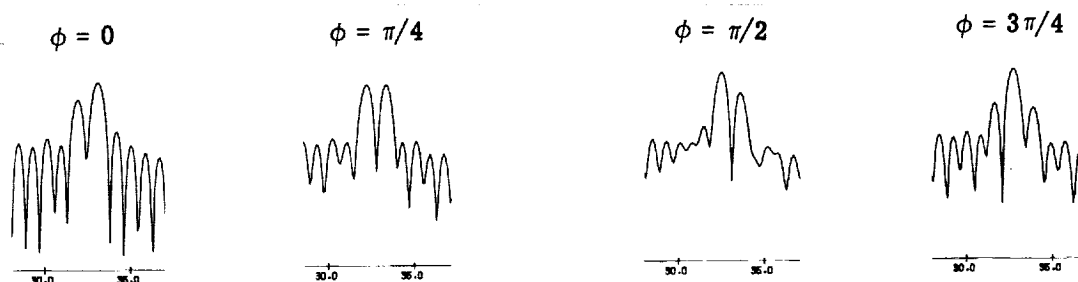


Fig. 4-8 — Effects of varying phase angle  $\phi$

#### 4.2.1.4 Variation of Central Obstruction Diameter Ratio

Figs. 4-9, 4-10, and 4-11 combine to illustrate the effects a central obstruction will have on a lens with wavefront error in the form of a cosine phase grating. Figs. 4-9 and 4-10 show how the PSF is affected by the phase grating alone and the central obstruction alone. The phase grating has the constants  $b = 20$  cycles per radius and  $a = 0.0707$  wavelength. The latter was selected to give an rms wavefront error  $\omega = 0.050$  wavelength ( $\omega = a \times 2^{-1/2}$  for a cosine phase grating). The central obstruction diameter ratios  $\epsilon = 0.40, 0.60$ , and  $0.80$  were selected to show the effects of varying the diameter ratio, rather than to be representative of the LST.

It is immediately evident that increasing the central obstruction diameter ratio spreads out the energy in the first order sideband for the cosine phase grating. Several more subtle effects become evident when the displaced energy data is examined closely: (1) A cosine phase grating will displace an amount of energy which is approximately equal to  $1 - \mathcal{D}$ , the Strehl definition. A central obstruction will displace more energy than its Strehl definition would indicate. (2) A combination of a cosine phase grating and a central obstruction will displace less energy from the central core of the image than the sum of the energy displacements for the two taken separately. (3) Conversely, at radii larger than that of the first order sideband, the combination will displace more energy than the sum of the two considered separately. The third effect may be an indication that a central obstruction affects scattered light more adversely than linear addition of effects might imply. However, the effect is quite subtle.

Fig. 4-12 shows the MTF's for a cosine phase grating with and without a central obstruction  $\epsilon = 0.60$ , and Fig. 4-13 shows the corresponding \*Autocorrelation functions. The upper curves in Fig. 4-12 represent the zero wavefront error case. The lower curves appear to have been multiplied by a degradation function which consists of a base spatial frequency independent constant overlayed with a spatial frequency dependent oscillation, and the \*Autocorrelation functions bear this out. The fact that the \*Autocorrelation functions oscillate about zero indicates that the constant term is  $\exp [-(2\pi\omega)^2]$ . The central obstruction damps out the overlaying oscillation at middle spatial frequencies, the size of the damped region being a direct function of the central obstruction diameter ratio. The \*Autocorrelation plots also indicate the degree to which truncation error affects the value of this function at  $\nu_n = 0$ , where  $\Phi_{11} = 1.0$ , by definition. (The PSF was truncated at 50 Airy radii for this computer run.)

Two conclusions can be drawn: (1) The central obstruction and the wavefront error do interact in degrading the MTF, but in a subtle manner. On a gross scale, the MTF degradation functions for each may be treated independently. (2) The MTF degradation function of Eq. 1 is valid for use with cosine phase gratings, although  $\Phi_{11}$  becomes a rather complicated function.

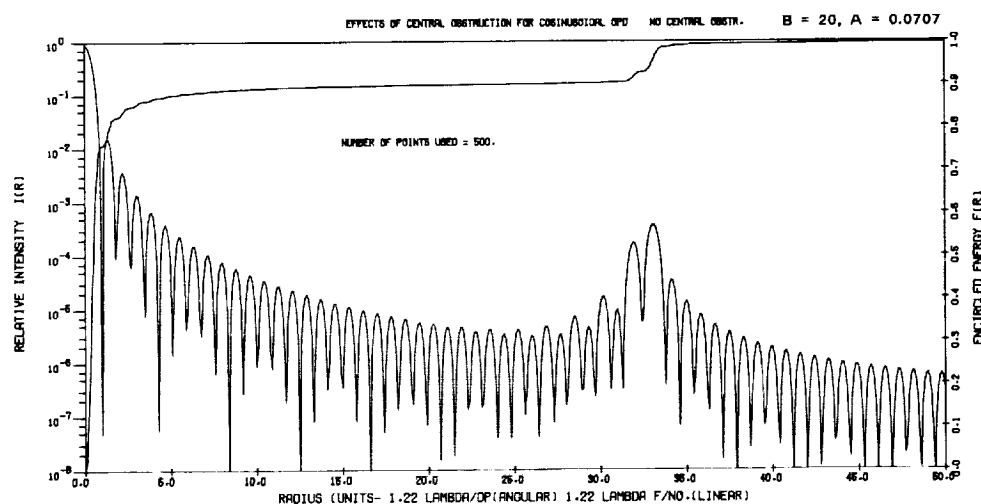


Fig. 4-9 — PSF without central obstruction

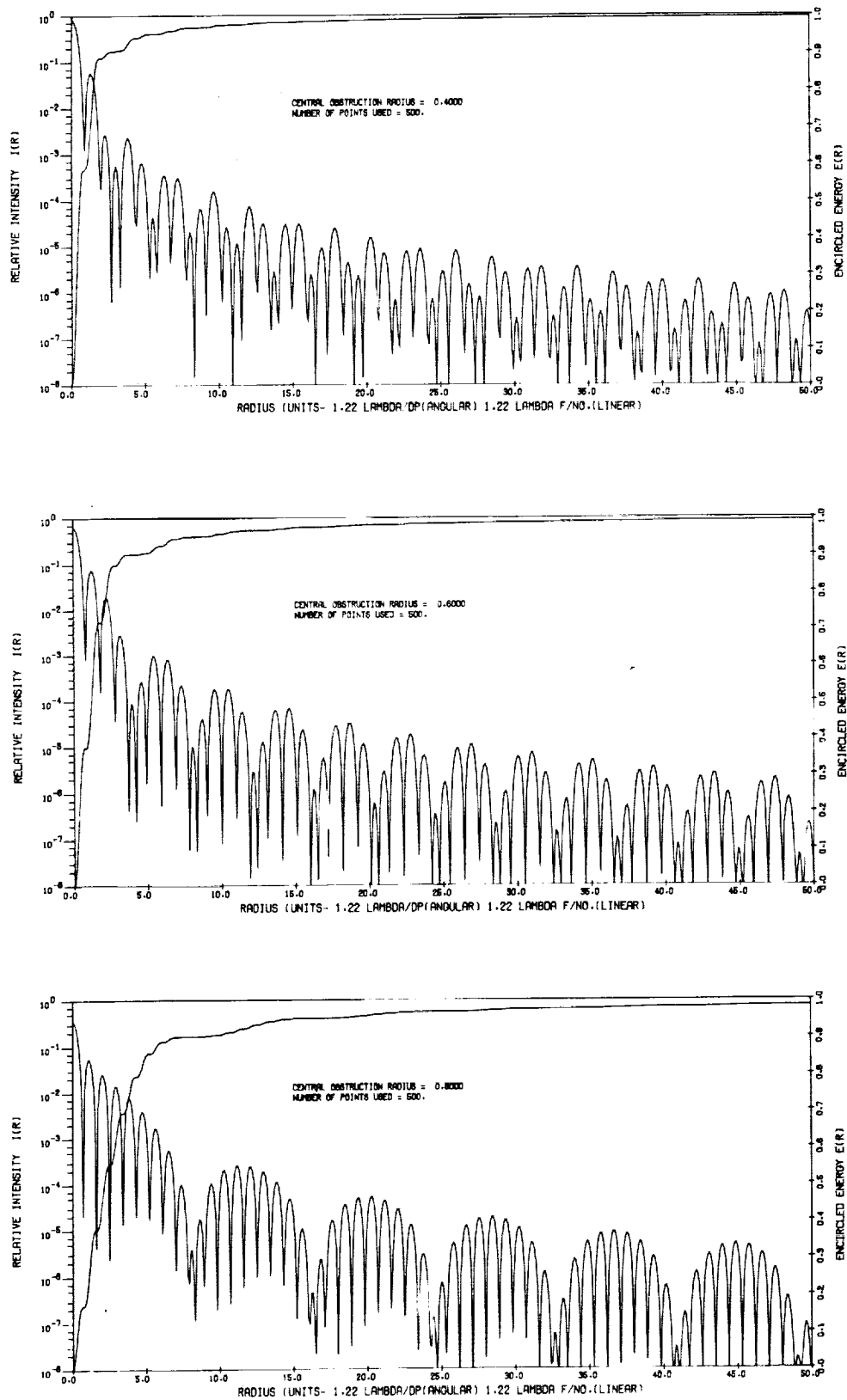


Fig. 4-10 — PSF for central obstruction alone

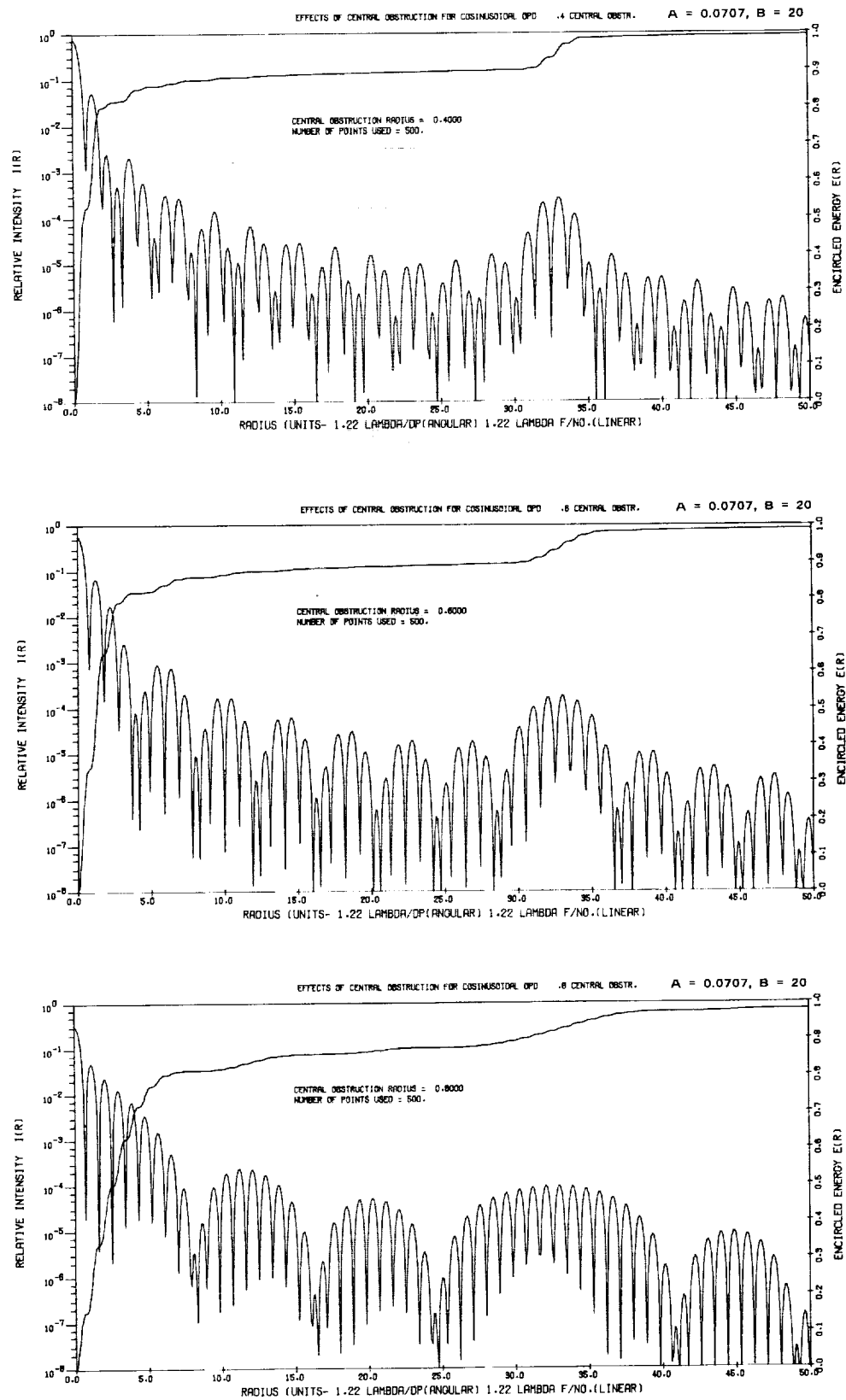


Fig. 4-11 — PSF for central obstruction with cosine phase grating

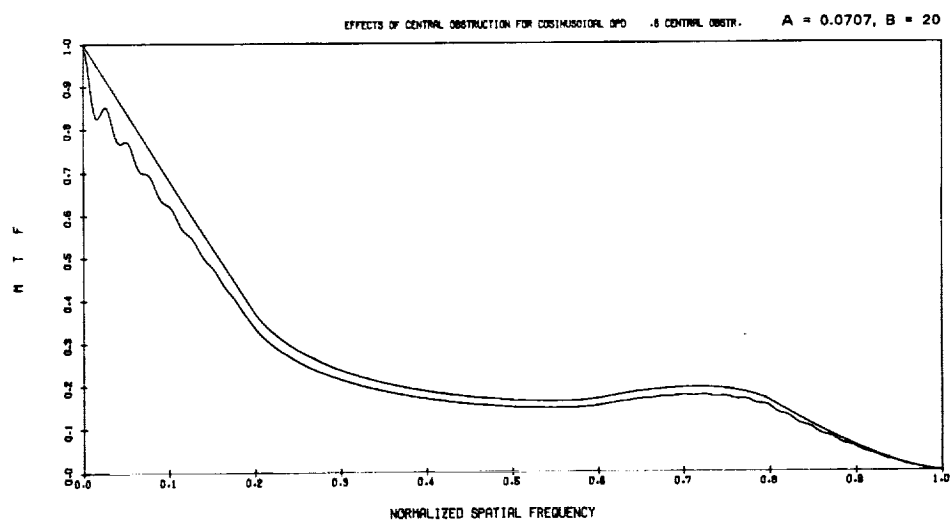
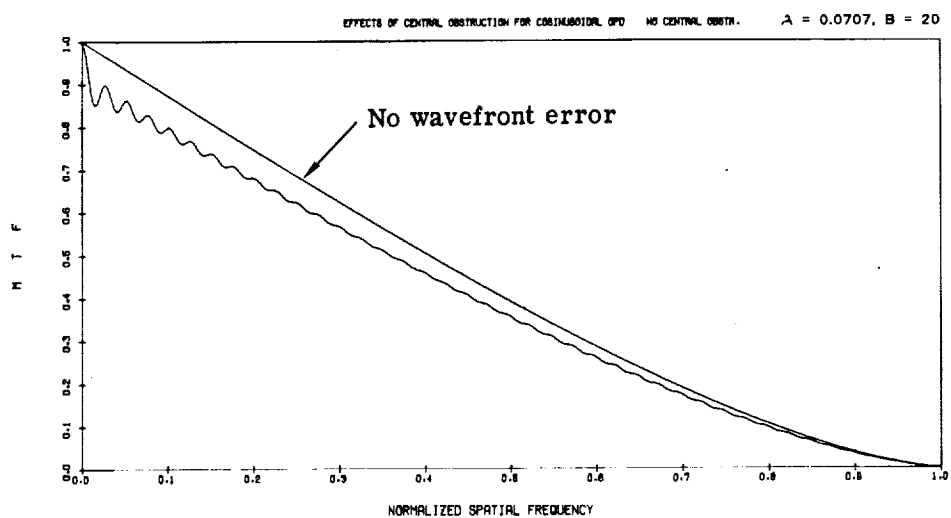


Fig. 4-12 — MTF with and without obstruction



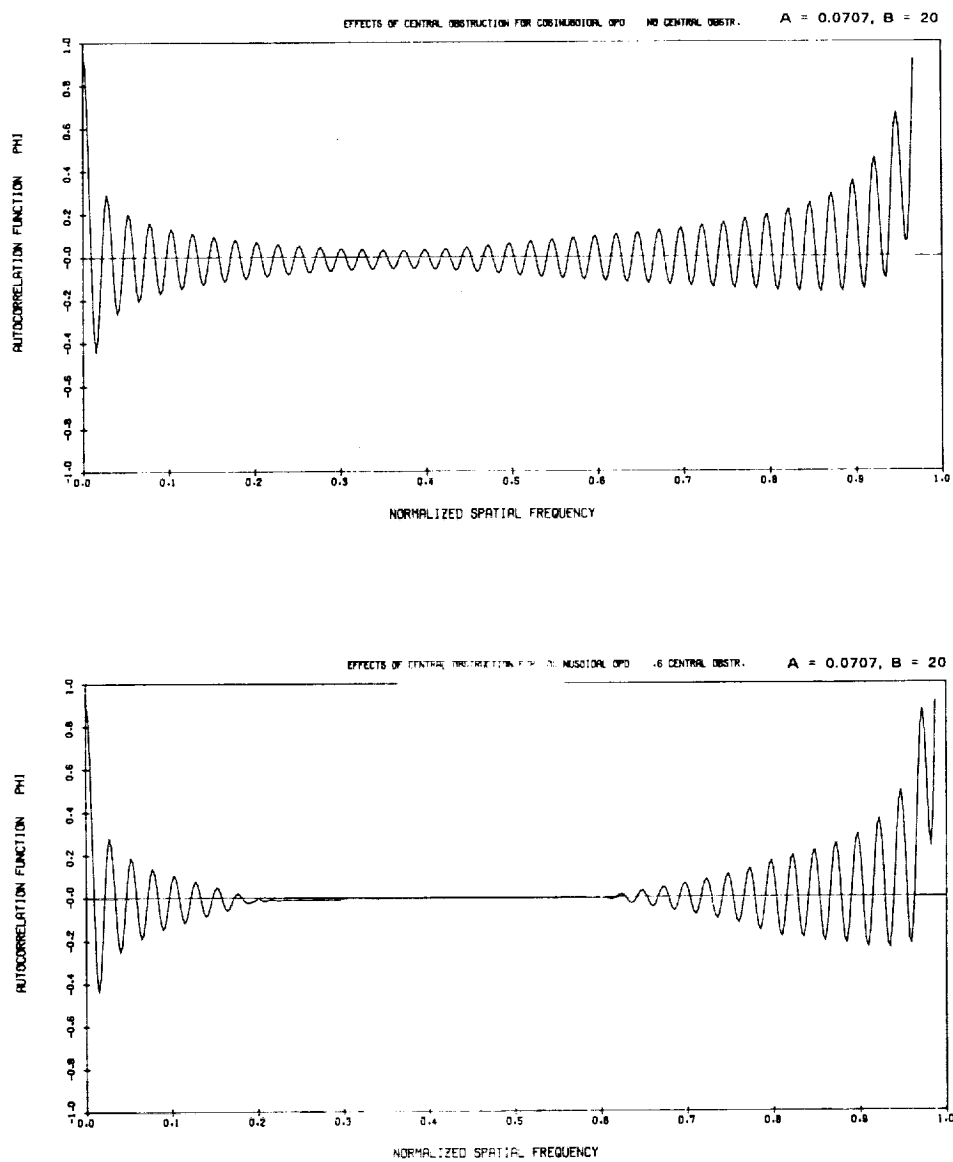


Fig. 4-13 — \*Autocorrelation function with and without obstruction

#### 4.2.2 Two Spatial Frequencies

Combining two cosine phase gratings in one OPD function gives some indication of the degree to which there is any interaction between sidebands produced by each. There are two significantly different cases: first, where one of the cosine phase gratings has a very low spatial frequency, and second, where both have high but well separated spatial frequencies. In this presentation, only one set of examples will be given for each, representing the principal conclusions to be drawn. Closely spaced high spatial frequency phase gratings will be dealt with in the section on multiple spatial frequencies.

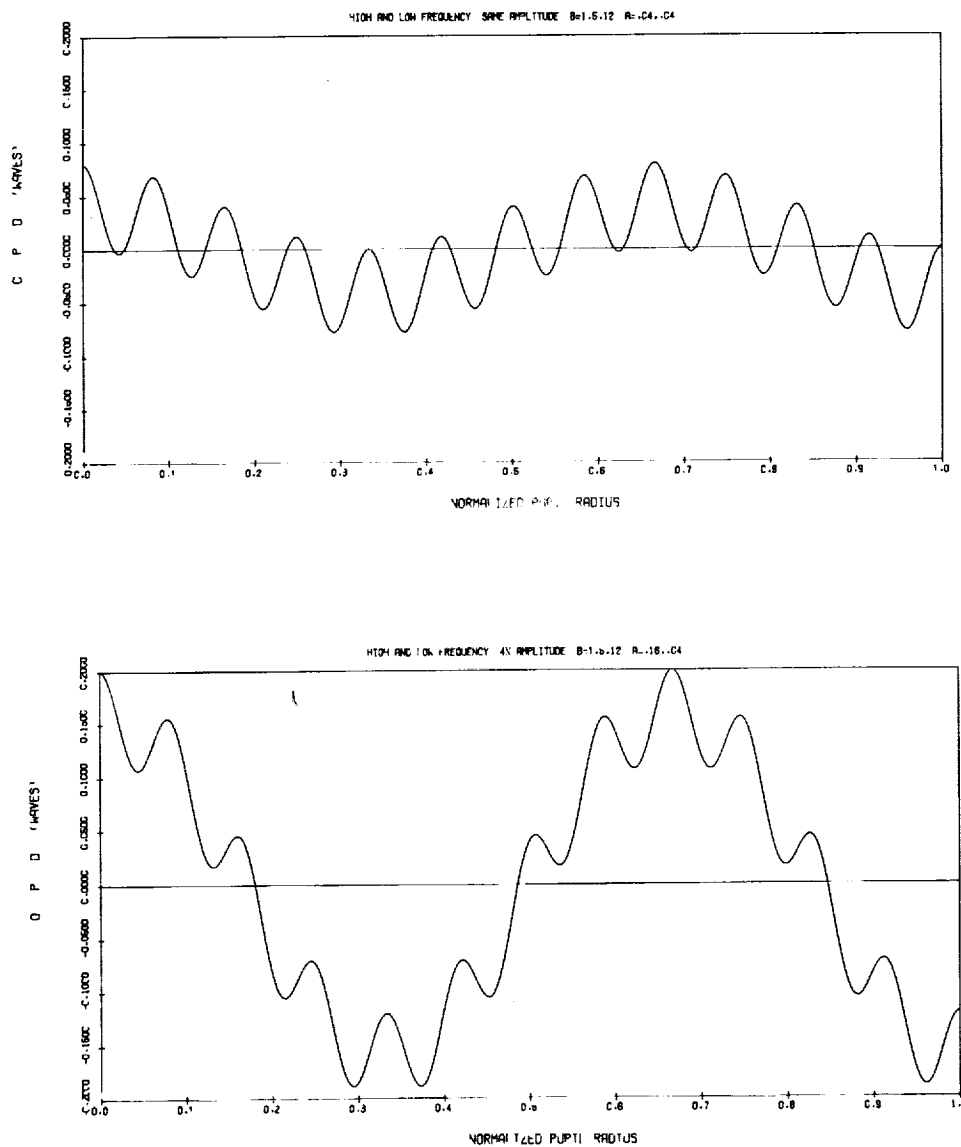


Fig. 4-14 — OPD waveforms for phase gratings

#### 4.2.2.1 Effect of Adding Very Low Spatial Frequency Component

The high spatial frequency component has the constants  $b = 12$  cycles per radius and  $a = 0.04$  wavelength. The PSF for this function alone is shown in Fig. 4-7a on a 100 Airy radii scale. The low frequency component has a spatial frequency of 1.5 cycles per radius, and can be considered to represent figure error. Its phase amplitude is set to 0.04 and 0.16 wavelengths, in the two examples shown. The OPD waveforms for both examples are shown in Fig. 4-14, and the resulting PSF's are shown in Fig. 4-15.

It is clear that the low spatial frequency component is significantly modifying the internal configuration of the sidebands due to the higher spatial frequency component. However, the amount of energy in the first order sideband has not been changed significantly, only spread out somewhat. Between 13 and 28 Airy radii,  $\Delta DE = 0.03025$ ,  $0.03033$ , and  $0.03059$  for  $a = 0$ ,  $0.04$ , and  $0.16$ , respectively, for the lower spatial frequency.

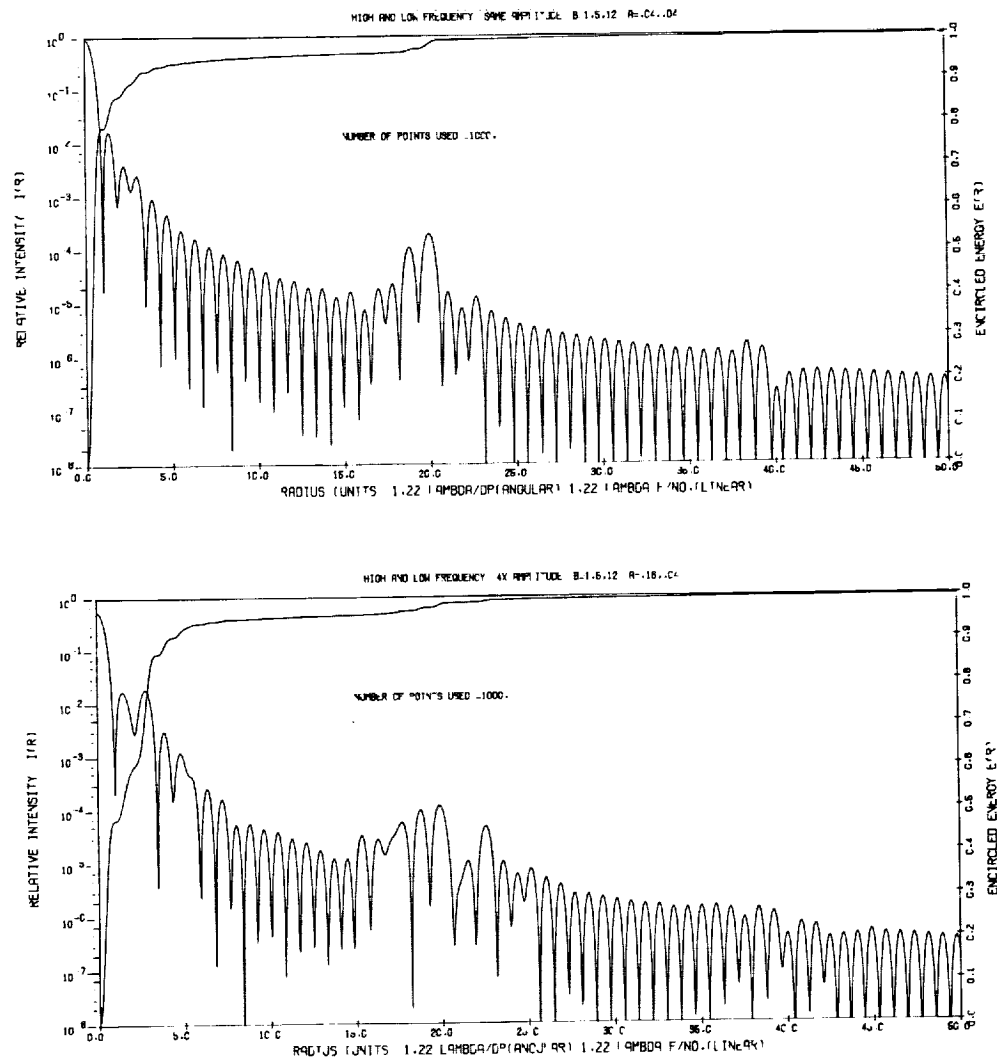


Fig. 4-15 — PSF's for combination high and low spatial frequency waveforms

#### 4.2.2.2 Interaction of High Spatial Frequency Components

Combinations of higher spatial frequency cosine phase gratings do not interact in the same way as the combination of a very low spatial frequency grating and a higher spatial frequency grating. This is illustrated in Figs. 4-16 and 4-17. The two cosine gratings are of spatial frequencies 18 and 25 cycles per radius. Both are maintained at the same phase amplitude which is scaled to 0.02, 0.08, and 0.16 wavelength. The phase angles are set to 0 and  $\pi$  radians to eliminate peaking at 1.0 normalized radii. Fig. 4-16 shows the composite OPD waveform for the 0.02 phase amplitude case. Fig. 4-17 shows the PSF plots for the three cases cited above.

At low phase amplitudes, there is very little interaction between the first order sidebands. As the amplitude is increased, however, a number of other sidebands show up in the PSF. Some of these are higher order terms of the two fundamental spatial frequencies. Thus, in accordance with Eq. 25, sidebands for  $b_1 = 18$  show up at  $r_{A11} = 29.8$ ,  $r_{A12} = 59.3$ , and  $r_{A13} = 88.9$ , and sidebands for  $b_2 = 25$  show up at  $r_{A21} = 41.3$  and  $r_{A22} = 82.3$  Airy radii. More interestingly, sidebands show up at beat frequencies: the two brightest sidebands for  $a = 0.16$  wavelength, with the exception of the first order sidebands, are at 11.8 and 70.8 Airy radii and correspond to  $b_2 - b_1$  and  $b_2 + b_1$ . These divert significant amounts of energy from the first-order sidebands, and consequently reduce their relative intensity, as predicted by Eq. 24. Note, however, that the internal structure of the individual sidebands is not altered significantly, as by a central obstruction or by figure error.

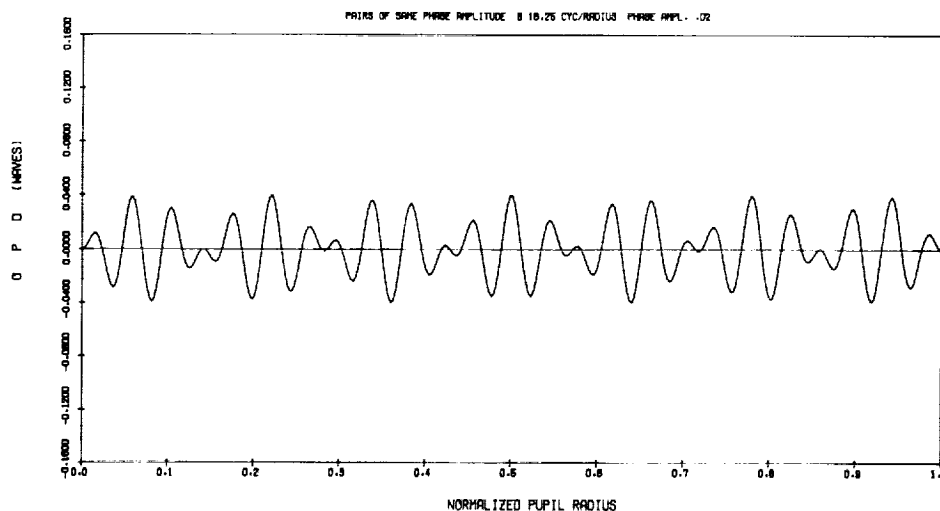


Fig. 4-16 — OPD waveform;  $b_1 = 18$ ,  $b_2 = 25$ ,  $a_1 = a_2 = 0.02$ ,  $\phi_1 = 0$ ,  $\phi_2 = \pi$

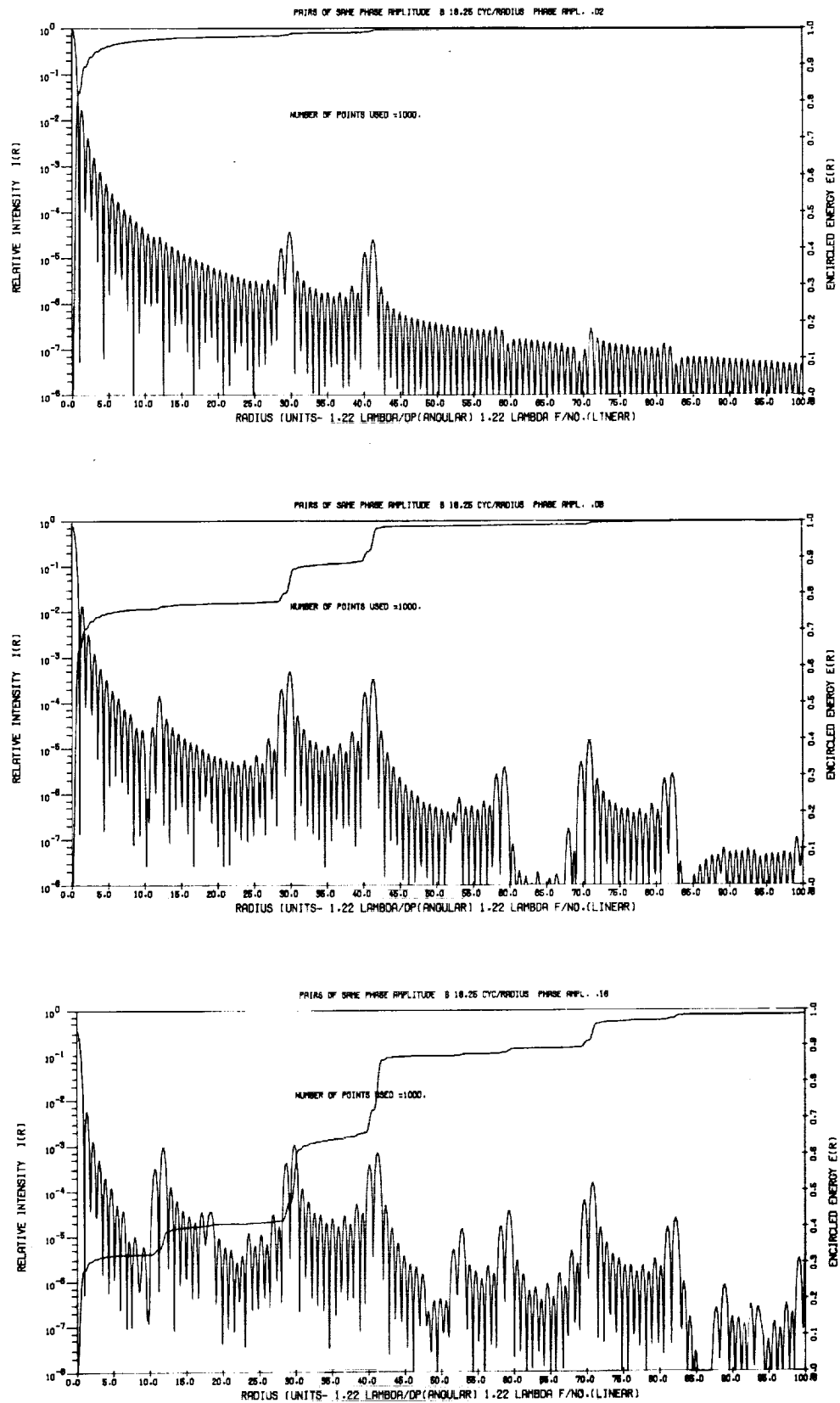


Fig. 4-17 — PSF's for two-cosine phase gratings of waveform of Fig. 4-16

### 4.2.3 Multiple Spatial Frequencies in Combination

The final cosine phase grating combination we examine is a combination of four spatial frequencies in which the difference in frequency between component phase gratings is varied. All components have the same phase amplitude,  $a = 0.04$  wavelength, and the phase angle  $\phi$  is alternated in order of increasing spatial frequency,  $0, \pi, 0, \pi$  radians. The spatial frequency combinations are: 24, 30, 36, 42 cycles per radius; 24, 26, 28, 30 cycles per radius; and 24, 24.5, 25, 25.5 cycles per radius. The OPD waveforms are shown in Fig. 4-18, the corresponding PSF's are in Fig. 4-19, and MTF's are in Fig. 4-20.

As the spacing between components is reduced, the character of the OPD waveforms changes, as do their effects on the PSF and MTF. Down to 2 cycles separation, the four components behave independently, except for the formation of sum and difference sidebands of the type discussed in the last section. (This latter reduces the first-order sideband intensities somewhat.) The total rms wavefront error obeys the formulation

$$\omega = (\omega_1^2 + \omega_2^2 + \dots + \omega_n^2) \quad (26)$$

giving  $\omega = 0.0566$  wavelength rms for the first two examples. For the third example, however,  $\omega = 0.0722$ , and the OPD waveform is more nearly characteristic of a single spatial frequency which has been modulated by a low spatial frequency component. The effects are noted in the PSF by a change in the internal structure of the sideband and a disappearance of the sum and difference sidebands. The encircled energy function drops considerably below the first sideband, and the MTF drops measurably. Note in particular the MTF reduction at high spatial frequencies, a sign of the presence of very low spatial frequency components.

Finally, it should be noted that the interaction of phase gratings spaced as closely as in the third example is strongly dependent on the value of the phase angle  $\phi$ . Had a phase angle of zero been used for all four components, the OPD waveform would have been reversed, with the large phase amplitude excursions occurring in the section near the center of the pupil. This would have significantly reduced the net rms wavefront error, and would have affected the PSF and MTF very differently.

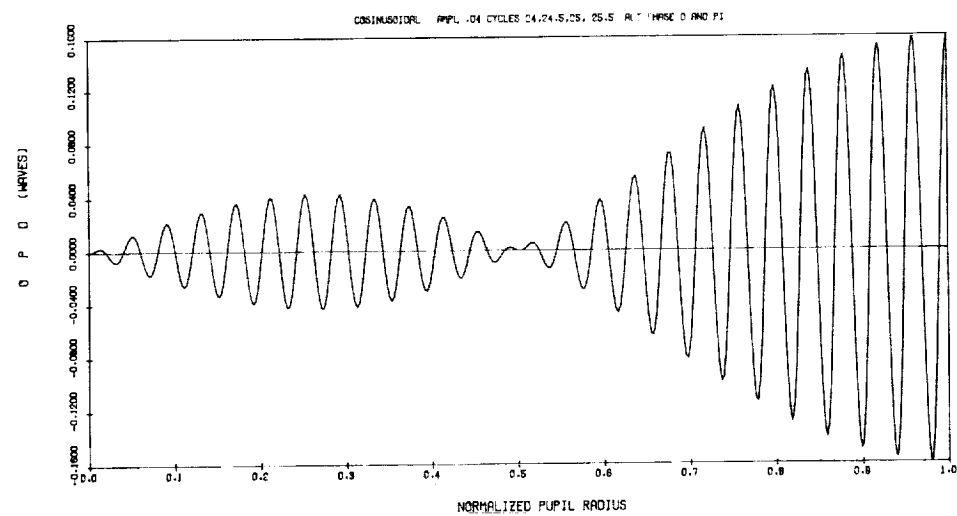
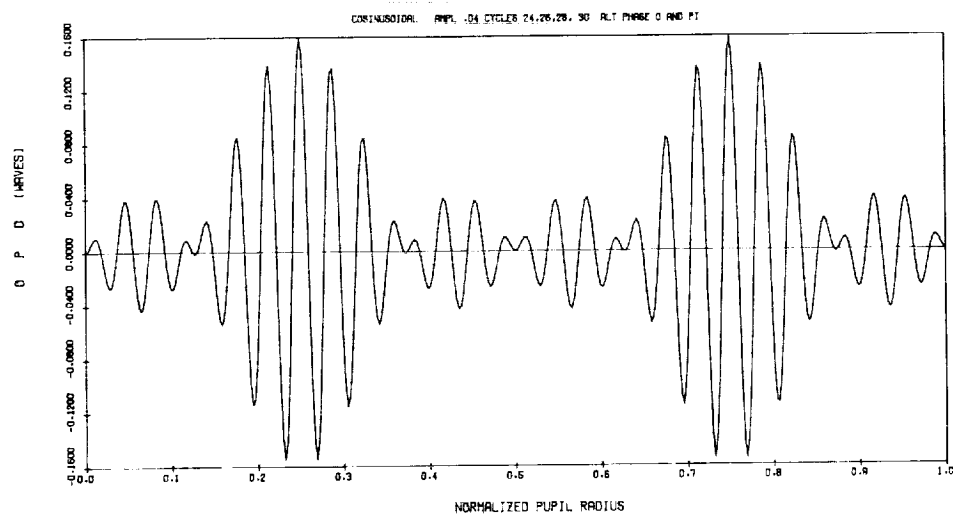
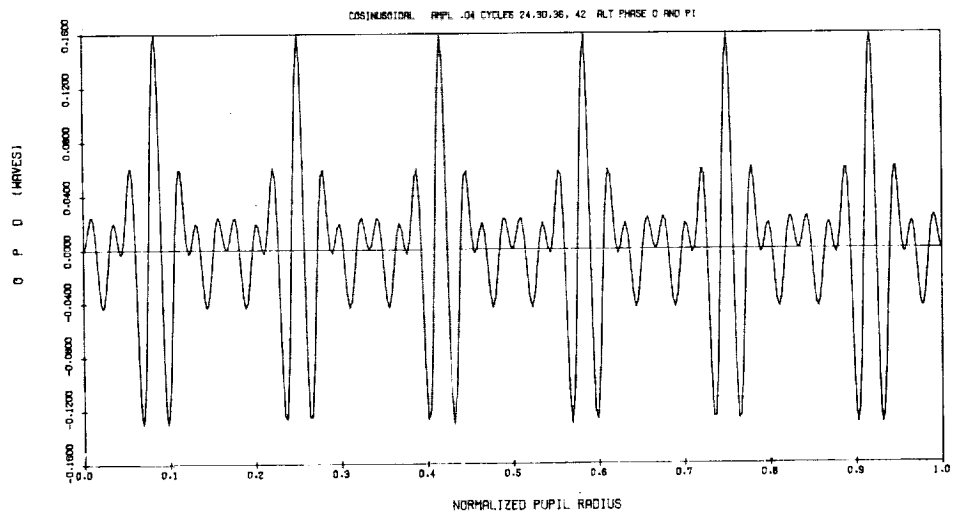


Fig. 4-18 — OPD waveforms for multiple spatial frequencies

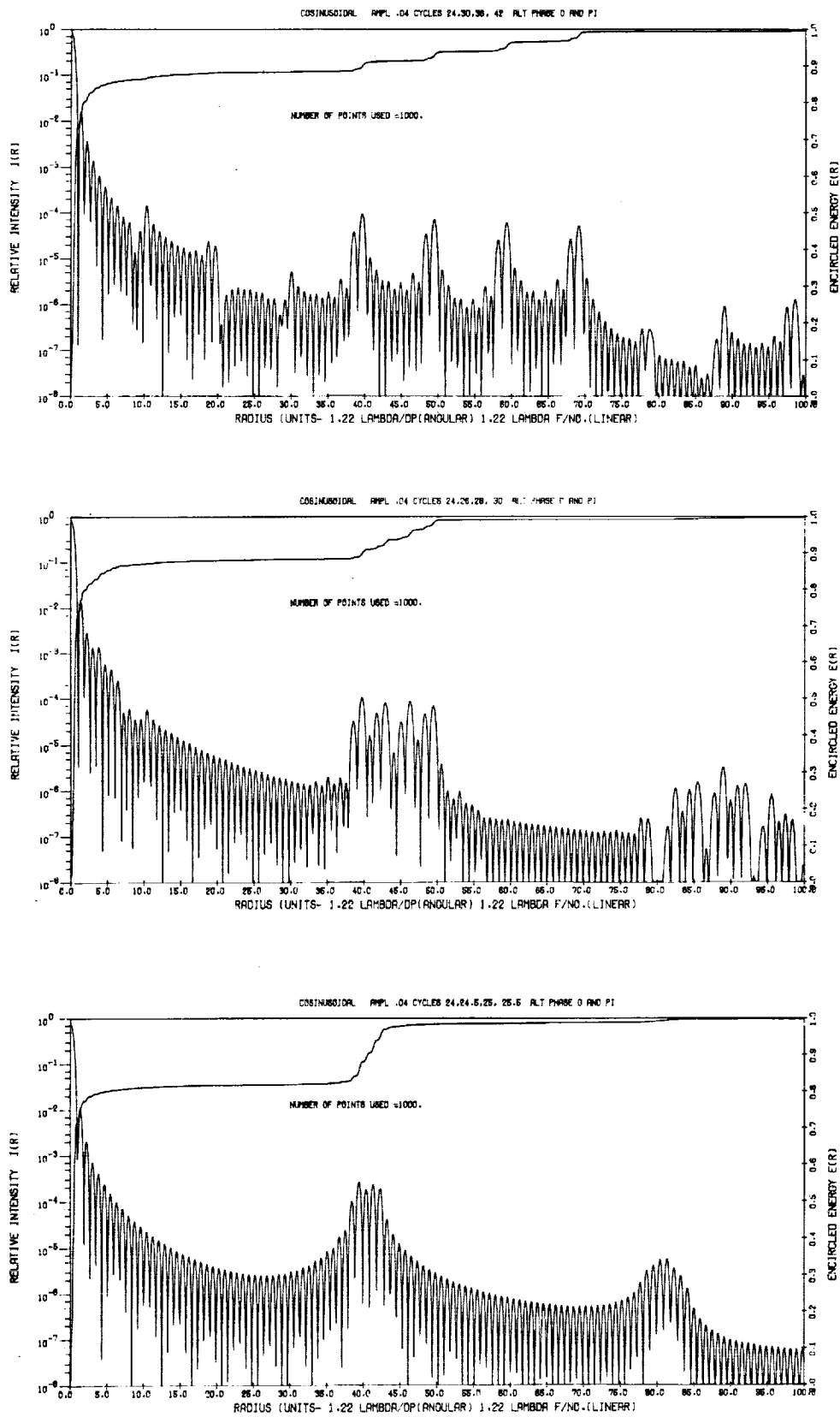


Fig. 4-19 — PSF's for multiple spatial frequencies



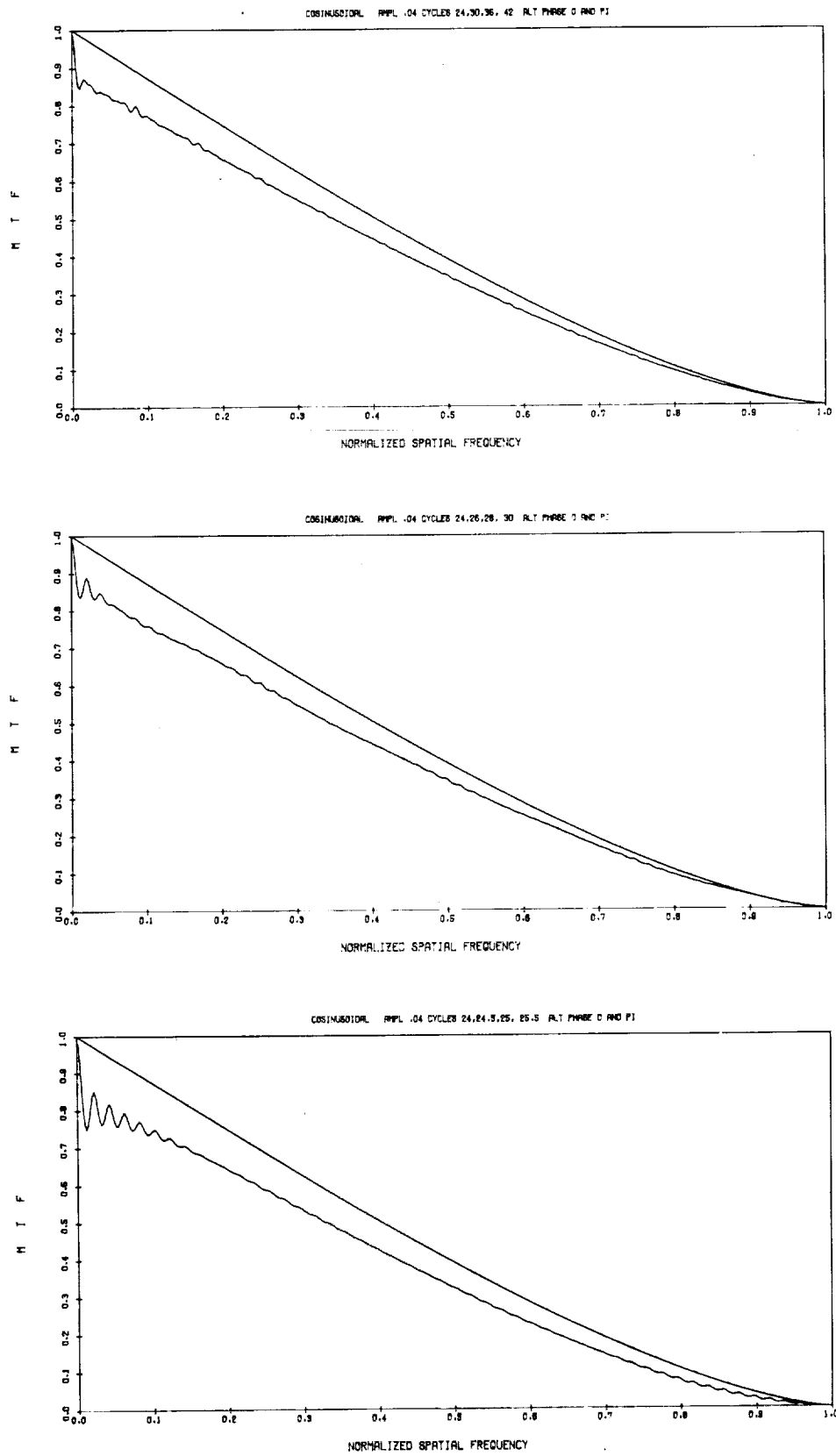


Fig. 4-20 — MTF's for multiple spatial frequencies

#### 4.2.4 Cosine Phase Gratings for Scatter Function Models

It seems logical to use Fourier decomposition of the wavefront error into a continuous or discrete spectrum of cosine phase gratings as a basis for modeling the scatter function. The preceding sections give graphic demonstrations of the difficulties involved. The interactions of different spectral components when closely spaced, or when in the presence of figure error or a central obstruction, make such analysis difficult except through programs such as GASPR. Nevertheless, some useful inferences can be drawn from a qualitative model which pictures the source of scattering as a series of very low phase amplitude cosine phase gratings well separated in spatial frequency. In building such a model, it is necessary to distinguish between linear phase gratings and rotationally symmetric phase gratings, since each affects the image in a different manner.

Eq. 23 gives the relative intensity of the first-order sideband of a rotationally symmetric cosine phase grating of small phase amplitude. The corresponding equation for a linear cosine phase grating is

$$I^* = \pi^2 a^2 \quad (27)$$

where  $a$  is the phase amplitude in wavelengths, as before. In a lens with a rotationally symmetric grating, the diffracted light will form a ring of light centered on the Airy disk of a star image. With a linear grating, the diffracted light will appear as two ghost images of the star. Note that with a linear grating, the relative intensity is independent of the spatial frequency of the grating, while for a rotationally symmetric grating, it is inversely proportional to the grating frequency. That is,

$$I_{\ell}^*(b_i) \propto a^2 \quad (\text{linear grating}) \quad (28)$$

and

$$I_{\ell}^*(b_i) \propto a^2/b \quad (\text{rotationally symmetric grating}) \quad (29)$$

It seems reasonable to presume that these proportionalities will remain valid, even if Eqs. 23 and 27 are not quantitatively correct.

As will be shown in discussing wide angle scattering in Section 5, scatter functions tend to be inverse power functions of the scatter angle. That is, plotting the logarithm of the scatter function against  $\log \sin \alpha$  produces curves which are roughly straight over extended lengths with a negative slope  $-s$ , where  $s$  usually lies in the range 1.5 to 3.0. (It is usually assumed that  $s$  drops to 0 at very small angles.) Thus, typical scatter intensities  $I_s^*(\alpha)$  are proportional to  $(\sin \alpha)^{-s}$ , and from Eq. 20,

$$I_s^*(\alpha) \propto (\sin \alpha)^{-s} \propto b^{-s} \quad (30)$$

If Eq. 30 is to hold for our phase grating model, clearly the phase amplitude of each spectral component must be proportional to its spatial frequency. Thus, from Eqs. 28 and 29,

$$a(b) \propto b^{-s/2} \quad (\text{linear grating}) \quad (31)$$

and

$$a(b) \propto b^{(1-s)/2} \quad (\text{rotationally symmetric grating}) \quad (32)$$

Eqs. 31 and 32 lead to different conclusions as to the distribution of phase amplitude as a function of spatial frequency required to produce a given slope in the scatter function, and one must therefore question which, if either, best represents scattering from real surfaces. Surface irregularity microstructure is usually considered to be completely random, and therefore best fit by a spectrum of linear phase grating of varying orientation. Some rotational symmetry will be found in the ripple on large aspheric mirrors, however, due to zonal figuring and polishing during fabrication. Thus both types of phase grating will be needed in any model purporting to be complete.

The cosine phase grating models have important implications concerning scaling of the scatter function with wavelength. Both Eqs. 31 and 32 imply that for a constant slope  $s$ , the amplitude  $a(b)$  must vary monotonically with the spatial frequency  $b$ . The amplitude  $a$  has been given in units of wavelengths. To scale to different wavelengths, we should write  $a(b) = w(b)/\lambda$ , where  $w(b)$  and  $\lambda$  are expressed in units of length. Thus the relative intensity for a single grating of spatial frequency  $b$  for either linear or rotationally symmetric cosine gratings will scale as the inverse square of the wavelength. Note from Eq. 20, however, that the scatter angle has also shifted with wavelength. Thus, if we wish to determine how the relative intensity at a specific scatter angle scales with wavelength, we must compare the appropriate spatial frequency components in the wavefront irregularity function  $w(b)$ , and take the change in magnitude of  $w(b)$  into consideration. If this is done for both linear and rotationally symmetric phase gratings, using Eqs. 20, 30, 31, and 32, it will be found that in both cases,

$$I_s^*(\alpha, \lambda) \propto (\sin \alpha)^{-s} / \lambda^{(2-s)} \quad (33)$$

Now  $I^*$  is a normalized intensity,  $I^* = I/I_0$ , where  $I_0$  is the intensity at the center of the diffraction pattern for a perfect, unaberrated lens. We know that

$$I_0(\lambda_2)/I_0(\lambda_1) = (\lambda_1/\lambda_2)^2 \quad (34)$$

Thus

$$\frac{I(\alpha, \lambda_2)}{I(\alpha, \lambda_1)} = \frac{I_0(\lambda_2)}{I_0(\lambda_1)} \times \frac{I^*(\alpha, \lambda_2)}{I^*(\alpha, \lambda_1)} = (\lambda_1/\lambda_2)^{(4-s)} \quad (35)$$

Note that when  $s = 0$ , Eq. 35 implies that the intensity scales by the inverse fourth power of the wavelength. To understand this physically, recall that intensity is measured in terms of power per unit solid angle: thus, when the wavelength is reduced by a factor of 2, for example, the amount of energy diffracted by a given spatial frequency grating is quadrupled, and the solid angle into which it is diffracted is divided by 4. This applies strictly only in the region where Eqs. 23 and 27 are valid, i.e., where one can safely assume that all diffracted energy appears in the first-order sidebands of the phase gratings.

Eq. 35 has implications which should be checked experimentally. We normally assume that scatter functions scale as the inverse square of the wavelength, and this is true as far as total scattered light is concerned. But scatter at a given angle will scale as the inverse square of the wavelength only if the scatter coefficient is itself an inverse square function of the scatter angle, according to Eq. 35. Since measurements of the scatter function have found  $s$  to vary between 1.5 and 3.0, wavelength scaling should vary accordingly (see Section 5).

### 4.3 ZONAL RIDGES

A zonal ridge is a high or low region of the mirror which extends around the total circumference at the same radius from the center. The most commonly encountered type of zonal ridge is edge roll-off, but such ridges can occur at any radius. They are commonly seen in the early stages of fabricating large aspheric mirrors where polishing is done with subaperture sized laps.

In examining zonal ridges, we will use the Gaussian profile OPD function described in Section 4.1.1. This profile is only a mathematical convenience, however, and many other profiles are possible.

#### 4.3.1 Gaussian Cross Section Ridge

Figs. 4-21 and 4-22 represent two Gaussian profile ridges centered at a normalized pupil height of 0.7, differing only in width. Wide ridges behave like zonal spherical aberration, having their principal effects within the first few Airy radii out from the central maximum. Narrow ridges have relatively little effect on the innermost portions of the ring structure, but tend to introduce oscillations into extended regions of the outer ring structure. In general, the latter involve very little net transfer of energy. Wide ridges affect the middle and outer portions of the MTF more than narrow ridges, although neither of the cases shown here affect the MTF drastically. The heights shown here,  $\lambda/10$ , are somewhat larger than is likely to be found in the highest quality mirrors, although the 154-inch mirror discussed in Section 4.7 has one or two ridges extending over partial zones which begin to approach this height. Zones of this order of magnitude are not too serious unless there are enough of them to act like a phase grating.

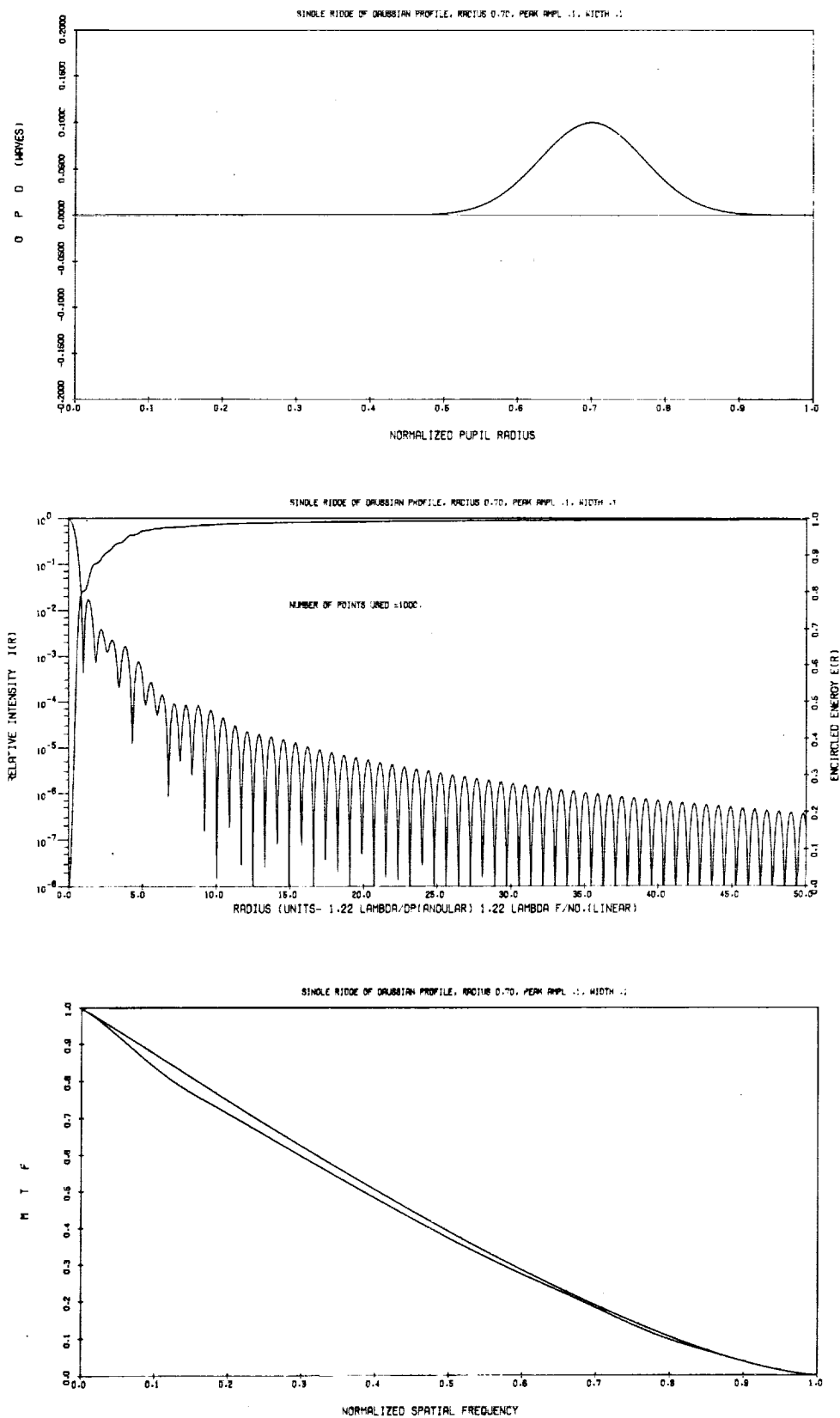


Fig. 4-21 — Single ridge of width 0.1

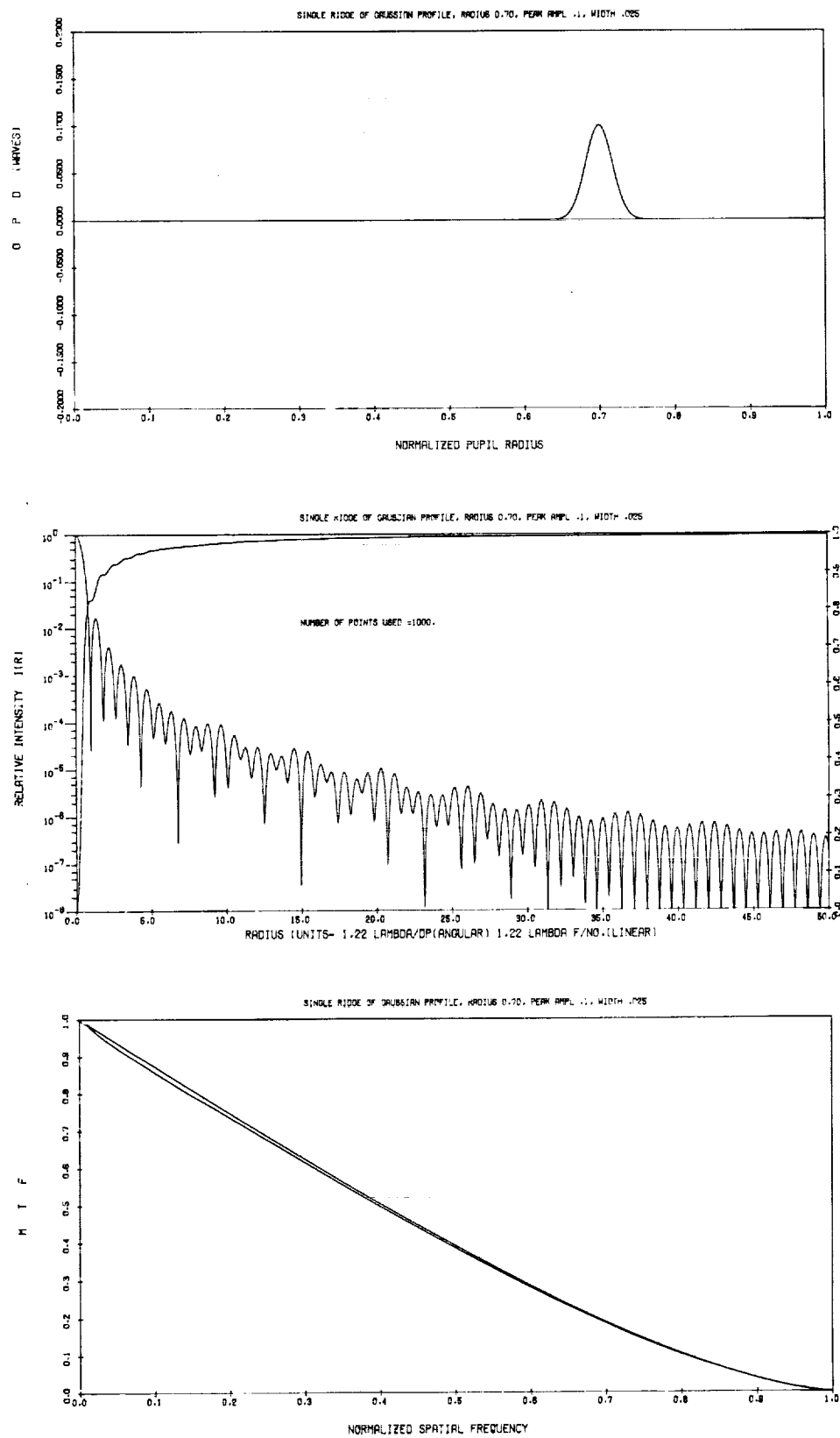


Fig. 4-22 — Single ridge of width 0.025

### 4.3.2 Edge Roll-Off

Edge roll-off is a very common fabrication error on all types of optical elements and can be quite large. With primary mirrors for Cassegrain type telescopes, edge roll-off may occur at both outer and inner edges. Fig. 4-23 shows the OPD waveforms for two hypothetical cases of primary mirrors for a telescope having a central obstruction diameter ratio of 0.32, one with roll-off on the outer edge only, and the other with roll-off on both edges. The corresponding PSF's are shown in Fig. 4-24 with the PSF of an unaberrated lens having the same central obstruction for comparison. (Fig. 4-25 shows the two MTF's.)

Both OPD waveforms displace energy from the central maximum. The energy is spread relatively uniformly through the first 20 to 25 Airy radii outward from the center of the pattern, judging from the PSF and encircled energy curves, with no local concentrations.

The manner in which the MTF is degraded emphasizes that the energy is displaced well outward from the central core. The MTF degradation function (not shown) is clearly quite smooth, although there is more high spatial frequency suppression than one would get from, say, a very high spatial frequency cosine phase grating of similar rms wavefront error. Note that the inner edge roll-off has no effect on the high spatial frequency MTF beyond the second inflection point due to the central obstruction.

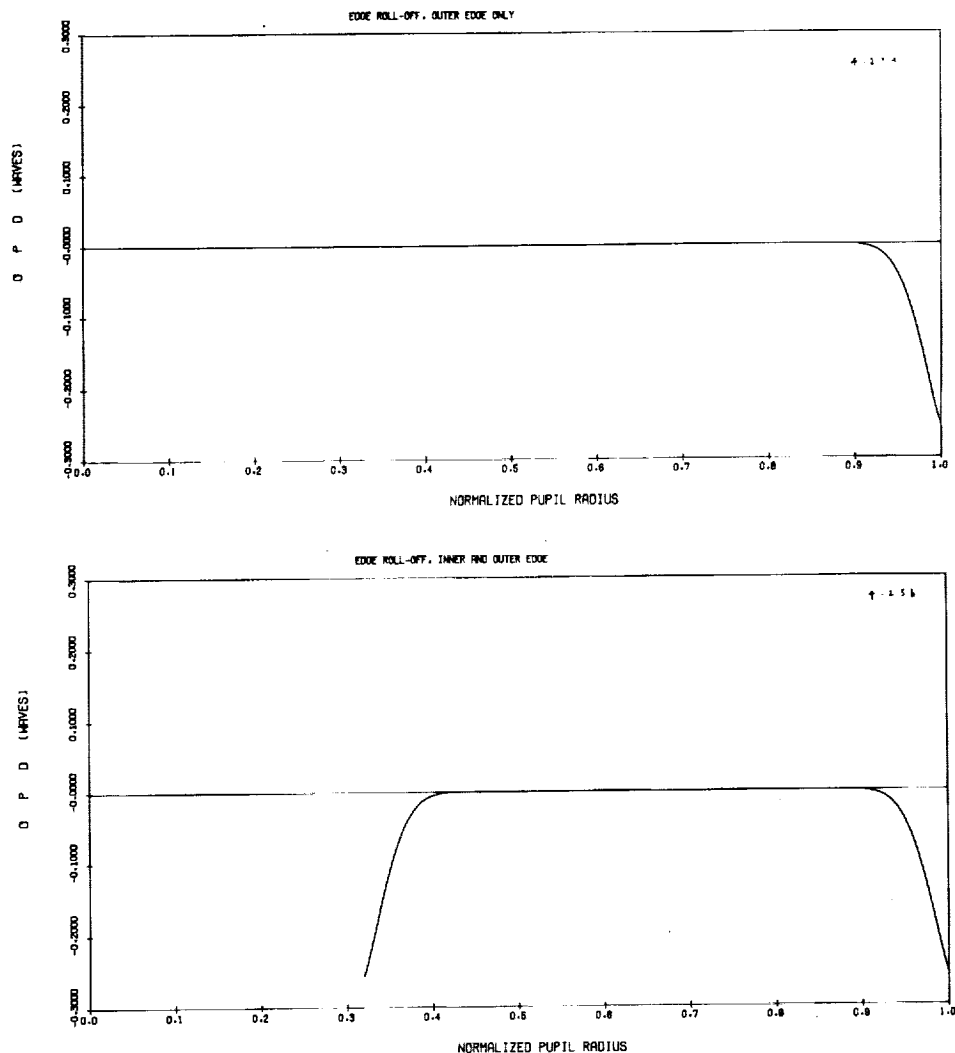


Fig. 4-23 — OPD waveforms for edge roll-off



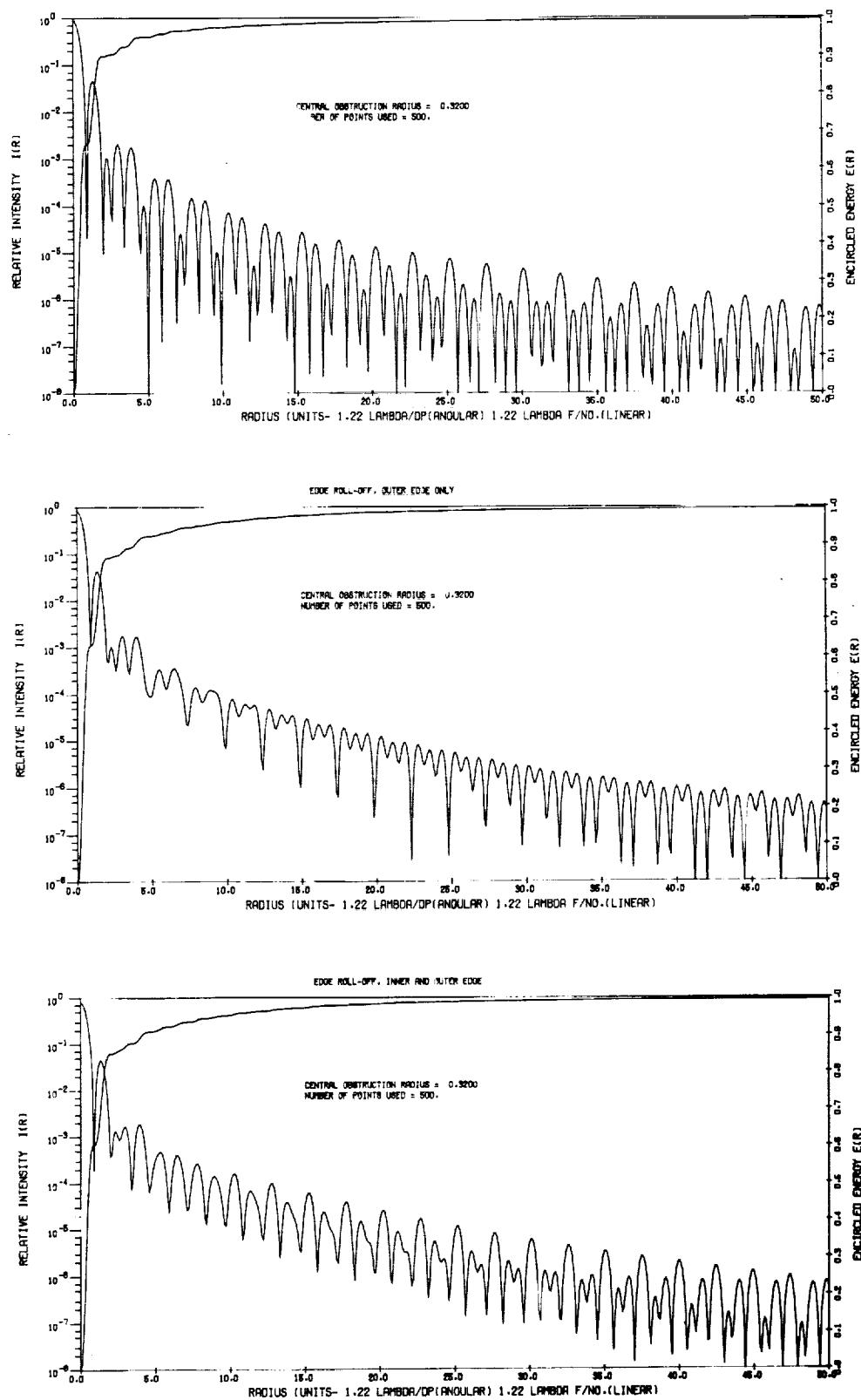


Fig. 4-24 — PSF's for edge roll-off

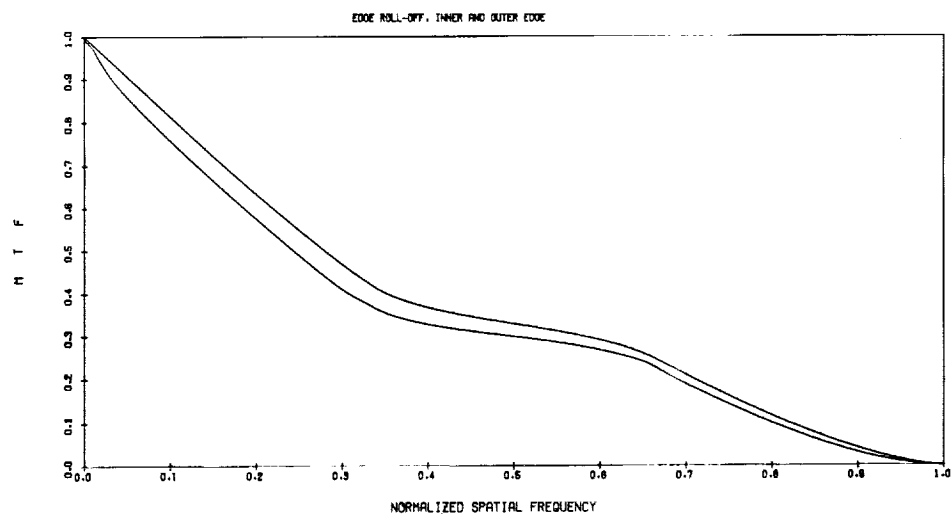
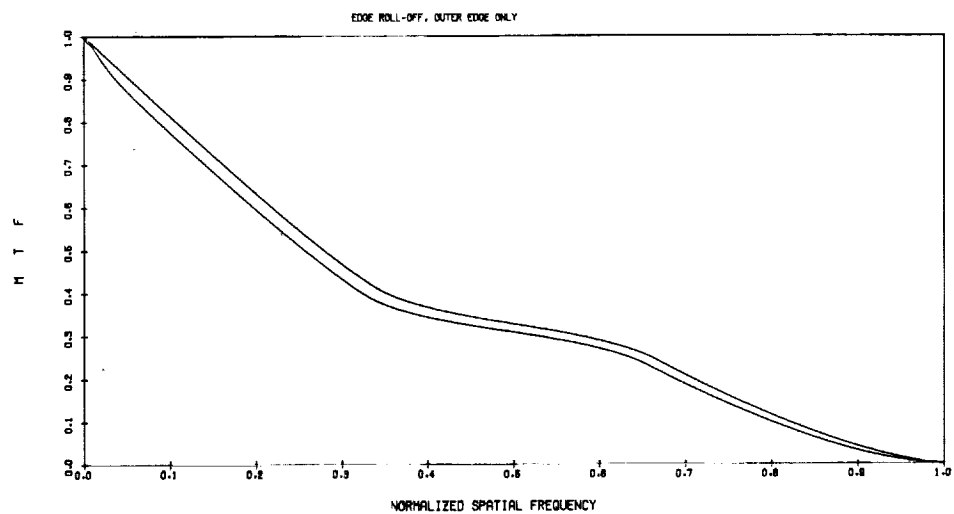


Fig. 4-25 — MTF's for edge roll-off

#### 4.4 ROTATIONALLY SYMMETRIC "RANDOM" WAVEFRONTS

"Random" is put in quotation marks in the title to emphasize that the OPD varies randomly along the pupil radius, and has a fixed value around the circumference of the pupil at any given radius. The image degrading properties of this wavefront may therefore be somewhat different from a fully random wavefront. The rotationally symmetric model is useful in studying the effects of varying the parameters of a random wavefront, however, which is the present intent.

Two parameters of the random wavefront will be varied in these examples, the correlation length (actually the width of the smoothing function) and the shape of the smoothing function. The rms wavefront error is held at 0.1 wavelength, and the seed used to define the random number array is fixed at 233425. The actual value of the seed is not important, only that it be the same, so that all examples start with the same random number array, simplifying direct comparison of the different examples.

##### 4.4.1 Variation of Correlation Length

Reducing correlation length introduces more high spatial frequency variations in the OPD, diffracting light further out into the PSF ring structure. In the examples shown in Figs. 4-26 through 4-29, the correlation lengths used are 0.33, 0.10, and 0.03 pupil diameters. Fig. 4-26 shows the OPD waveforms, Fig. 4-27 the PSF's and encircled energy functions, Fig. 4-28 the MTF's, and Fig. 4-29 the \* Autocorrelation functions.

The effects of varying the correlation length are self-evident, but some are worth commenting on. Some of the more interesting variances are summarized in Table 4-6. A Gaussian smoothing function 0.33 wide reduces the high spatial frequency oscillations so much that the wavefront appears to be a form of spherical aberration. Note that the peak-to-peak wavefront error is smaller than one would expect from the usual rule of thumb that OPD (peak to peak) =  $5 \times$  OPD (rms). The actual ratios are listed in the table. Strehl definition is usually associated solely with the rms wavefront error, but here we see a small variation which indicates the Strehl definition to be somewhat less sensitive to high spatial frequency wavefront errors than to low spatial frequency errors. The fraction of energy displaced outward by the wavefront error is about the same in all cases, roughly 28 percent. Where it reappears is indicated in Table 4-6 by listing the values of the radii corresponding to 10 percent and 1 percent displaced energy. For experiments requiring, say 99 percent encircled energy in the smallest possible circle, high spatial frequency wavefront error is very destructive.

Table 4-6 — Some Quantities Affected by Varying Correlation Length

Correlation length	0.33	0.10	0.03
OPD(p-p)/OPD(rms)	2.9×	4.2×	5.0×
Strehl definition	0.662	0.672	0.677
$r_A$ (Airy radii) for:			
10% displaced energy	2.0	7.7	20.8
1% displaced energy	3.4	10.1	41.0

The changes in the MTF and \* Autocorrelation function are what would be expected from the addition of higher spatial frequency wavefront errors. Low spatial frequency MTF is degraded more severely, and high spatial frequency MTF less so. \* Autocorrelation function values drop to zero more rapidly, and show smaller excursions about zero for short correlation lengths.

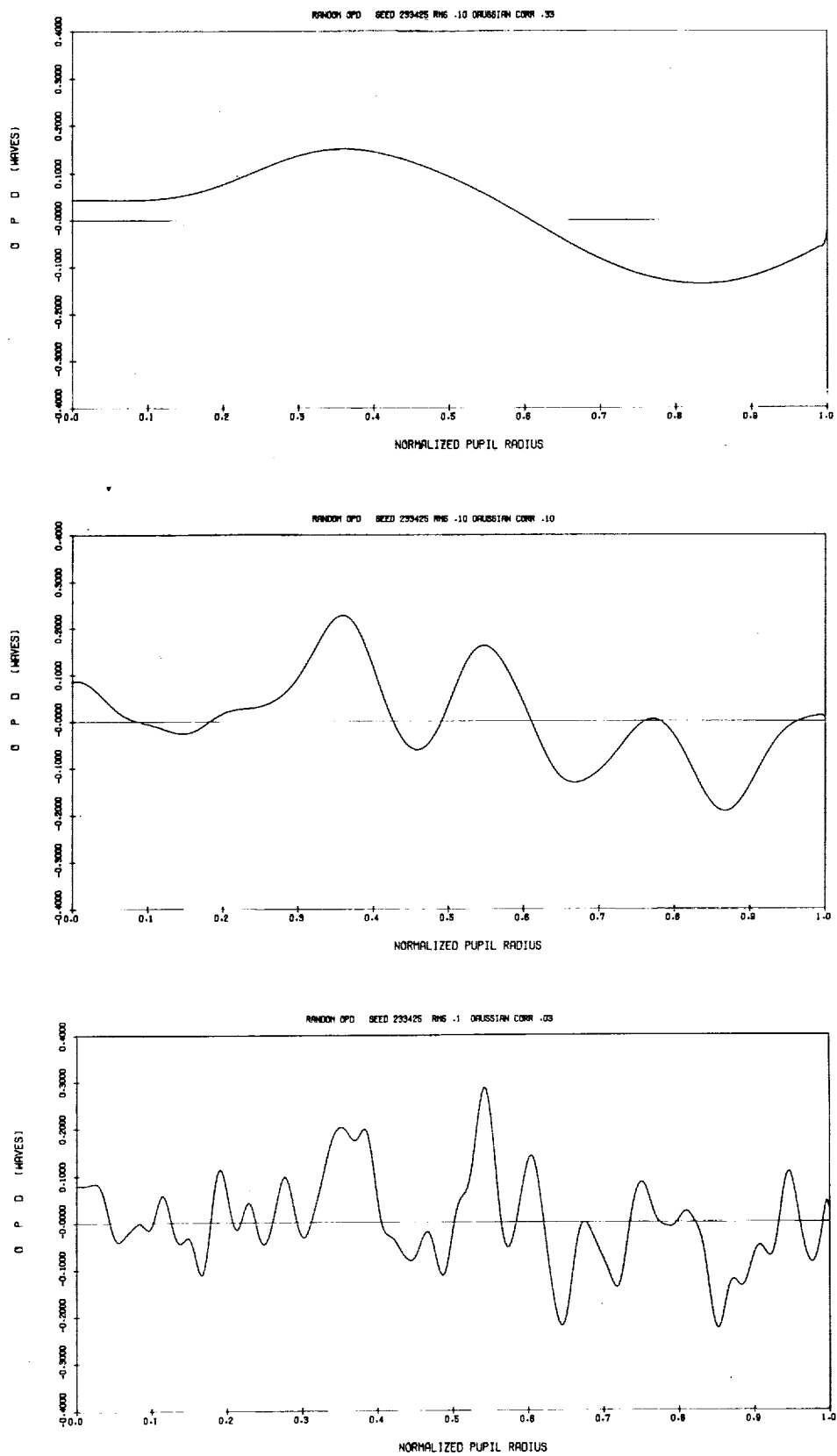


Fig. 4-26 — OPD waveforms, random wavefronts of different correlation lengths

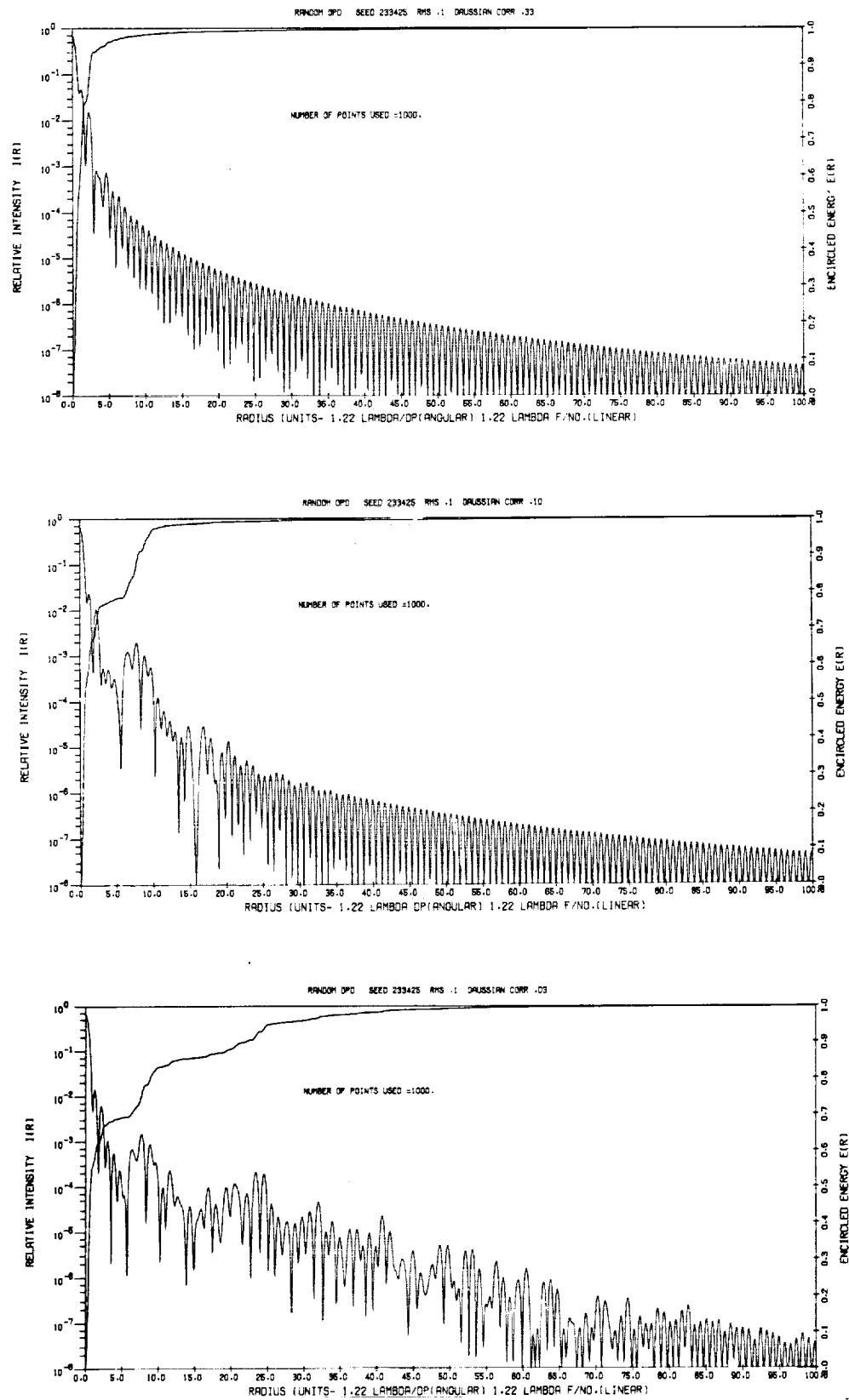


Fig. 4-27 — PSF's, random wavefronts of different correlation lengths

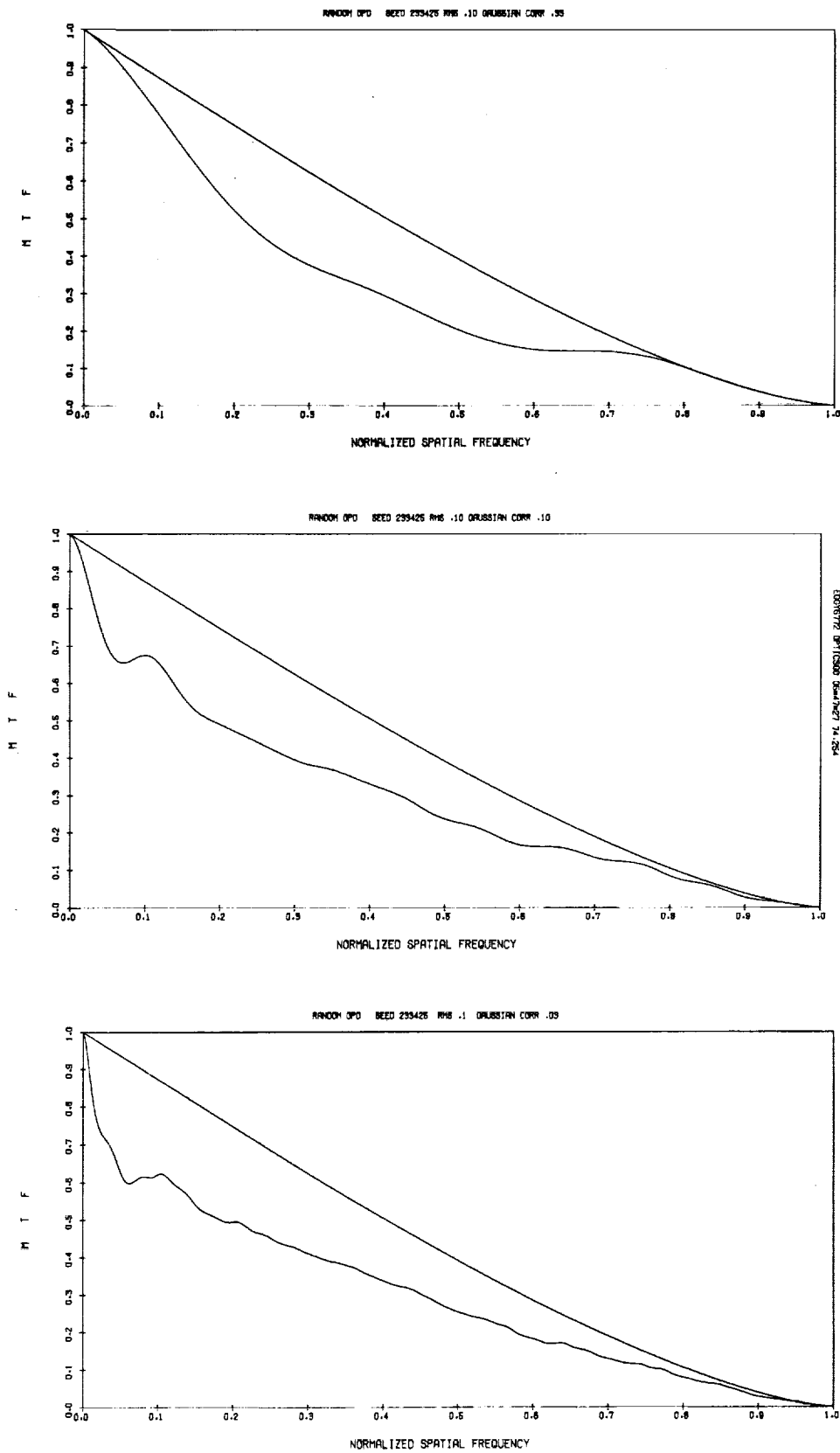


Fig. 4-28 — MTF's, random wavefronts of different correlation lengths

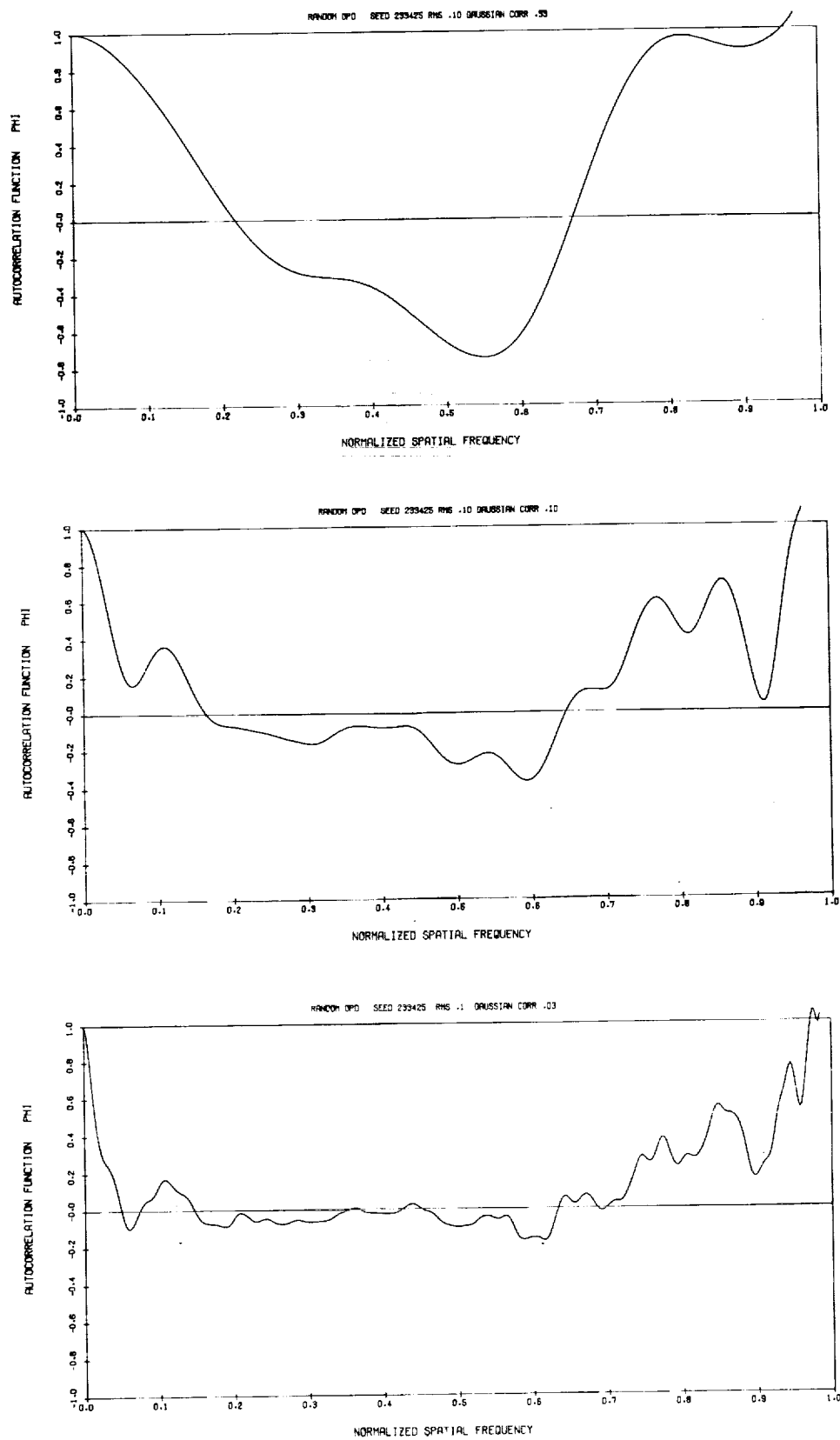


Fig. 4-29 — \* Autocorrelation functions, random wavefronts of different correlation lengths

#### 4.4.2 Variation of Smoothing Function

Four smoothing functions are available for use in generating random OPD functions with GASPR: Gaussian, square, triangular, and linear exponentials. Examples of all four are given here, for a common correlation length of 0.1. Plots are given for OPD waveform, PSF and encircled energy, and \* Autocorrelation function. Plots for the Gaussian smoothing function examples are found in Figs. 4-26, 4-27, and 4-29. The remaining three examples are shown in Figs. 4-30, 4-31, and 4-32.

The main difference between the different smoothing functions is in the degree to which each reduces the high spatial frequency components of the OPD waveform. The Gaussian smoothing function completely eliminates the highest frequency components, while the square smoothing function leaves the largest high spatial frequency residual. (This residual is a result of a form of "aliasing," due to the sharp edge of the square smoothing function. As the edge of the smoothing function passes each point in the set of random numbers defining the OPD, there is an incremental change in the "smoothed" function, which shows up as a high spatial frequency residual component.) The triangular and linear exponential smoothing functions produce intermediate smoothing, resembling the effects of the Gaussian function more closely than those of the square smoothing function. The principal changes are clearly related to the increased high spatial frequency content of the OPD waveform with square smoothing. Note in particular the behavior of the \* Autocorrelation function near its origin. In all examples except that involving square smoothing, the curves appear roughly Gaussian near the origin. For square smoothing, however, the early parts of the curve appear to be dropping linearly. Similar patterns will be observed for the 154-inch mirror discussed in Section 4.7.

Table 4-7 summarizes the effects of different smoothing functions on the same quantities listed in Table 4-6. Note in particular the radii for 10 percent and 1 percent displaced energy for square smoothing. None of the other variations is at all significant.

Table 4-7 — Some Quantities Affected by Varying the Smoothing Function

Smoothing function	GAUS	SQUA	TRIA	LEXP
OPD(p-p)/OPD(rms)	4.2×	4.3×	4.0×	4.1×
Strehl definition	0.672	0.670	0.670	0.671
$r_A$ (Airy radii) for:				
10% displaced energy	7.7	7.2	7.2	6.3
1% displaced energy	10.1	9.9	9.9	9.9



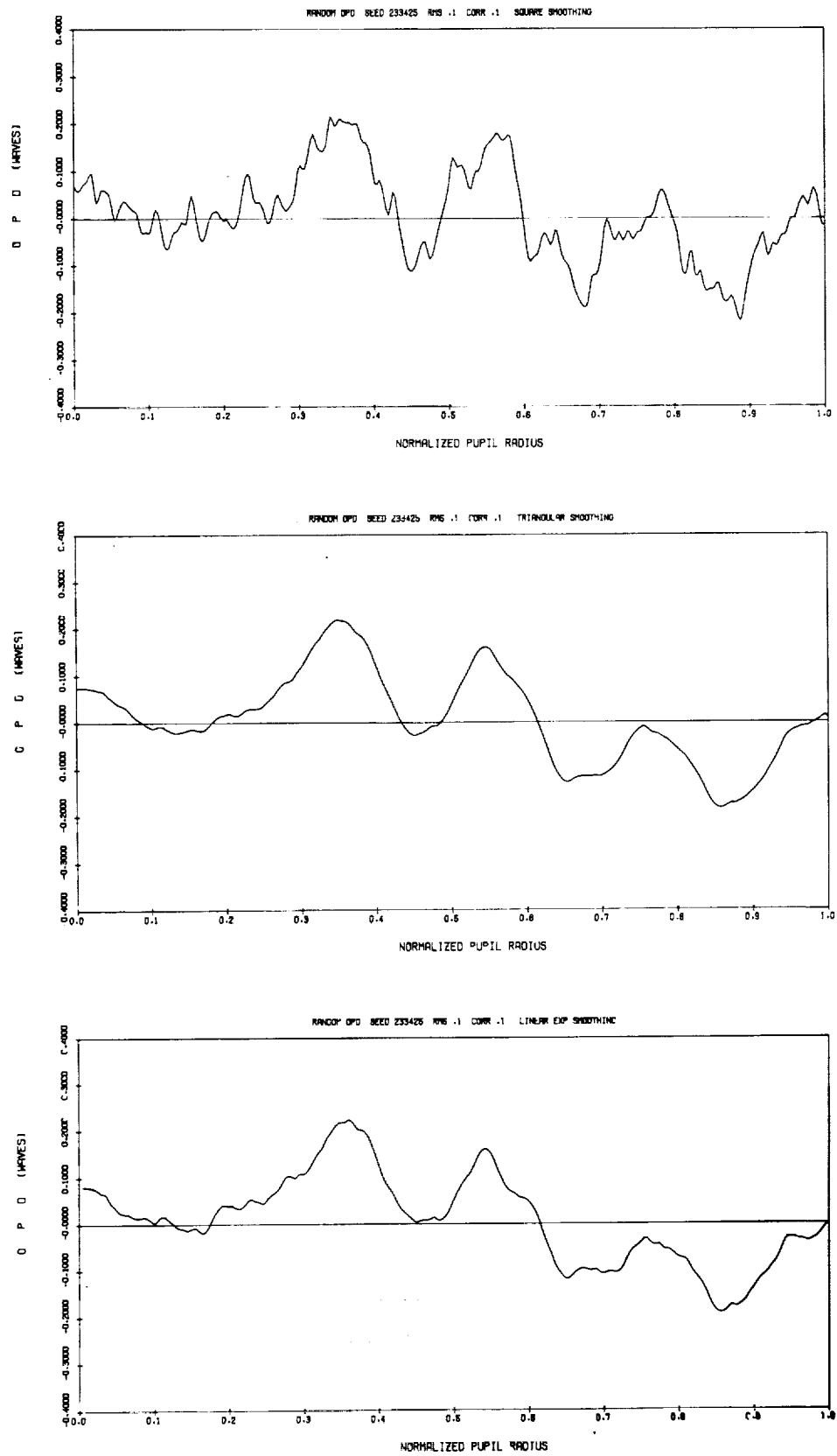


Fig. 4-30 — OPD waveforms, random wavefronts generated with different smoothing functions

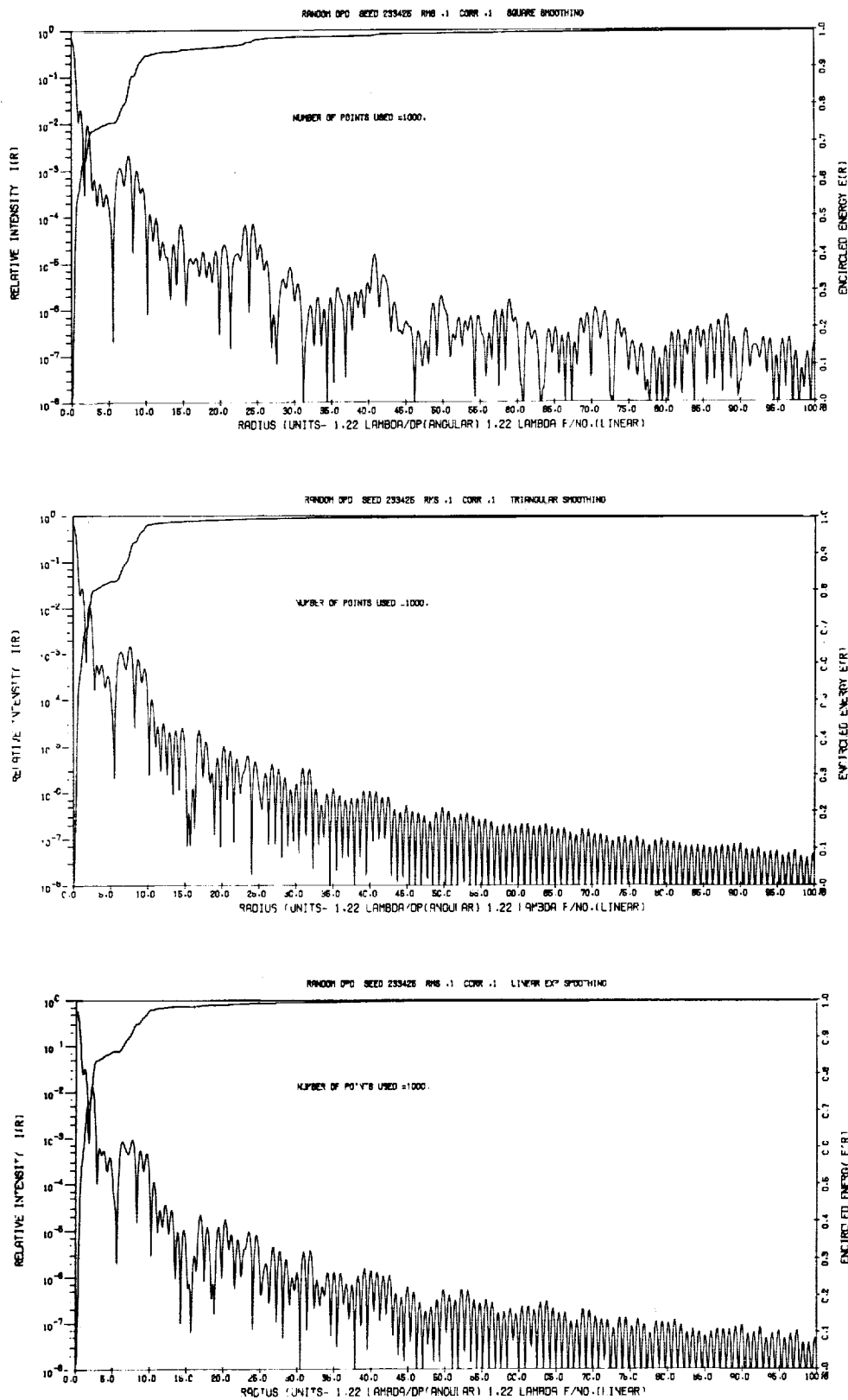


Fig. 4-31 — PSF's, random wavefronts generated with different smoothing functions

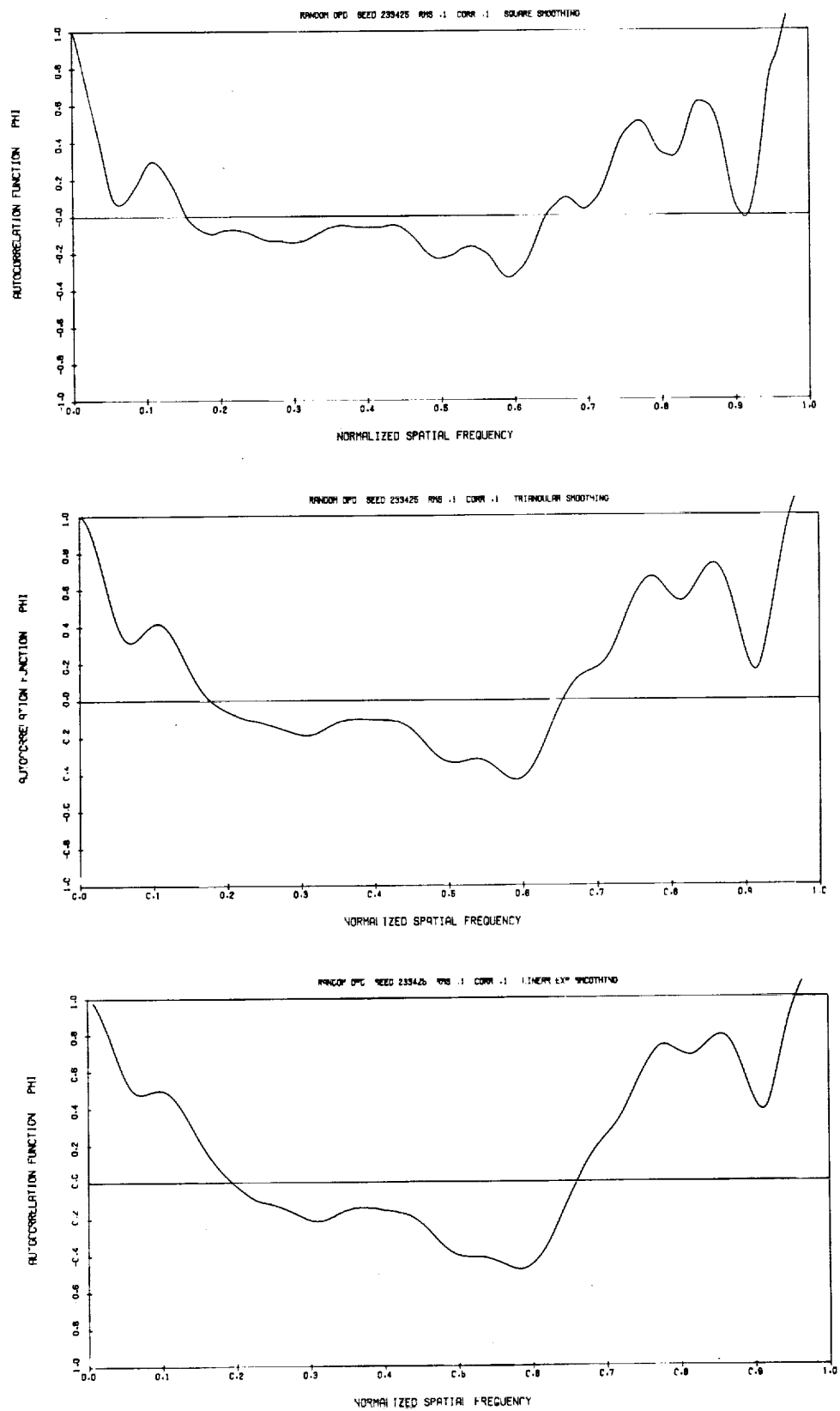


Fig. 4-32 — \* Autocorrelation functions, random wavefronts generated with different smoothing functions

#### 4.5 EFFECTS OF APODIZATION IN THE PRESENCE OF WAVEFRONT ERROR

Apodization, or reduction in the PSF sidebands through gradation in the aperture transmittance from center to edge of the entrance pupil, is sometimes cited as a technique for improving the image quality of optical systems. An extensive review article on the technique has been written by Jacquinot<sup>3</sup> in "Progress in Optics." We have seen no articles which discuss how apodization affects systems with wavefront error; however, the program GASP, from which we derived GASPR, contained a Gaussian apodization function for use with Gaussian cross section laser beams. We have retained the capability in GASPR (see Section 4.1.1). Results of our tests with this apodization function are of interest in dealing with the scattered light problem.

Fig. 4-33 shows the effects of applying Gaussian apodization to a perfect, unaberrated lens. The top PSF is for the unapodized lens. The other PSF's represent Gaussian apodization of a form such that the transmittance has dropped to  $1/e = 0.3679$  at radius 0.5 and 0.25, respectively. The degree to which the sidebands have been suppressed is clearly evident, although in the  $R = 0.25$  case, the effective aperture diameter has also been reduced, increasing the effective diameter of the image.

Fig. 4-34 shows the effects of apodization when a cosine phase grating,  $a = 0.0707$  wavelength,  $b = 12$  cycles per radius, is present. While it is clear that a portion of the PSF has been suppressed, it is also clear that the sidebands due to the cosine phase grating have not been reduced significantly, only modified by convolution with a different pupil. In fact, the third and fourth order sidebands are now visible, where they had been masked by the Airy pattern. What has happened is that pupil diffraction (for want of a better name) has been suppressed while wavefront error diffraction has not.

The effect is even more striking in Fig. 4-35, which involves a random wavefront error of 0.005 wave rms and 0.01 correlation length. 0.005 wave rms corresponds to a wavefront surface deformation  $\sigma = 25 \text{ \AA}$  in the middle of the visible spectrum. The top curve shows the OPD waveform. The second curve shows the unapodized case, where the presence of wavefront error is barely detectable (Strehl definition = 0.999). The third curve shows apodization,  $R = 0.5$ , and the presence of the wavefront error is now clearly evident.

There are two points in this presentation. First, apodization will not produce significant reductions in the sideband structure if significant amounts of wavefront error are present. Second, apodization may be useful in measuring (or at least finding) any small amplitude wavefront error by removing pupil diffraction as a masking element. This may be of significant benefit in tests for wide angle scatter due to surface microstructure (see Section 7.1 for further discussion).

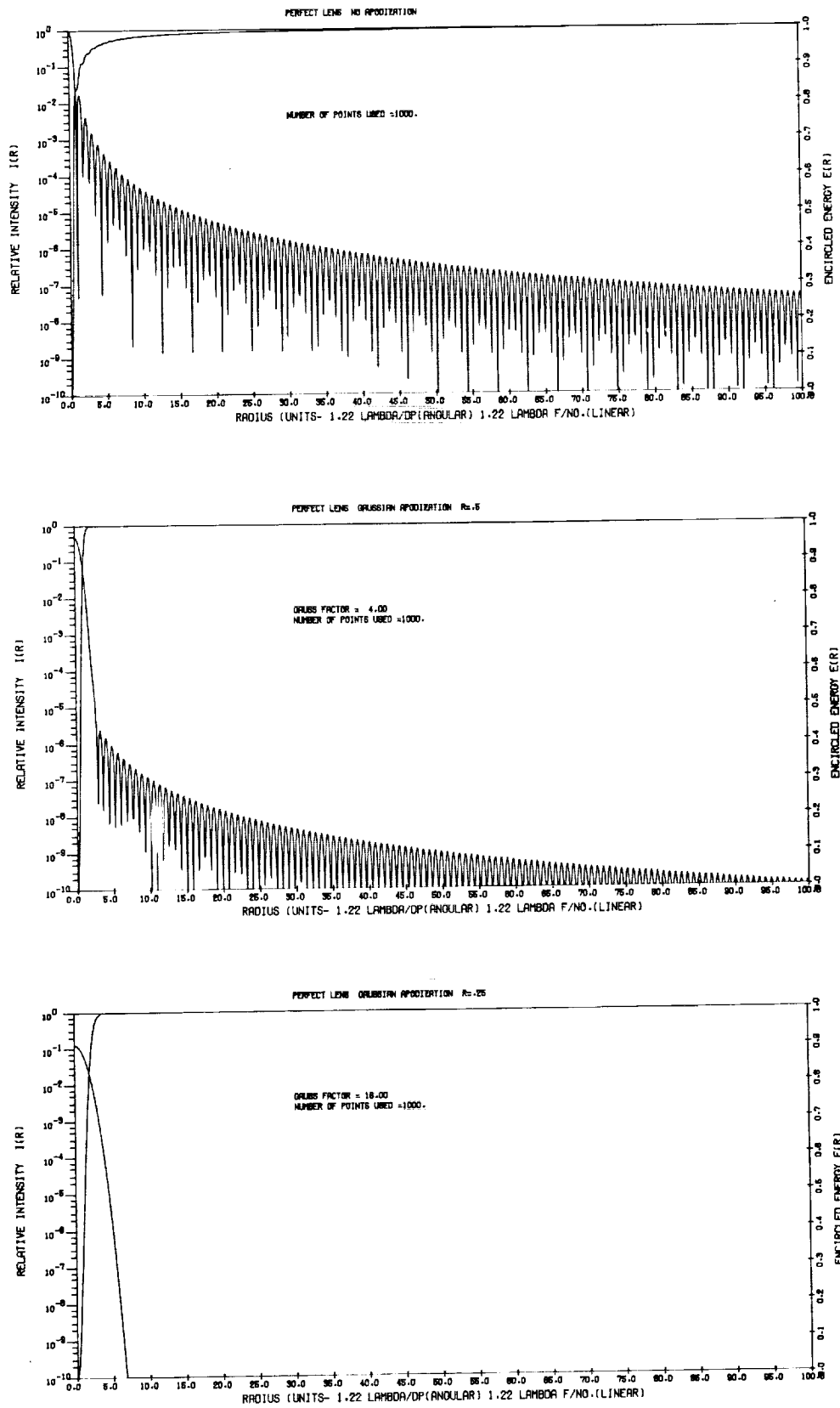


Fig. 4-33 — Apodization of a perfect lens

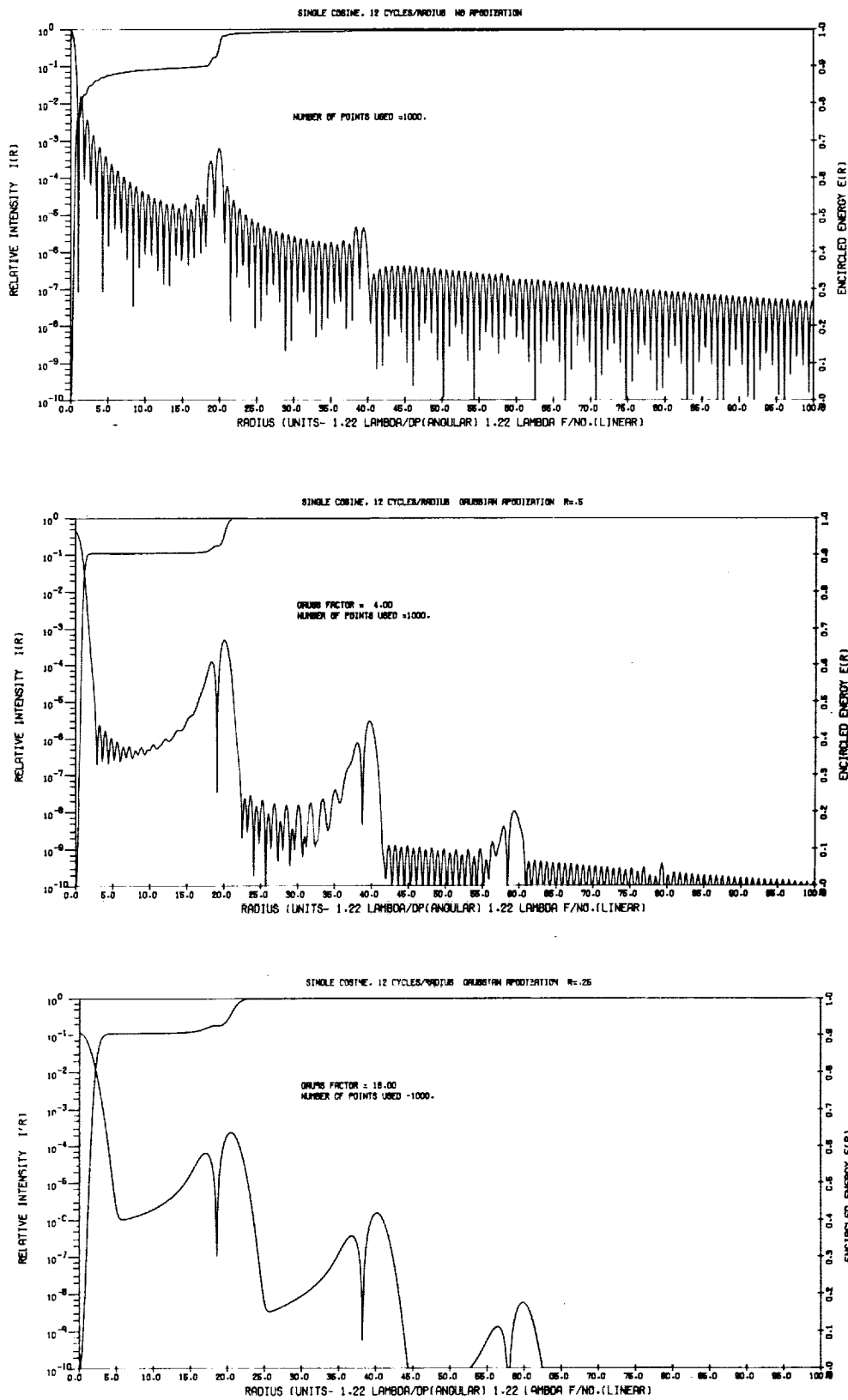


Fig. 4-34 — Apodization in the presence of a cosine phase grating;  $a = 0.0707$ ,  $b = 12$

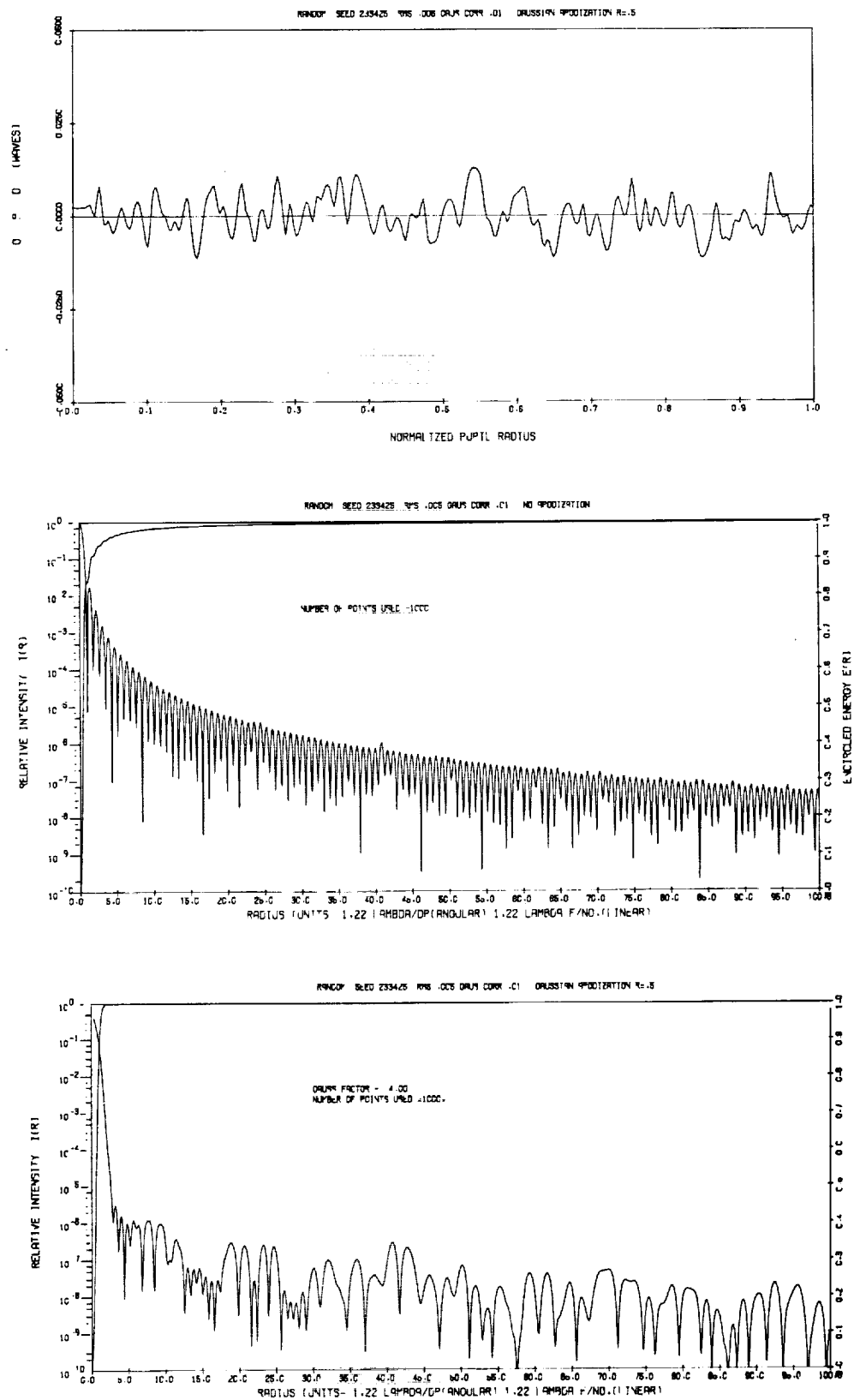


Fig. 4-35 — Apodization in the presence of a very small random wavefront error;  $w = 0.005$

#### 4.6 "WAFFLE" WAVEFRONT DUE TO CELL STRUCTURE OF MIRROR SUBSTRATE

The primary mirror substrate for the LST will be a lightweighted structure of ULE fused silica or Cer-Vit. In either case, it will in effect consist of a thin plate supported by an eggcrate structure. If made of ULE, the structure will be formed by fusing thin plates of the material, and the cells will be square. If made of Cer-Vit, the structure will be machined from a solid blank, and the cells will be hexagonal. At present, plans are to use ULE, with a 12- by 12-centimeter cell size. It is this configuration which is examined here.

There is some concern that elastic deformation and restoration of the front plate during polishing, and/or gravity release after insertion in orbit, will result in the appearance of bumps at the center of each cell. These will produce a regularly spaced array of dimples in the wavefront, which will give the OPD waveform map a waffled appearance, in turn producing an array of spikes in the ring structure of the PSF. G. Lenertz has provided a simplified first order model for estimating the maximum possible surface deformation. We have used the program FRAP-2D to estimate the effects of this waffle wavefront on the PSF.

The model for computing the maximum deflection  $\delta$  is

$$\text{Max } \delta = \frac{0.0487 w a^4 (1 - \mu^2)}{E t^3} \quad (36)$$

where  $\delta$  = peak-to-valley surface deformation, inches

w = unit applied load =  $\rho t$

$\rho$  = density  $\approx 0.1$  lb/inch<sup>3</sup>

a = cell dimensions = 4.72 inches (12 cm)

$\mu$  = Poisson's ratio  $\approx 0.2$

E = Young's modulus  $\approx 10^7$  psi

t = plate thickness, inches

(Lenertz' original notation is used here.) For a nominal plate thickness of 1 inch (2.54 cm), Eq. 36 leads to a maximum  $\delta = 2.32 \times 10^7$  inches, or 0.0093 wavelength surface deformation at  $\lambda = 0.6328$  micrometer. The peak-to-valley wavefront deformation will therefore be 0.0186 wavelength at  $\lambda = 0.6328$  micrometer, 0.0363 wavelength at  $\lambda = 0.325$  micrometer and 0.0970 wavelength at  $\lambda = 0.1215$  micrometer, according to this estimate.

FRAP-2D was used to estimate the effects of a waffle wavefront on the PSF. A 256 by 256 matrix was used to define the pupil function, with the pupil diameter being 125 units. The OPD waveform was defined by the equation

$$\text{OPD}(x, y) = (K/4)[1 + \cos(2\pi x/5)][1 + \cos(2\pi y/5)], \quad (37)$$

with the cells being 5 units on a side (12 cm for a 3-meter diameter, or  $b = 12.5$  cycles per radius). K is the peak-to-valley wavefront error in radians. Values of 0.1, 0.25, and 0.5 radians were used, corresponding to 0.0159, 0.0398, and 0.0796 wavelengths peak to valley, respectively. (To convert to rms, multiply by  $\sqrt{5}/8 = 0.28$ .)

FRAP-2D uses a fast Fourier transform technique which restricts the output format for the PSF. With a 125-unit diameter pupil in a 256-point square pupil matrix, sample points in the PSF are spaced at  $125 \lambda / 256 D_p$  radian intervals in image space. This is a spacing of 0.40 Airy radii, which does not give very good resolution in the ring structure. The results are good enough to show the spikes due to the waffle wavefront with OPD values of the magnitude indicated above. The output plots are two-dimensional perspective plots. A log relative intensity scale has been used for the PSF's to bring out the diffraction spikes. A selection of outputs are shown in Figs. 4-36 through 4-39.



Fig. 4-36 is the PSF for a perfect lens for comparison. (It also illustrates why rotationally symmetric wavefronts have been used for most of the analysis in this paper.) Fig. 4-37 is the PSF for a 0.5-radian peak-to-valley waffle wavefront. Fig. 4-38 is the same wavefront with an  $\epsilon = 0.32$  diameter ratio central obstruction. Fig. 4-39 shows the MTF for the latter case.

The diffraction spikes appear in a 3 by 3 array including the central maximum for the PSF. The eight added spikes fall into two height categories, with the side spikes being high than the corner spikes. Relative heights  $h^*$ , measured with respect to the central maximum are the same with or without the central obstruction, at least in the examples we examined. The results are summarized in Table 4-8.

Table 4-8 — Relative Heights for Diffraction Spikes

$\Delta\phi$	OPD(p-v)	$\omega$	$h^*(\text{side})$	$h^*(\text{corner})$
0.5	0.0796	0.0222	0.00382	0.000942
0.25	0.0398	0.0111	0.000953	0.000234
0.1	0.0159	0.0044	0.000154	0.000037

An equation of the form

$$h^* = C (\text{OPD})^2 \quad (38)$$

was fit to this data. Constants of 0.604 for the side spikes and 0.149 for the corner spikes fit the data to within 3 in the third significant figure, generally. This is probably near the limit of accuracy of the computer derived results.

The positions of the spikes can be determined using the grating equation, which gives x and y coordinates for each spike. This gives values for the distance from the central maximum of 20.50 and 28.99 Airy radii for the side spikes and corner spikes, respectively. The relative intensity for the diffraction pattern envelope is given by

$$I_d^* = 0.0452/r_A^3 \quad (39)$$

Thus  $I_d^* = 5.25 \times 10^{-6}$  and  $1.86 \times 10^{-6}$  for the side and corner spike positions, respectively.

Eq. 38 can be used in conjunction with Lenertz' data for expected surface deflections to compute the probable diffraction spike heights to be expected in the LST image. This has been done and the results summarized in Table 4-9. Relative heights are listed in terms of  $h^*$ ,  $h^*/I_d^*$  and  $m^*$  stellar magnitudes.

Table 4-9 — Estimated Diffraction Spike Heights for LST

$\lambda, \mu\text{m}$	OPD(p-v)	Side Spikes			Corner Spikes		
		$h^*$	$m^*$	$h^*/I_d^*$	$h^*$	$m^*$	$h^*/I_d^*$
0.6328	0.0186	0.000210	9.2	39.9	0.000052	10.7	27.8
0.3250	0.0363	0.000794	7.8	151	0.000196	9.3	105
0.1215	0.0970	0.00568	5.6	1,080	0.00140	7.1	754

It should be understood that these are first-order calculations which use simplified models for the surface deformation and the shape of the wavefront deformation, and do not consider inter-

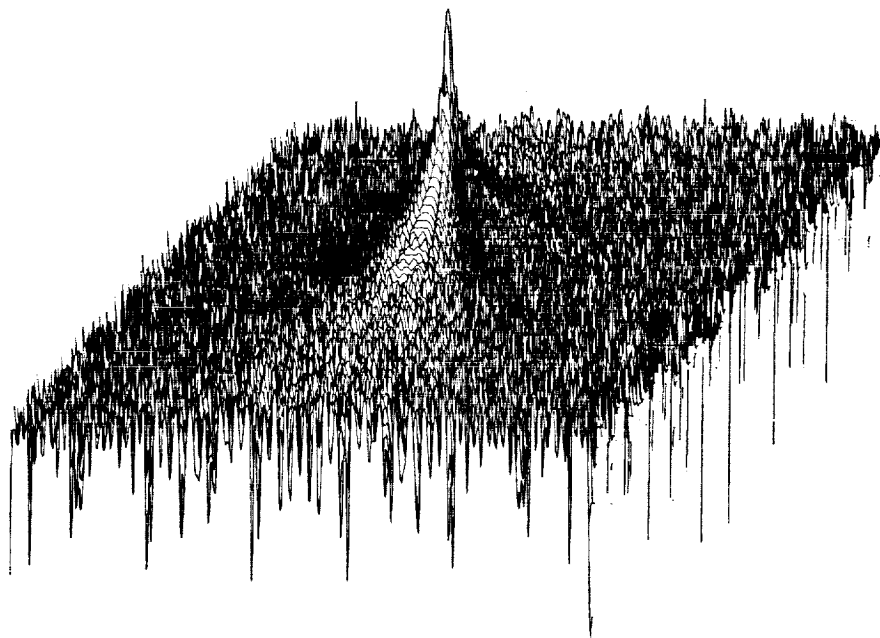


Fig. 4-36 — PSF for perfect lens

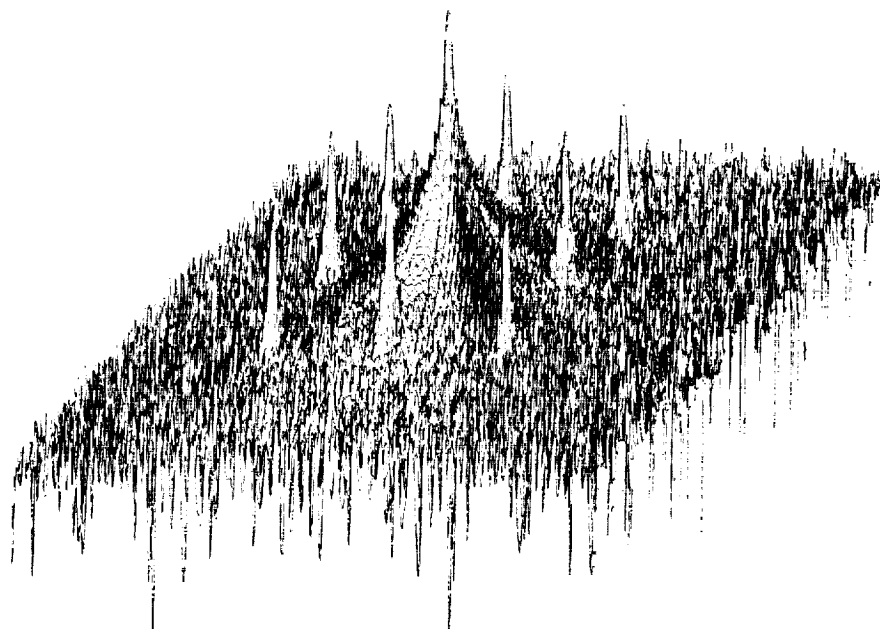


Fig. 4-37 — PSF for a 0.50-radian waffle wavefront error (0.0796 wavelength)

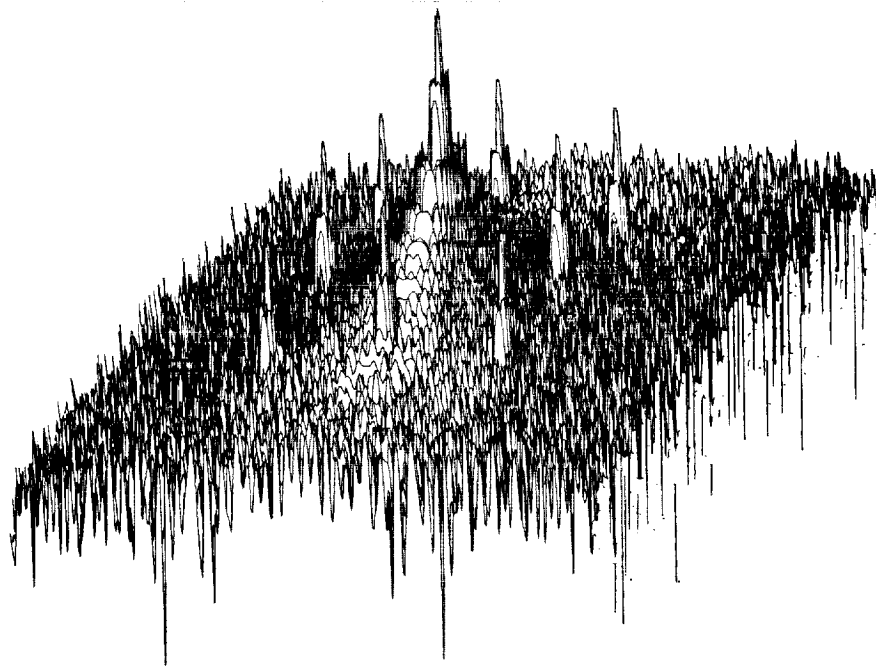


Fig. 4-38 — PSF for 0.50-radian waffle wavefront error plus 0.32 central obstruction

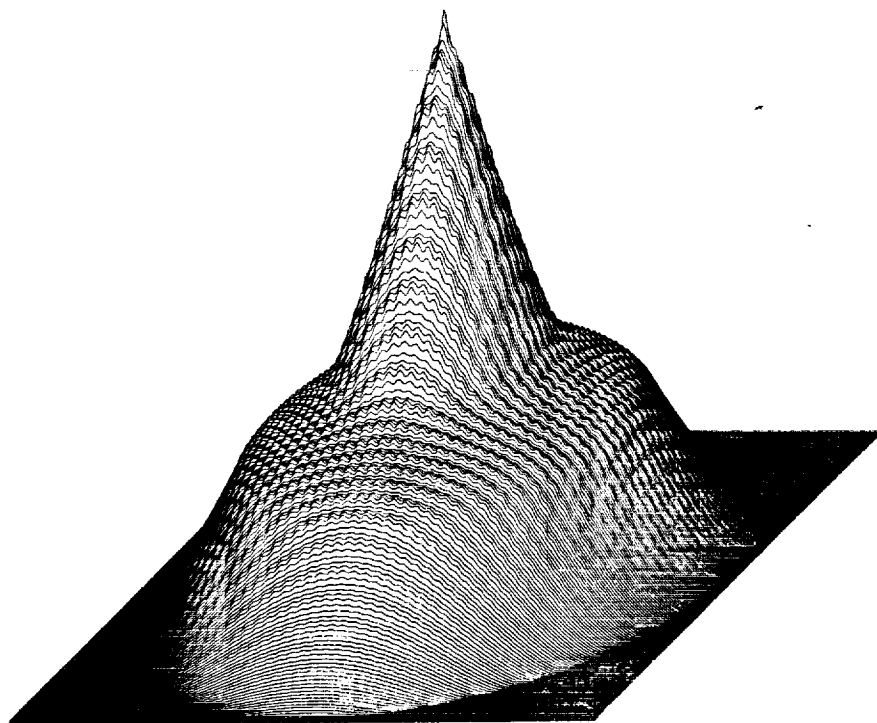


Fig. 4-39 — MTF for example of Fig. 4-38

actions with other types of wavefront error. The analysis is also monochromatic; in white light, the eight diffraction spikes will be replaced by dispersed spectra spread along lines radiating outward from the central maximum. These qualifications having been stated, however, this data makes it appear that diffraction spikes may present a significant problem.

## 4.7 ANGLO-AUSTRALIAN TELESCOPE PRIMARY MIRROR

Dr. David S. Brown of Sir Howard Grubb Parsons and Company, England, has provided us with interferometric measurements of the surface irregularities of the 154-inch-diameter primary mirror of the Anglo-Australian Telescope (A.A.T.), which they have recently completed. This data is unique in that it contains the only quantitative high spatial frequency measurements of mirror surface irregularities which is currently available. The data was taken with a shearing interferometer, and measures wavefront deviation at 1-inch increments along 20 mirror radii. This puts the results in an ideal format for analysis using GASPR. The results of such analysis do not duplicate the actual PSF of the A.A.T. primary mirror, but they show the effects of the types of ripple actually encountered in a real telescope mirror.

### 4.7.1 The Input Data

Two forms of data were supplied by Dr. Brown. One is a coarse wavefront map of the entire mirror, specified by an 11 by 11 grid of data points (see Fig. 4-40). The other is a table of OPD values at 1-inch increments along 20 mirror radii (see Table 4-10). All measurements were made at  $\lambda = 5780 \text{ \AA}$ , and each value represents a wavefront error, not a mirror surface error. The 20 radii were grouped into two sets, as indicated in Fig. 4-41. The wavefront error data has been plotted in Fig. 4-42.

In his letter, Dr. Brown describes the measurement and data reduction technique as follows:

"The radial wavefront profiles were obtained from interferograms, all taken at the same focal setting with the interferometer (and slit source) rotated to different position angles. For each interferogram orientation, a zero shear interferogram was also taken and the difference of the sheared and unsheared interferograms used in the reduction process to avoid any systematic errors due to gravitationally induced flexures in the interferometer itself. This procedure was repeated for each of four positions of the mirror on its support system (at position angles of  $0^\circ$ ,  $90^\circ$ ,  $180^\circ$ ,  $270^\circ$ ) and each profile represents the mean of the profiles obtained in the four positions of the test support. Interferogram measurements were made on prints using a simple interpolating device (developed by Grubb Parsons), and the reduction technique was essentially the simple summation method given in my paper of 1955<sup>4</sup>, though with the volume of data involved the measurements had to be computer processed.

"The profiles were obtained along a single diameter per interferogram, parallel to the shear direction. The relative heights of the different profiles were obtained by summing along short chords above and below the central hole to link the starting points of different profiles. Significant closing errors were found for the polygon composed of these short chords and for this reason it is possible that the absolute height of some of the profiles could be in error by as much as  $\lambda/20$ . A more satisfactory procedure would have been to link the various profiles using several different polygons but available time and effort did not permit this at the time."

Figuring of the mirror was carried out by a computer assisted process which has been described in reference 5. In his letter, Dr. Brown describes the mirror fabrication process as follows:

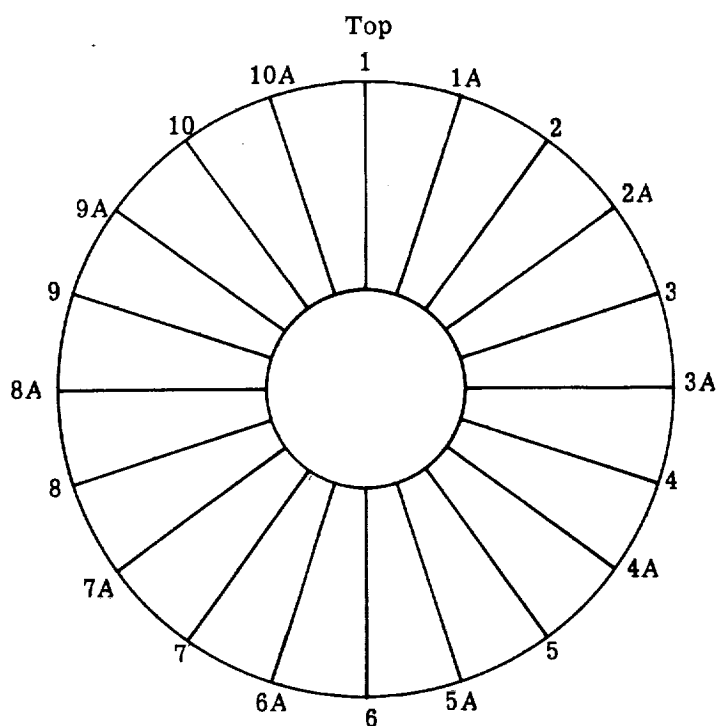
"Polishing and figuring the mirror was carried out almost entirely with a single, full size "Flexible" lap. The figuring to stage 1 specification followed the fairly standard (for us) routine of reducing astigmatism to an acceptably small value followed by aspherizing and figuring, treating the mirror as a figure of rotation. This approach proved completely adequate to completion of stage 1 work (99 percent of energy within 1.0 arc-second image diameter, 95 percent within 0.7 arc-second, and 80 percent within 0.4 arc-second). On completion of stage 1, measured primary astigmatism was about 0.25 arc-second circle of confusion and at commencement of stage 2

figuring it was thought necessary to reduce primary astigmatism to have a good probability of achieving stage 2 specifications. From then on the mirror was not considered to have rotational symmetry and described by a series of profiles obtained by the techniques outlined earlier in this letter. During most of this stage an adequate description of mirror errors was obtained by use of 10 profiles each with measurements at 1-inch intervals, though at times greater volumes of data had to be handled. During both stages the figuring was carried out with computer assistance apart from a limited period midway through stage 2 when industrial action limited our data handling capacity . . ."

Both the coarse wavefront error map and several of the radius profiles have been used in the analysis described below.

			4	8	4				
	-27	-10	15	17	15	16	16		
-27	-10	3	3	4	3	10	19	16	
	-7	2	15	0	-17	-16	4	0	0
-25	4	4	-4				-7	5	2 -32
-17	0	10	0				0	5	2 -18
-17	0	0	2				-4	0	0 -18
	-11	3	5	-12	-18	1	7	-2	0
-17	12	3	0	2	0	3	-5	-31	
	23	19	17	15	17	-9	-31		
			13	9	13				

**4-63**



Wavefront profiles give profile heights at 1-inch intervals from a radius of 25 inches to a radius of 77 inches.

Profiles are wavefront errors for  $\lambda = 578 \text{ nm}$

Profiles 1-10 are referred to mean focus for 1-10 profiles

Profiles 1A-10A are referred to mean focus for 1A-10A profiles

All profiles unrelated to absolute height

Fig. 4-41 — Arrangement of wavefront profiles on Anglo-Australian telescope 154-inch primary mirror



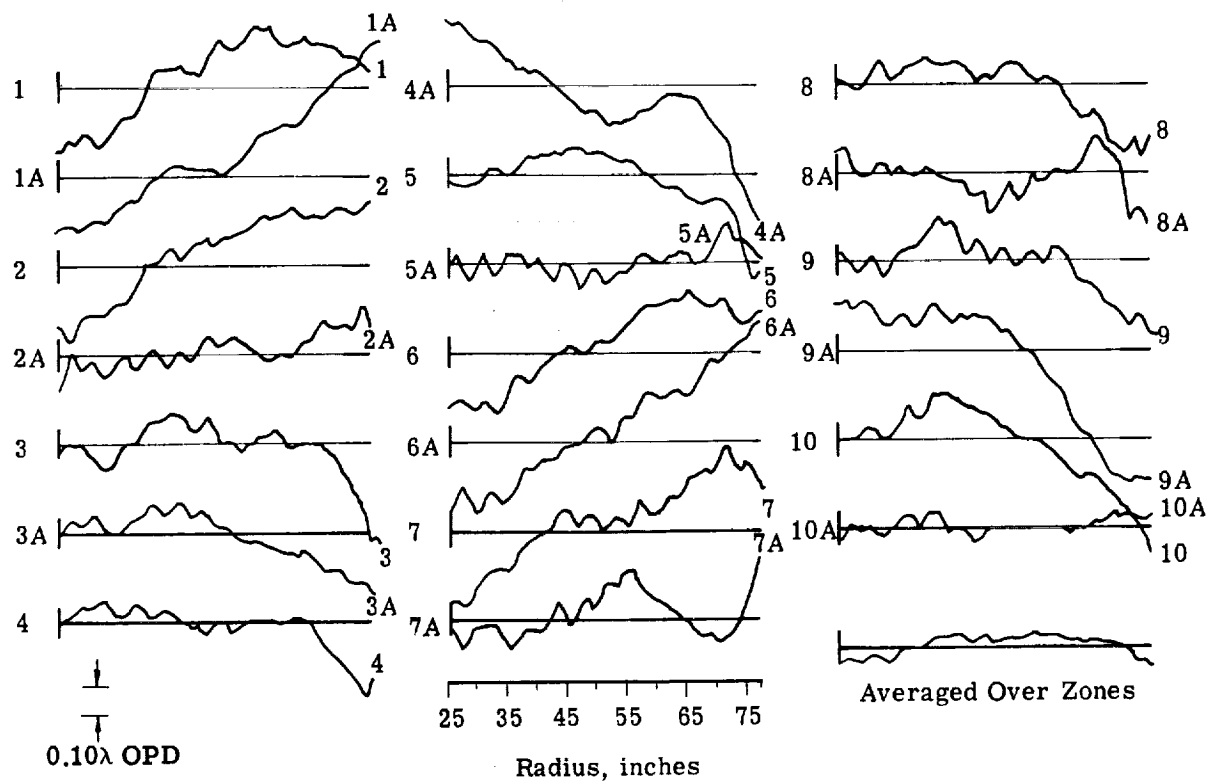


Fig. 4-42 — Radial wavefront profiles for Anglo-Australian telescope 154-inch primary mirror

Table 4-10 — Wavefront Error Profiles for A.A.T. 154-Inch-Diameter Primary Mirror, Measured Along Radii 18 Degrees Apart

Optical Path Difference in Wavelengths, Measured at  $\lambda = 5780 \text{ \AA}$

radius	1	1a	2	2a	3	3a	4	4a	5	5a	6	6a	7	7a	8	8a	9	9a	10	10a	average
1	25"	-0.23	-0.20	-0.22	-0.13	-0.03	-0.01	-0.00	0.22	-0.02	0.00	-0.19	-0.25	-0.01	0.01	0.08	0.01	0.15	-0.05	-0.03	-0.058
2	26"	-0.23	-0.19	-0.23	-0.06	-0.01	0.02	0.00	0.20	-0.03	-0.00	-0.17	-0.21	-0.06	0.01	0.09	0.03	0.15	-0.00	-0.03	-0.048
3	27"	-0.20	-0.19	-0.28	-0.00	-0.01	0.04	0.02	0.21	-0.03	0.02	-0.16	-0.16	-0.09	0.00	0.05	0.01	0.16	-0.00	0.01	-0.042
4	28"	-0.21	-0.19	-0.27	-0.02	-0.02	0.03	0.19	-0.03	-0.03	-0.03	-0.18	-0.22	-0.07	-0.02	0.00	-0.01	0.14	-0.01	0.00	-0.056
5	29"	-0.18	-0.20	-0.21	-0.06	-0.01	0.02	0.05	0.17	-0.03	-0.06	-0.19	-0.22	-0.03	-0.03	-0.01	-0.04	0.15	0.00	-0.01	-0.056
6	30"	-0.18	-0.18	-0.19	-0.04	-0.05	0.04	0.04	0.15	-0.02	-0.01	-0.19	-0.24	-0.18	-0.03	-0.00	-0.02	0.16	-0.03	-0.01	-0.047
7	31"	-0.17	-0.17	-0.19	-0.03	-0.06	0.06	0.06	0.15	0.01	0.03	-0.16	-0.20	-0.15	-0.03	0.04	0.00	0.15	0.03	-0.00	-0.033
8	32"	-0.22	-0.17	-0.19	-0.06	-0.09	0.04	0.07	0.15	0.02	-0.02	-0.18	-0.17	-0.13	-0.03	0.07	-0.03	0.11	0.02	-0.02	-0.040
9	33"	-0.21	-0.18	-0.19	-0.07	-0.09	0.01	0.06	0.14	0.00	-0.04	-0.22	-0.19	-0.13	-0.03	0.05	-0.07	0.07	-0.00	-0.03	-0.055
10	34"	-0.19	-0.17	-0.17	-0.07	-0.08	-0.00	0.02	0.12	0.01	-0.01	-0.18	-0.20	-0.13	-0.08	0.02	0.01	0.10	0.03	0.01	-0.055
11	35"	-0.15	-0.14	-0.15	-0.03	-0.04	0.00	0.02	0.08	-0.00	0.03	-0.13	-0.20	-0.14	-0.11	0.03	0.01	0.10	0.03	0.02	-0.039
12	36"	-0.12	-0.13	-0.15	-0.01	-0.01	0.02	0.02	0.08	0.01	0.03	-0.09	-0.18	-0.11	-0.08	0.04	0.02	0.11	0.09	0.03	-0.005
13	37"	-0.12	-0.10	-0.14	-0.01	0.00	0.04	0.05	0.05	0.03	0.03	-0.08	-0.12	-0.07	-0.04	0.06	0.00	0.11	0.11	0.04	-0.006
14	38"	-0.12	-0.11	-0.10	-0.05	0.00	0.05	0.06	0.06	0.06	0.00	-0.10	-0.09	-0.04	-0.03	0.06	0.00	0.08	0.07	0.02	-0.008
15	39"	-0.09	-0.10	-0.04	-0.00	0.05	0.06	0.04	0.04	0.06	-0.01	-0.10	-0.10	-0.03	-0.04	0.07	0.01	0.05	0.06	0.00	-0.002
16	40"	-0.02	-0.07	-0.01	0.00	0.07	0.09	0.01	0.05	0.06	0.02	-0.07	-0.09	-0.02	-0.05	0.08	0.02	0.10	0.09	0.03	0.019
17	41"	0.02	-0.02	-0.00	0.02	0.07	0.09	0.02	0.03	0.07	0.00	-0.04	-0.06	-0.01	-0.04	0.07	0.00	0.12	0.14	0.05	0.034
18	42"	0.04	-0.01	0.00	0.00	0.08	0.08	0.04	0.02	0.06	-0.02	-0.02	-0.06	0.00	0.01	0.07	-0.01	0.14	0.14	0.05	0.038
19	43"	0.04	-0.01	0.04	-0.04	0.08	0.05	0.04	0.00	0.07	-0.06	-0.01	-0.05	0.05	0.06	0.06	0.02	0.11	0.15	0.00	0.034
20	44"	0.04	0.02	0.05	-0.03	0.10	0.08	0.03	-0.02	0.06	-0.00	-0.00	-0.04	0.06	0.03	0.06	-0.02	0.10	0.15	-0.02	0.038
21	45"	0.04	0.02	0.03	0.01	0.09	0.10	0.01	-0.05	0.09	-0.00	0.02	-0.01	0.06	-0.02	-0.03	0.13	0.09	0.13	-0.01	0.039
22	46"	0.05	0.02	0.02	0.00	0.08	0.08	-0.00	-0.06	0.09	-0.01	0.01	0.00	0.04	0.00	0.06	0.10	0.11	0.12	-0.01	0.034
23	47"	0.03	0.01	0.04	-0.01	0.05	0.05	-0.02	-0.08	0.09	-0.09	-0.01	0.01	0.02	0.06	0.03	-0.04	0.10	0.11	-0.03	0.017
24	48"	0.03	-0.01	0.07	-0.00	0.04	0.06	-0.01	-0.10	0.07	-0.08	-0.03	0.01	0.05	0.07	-0.08	0.04	0.11	0.09	-0.04	0.017
25	49"	0.02	0.01	0.07	0.04	0.07	0.07	-0.04	-0.09	0.08	-0.02	0.03	0.05	0.04	0.02	0.00	0.06	0.10	0.09	-0.04	0.027
26	50"	0.06	0.01	0.08	0.06	0.08	0.04	-0.02	-0.09	0.08	-0.02	0.04	0.05	0.04	0.06	0.03	-0.07	0.10	0.09	-0.00	0.033
27	51"	0.10	0.01	0.06	0.05	0.03	0.02	-0.00	-0.12	0.08	-0.06	0.03	0.04	0.01	0.11	0.02	-0.02	0.09	0.07	-0.01	0.019
28	52"	0.13	-0.00	0.08	0.03	0.00	0.02	-0.00	-0.14	0.07	-0.06	0.04	0.00	0.03	0.12	0.05	-0.12	0.08	0.04	0.00	0.021
29	53"	0.13	-0.01	0.08	0.04	-0.01	-0.03	-0.12	0.05	-0.04	-0.04	0.02	0.05	0.11	0.06	-0.09	0.04	0.06	0.03	0.00	0.019
30	54"	0.12	0.01	0.10	0.05	-0.01	-0.03	-0.13	0.04	-0.02	-0.04	0.07	0.03	0.15	0.07	-0.04	0.02	0.06	0.03	0.00	0.029
31	55"	0.11	0.02	0.10	0.05	-0.03	-0.03	-0.02	-0.13	0.04	-0.04	0.09	0.08	0.02	0.16	0.07	-0.08	0.02	-0.00	-0.00	0.021
32	56"	0.12	0.02	0.11	0.03	-0.00	-0.04	0.00	-0.12	0.04	-0.02	0.12	0.08	0.05	0.16	0.07	-0.09	0.02	-0.01	-0.00	0.026
33	57"	0.16	0.05	0.13	0.02	0.00	-0.02	0.01	-0.09	0.01	0.02	0.13	0.11	0.10	0.11	0.04	0.01	0.00	-0.01	-0.00	0.037
34	58"	0.18	0.10	0.15	0.01	0.02	-0.03	0.01	-0.08	0.00	0.03	0.15	0.16	0.08	0.10	0.00	-0.00	-0.01	0.00	-0.00	0.045
35	59"	0.17	0.13	0.16	-0.02	0.02	-0.04	0.01	-0.08	0.00	0.01	0.15	0.16	0.05	0.07	-0.00	-0.03	-0.05	-0.01	-0.00	0.036
36	60"	0.17	0.13	0.16	-0.03	0.03	-0.05	0.01	-0.06	-0.03	0.00	0.15	0.15	0.07	0.06	0.01	-0.03	-0.09	-0.03	-0.00	0.031
37	61"	0.18	0.14	0.15	-0.02	0.04	-0.05	-0.01	-0.04	-0.05	0.00	0.16	0.14	0.09	0.04	-0.00	0.00	-0.11	-0.04	-0.00	0.031
38	62"	0.15	0.15	0.16	0.00	0.02	-0.06	-0.00	-0.04	-0.05	0.02	0.17	0.16	0.11	0.03	-0.01	0.01	-0.16	-0.06	-0.01	0.034
39	63"	0.13	0.16	0.17	-0.01	-0.01	-0.06	0.00	-0.04	-0.05	0.02	0.17	0.17	0.10	0.02	-0.02	0.02	-0.16	-0.09	0.01	0.026
40	64"	0.12	0.15	0.19	-0.01	-0.02	-0.07	0.02	-0.04	-0.06	0.03	0.17	0.17	0.12	0.00	-0.05	-0.00	-0.21	-0.11	-0.02	0.019
41	65"	0.13	0.15	0.17	0.02	0.00	-0.05	0.01	-0.04	-0.09	0.03	0.20	0.15	0.17	-0.00	-0.09	0.00	-0.25	-0.11	-0.00	0.018
42	66"	0.13	0.16	0.15	0.04	0.00	-0.06	-0.00	-0.04	-0.09	0.00	0.19	0.16	0.18	-0.03	-0.12	-0.08	-0.28	-0.13	-0.00	0.010
43	67"	0.14	0.18	0.16	0.04	-0.00	-0.07	-0.01	-0.04	-0.10	-0.01	0.17	0.18	0.19	-0.05	-0.12	0.07	-0.29	-0.11	0.00	0.013
44	68"	0.13	0.22	0.16	0.08	-0.00	-0.11	-0.05	-0.08	-0.09	0.00	0.16	0.24	0.06	-0.06	-0.10	0.12	-0.32	-0.12	0.02	0.016
45	69"	0.13	0.25	0.15	0.11	-0.01	-0.13	-0.08	-0.12	-0.08	0.02	0.15	0.27	0.19	-0.05	-0.12	0.10	-0.36	-0.13	0.01	0.010
46	70"	0.13	0.27	0.17	0.09	-0.04	-0.12	-0.11	-0.16	-0.08	0.07	0.16	0.26	0.23	-0.07	-0.15	0.08	-0.41	-0.16	0.02	0.002
47	71"	0.12	0.29	0.18	0.09	-0.05	-0.12	-0.12	-0.18	-0.09	0.12	0.17	0.28	0.28	-0.07	-0.20	0.07	-0.42	-0.20	0.05	0.002
48	72"	0.11	0.32	0.19	0.09	-0.09	-0.12	-0.15	-0.20	-0.12	0.13	0.16	0.30	0.28	-0.06	-0.21	0.05	-0.43	-0.20	0.04	-0.004
49	73"	0.08	0.33	0.18	0.09	-0.12	-0.16	-0.17	-0.22	-0.16	0.08	0.12	0.32	0.22	-0.03	-0.23	-0.04	-0.43	-0.23	0.05	-0.029
50	74"	0.08	0.34	0.17	0.08	-0.17	-0.17	-0.19	-0.32	-0.25	0.06	0.09	0.33	0.21	0.01	-0.21	-0.15	-0.45	-0.26	0.05	-0.049
51	75"	0.08	0.34	0.16	0.15	-0.17	-0.17	-0.22	-0.37	-0.32	0.06	0.09	0.35	0.23	0.08	-0.18	-0.12	-0.44	-0.28	0.03	-0.044
52	76"	0.07	0.40	0.17	0.15	-0.24	-0.16	-0.26	-0.40	-0.36	0.04	0.12	0.39	0.18	0.13	-0.24	-0.13	-0.44	-0.30	0.02	-0.053
53	77"	0.04	0.42	0.20	0.10	-0.33	-0.21	-0.19	-0.46	-0.34	0.02	0.13	0.41	0.13	0.21	-0.18	-0.17	-0.44	-0.38	0.04	-0.063

#### 4.7.2 Two-Dimensional Wavefront Analysis

A brief two-dimensional wavefront analysis of the 154-inch mirror has been performed, based on the 11- by 11-point wavefront error map of Fig. 4-40. The purpose of the analysis was to show the presence of rotational asymmetry in the wavefront, and to indicate how this will affect image quality at various wavelengths. The results are shown in Figs. 4-43 through 4-46.

A polynomial equation was fit to the 11- by 11-point grid and used to interpolate data points in a 33- by 33-point grid. This smoothed wavefront is plotted in Fig. 4-43. This wavefront map shows the saddle-shape characteristic of astigmatism. The peak-to-peak wavefront error is 0.65 wavelength, and the rms is 0.12 wavelength. A comparison of this data to the more detailed measurements along separate radii shown in Figs. 4-41 and 4-42 and Table 4-10 shows general agreement as to the shape of the wavefront. The more detailed measurements indicate a peak-to-peak wavefront error of 0.88 wavelength, due to high and low points along the rim of the mirror missed by the coarse grid. Note also that the peak-to-peak wavefront error of the wavefront averaged over each zone is only 0.108 wavelength, indicating that the truly rotationally symmetric component of the wavefront error is a small fraction of the asymmetric component.

Point spread functions were computed directly from the 11- by 11-point grid. The wavefront error values were scaled to simulate use of the telescope at  $\lambda = 3250$  and  $1215 \text{ \AA}$ , as well as the test wavelength of  $5780 \text{ \AA}$ . In examining the resulting PSF's, shown as linear scale perspective plots in Figs. 4-44 through 4-46, it should be noted that these plots are normalized to 1.0 for the highest peak in the PSF. Thus as the wavelength decreases and the central peak intensity (the Strehl definition) decreases, the ring structure becomes more prominent in part because of scale change in the plot. Thus the three PSF's should not be compared directly, but used only to indicate relative differences in height between the central maximum and the ring structure. Note that in Fig. 4-46 ( $\lambda = 1215 \text{ \AA}$ ) the central maximum is no longer the highest point in the pattern.

The three figures show an increasing prominence in the ring structure as the wavelength decreases. They also show large numbers of bumps in the ring structure. It is difficult to be certain whether these are real, or an artifact of the small number of sampling points used to define the wavefront. We have run similar calculations using the 33 by 33 interpolated data point grid, and the same lumpiness appears at  $\lambda = 1215 \text{ \AA}$ . This would rule out the simplest forms of aliasing. Note, however, that the rms wavefront error at  $\lambda = 1215 \text{ \AA}$  is roughly 0.6 wavelength, which is enough to thoroughly destroy the inner structure of the PSF.

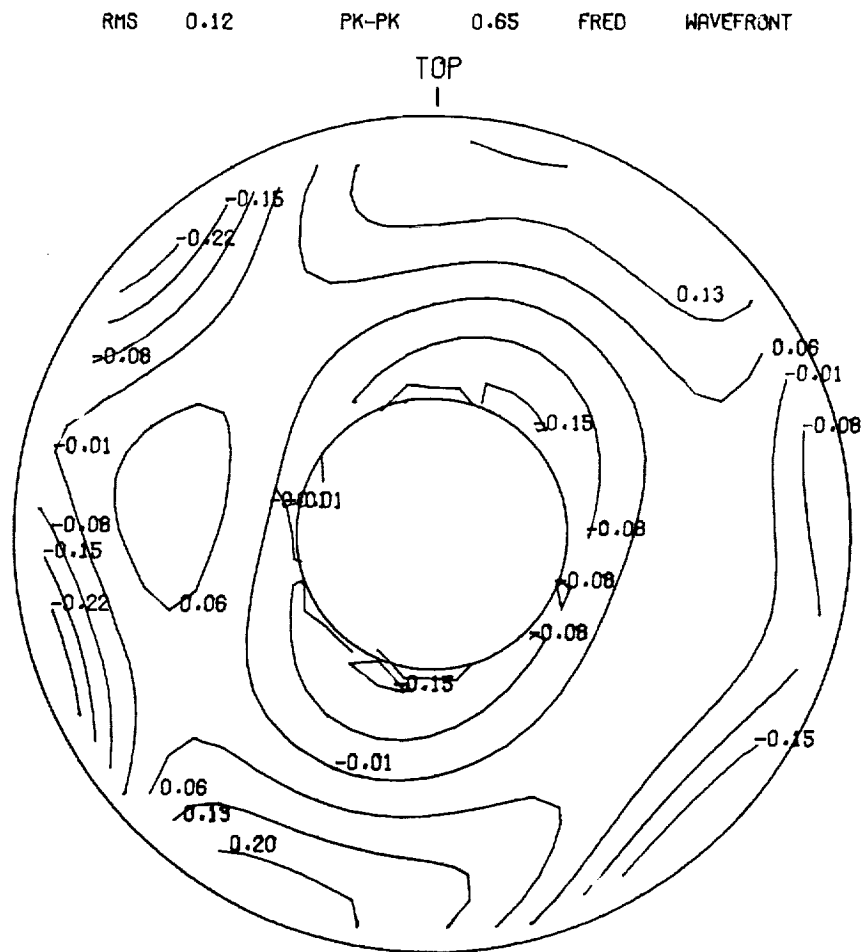


Fig. 4-43 — Wavefront map: interpolated from data grid

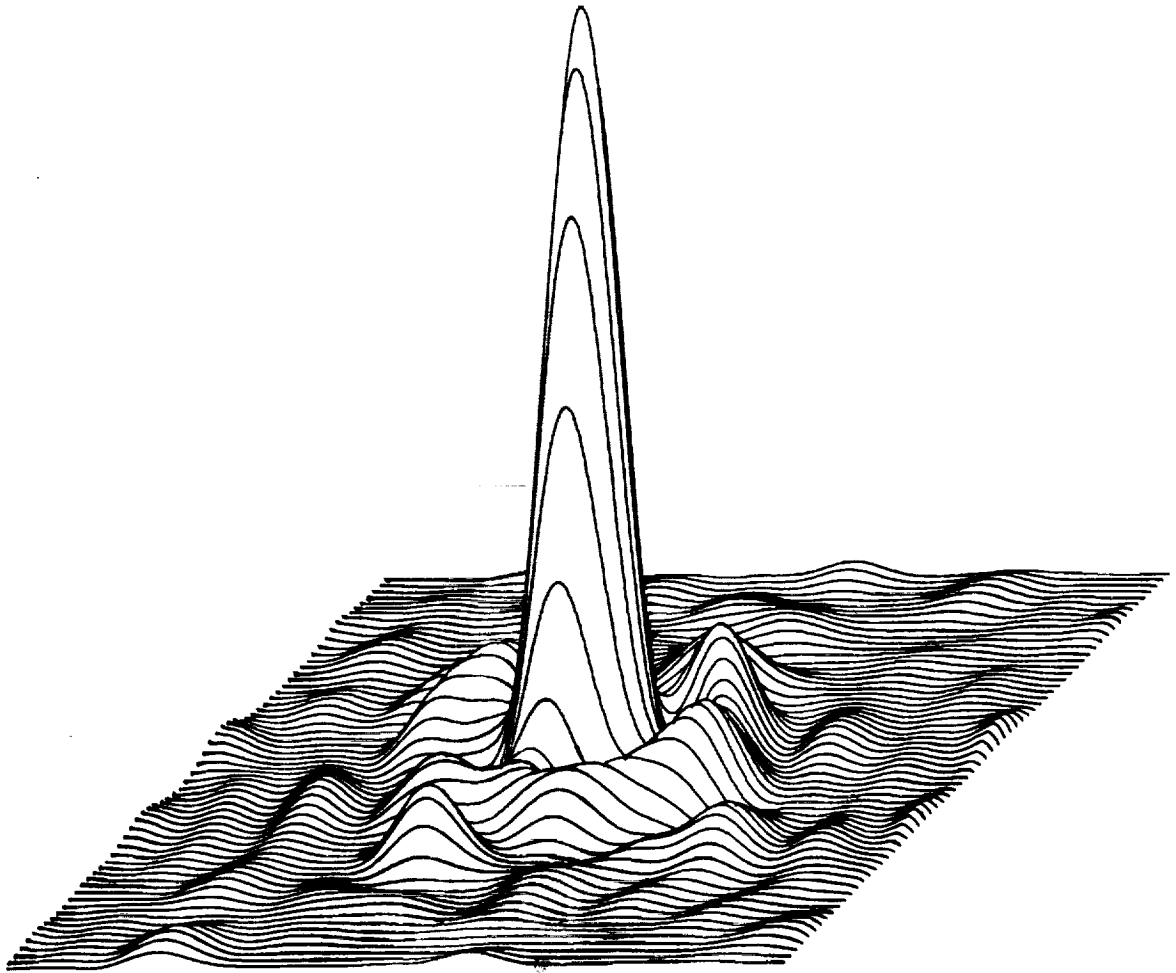


Fig. 4-44 — Point spread function at  $\lambda = 578 \text{ nm}$

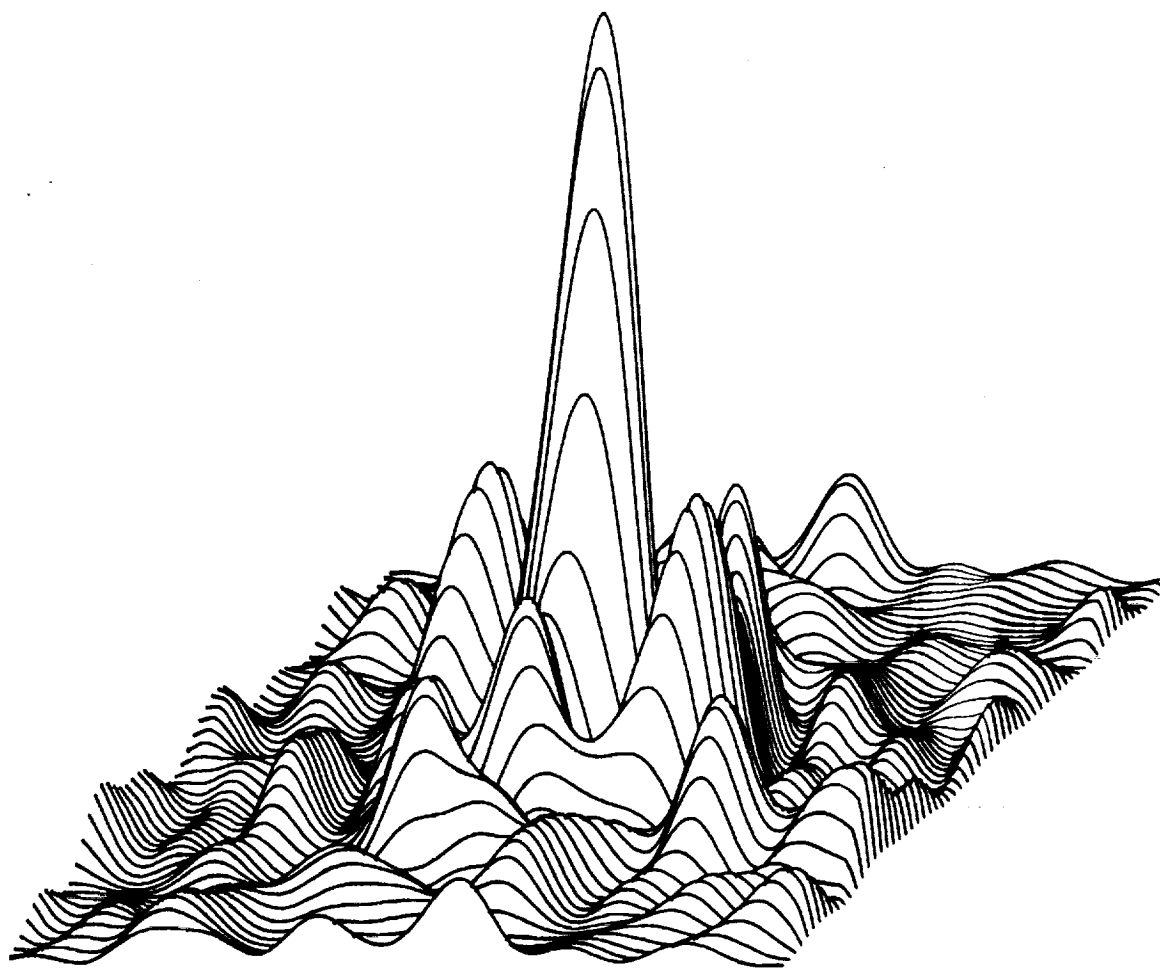


Fig. 4-45 — Point spread function at  $\lambda = 325$  nm

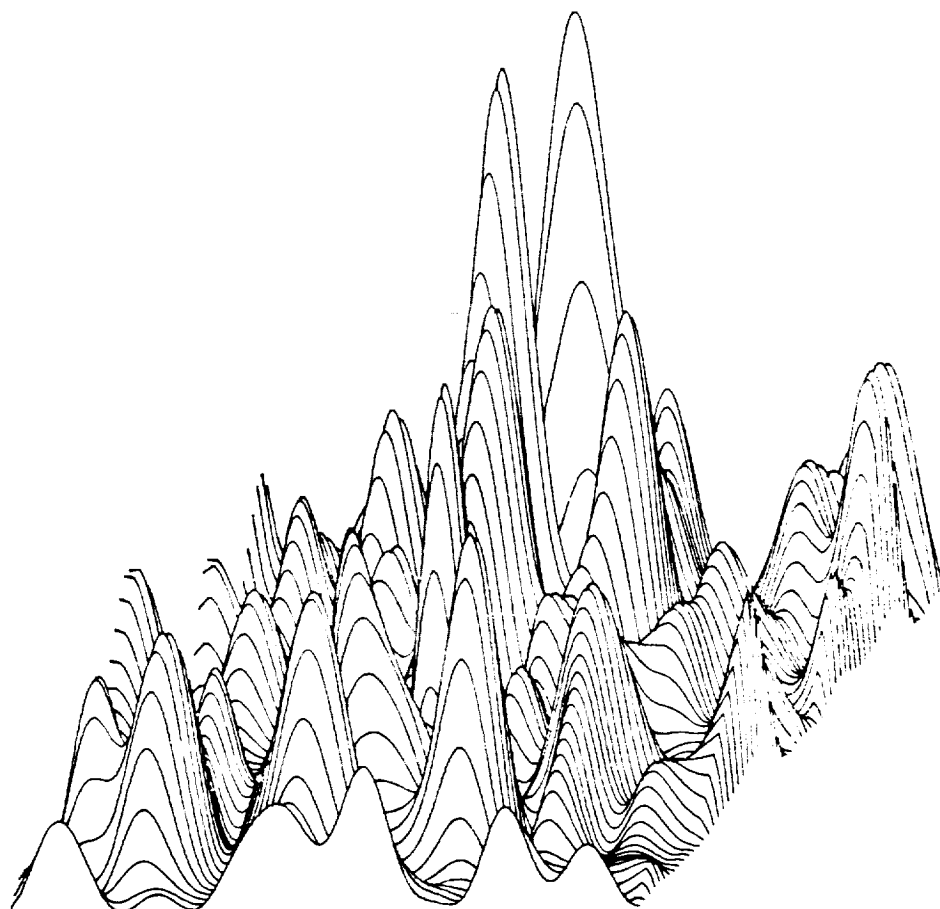


Fig. 4-46 — Point spread function at  $\lambda = 121.5 \text{ nm}$

### 4.7.3 Rotationally Symmetric Wavefronts Based on A.A.T. Radius Profiles

Fig. 4-42, which plots all twenty radial wavefront profiles supplied by Dr. Brown, shows that there is a considerable amount of fine structure in the mirror surface. Periods of the fine structure appear to be on the order of 4 to 5 inches, and heights generally do not exceed 0.1 wavelength at 5780 Å, the test wavelength. Much of this fine structure is damped out in taking the average over the same zone height (radius) in all twenty profiles, which indicates that it is not truly rotationally symmetric. However, individual ridges appear to be present over several adjacent radius profiles, and sometimes vary in zone height from profile to profile. It is possible that averaging around an elliptical zone would reveal a more prominent fine structure in the averaged profile. If so, or if the ridges merely extend over portions of a complete zone, using the individual radius profiles as the profile of a rotationally symmetric wavefront allows us to examine the effects of such fine structure on image quality, knowing that this particular example exists in a real mirror.

Three profiles have been selected from Table 4-10 for examination using GASPR. Radius 5A was selected because it has considerable fine structure with almost no obvious low spatial frequency structure. Radius 9 has both low and high spatial frequency components, and thus is a somewhat better representative of the real wavefront. The averaged wavefront profile was chosen as the third example to see if the rotationally symmetric component was of a large enough magnitude to be noticeable when scaling the wavefront error to model performance at shorter wavelengths. Three wavelengths were chosen, the test wavelength of 5780 Å, and 3250 and 1215 Å. The results are shown in Figs. 4-47 through 4-54.

In each case, the 53 data points from Table 4-10 were interpolated using a parabolic fit, generating the 512 points required for Gaussian quadrature. These were then scaled to the appropriate values of OPD for the three wavelengths. The results are shown in Fig. 4-47, for each radius at the shortest wavelength. (In comparing the plots, note that a different OPD scale is used in each case.) All show evidence of what appears to be a relatively high spatial frequency harmonic component. This will be discussed further in Section 4.7.4. Table 4-11 gives rms wavefront errors for all nine wavefronts. Note that these are all significantly lower than the value of 0.12 wavelength rms at  $\lambda = 5780$  Å given for the coarse two-dimensional wavefront map in Fig. 4-43.

Table 4-11 — RMS Wavefront Error for the Rotationally Symmetric Wavefronts Generated From the A.A.T. Data

Wavelength	Radius Profile		
	5A	9	Average
5780 Å	0.0465	0.0963	0.0317
3250 Å	0.0810	0.1713	0.0564
1215 Å	0.2167	0.4581	0.1508

Figs. 4-48 through 4-53 show the PSF's and MTF's for these nine cases, grouped by radius profile and wavelength. All show heavily degraded image quality at the shortest wavelengths, particularly in terms of MTF degradation. This is most evident for radius 9 and least evident for the averaged radius, as expected from the rms wavefront error data.

It is interesting to examine the PSF's for evidence of single harmonic cosine phase gratings. There is some evidence that a sideband from such a phase grating exists at about 28 to 30 Airy radii. This is most strongly evident for radius profile 9 at 1215 Å (Fig. 4-50c), both from increase



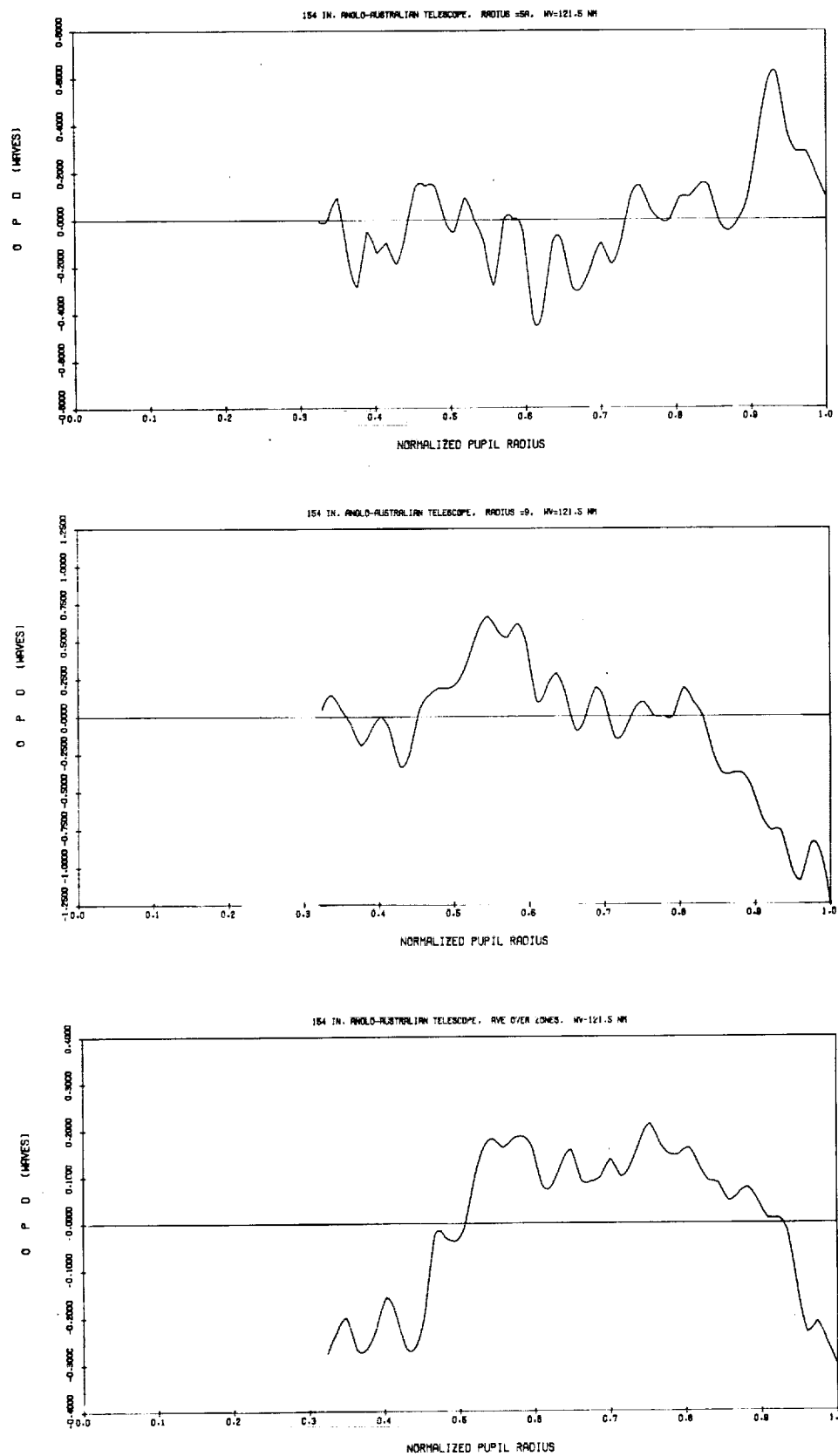


Fig. 4-47 — Wavefront profiles for radii 5A, 9, and for averaged over zones case, as used in GASPR;  $\lambda = 121.5$  nm

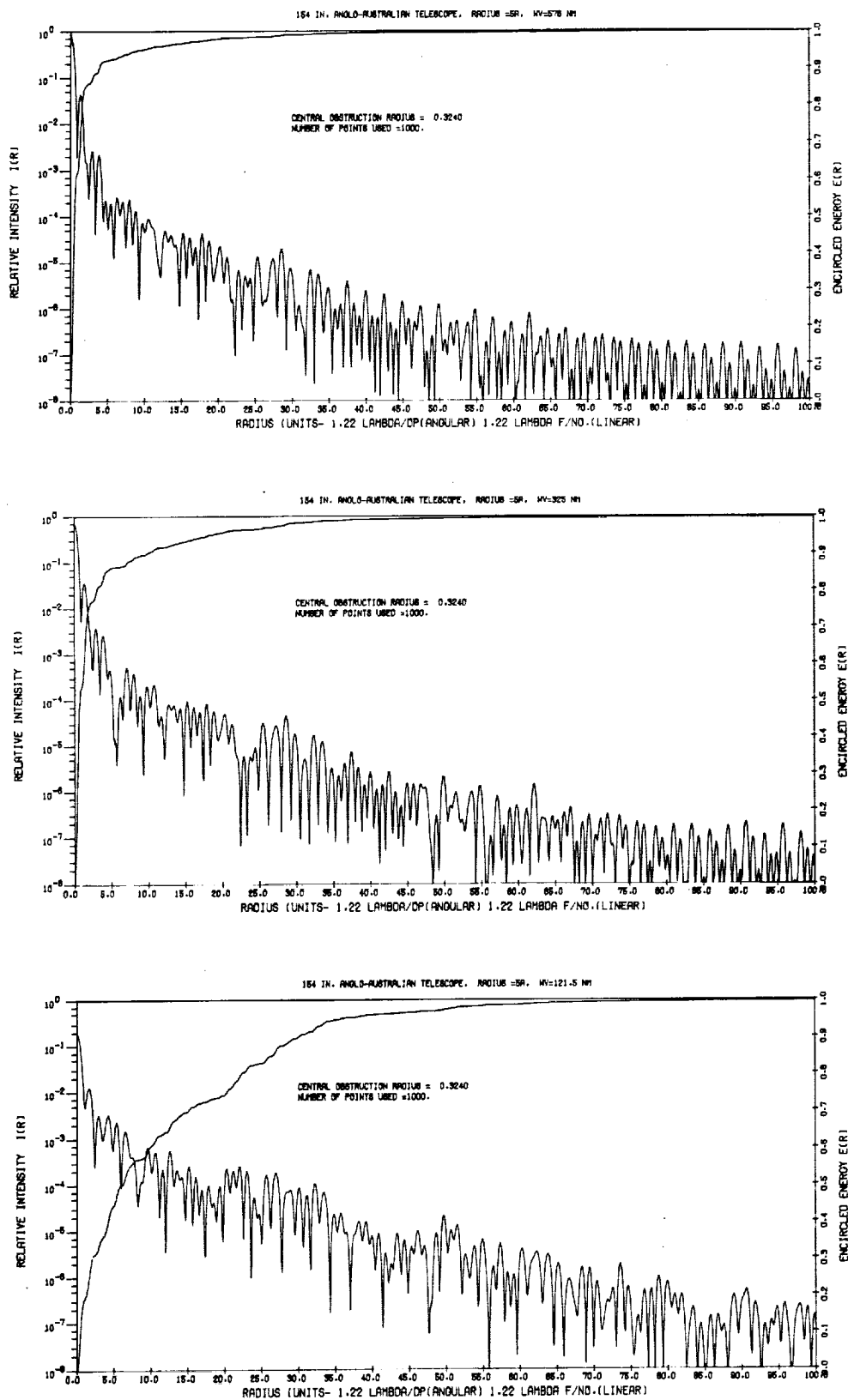


Fig. 4-48 — PSF's for radius 5A

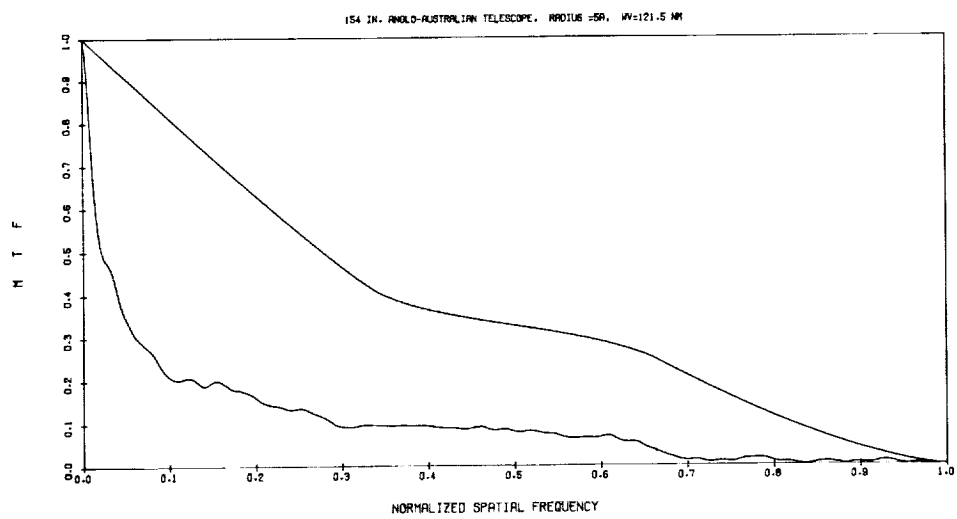
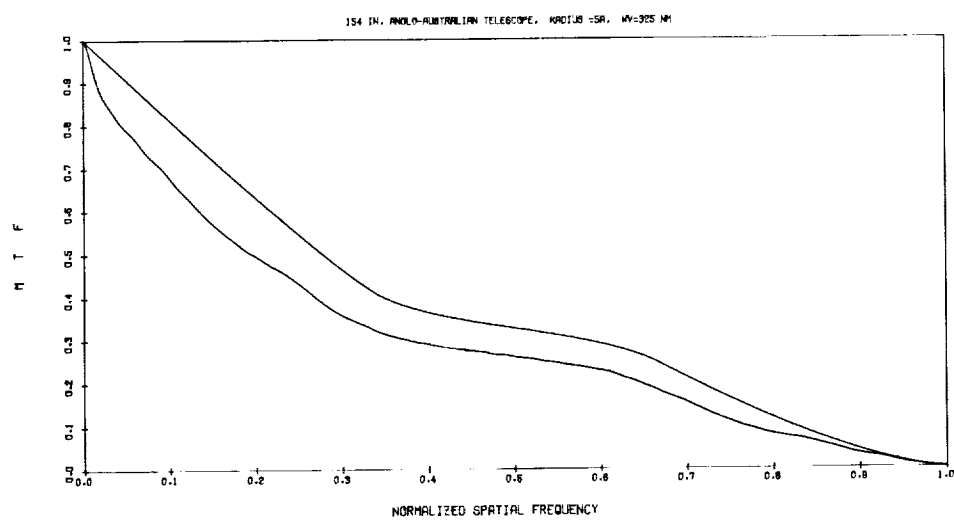
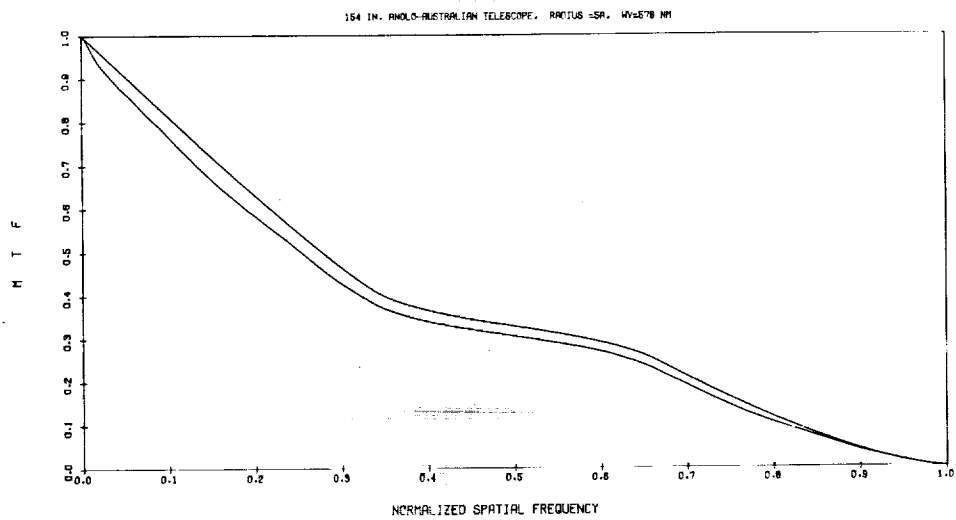


Fig. 4-49 — MTF's for radius 5A

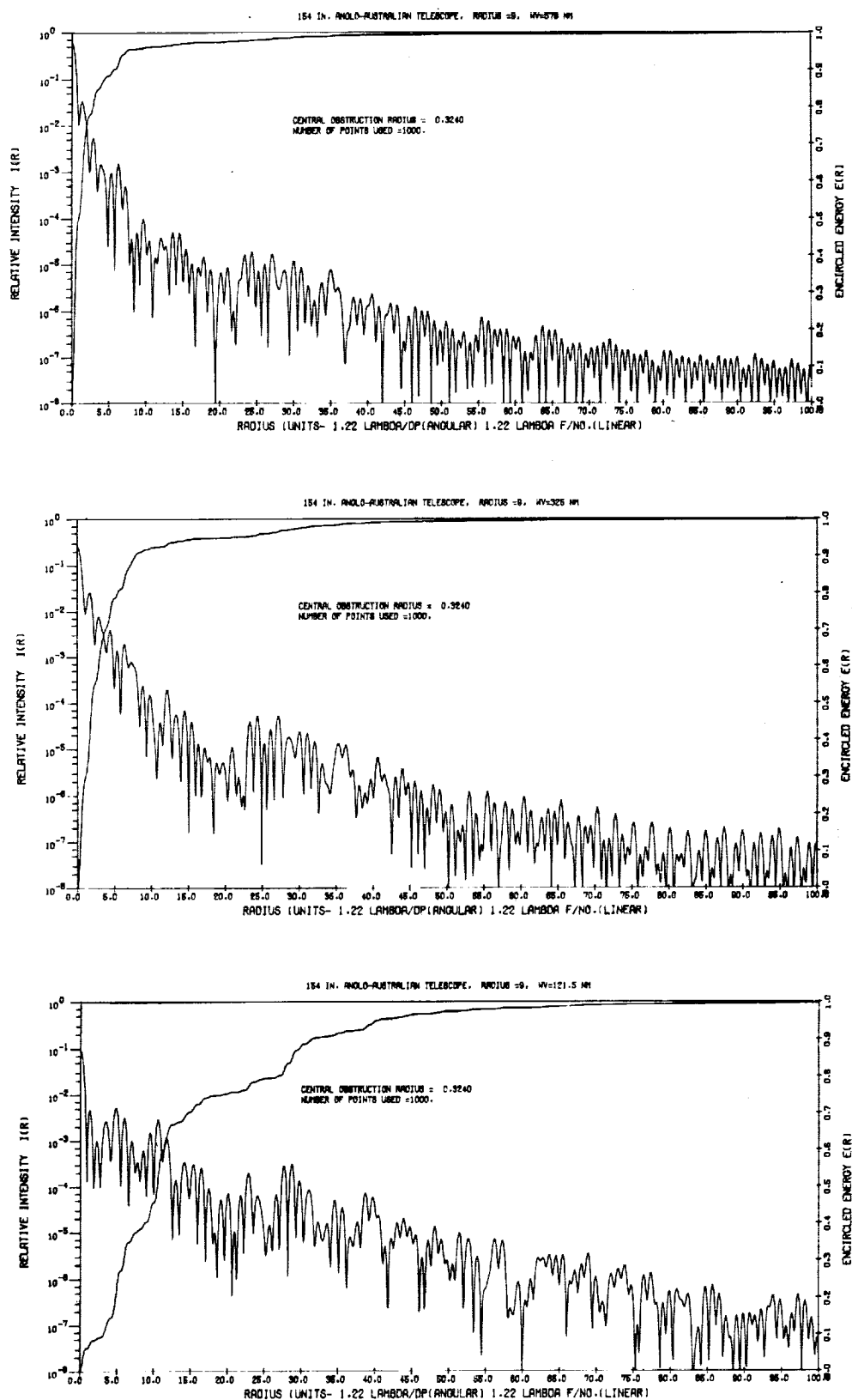


Fig. 4-50 — PSF's for radius 9

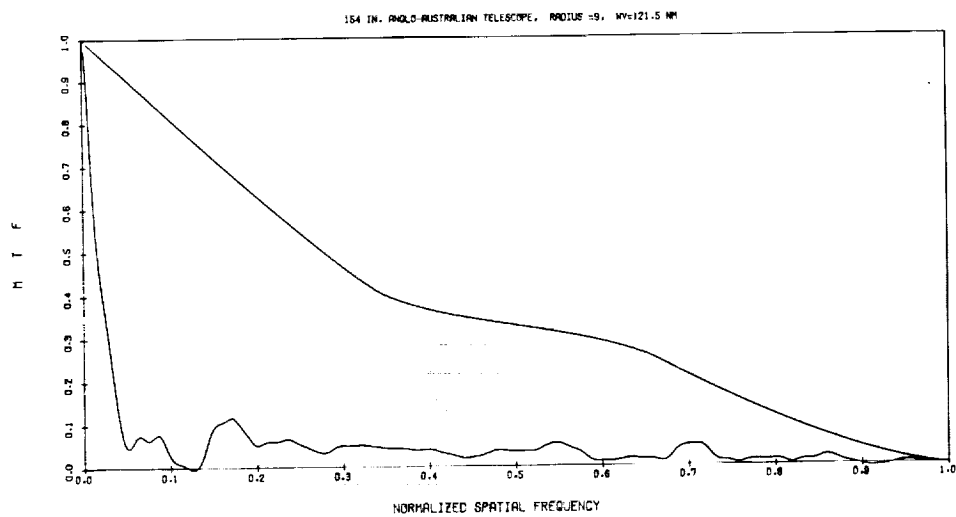
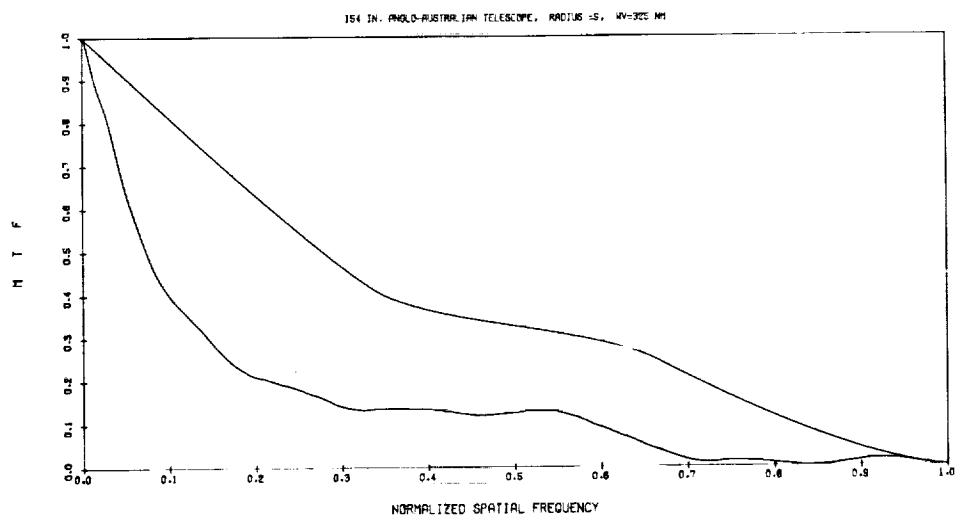
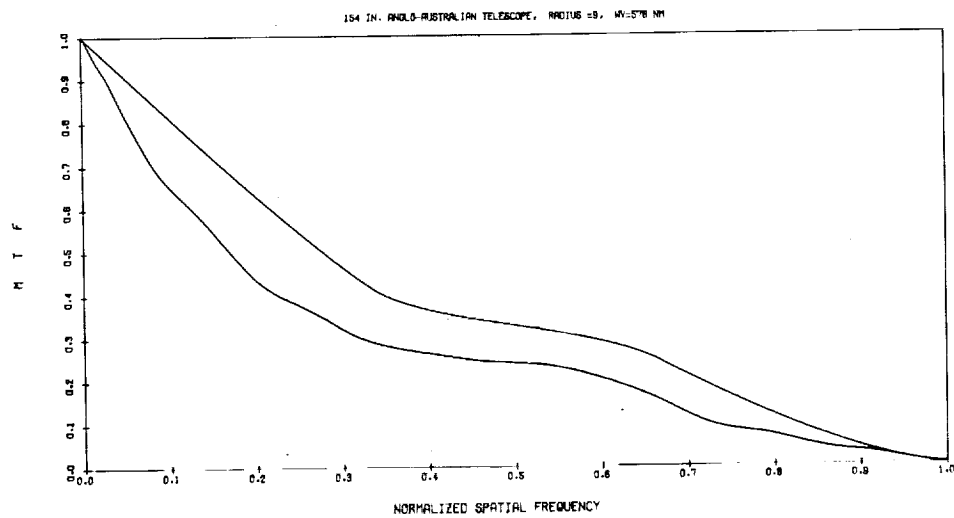


Fig. 4-51 — MTF's for radius 9

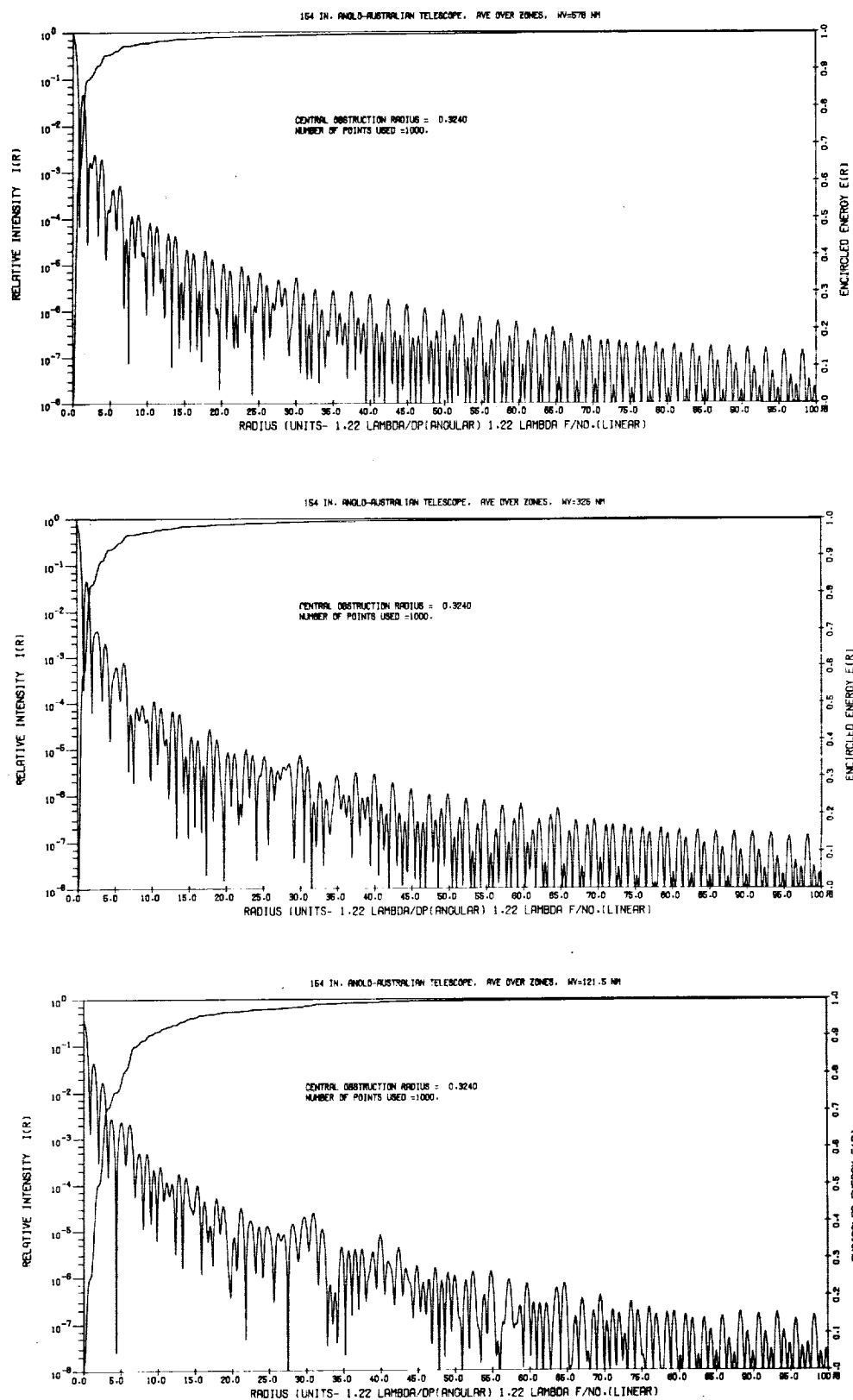


Fig. 4-52 — PSF's, wavefront error averaged over zones

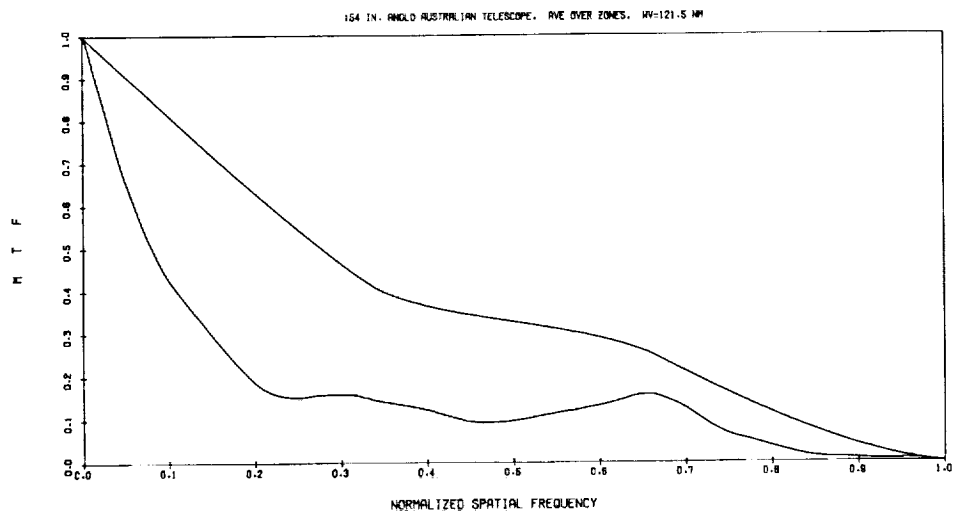
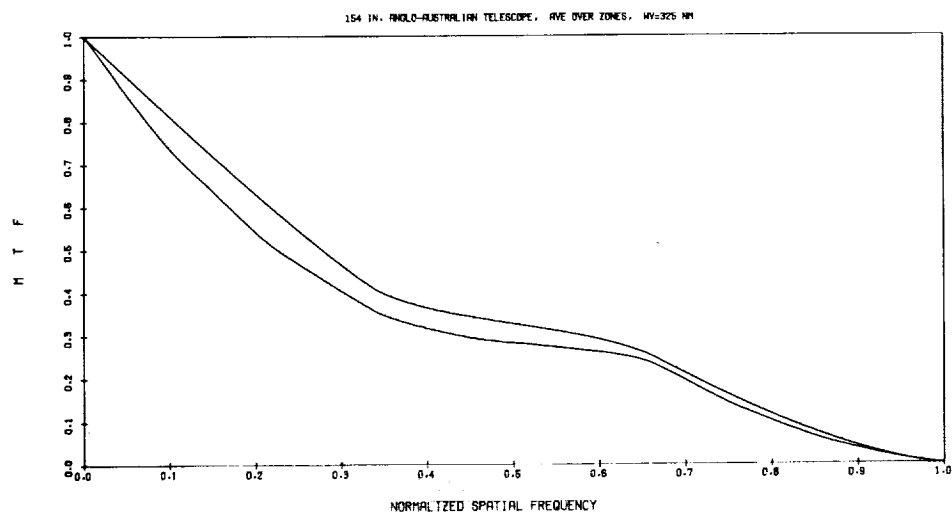
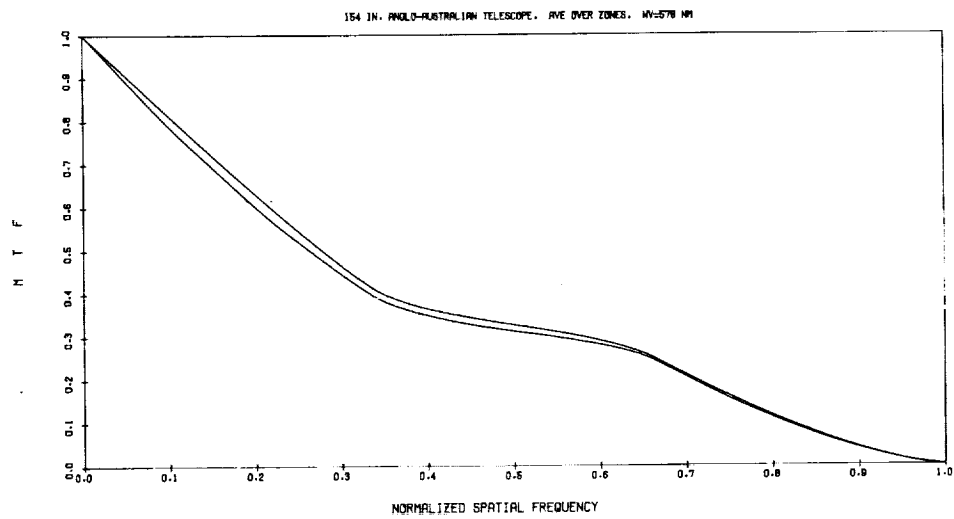


Fig. 4-53 — MTF's wavefront error averaged over zones

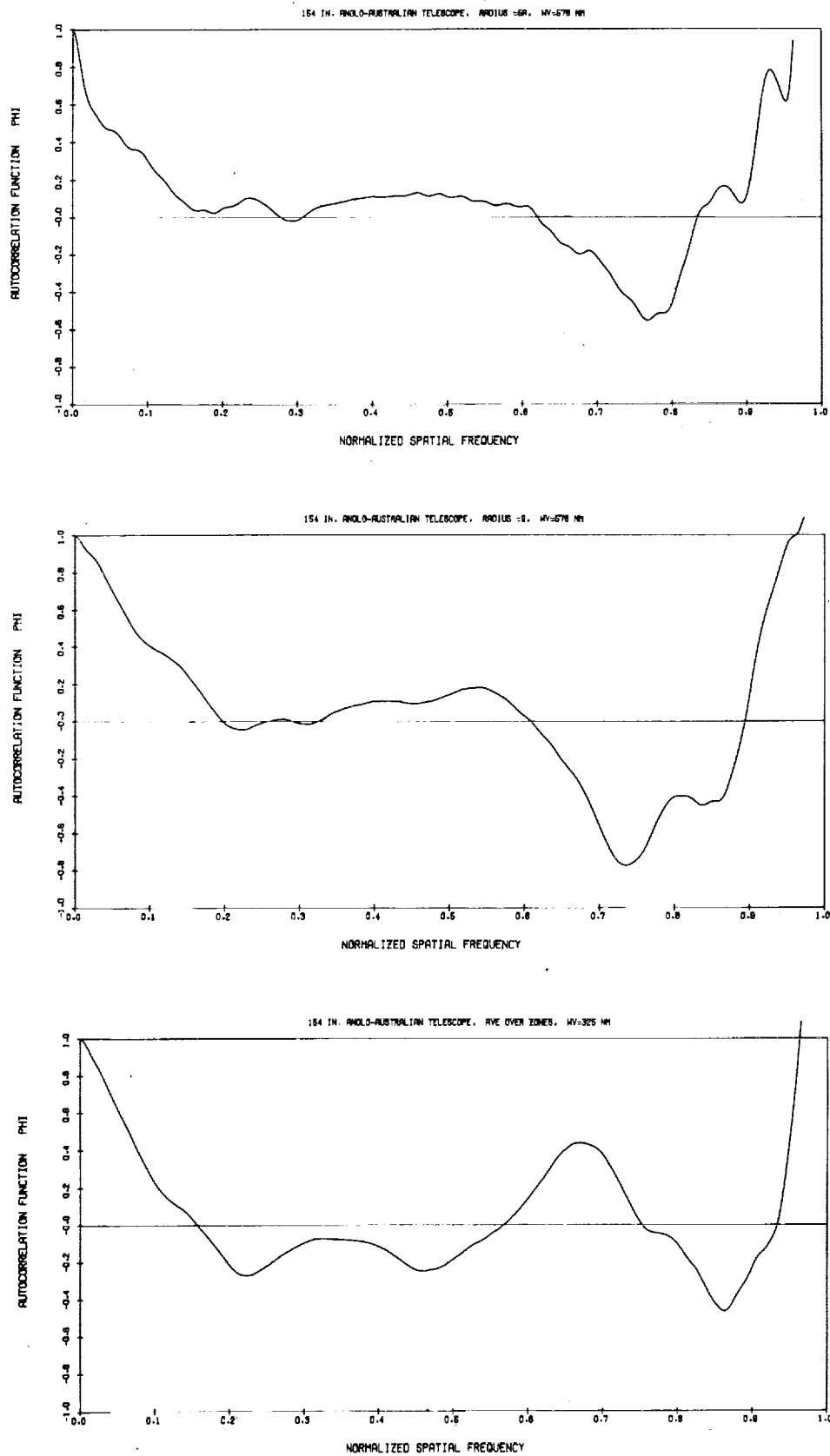


Fig. 4-54 — \*Autocorrelation functions for radii 5A, 9, and averaged over zones wavefronts



in relative intensity and from the shoulder in the encircled energy curve. It can also be seen for the averaged profile (Fig. 4-52c), although not as prominently. The evidence is not as strong for radius 5A, except in that the relative intensity seems to be raised somewhat over the entire region from 20 to about 34 Airy radii. This could indicate a series of closely spaced spatial frequencies.

Finally, Fig. 4-54 shows \*Autocorrelation functions for each radius profile. In this case, different wavelengths were chosen to minimize the computational errors by setting the rms wavefront error to between 0.05 and 0.10 wavelength. Note that none of these curves show any Gaussian characteristics near zero radius. The rapid (compared to Gaussian) drop in the \*Autocorrelation function near zero radius is indicative of the presence of high spatial frequency components in the wavefront error, and is most prominent for radius 5A (Fig. 4-54a), where the low spatial frequency component has been suppressed. The roughly linear drop for the averaged profile \*Autocorrelation function is similar in appearance to that for the square-smoothed random wavefront (see Fig. 4-32a), near zero radius.

#### 4.7.4 Spatial Frequency Spectrum Versus Displaced Energy

The GASPR printout includes the function displaced energy,  $DE = EE(\text{perf}) - EE$ , the difference between the encircled energy for a perfect, unobstructed lens and for the wavefront error function under study. The displaced energy indicates the fraction of the total energy in the image which has been displaced outward beyond a given radius. The incremental displaced energy  $\Delta DE = DE(r_1) - DE(r_2)$  may be computed from this data. The incremental energy function indicates the amount of energy which has been added to (positive value) or subtracted from (negative value) the zone  $\Delta r = r_2 - r_1$ , compared to the PSF for a perfect lens. It is, in effect, the zonal scatter function. The true scatter function is proportional to  $\Delta DE / \pi(r_2 + r_1)$ . The integral of  $\Delta DE$  from  $r = 0$  to  $r = \infty$  is by definition zero, since it measures both where the scattered light comes from and where it goes to. The energy "scattered" by the central obstruction is also included.

For our rotationally symmetric wavefronts, it is possible to determine the spatial frequency distribution of the wavefront irregularities by taking the one-dimensional Fourier transform of the radius profile. An example of the resultant amplitude spectrum is shown in Fig. 4-55 for the wavefront profile averaged over zones. The spatial frequency scale is in cycles per inch, and the spectral density scale in arbitrary units of the form wavelengths amplitude per cycle. The maximum spatial frequency is limited to 0.5 cycle per inch by the sampling interval, which is 1 inch.

Coupling the amplitude spectrum plot with the incremental displaced energy function allows comparison of the scatter function with the spatial frequency distribution of the wavefront irregularities causing the scattering. This gives some measure of the validity of models based on a spectrum of cosine phase gratings. To carry out the comparison, both the spatial frequency spectrum and incremental displaced energy have been computed for radius 5A and 9 of the A.A.T. wavefront profiles. The results are given in Table 4-12 and Figs. 4-56 through 4-59.

Table 4-12 lists the incremental displaced energy values for 1 Airy radius zones from  $r = 0$  to  $r = 50$  Airy radii. Data is given for a perfect lens with a 0.324-diameter ratio central obstruction, and for the two wavefront profiles, scaled for  $\lambda = 3250 \text{ \AA}$ . The values are fractions of the total energy in the image. Figs. 4-56 and 4-58 are the amplitude spectra for the two profiles, and Figs. 4-57 and 4-59 are the corresponding incremental displaced energy curves. To facilitate the comparison of the two curves, the square root of  $\Delta DE$  has been plotted instead of  $\Delta DE$ , since this corresponds more directly to the amplitude of the source phase grating. The radius scales have also been matched, with one Airy radius corresponding to a spatial frequency of 0.007919 cycle per inch.

The correlation between peaks in  $\Delta DE^{1/2}$  and spatial frequency components in the amplitude spectrum is most striking in the case of radius profile 5A, where the low spatial frequency components are of relatively small amplitude. The variation of amplitude with radius/spatial frequency also corresponds well between the two curves. The correlation is less striking for profile radius 9, where the low spatial frequency components are of considerably larger phase amplitude. Some peaks in the incremental displaced energy function correspond directly to peaks in the amplitude spectrum, but others do not, and the differences in amplitudes are more marked than for radius 5A. This is undoubtedly due to interactions between different spectral components of the type noted in, for example, Figs. 4-15b and 4-17c. (The central obstruction contributes to this process as well.) To facilitate analysis for any reader interested in tracking down the interactions, the position of the first few orders of sidebands for the five largest amplitude spatial frequency components has been marked in Fig. 4-59. Note that there is a definite scattering maximum corresponding to the second harmonic of spatial frequency B.

Several points of interest should be noted in this data. All of these curves show the presence of strong spectral components, and some of the strongest are present in all three cases (including

the averaged profile). There is a slight shift in the exact spatial frequency from curve to curve, which may only be an indication that the zonal ridges which go to make up a spatial frequency component are slightly elliptical, rather than circular. Note in particular the E component in Fig. 4-58, which has a relatively high spatial frequency (0.22 cycle per inch, or roughly 17 cycles per radius). This does persist through all three cases, and indicates that fairly strong high spatial frequency irregularities can exist even when the mirror is polished with a single flexible lap. Such zonal structure is usually attributed to the use of subaperture laps to polish aspheric surfaces.

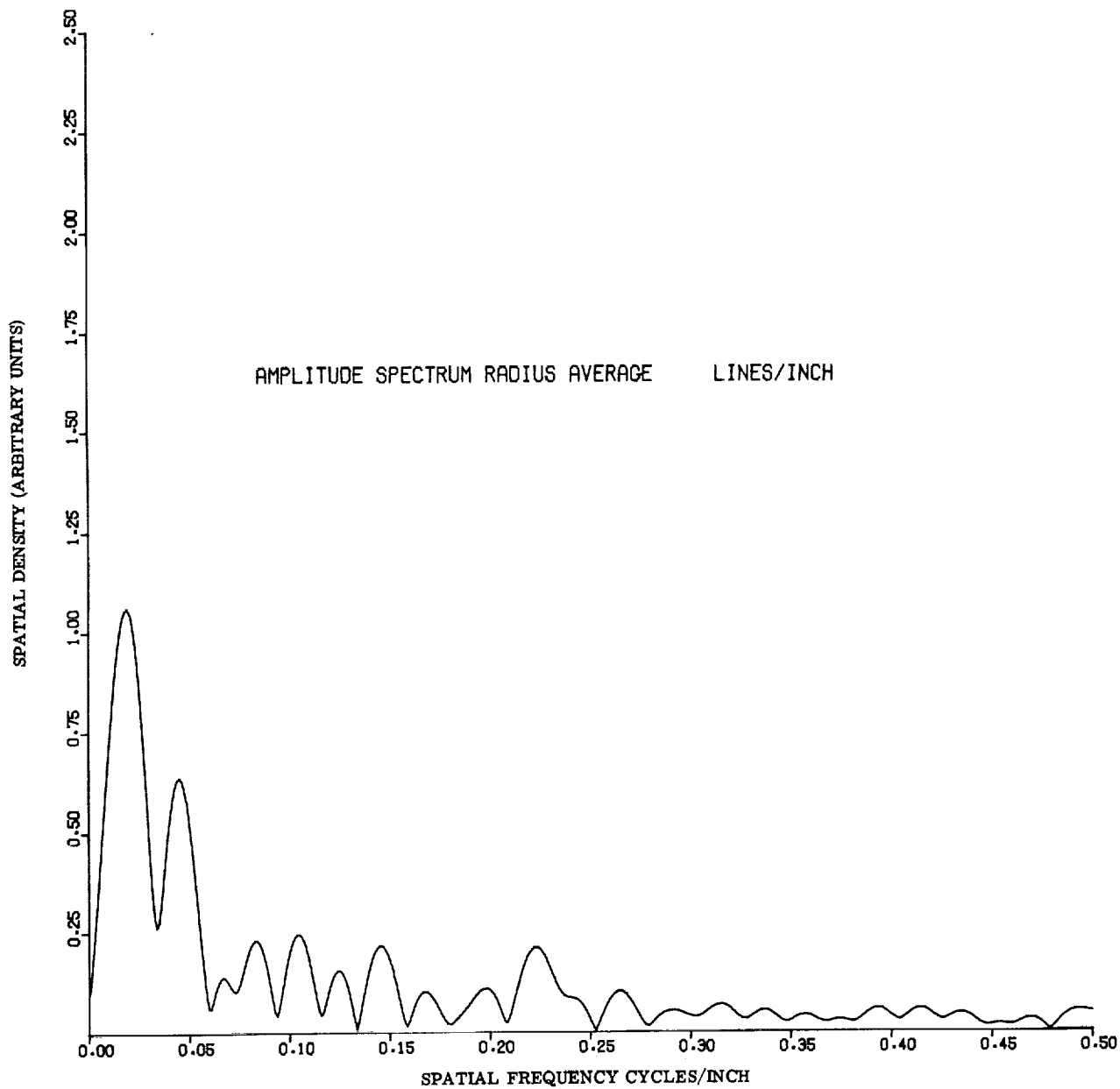


Fig. 4-55 — Amplitude spectrum for wavefront profile averaged over zones

Table 4-12 —  $\Delta DE$  for the A.A.T. Radius Profiles 5A and 9, and for  
a Perfect Lens With a Central Obstruction  $\epsilon = 0.324$

zone	perfect lens $\epsilon = 0.324$	radius 5A	radius 9
0-1	-0.175691	-0.298612	-0.542428
1-2	0.162340	0.142927	0.140169
2-3	-0.016152	0.009363	0.078501
3-4	0.011289	0.026041	0.072866
4-5	0.001120	0.014215	0.069280
5-6	0.002056	-0.002934	0.021566
6-7	0.005453	0.004631	0.053941
7-8	-0.000684	0.011390	0.032721
8-9	0.002261	0.006046	0.008297
9-10	-0.000506	0.005727	0.004830
10-11	0.001071	0.010052	0.000809
11-12	0.001205	0.002579	0.003003
12-13	0.000165	0.003214	0.006676
13-14	0.000858	0.004877	0.002442
14-15	-0.000368	0.003248	0.003151
15-16	0.000672	0.005131	0.002024
16-17	0.000320	0.004691	0.000061
17-18	0.000321	0.004686	0.000345
18-19	0.000374	0.004215	-0.000049
19-20	-0.000267	0.002723	0.000204
20-21	0.000480	0.004381	0.000332
21-22	0.000115	0.002373	0.000097
22-23	0.000292	0.000209	0.000054
23-24	0.000154	0.000320	0.003375
24-25	-0.000092	0.000737	0.004545
25-26	0.000295	0.003502	0.001292
26-27	-0.000049	0.001506	0.003070
27-28	0.000314	0.003123	0.004029
28-29	0.000043	0.005664	0.002998
29-30	-0.000009	0.001984	0.001712
30-31	0.000187	0.000535	0.002373
31-32	-0.000070	0.000521	0.002267
32-33	0.000272	0.002079	0.001268
33-34	-0.000011	0.001795	0.000535
34-35	0.000045	0.000292	0.000785
35-36	0.000108	0.000151	0.002465
36-37	-0.000062	0.000425	0.001959
37-38	0.000225	0.000934	0.000422
38-39	-0.000034	0.000347	0.000191
39-40	0.000076	0.000257	0.000281
40-41	0.000051	0.000177	0.001103
41-42	-0.000042	0.000105	0.000607
42-43	0.000177	0.000340	0.000254
43-44	-0.000038	0.000060	0.000504
44-45	0.000090	0.000118	0.000426
45-46	0.000012	0.000214	0.000255
46-47	-0.000020	0.000230	0.000130
47-48	0.000131	0.000229	0.000088
48-49	-0.000031	0.000039	0.000267
49-50	0.000092	0.000280	0.000120

REPRODUCIBILITY OF THE  
ORIGINAL PAGE IS POOR

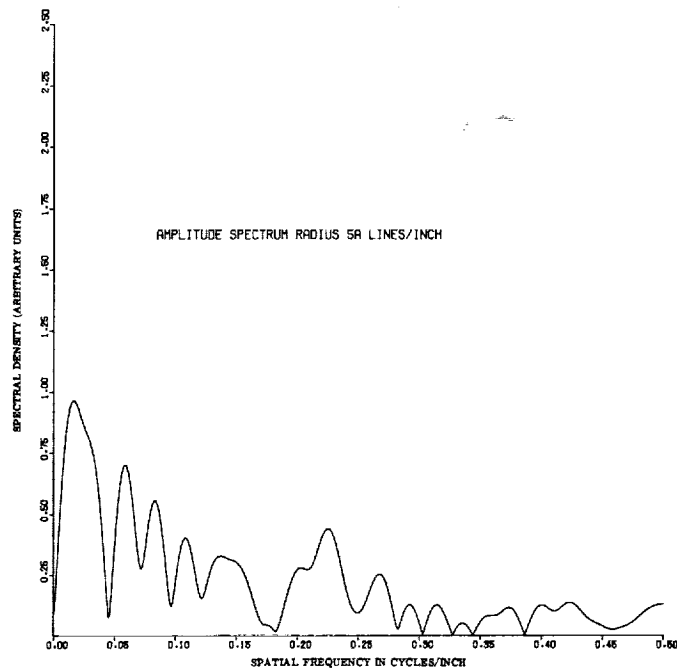


Fig. 4-56 — Amplitude spectrum for radius 5A

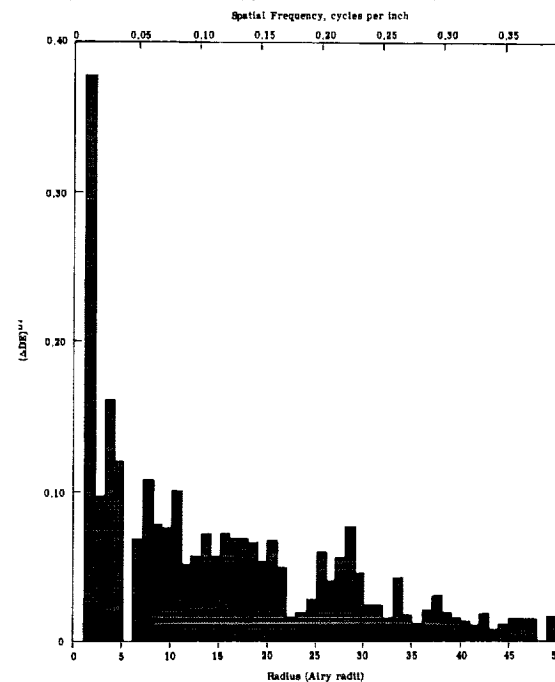


Fig. 4-57 —  $\Delta DE$  for radius 5A; plotted as  $\sqrt{\Delta DE}$  for direct comparison to amplitude spectrum plot

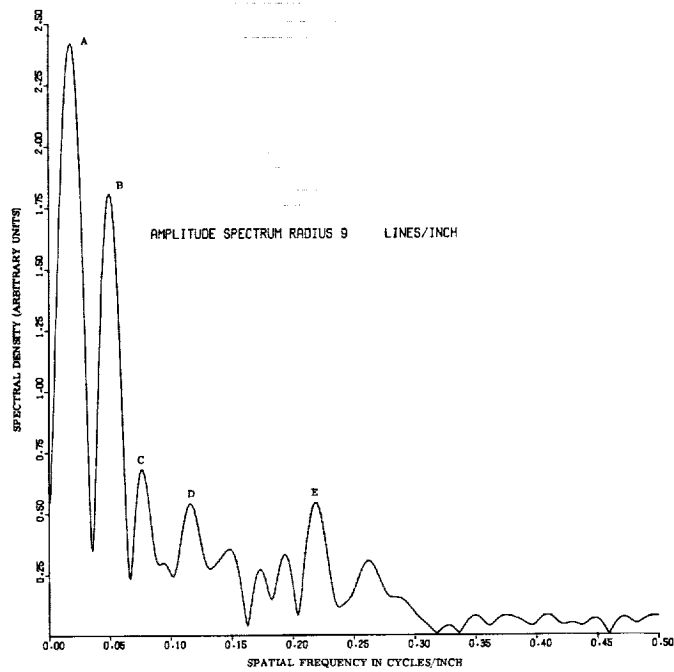


Fig. 4-58 — Amplitude spectrum for radius 9

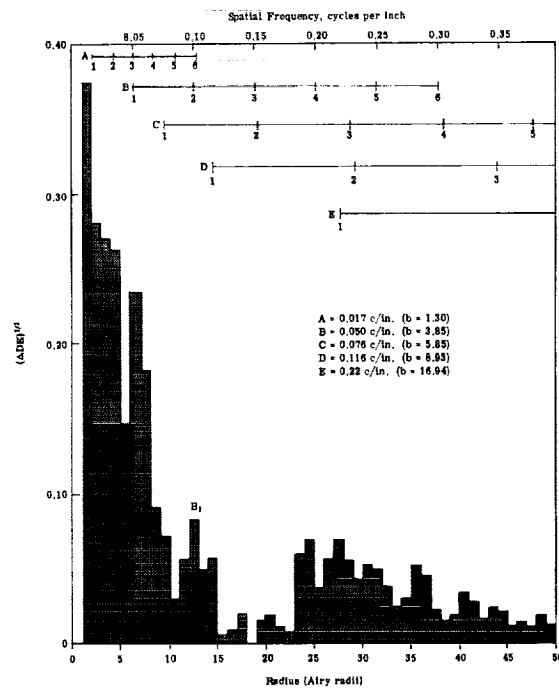


Fig. 4-59 —  $\Delta DE$  for radius 9; plotted as  $\sqrt{\Delta DE}$  for direct comparison to amplitude spectrum plot

#### 4.7.5 Effective Radiance Plots

The PSF data presented in Section 4.7.3 is all in normalized optical units. For comparison of performance at different wavelengths, effective radiance plots are more useful, giving the effective radiance and encircled energy as a function of image radius in arc-seconds. Six such curves are presented in Figs. 4-60 and 4-61 for wavefront radius profiles 5A and 9, at the previously specified wavelengths. A stellar magnitude of 10 was selected to define the effective radiance in magnitudes per square arc-second. The curves may be scaled appropriately for other stellar magnitudes.

Only one comment will be made here concerning the results shown in these figures. It is interesting to note that if one were to define image quality in terms of the diameter blur circle containing roughly 95 to 96 percent of the energy in the point source image, the diameter in arc-seconds would be very nearly the same at all three wavelengths.

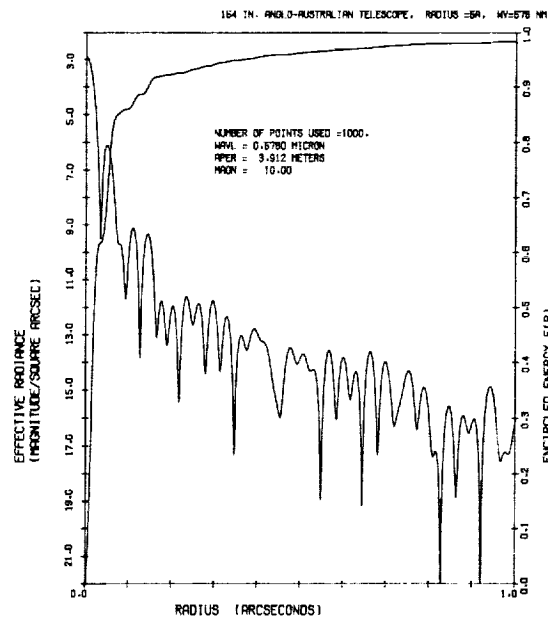


Fig. 4-60 — Effective radiance plots for radius 5A



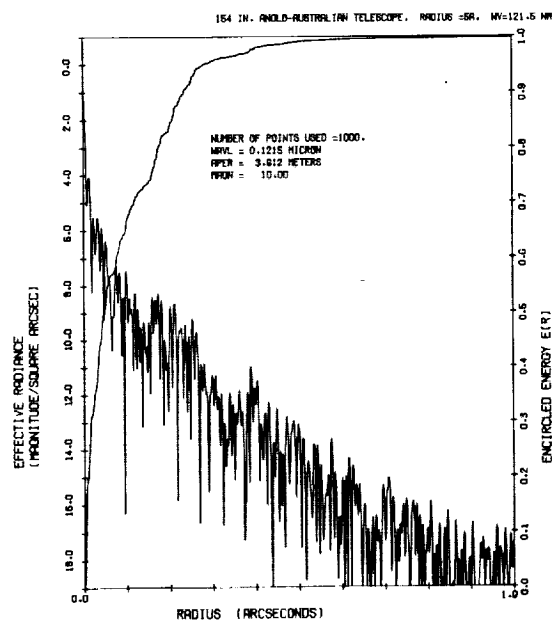
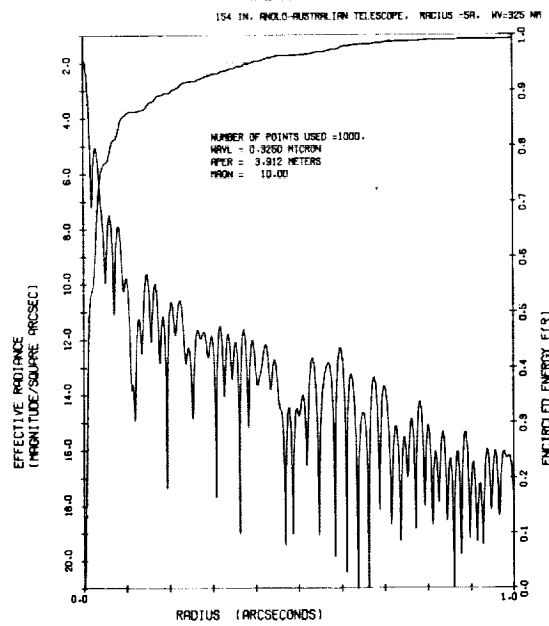


Fig. 4-60 — Effective radiance plots for radius 5A (cont.)

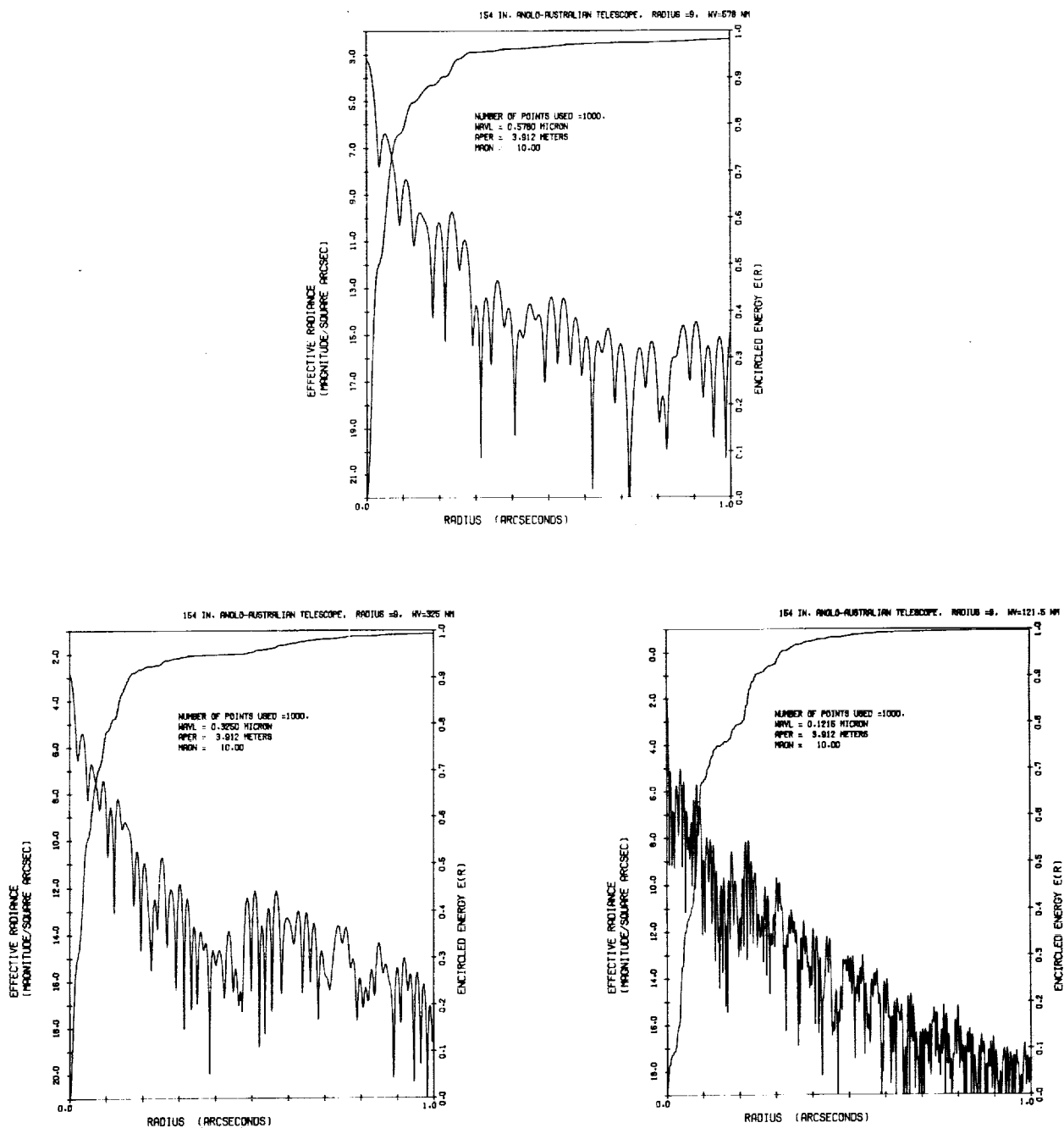


Fig. 4-61 — Effective radiance plots for radius 9

#### 4.8 SIMULATED LST WAVEFRONT

Wavefront profile data for the A.A. T. primary mirror arrived before the curve-fitting option had been added to GASPR. An early attempt at fitting one of the radius profiles (the averaged profile) by hand was made using sums of cosine phase gratings and Gaussian profile ridges. The attempt was successful, and produced results comparable to those obtained later with the curve-fitting option. We have revived this hand-fit model, with minor modifications, to simulate the type of wavefront error which might be expected from the LST (as much as this is possible with a rotationally symmetric wavefront.) Thus the larger scale wavefront irregularities in this model are similar to those found in a real telescope mirror. The only significant difference between this model and the A.A.T. profile from which it is derived lies in the addition of a high spatial frequency random component representing small irregularities of too high a spatial frequency to show up in the A.A.T. data.

Table 4-13 shows the basic input data used to define the simulated LST wavefront, scaled to the three indicated wavelengths. The scale factor was selected to give an rms wavefront error of 0.050 wave at 632.8 nanometers. This scales to 0.097 and 0.260 wavelength at 325 and 121.5 nanometers, respectively. The telescope has a central obstruction of diameter ratio 0.32.

The RAND term defines the high spatial frequency component and is intended to simulate surface roughness. The rms wavefront error of 0.005 wave at 632.8 nanometers corresponds to a mirror surface irregularity of 15.8 Å rms (31.6 Å rms on the wavefront), which would represent a very smooth surface, if the characteristic lateral dimensions were small enough. True surface microstructure has lateral dimensions on the order of a few wavelengths. The sample point spacing for RAND is 0.006 of a radius, or 7.2 to 9 millimeters for the 2.4- to 3.0-meter aperture being considered. The spatial frequency bandwidth of the RAND component is thus far too small to accurately represent real microstructure. The resultant errors will be in the angles at which scattering occurs, not in the total scattered light; however, total scattered light is proportional to the rms wavefront error.

Figure error is represented by the first two GAUS terms coupled with the 1.0-cycle-per-radius COSF term. The 17.05-cycle-per-radius COSF term in brackets represents a visibly prominent harmonic component which was apparent at zone heights of 0.45 and 0.75 in the A.A.T. profile. The rest of the Gaussian ridge terms were used to fit individual bumps and dips in the original wavefront. (Note: The original hand-fit was done prior to computing the amplitude spectrum shown in Fig. 4-55. It is interesting to note that that figure shows prominent peaks at 1.4 and 17.1 cycles per radius.)

Fig. 4-62 shows the wavefront profile and \*Autocorrelation function for the simulated LST wavefront at 325 nanometers. Figs. 4-63 and 4-64 show the PSF and MTF curves for all three wavelengths in normalized optical units. These are similar to the corresponding curves for the A.A.T. mirror. A comparison of Figs. 4-52c and 4-63c illustrates the changes caused by addition of the high spatial frequency RAND component.

To compare performance at different wavelengths, it is desirable to plot the PSF in the form of effective radiance versus radius in arc-seconds, and to plot MTF as a function of spatial frequency in cycles per millimeter or cycles per arc-second. We also wish to compare performance of the 2.4-meter and 3.0-meter aperture telescopes. Figs. 4-65 through 4-67 show the effective radiance plots at three wavelengths for both telescopes, paired by wavelength. Fig. 4-68 shows the MTF at each wavelength, with separate spatial frequency scales for each telescope.

The differences between the two telescopes are purely ones of coordinate scale factors, speaking in terms of the plots. The more interesting variations are a function of wavelength. Note, for example, that the radius for 96 percent encircled energy is roughly the same at all three wavelengths, being 0.35 arc-second for the 3.0-meter telescope and 0.45 arc-second for the

Table 4-13 — Inputs to Generate Simulated LST Wavefronts

WAVL 682.8 NM						WAVL 325.0 NM						WAVL 121.5 NM					
RAND 233425 0.005 SQUA 0.01						RAND 233425 0.010 SQUA 0.01						RAND 233425 0.026 SQUA 0.01					
GAUS	0.75	-0.111	0.25	1		GAUS	0.75	-0.216	0.25	1		GAUS	0.75	-0.578	0.25	1	
GAUS	0.25	0.085	0.25	1		GAUS	0.25	0.166	0.25	1		GAUS	0.25	0.443	0.25	1	
GAUS	1.02	-0.060	0.11	1		GAUS	1.02	-0.117	0.11	1		GAUS	1.02	-0.312	0.11	1	
GAUS	0.44	-0.026	0.05	1		GAUS	0.44	-0.051	0.05	1		GAUS	0.44	-0.135	0.05	1	
GAUS	0.56	0.034	0.04	1		GAUS	0.56	0.066	0.04	1		GAUS	0.56	0.177	0.04	1	
GAUS	0.68	-0.017	0.05	1		GAUS	0.68	-0.033	0.05	1		GAUS	0.68	-0.089	0.05	1	
GAUS	0.53	0.026	0.04	1		GAUS	0.53	0.051	0.04	1		GAUS	0.53	0.135	0.04	1	
GAUS	0.48	0.017	0.02	1		GAUS	0.48	0.033	0.02	1		GAUS	0.48	0.089	0.02	1	
GAUS	0.71	-0.026	0.01	1		GAUS	0.71	-0.051	0.01	1		GAUS	0.71	-0.135	0.01	1	
GAUS	0.84	-0.021	0.03	1		GAUS	0.84	-0.041	0.03	1		GAUS	0.84	-0.109	0.03	1	
COSF	0.170	1.0	1.5708	1		COSF	0.331	1.0	1.5708	1		COSF	0.885	1.0	1.5708	1	
[COSF 0.026 17.05 0.0 2]						[COSF 0.051 17.05 0.0 2]						[COSF 0.135 17.05 0.0 2]					
[GAUSF 0.45 1.0 0.2 2]						[GAUSF 0.45 1.0 0.2 2]						[GAUSF 0.45 1.0 0.2 2]					
[GAUSF 0.75 0.5 0.05 2]						[GAUSF 0.75 0.5 0.05 2]						[GAUSF 0.75 0.5 0.05 2]					

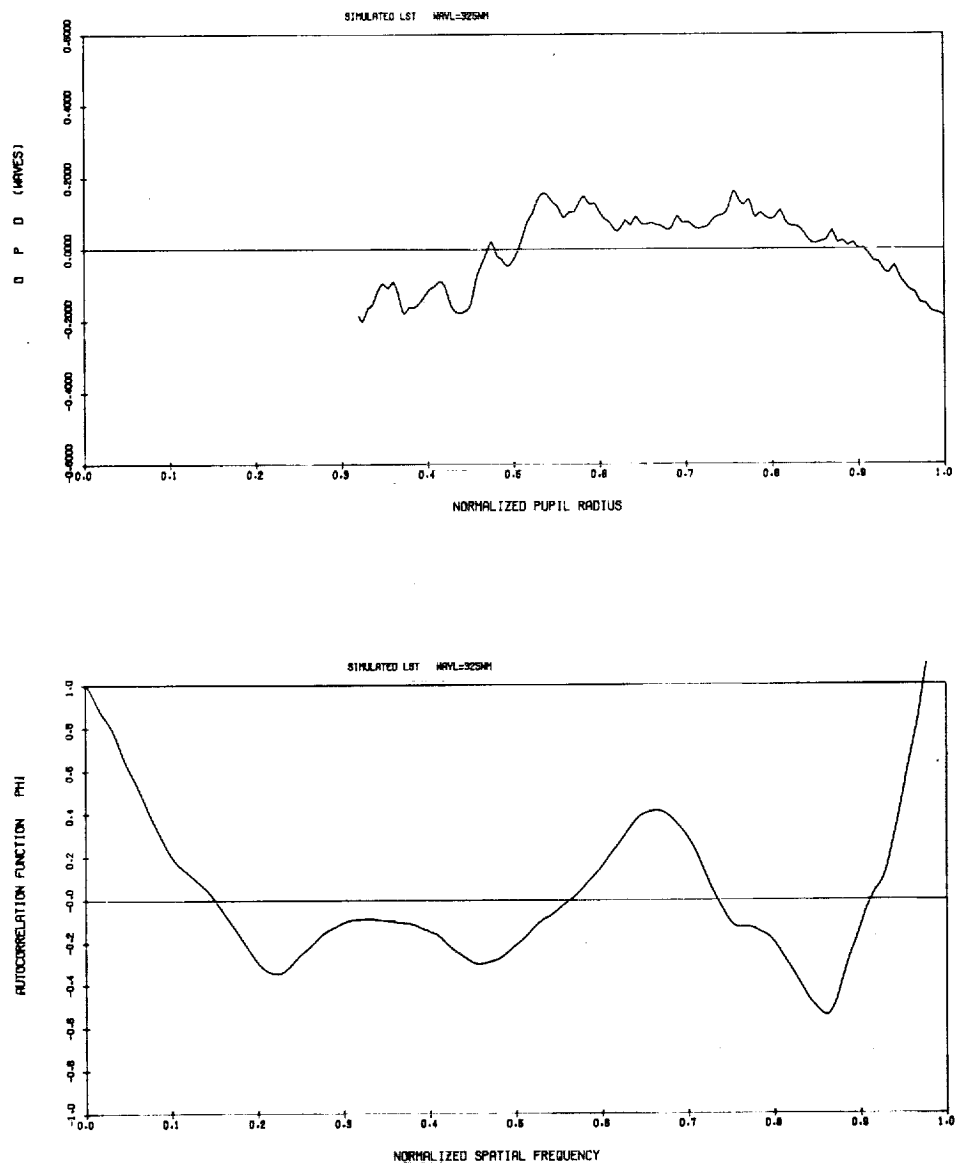


Fig. 4-62 — OPD waveform and \* Autocorrelation function for simulated LST,  
 $\lambda = 325 \text{ nm}$

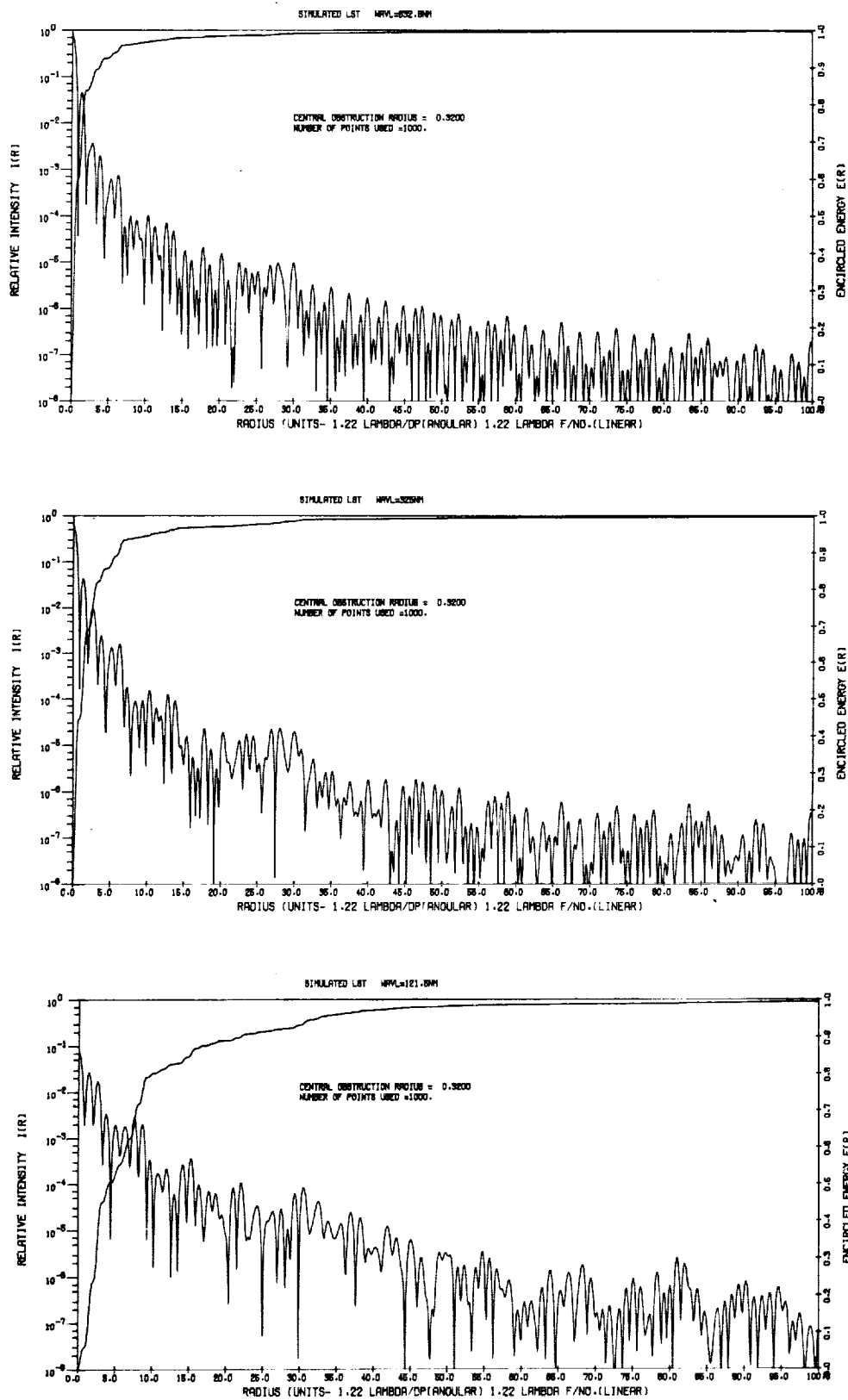


Fig. 4-63 — PSF's for simulated LST

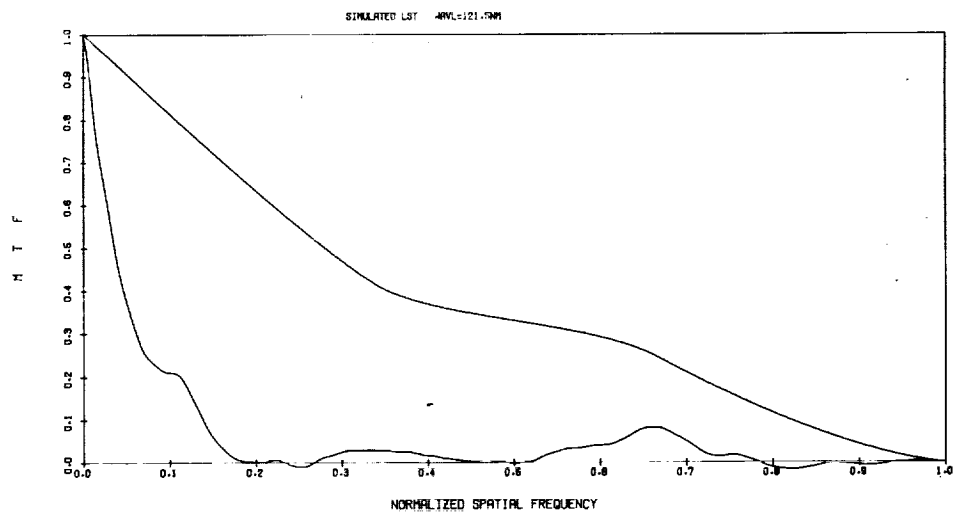
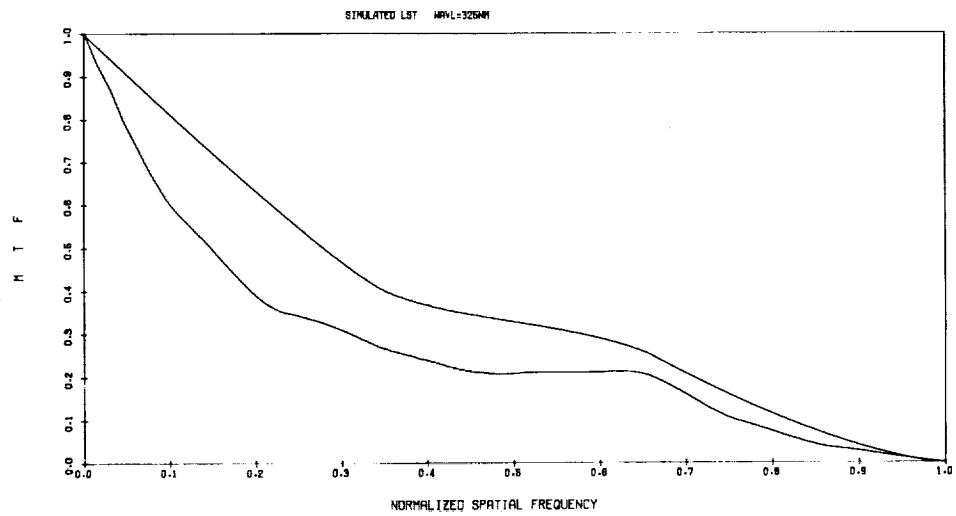
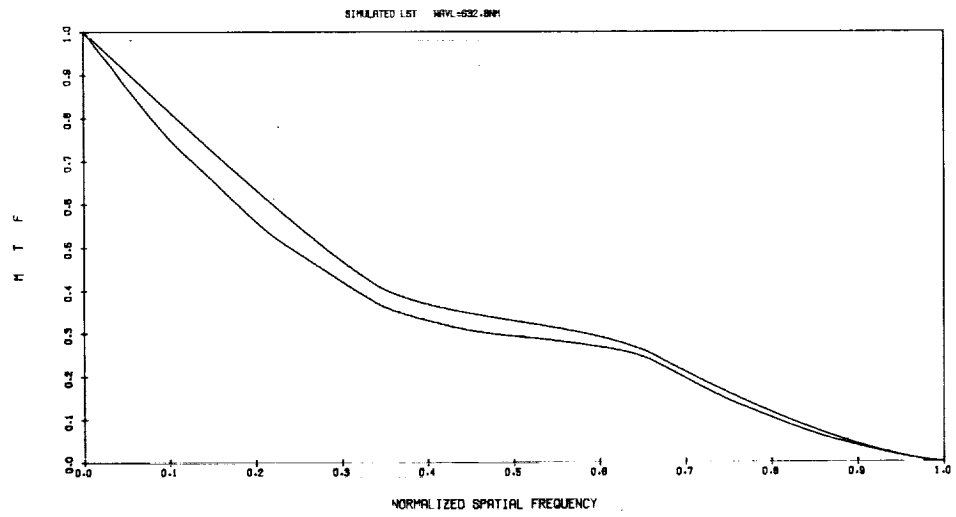


Fig. 4-64 — MTF's for simulated LST

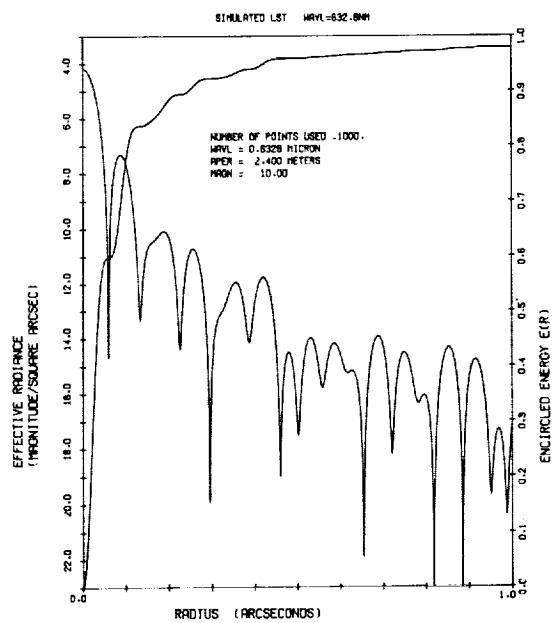
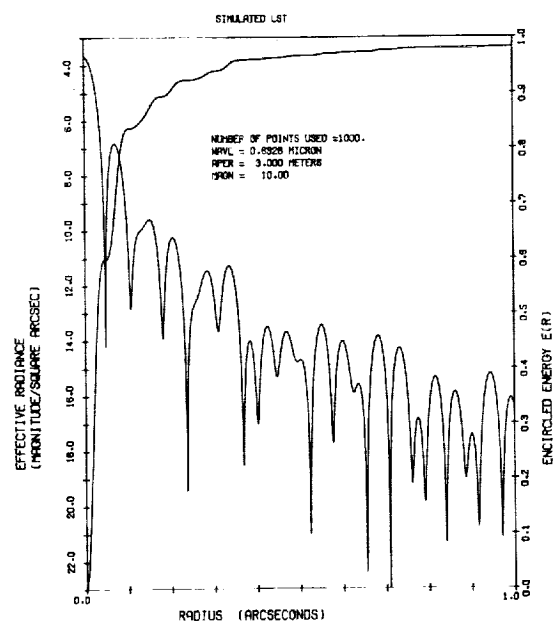


Fig. 4-65 — Effective radiance plots for 3.0- and 2.4-meter telescopes at  $\lambda = 632.8 \text{ nm}$



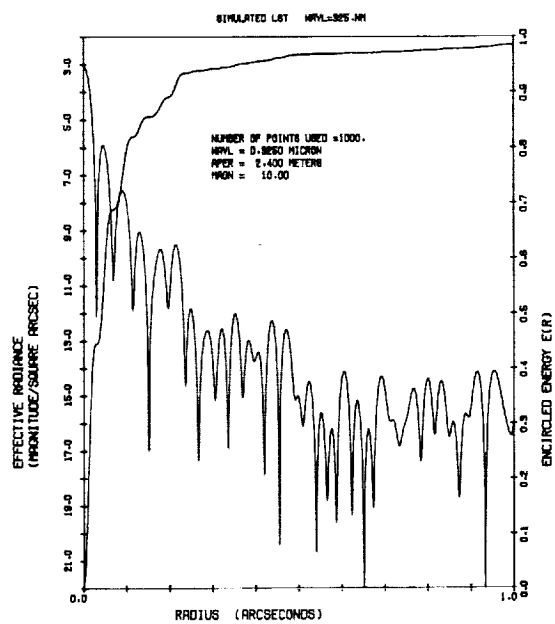
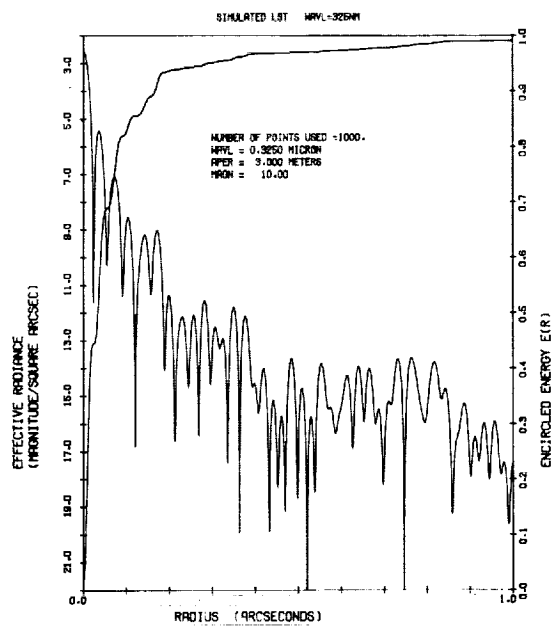


Fig. 4-66 — Effective radiance plots for 3.0- and 2.4-meter telescopes at  $\lambda = 325 \text{ nm}$

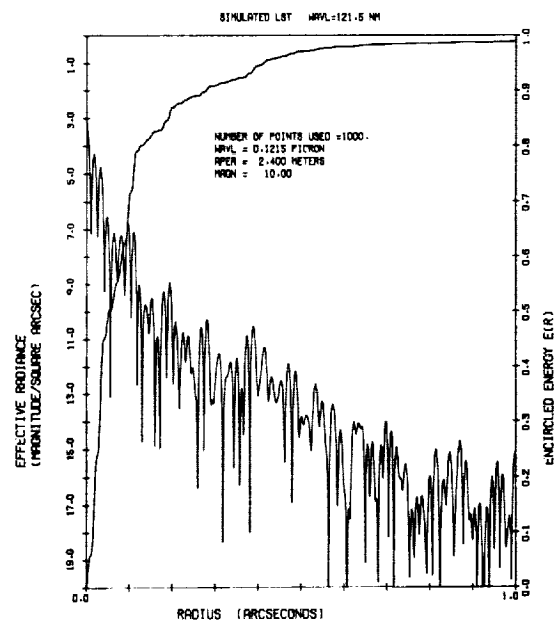
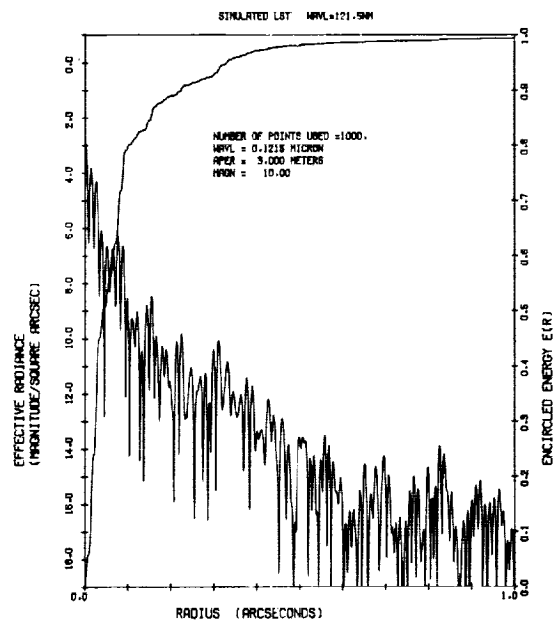


Fig. 4-67 — Effective radiance plots for 3.0- and 2.4-meter telescopes at  $\lambda = 121.5 \text{ nm}$

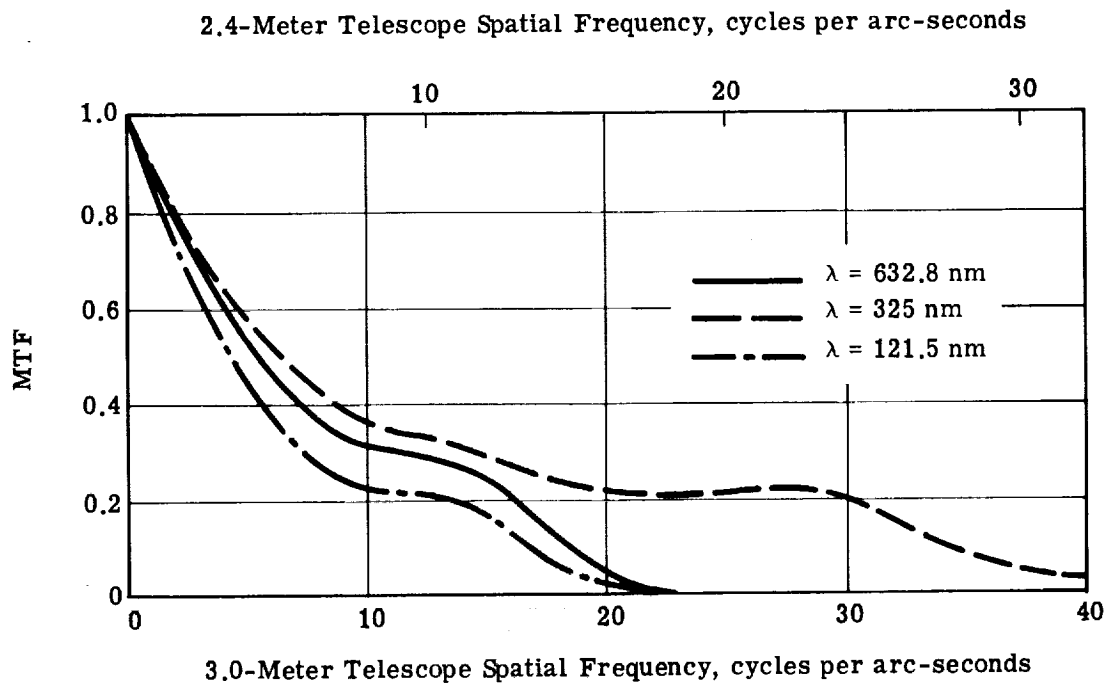


Fig. 4-68 — MTF plots for 3.0- and 2.4-meter telescopes at three wavelengths with spatial frequency in cycles/arc-second

2.4-meter telescope. Note also the remarkable similarity between the MTF's at 632.8 and 121.5 nanometers. The nominal cutoff frequencies for the 3.0-meter telescope are 23.0, 44.8, and 119.7 cycles per arc-second at 632.8, 325, and 121.5 nanometers, respectively. The apparent cutoff of the 121.5-nanometer MTF at 23 cycles per arc-second is a function of wavefront error. So too is the shoulder in the MTF at 14 to 15 cycles per arc-second, although it looks very much like the shoulder in the 632.8-nanometer MTF, which is due to the central obstruction. The similarity in these MTF's may be useful. A TV sensor designed to exploit the optical system resolution to its maximum at 632.8 nanometers will be nearly optimally coupled at 121.5 nanometers (assuming it has adequate spectral coverage). Below 10 to 12 cycles per arc-second, the performance is rather similar at all wavelengths. Only the tail of the MTF is extended greatly at 325 nanometers.

An MTF of 0.10 is sometimes used to indicate the maximum possible spatial frequency that can be resolved in practice. Table 4-14 summarizes the 0.10 modulation spatial frequencies for both telescopes.

Table 4-14 — Spatial Frequency at Which MTF = 0.10 for 2.4-Meter and 3.0-Meter Simulated LST's (cycles per arc-second)

$\lambda$ , nanometers	3.0-Meter	2.4-Meter	Fraction of Cutoff
632.8	18.4	14.7	0.80
325	33.9	27.1	0.76
121.5	16.5	13.2	0.14

#### 4.9 STATISTICAL MODELS FOR RIPPLE AND FIGURE ERROR

The analyses of the preceding sections have been of a deterministic nature, using specific wavefronts to calculate specific PSF and MTF curves. Deterministic analyses can produce accurate results for the specific cases analyzed, but there is some question as to the validity of using one specific example as an indication of the performance to be expected from other examples. Different optical systems are bound to produce wavefront irregularities which differ in structural details. Thus in using a specific wavefront to predict expected performance from a different optical system, there is always a strong chance that the choice of model wavefront is inappropriate.

In general, optical analysts prefer to use statistical models, since these are presumed to define the average performance of a large number of cases. Thus the chance of picking a singularly inappropriate model is presumed to be smaller. This is not the case if the statistical model is based on an inappropriate statistical foundation, however. There is mounting evidence that the statistical model based on a Gaussian autocorrelation function, which is commonly used in optics, is not rigorously valid, and may be a poor approximation for some applications. Of particular interest to this study, the Gaussian autocorrelation function implies that the wavefront it represents has little or no high spatial frequency irregularities. Thus Gaussian autocorrelation functions are singularly inappropriate in a study of ripple and surface microstructure.

The complete statistical model we refer to is based on the MTF degradation function of Eq. 1. The underlying assumption is that the MTF degradation due to random wavefront error,  $T_{\omega}$ , is independent and separable from the MTF degradation due to the finite pupil size and systematic aberrations. Thus if  $T_1$  is the perfect lens MTF (we generally ignore the systematic aberrations as being too small in LST-type telescopes) the system MTF is given by

$$T(\nu) = T_{\omega}(\nu) \times T_1(\nu) \quad (40)$$

$T_\omega$  is then defined by Eq. 1, coupled with a Gaussian autocorrelation such as that of Eq. 2. The attraction of this model is its mathematical simplicity. We have used it extensively ourselves, to good advantage, in analyzing image quality criteria for the LST<sup>6</sup>.

Eq. 40 has been proven valid by E. L. O'Neill<sup>7</sup>. In the same reference he has derived Eq. 1, in slightly different form, based on the assumption that the random wavefront irregularities have a Gaussian height distribution. There is no implicit assumption as to the shape of the autocorrelation function in that derivation, but a Gaussian shape is usually assumed for reasons of convenience. The assumption of Gaussian height distribution appears valid, and therefore Eq. 1 should be reasonably accurate. Indeed, Schwesinger<sup>8</sup> has shown it to be a good numerical approximation for small wavefront errors even when the height distribution departs radically from Gaussian. (He gives the corresponding equation for a triangular height distribution in the appendix to his article and compares numerical values for different amounts of wavefront error.) We have shown evidence of the validity of Eq. 1 for cosine phase gratings of small phase amplitude in earlier sections. Thus, questions of validity are tied entirely to the autocorrelation function.

The original treatments of random wavefront error arose out of a study of the propagation of plane wavefronts through the turbulent atmosphere, and this may be part of the reason the Gaussian autocorrelation function was so easily accepted. In treating random surface irregularities on telescope mirrors, the atmospheric turbulence models were adapted without significant change. But atmospheric turbulence and mirror surface irregularities differ in two important respects. First, atmospheric turbulence varies with time, and the long exposures of astronomy average the effects over many changes in the wavefront irregularity function. Thus, ensemble averaging should be a legitimate model. A mirror surface represents a fixed wavefront irregularity function, however, and it is not clear that models based on ensemble averaging are legitimate. Second, the wavefront irregularities introduced by atmospheric turbulence of the type encountered in astronomy are free of very high spatial frequency components. This is definitely not true of mirror surfaces where the characteristic lateral dimensions of surface irregularities may range from large fractions of an aperture diameter down to small fractions of a wavelength.

In previous sections we have shown through the \*Autocorrelation function how non-Gaussian the autocorrelation function can be, even for Gaussian smoothed random functions having rotational symmetry. In this section, we will examine the nature of the autocorrelation function in more detail. First, we will consider some of its fundamental properties, related to the form it should take for mirrors. In this regard, we will make extensive reference to the paper by Schwesinger cited above. (Note: An English translation of this paper will be found in Appendix A.) Second, we will look at a number of real and generated two-dimensional and rotationally symmetric autocorrelation functions. Since these are calculated from measurements passing only low spatial frequency components, we will discuss the effects of high spatial frequency components using the \*Autocorrelation functions as examples. Third, both our deterministic and statistical models are rotationally symmetric. We will therefore give some attention to the degree of variation from the performance predicted by these models to be found in real telescopes, where the wavefront error is far from rotationally symmetric.

The shape of the autocorrelation function for real telescope mirrors, and for mirrors in general, is a subject being actively pursued by a number of people, most of whom will be identified in the course of this section and Section 5. Although a number of the properties of the real autocorrelation functions are now evident, there still exists no specific agreed upon model. The material presented in this section was collated too late to have an impact on the computer program models we have generated, which therefore took the deterministic route of GASPR. We hope this material will contribute to generating a more complete statistical model for future use.

#### 4.9.1 General Properties of Wavefront Autocorrelation Functions

Most early analysis of random wavefront error was done in terms of a deformed plane wavefront of infinite lateral extent, and this forms a convenient point of departure for our discussion. The random wavefront error represents departure from flatness in the phase front of this plane wave. We represent this wavefront error by a scalar optical path difference function  $f(x, y)$ , which measures the distance in wavelengths by which the phase front leads or lags behind the reference plane. The OPD function is defined to have a zero mean,  $\overline{f(x, y)} = 0$ , by positioning the reference plane such that

$$\iint_{-\infty}^{\infty} f(x, y) dx dy = 0 \quad (41)$$

The autocorrelation function for this wavefront is

$$\iint_{-\infty}^{\infty} f(x, y) f(x - u, y - v) dx dy$$

We will generally use the normalized form,

$$K(u, v) = \frac{\iint_{-\infty}^{\infty} f(x, y) f(x - u, y - v) dx dy}{\iint_{-\infty}^{\infty} f^2(x, y) dx dy} \quad (42)$$

and it will be convenient to convert to polar coordinates for comparison to Schwesinger's results:

$$K(r, p) = \frac{\int_0^{2\pi} \int_0^{\infty} f(\rho, \phi) f(\rho - r, \phi - p) \rho d\rho d\phi}{\int_0^{2\pi} \int_0^{\infty} f^2(\rho, \phi) \rho d\rho d\phi} \quad (43)$$

Returning to the OPD function, its Fourier transformation is

$$F(\nu_x, \nu_y) = \iint_{-\infty}^{\infty} f(x, y) \exp [-2\pi i(\nu_x x + \nu_y y)] dx dy \quad (44)$$

From Eqs. 41 and 44 then, it follows that

$$F(0, 0) = \iint_{-\infty}^{\infty} f(x, y) dx dy = 0 \quad (45)$$

The energy density spectrum  $P(\nu_x, \nu_y)$  is given by

$$P(\nu_x, \nu_y) = \frac{1}{2\pi} |F(\nu_x, \nu_y)|^2 \quad (46)$$

Thus if  $\overline{f(x, y)} = 0$ , it follows from Eqs. 45 and 46 that  $P(0, 0) = 0$ .

Now Lee<sup>8</sup> shows that the energy density spectrum and the autocorrelation function are Fourier transform pairs,

$$P(\nu_x, \nu_y) = \frac{1}{2\pi} \iint_{-\infty}^{\infty} K(u, v) \exp [-2\pi i(\nu_x u + \nu_y v)] du dv \quad (47)$$

From Eqs. 45, 46, and 47 then, it follows that

$$P(0, 0) = \frac{1}{2\pi} \iint_{-\infty}^{\infty} K(u, v) du dv = 0 \quad (48)$$

or in polar coordinates,

$$\int_0^{2\pi} \int_0^{\infty} K(r, p) r dr dp = 0 \quad (49)$$

This result is identical to that which Schwesinger (page A-14) attributes to Fried<sup>10</sup>, except in that both have integrated in  $p$  to give a zonally averaged autocorrelation function. The important inference to be drawn from these derivations is that a zero mean OPD function implies that the integral under the autocorrelation function is also zero. Since all quantities in the integral are positive except  $K(r, p)$ , then  $K(r, p)$  must have both positive and negative values, and therefore cannot be represented by a Gaussian function.

E. L. O'Neill (personal communication) has pointed out that there are some classic examples in communication theory which appear to violate this condition, e.g., the "random telegraph" signal in which a signal switches instantaneously from +1 to -1 at random intervals, with the long term average being zero. Textbooks<sup>11</sup> give a triangular (all-positive) autocorrelation function for this example, and show  $P(0)$  to be equal to 1.0. The problem appears to lie in the fact that the Fourier transformation calculations are carried out for the ensemble functions, and not for the function itself. If any finite section of the random telegraph signal pulse train is itself autocorrelated, the autocorrelation function will have both positive and negative values, and the ensemble analysis will break down. In fact, we can state the condition more formally: If  $T$  is the total sampling interval

and  $t_c$  the correlation interval, then solutions approximating the ensemble average results will be approached only as  $T/t_c \rightarrow \infty$ . Conversely, the statistics break down completely when  $T/t_c \rightarrow 1.0$ .

The wavefront errors introduced by surface irregularities in a telescope mirror are obviously stationary with time, and ensemble averaging can be approached only by averaging the wavefront irregularities of a large number of mirrors. The autocorrelation length  $L$  is generally a moderately large fraction of the pupil diameter  $D_p$ ,  $D_p/L$  seldom exceeding 3 to 10 in real telescope mirrors. Because of this, autocorrelation functions generated for individual wavefronts are likely to depart significantly from any true ensemble averaged autocorrelation function. For such a bounded waveform, including bounded random telegraph signals, Eq. 48 or 49 should apply. In fact, deviation of the integral (49) from zero is more likely to be an indication that  $D_p/L$  is too small for the statistical model to work properly.

When dealing with a finite sample of a random wavefront bounded by a circular pupil, some special considerations enter into the definition of the autocorrelation function. These are illustrated in Fig. 4-69, which also defines the coordinates used in Eqs. 42 and 43. The product  $f(x, y)f(x - u, y - v)$  exists only within the shaded region where the pupil and displaced pupil overlap. Thus the value of the unmodified autocorrelation function decreases in proportion to the normalized transmitting area of the pupil as  $r$  is increased from 0 to  $2R$ , even in the absence of wavefront error. We compensate for this by dividing the right side of Eqs. 42 and 43 by the normalized pupil transmittance. This function is identical to the perfect lens MTF  $T_I$ , where, for an unobstructed lens

$$T_I(\nu_n) = \frac{2}{\pi} [\arccos \nu_n - \nu_n \sin(\arccos \nu_n)] \quad (50)$$

$\nu_n$  being the normalized spatial frequency.

At this point, several comments on notation are in order. Schwesinger uses a normalized form of the displacement radius using  $R$  as the normalization factor. Thus  $0 \leq r \leq 2.0$ . In this report, we use a normalized spatial frequency  $\nu_n = \nu/\nu_0$ , where  $\nu_0 = D_p/\lambda$ ,  $D_p$  being the pupil diameter. Thus  $0 \leq \nu_n \leq 1.0$ . These coordinates are interchangeable, in that numerically,  $r = 2\nu_n$ . In the remaining discussion of the autocorrelation function we will refer usually to the zonally averaged autocorrelation function  $K(r) = [\overline{K(r, p)}]_p$ . Note that this is numerically equivalent to using the zonally averaged OPD function  $f(\rho) = [f(\rho, \phi)]_\rho$  in Eq. 43.

The compensated form of the autocorrelation function in Schwesinger's notation thus becomes

$$K(r) = \frac{\int_0^\infty f(\rho)f(\rho - r)\rho d\rho}{T_I(r/2) \int_0^\infty f^2(\rho)\rho d\rho} \quad (51)$$

In the notation of Eqs. 1 and 2,



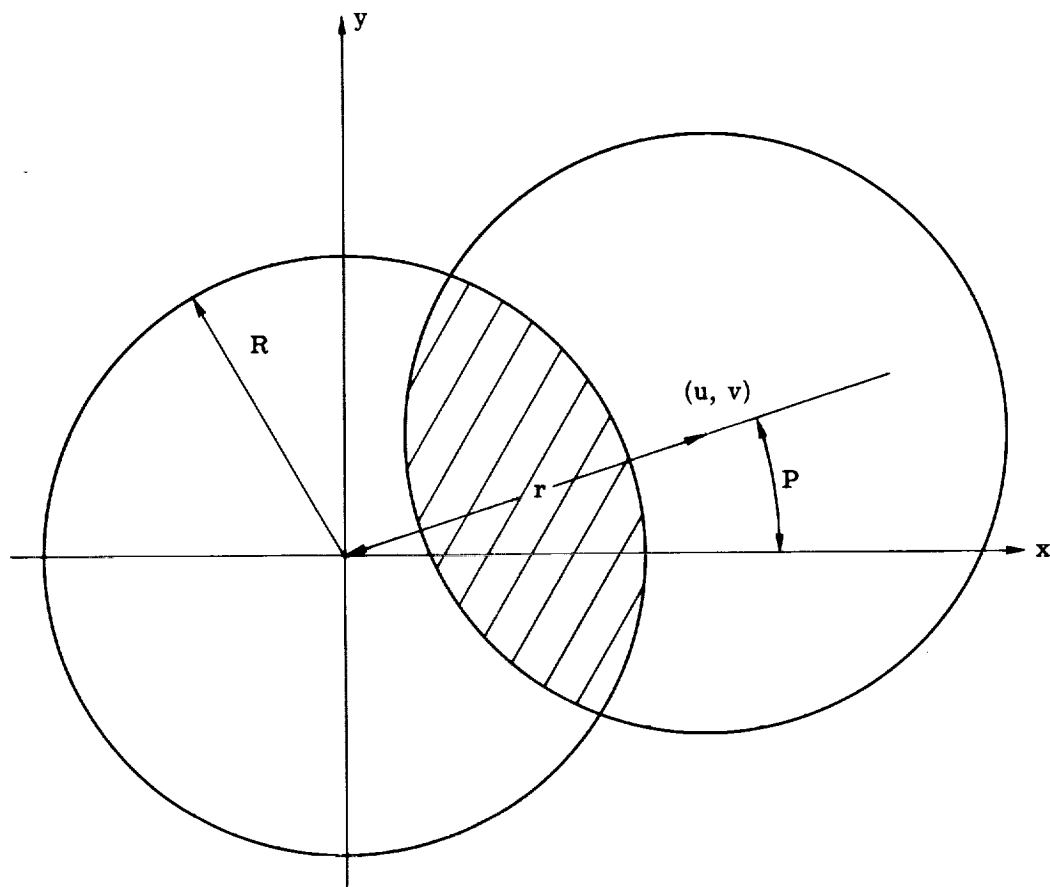


Fig. 4-69 — Pupil displacement coordinates for computing autocorrelation function of OPD function over pupil of telescope

$$\Phi_{11}(\nu_n) = \frac{\int_0^\infty f(\rho)f(\rho - 2\nu_n)\rho d\rho}{T_I(\nu_n) \int_0^\infty f^2(\rho)\rho d\rho} \quad (52)$$

In performing the integral of the volume under the autocorrelation function for a bounded wavefront, Schwesinger introduces a weighting function  $\phi(r)$  (see Eq. 15, Appendix A). He claims that the bounded wavefront equivalent to Eq. 49 is

$$\int_0^2 \phi(r)K(r)dr = 0 \quad (53)$$

In examining his weighting function  $\phi(r)$ , we have noted that

$$\phi(2\nu_n) = 4T_I(\nu_n)\nu_n \quad (54)$$

Thus, Eq. 53 is equivalent to

$$8 \int_0^1 \Phi_{11}(\nu_n)T_I(\nu_n)\nu_n d\nu_n = 0 \quad (55)$$

This is the zed integral discussed in Section 4.1.2. (In the computer calculation, we ignore the factor 8.)

[It is interesting to compare this equation to Eq. 4-5 of reference 6, which gives the Strehl definition  $\mathcal{D}$  for rotationally symmetric MTF's: In the present terminology, using the normalized spatial frequency,

$$\mathcal{D} = 8 \int_0^{\nu_n} T_\omega(\nu_n)T_I(\nu_n)\nu_n d\nu_n \quad (56)$$

The similarity is striking, but probably not too significant. The Strehl definition equals 1.0 for a perfect lens. Eq. 1 shows that this can occur if  $\omega = 0$  or if  $\Phi_{11}(\nu_n) = 1.0$  for all  $\nu_n$ . In practice, the latter will occur only when  $\omega = 0$ , and may not occur then. It implies that the correlation length is very long with comparison to the pupil diameter. Note that if  $\Phi_{11}(\nu_n) = 1.0$  for all  $\nu_n$ , Eq. 55 equals 1.0. This is equivalent to the earlier statement that when  $T/t_c \rightarrow 1.0$ , the statistics break down. Thus the zed integral = 0 only if the autocorrelation length is a reasonably small fraction of the pupil diameter.]

Proof of the validity of Eqs. 49 and 55 would constitute evidence that the Gaussian autocorrelation function is formally unacceptable. There may exist conditions under which the Gaussian autocorrelation function is a satisfactory and useful approximation, however. To examine this

possibility and to test Eq. 50, we must look at the autocorrelation functions for real mirrors and for generated wavefronts.

#### 4.9.2 Autocorrelation Functions for Generated Wavefronts and Real Mirrors

Two forms of generated wavefronts are used in computing autocorrelation functions here, but both start with a random number table and a smoothing function. One is the rotationally symmetric wavefront of GASPR, which produces the \*Autocorrelation function. The other produces a wavefront irregularity function varying in two dimensions, defined by a 20- by 20-point data matrix. This wavefront is autocorrelated by carrying out the integral (Eq. 52). Two orthogonal sections of the two-dimensional autocorrelation function are calculated by displacing the data matrix incrementally in the x and y directions. The model wavefront is then rotated 15 degrees with respect to the data point matrix, and the process is repeated. When a complete set of profiles spaced by 15 degrees has been obtained, they are averaged by hand. The same technique was used in reference 6 to obtain autocorrelation functions for real mirrors; this will be shown below.

Since we will compare these autocorrelation functions to the Gaussian autocorrelation function, we should cite the Gaussian autocorrelation function forms used in our principal references:

$$\Phi_{11}(\nu_n) = \exp(-2N_H^2 \nu_n^2) \quad (\text{reference 6}) \quad (57)$$

$$K(r) = \exp(-r^2/\ell^2) \quad (\text{Schwesinger}) \quad (58)$$

$$\Phi_{11}(\nu_n) = \exp(-4\nu_n^2 c^2) \quad (\text{GASPR notation}) \quad (59)$$

$\ell$  and  $c$  are the normalized autocorrelation lengths in each notation, and they are numerically equal,

$$c = \ell = 1/(\sqrt{2} N_H) \quad (60)$$

The normalized autocorrelation lengths are so defined that when  $r = \ell$  or  $\nu_n = c/2$ , the autocorrelation function =  $1/e = 0.3679$ .

Fig. 4-70 shows five autocorrelation functions for five two-dimensional wavefronts of correlation length  $c = 0.3$ , each generated from the random numbers table starting with the same seed. Each curve represents the average of a two-dimensional autocorrelation function. To indicate the degree by which the latter varies from its mean, we have plotted the standard deviation curve for each case in Fig. 4-71, along with an average of the five standard deviation curves. In Fig. 4-72, the average of the five autocorrelation curves is plotted with its standard deviation curve. The corresponding Gaussian autocorrelation curve for  $c = 0.30$  is included for comparison.

Three conclusions can be drawn from this data: First, the variance within the individual autocorrelation function is considerable, as is the variance between different wavefronts which nominally have the same statistics. Second, all cases show both positive and negative values, although averaging over many cases seems to reduce the maximum negative excursion of the curve somewhat. Third, the Gaussian model seems to match the shape of the lowest frequency portion of the real autocorrelation function. This latter can be attributed in part to the absence of high spatial frequency components in the wavefront model.

In Fig. 4-73 we show autocorrelation functions for three different correlation lengths, each the average of three two-dimensional functions. The same three seeds were used in generating each set of wavefronts. Again, note that the lower spatial frequency portions of the curves look Gaussian in shape. (This is not too apparent for  $c = 0.1$ , where the 0.05 spatial frequency sampling

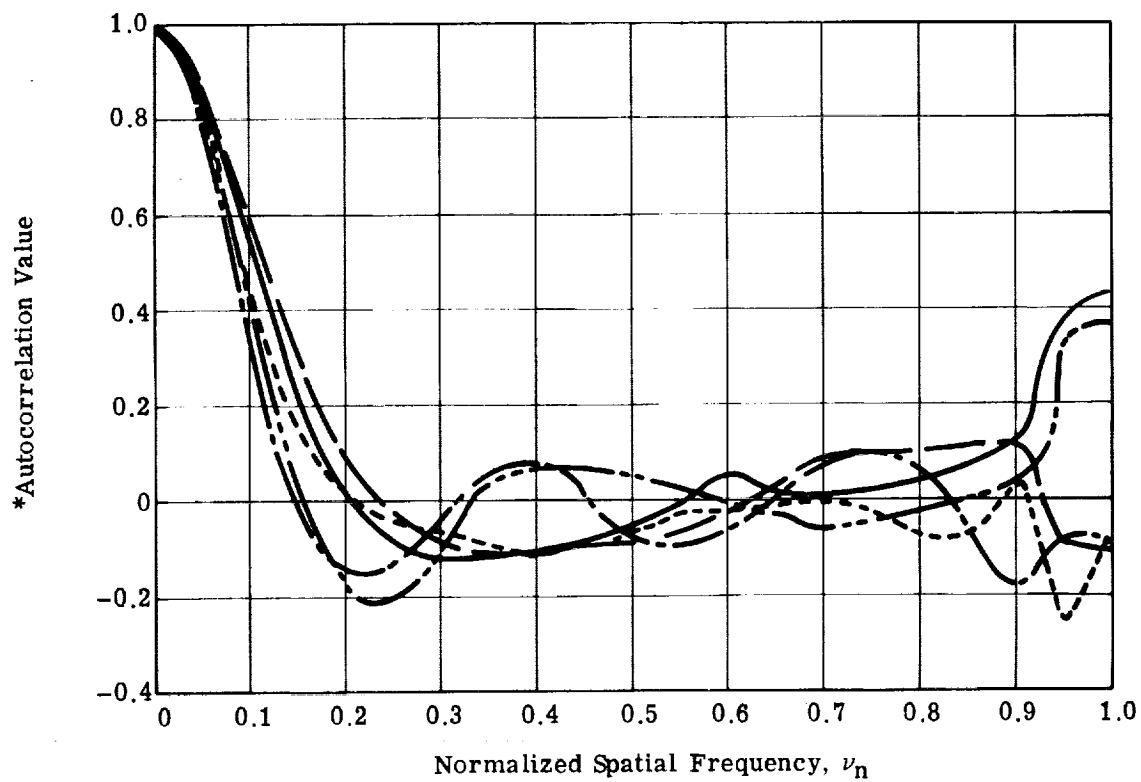


Fig. 4-70 — Five autocorrelation functions for two-dimensional, Gaussian, smoothed random wavefronts of 0.3 correlation length; generated by random number generator with five different seeds

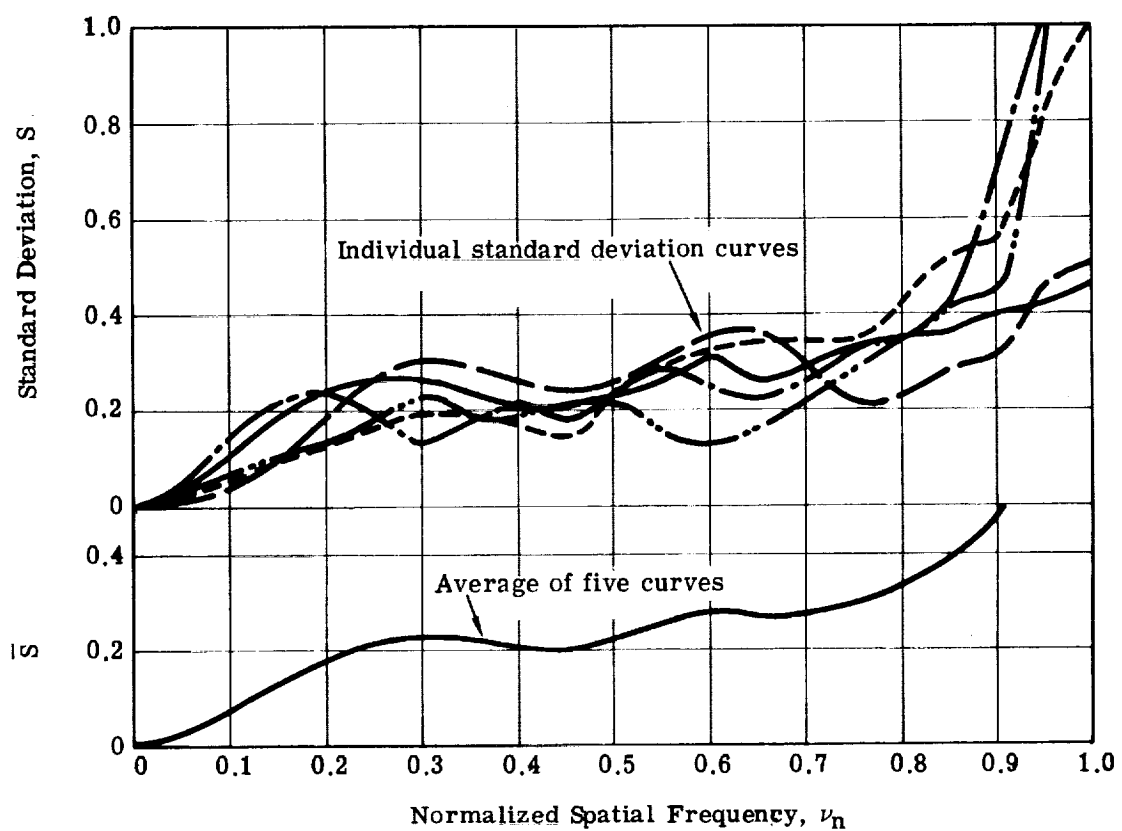


Fig. 4-71 — Standard deviation curves for the five autocorrelation functions of Fig. 4-70

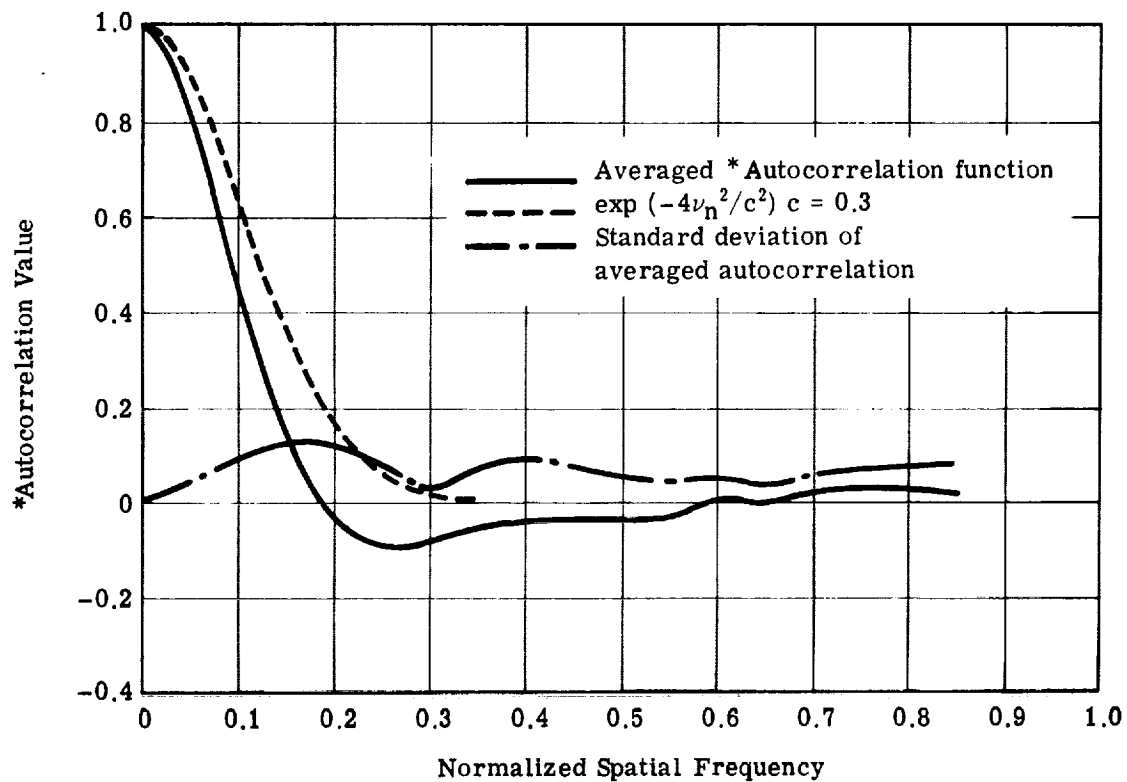


Fig. 4-72 — Average of five autocorrelation functions of Fig. 4-70, compared to Gaussian autocorrelation functions

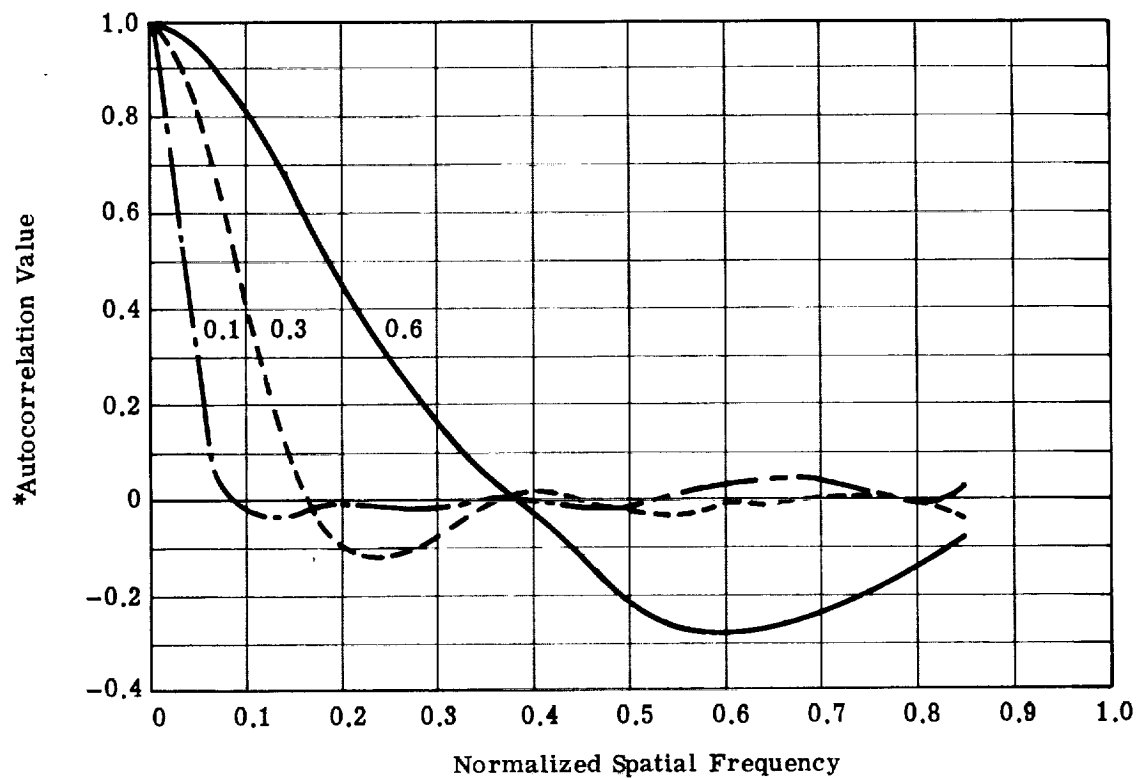


Fig. 4-73 — Autocorrelation functions for two-dimensional, Gaussian, smoothed random wavefronts of varying correlation length; each curve represents averaging over three wavefronts; same three seeds used in generating wavefronts for different correlation lengths; correlation lengths = 0.1, 0.3, and 0.6

increment is too coarse to resolve details.) The most significant thing to note is the manner in which the magnitude of the negative excursion varies with correlation length. If Schwesinger's form of the zed integral is considered along with the shape of his weighting function  $\phi(r)$  (Appendix A, Fig. 3), it will be seen that the autocorrelation function must vary with correlation length in this manner if the zed integral is to equal zero.

The zed integrals for these three autocorrelation functions and the corresponding Gaussian autocorrelation functions are given in Table 4-15, along with the zed integrals for the nine two-dimensional autocorrelation functions used to generate the averaged curves. Several conclusions can be drawn from this data: First, the value of the zed integral decreases as  $c$  decreases. Below  $c = 0.3$ , however, this variation with  $c$  seems to be of a magnitude comparable to the variance between different individual samples. Second, the zed integral for the Gaussian autocorrelation function is much larger than that for the real autocorrelation functions. It too decreases as  $c$  decreases, and it is evident that at some point  $c < 0.1$ , it will be reduced to within the statistical variance between real samples.

To examine the effects of higher frequency components, we must use the \*Autocorrelation function output of GASPR. Fig. 4-74 shows the \*Autocorrelation functions for five wavefronts generated with the random wavefront option, all having a correlation length of 0.1 and a square smoothing function, but each being generated with a different seed. The average of the five \*Autocorrelation functions and its standard deviation are shown in Fig. 4-75, along with the corresponding Gaussian autocorrelation function.

Table 4-15 — Zed Integrals (Eq. 49) for the Two-Dimensional Autocorrelation Functions Used in Generating Fig. 4-73 (Zed integrals for the corresponding Gaussian autocorrelation functions are included for comparison)

$c$	1	2	3	Average	Gaussian
0.6	0.0584	0.0064	0.0104	0.0256	0.2392
0.3*	0.0096	-0.0008	0.0064	0.0056	0.0728
0.1	-0.0024	0.0052	0.0109	0.0040	0.0072

\*Averaged over the five samples in Fig. 4-70, zed = 0.012.

This averaged \*Autocorrelation function bears similarities to the corresponding two-dimensional averaged autocorrelation functions. It has both positive and negative values, and it tends to oscillate about zero at higher spatial frequencies. The calculations were made for  $\omega = 0.10$  wavelength rms, which introduces some errors at higher spatial frequencies. (Among other things, this drives the zed integral negative. Zed = -0.0238 for the averaged curve.) The most significant difference from the previous examples is at low spatial frequencies, where the \*Autocorrelation function drops off considerably more rapidly than the Gaussian curve. That this is due to the presence of higher spatial frequency components is borne out by the results discussed in Section 4.4.

What of real mirrors? Figs. 4-76 and 4-77 show two examples taken from reference 6. Three more examples are shown in Fig. 2 of Appendix A. All five show the autocorrelation function to have both positive and negative values, and to oscillate about zero at high spatial frequencies. [Note that the autocorrelation function has been multiplied by  $T_1(\nu_n)$  to damp down these oscillations in Figs. 4-76 and 4-77.] Note that at low spatial frequencies most of these curves fall off more rapidly than Gaussian, in spite of having been measured with a relatively coarse sampling point spacing. This behavior is also apparent in the \*Autocorrelation functions for the A.A.T. primary mirror (Section 4.7.3), particularly in the case of radius 5A.



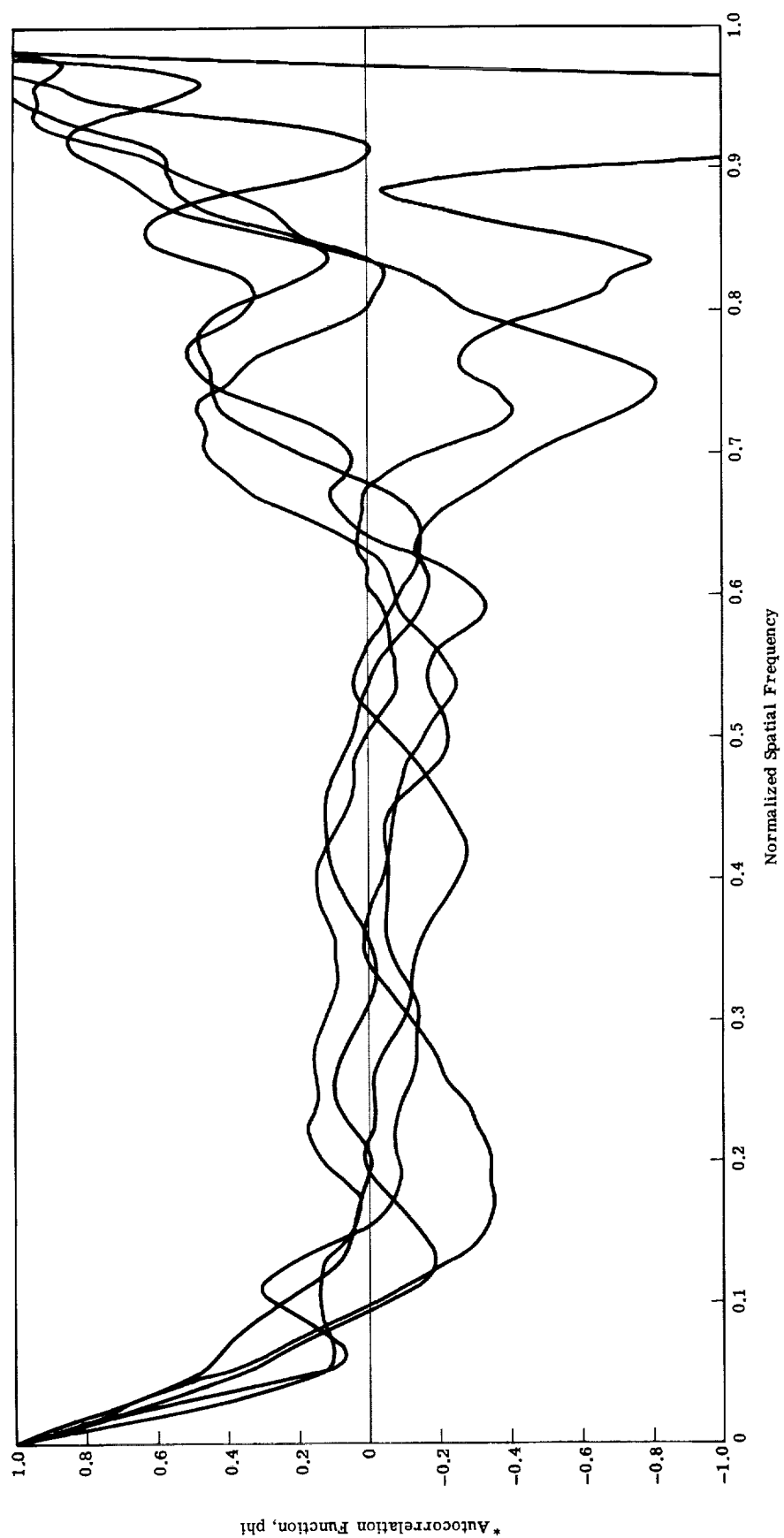


Fig. 4-74 — Five \* autocorrelation functions having same correlation length (0.10) and smoothing function (square) but different seeds

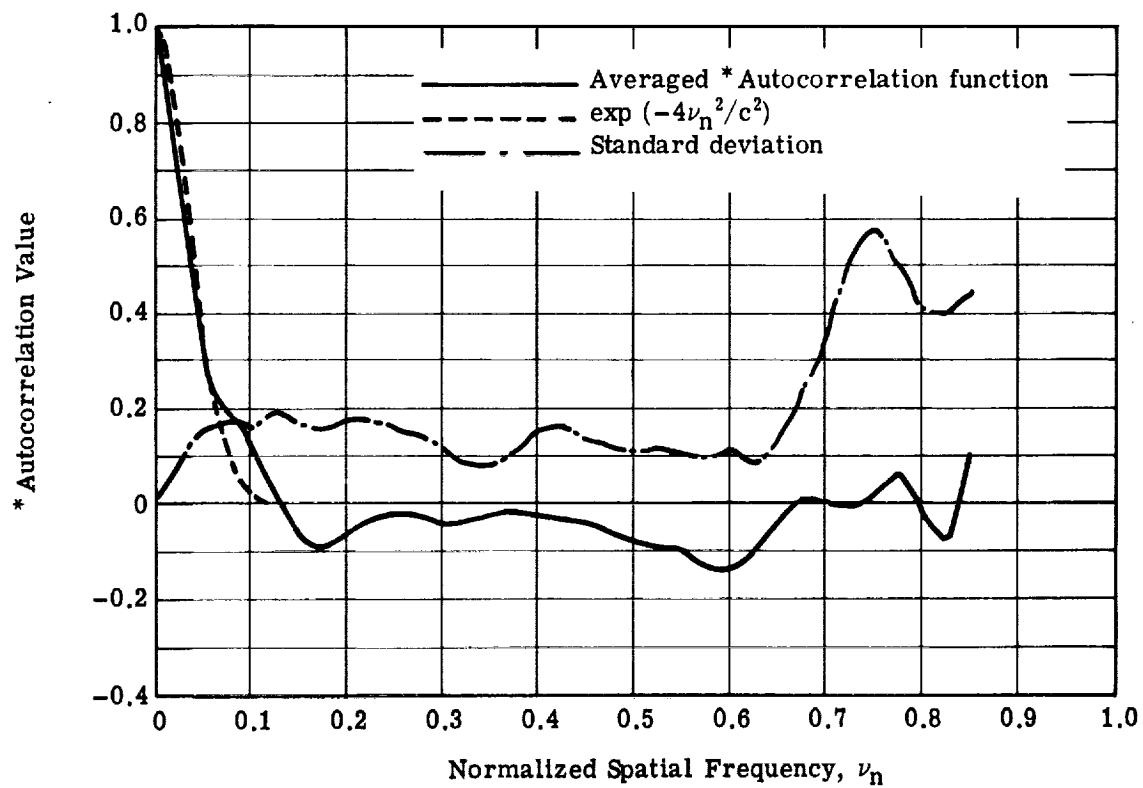


Fig. 4-75 — \* Autocorrelation function for rotationally symmetric, random wavefront of correlation length 0.1; averaged over five wavefronts generated with a square smoothing function

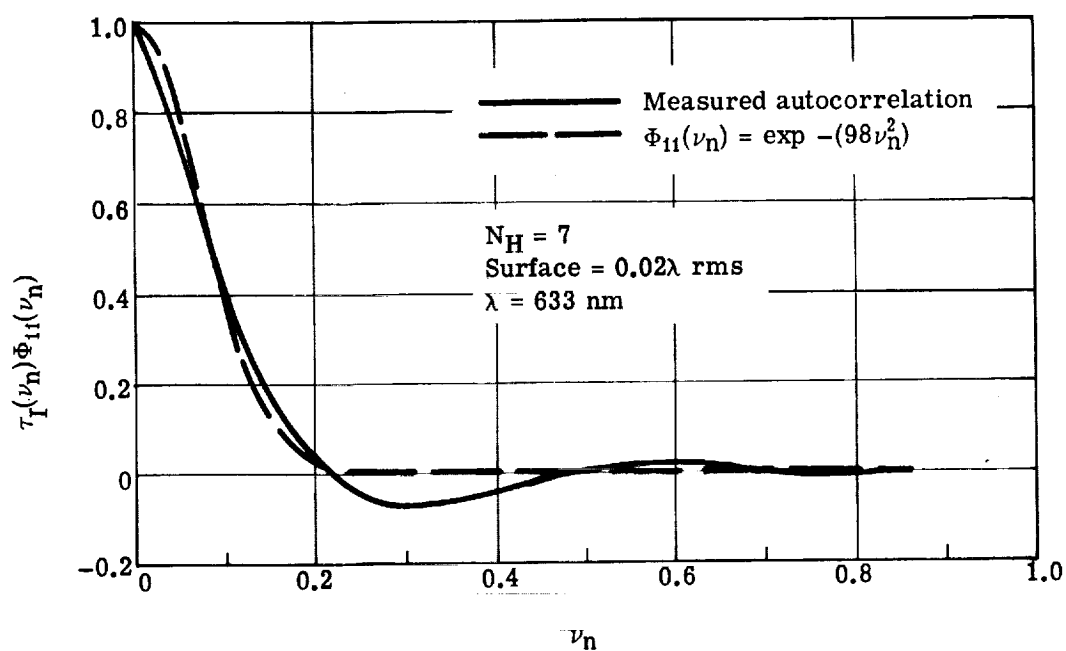


Fig. 4-76 — Autocorrelation function for "Patrick" 48-inch-aperture, f/2.5 parabolic primary

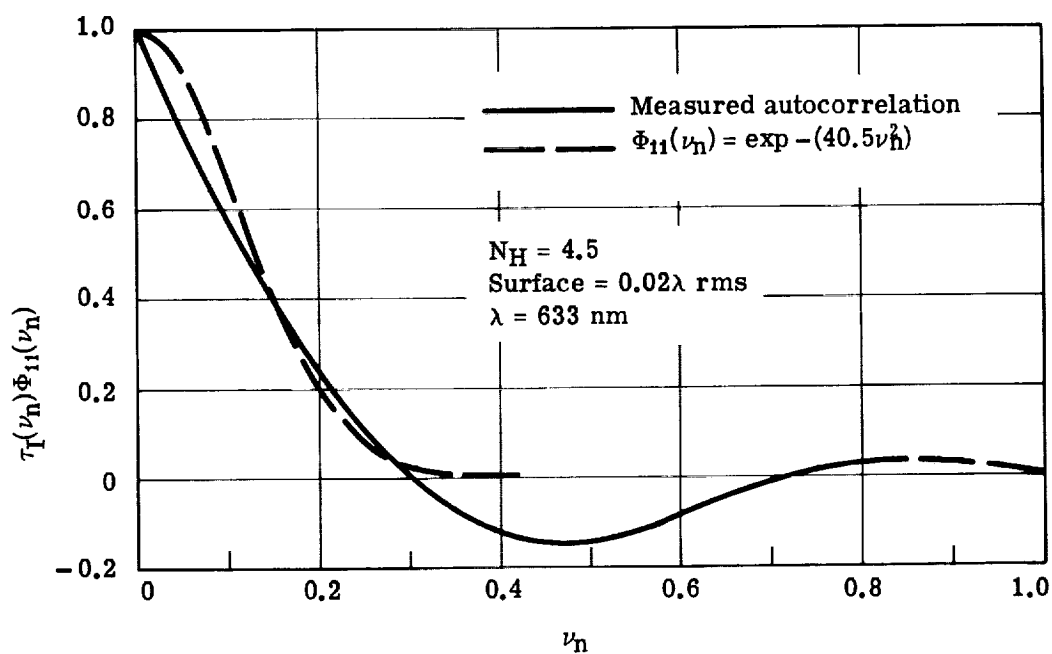


Fig. 4-77 — Autocorrelation function for 12-inch spherical mirror

We will show in Section 5 that the autocorrelation functions for surface microstructure are also significantly non-Gaussian in character.

#### 4.9.3 Deviations From Rotational Symmetry

The wavefront irregularity function of any real telescope will deviate from rotational symmetry. This is clearly evident from the A.A.T. primary mirror wavefront profiles, and is further shown in the above discussion of the autocorrelation function. The question of the magnitude of variance to be expected between the rotationally symmetric statistical models and real system performance is being pursued by several workers. Barakat has published papers<sup>12,13</sup> dealing with the question, although not in terms readily applied to the present effort. E. O'Neill and others (personal conversations) are actively pursuing the topic at various levels of effort, but have not published results as yet. The most interesting and relevant recent paper is by D. Nicholson<sup>14</sup>, which shows variance in the MTF for lens models with two-dimensionally random wavefront errors generated in a manner similar to that used in studying autocorrelation functions here. Three of his figures are reproduced in Fig. 4-78.

Performing variance analyses on the autocorrelation function and MTF is fairly straightforward. Extending this effort to the PSF is more difficult, and has not been done as yet. Hopefully, development of a valid autocorrelation function model including the effects of ripple will help in this direction. The variance analysis of Nicholson uses a low spatial frequency bandpass model of the wavefront, and therefore cannot deal with effects on any part of the PSF beyond the first few rings. There has not been time to try any similar analysis using the rotationally symmetric GASPR model, and applying the results of analyses of multiple rotationally symmetric wavefronts to variations from rotational symmetry is questionable. It is probable that any study of asymmetric effects in scatter due to ripple will have to be done experimentally.

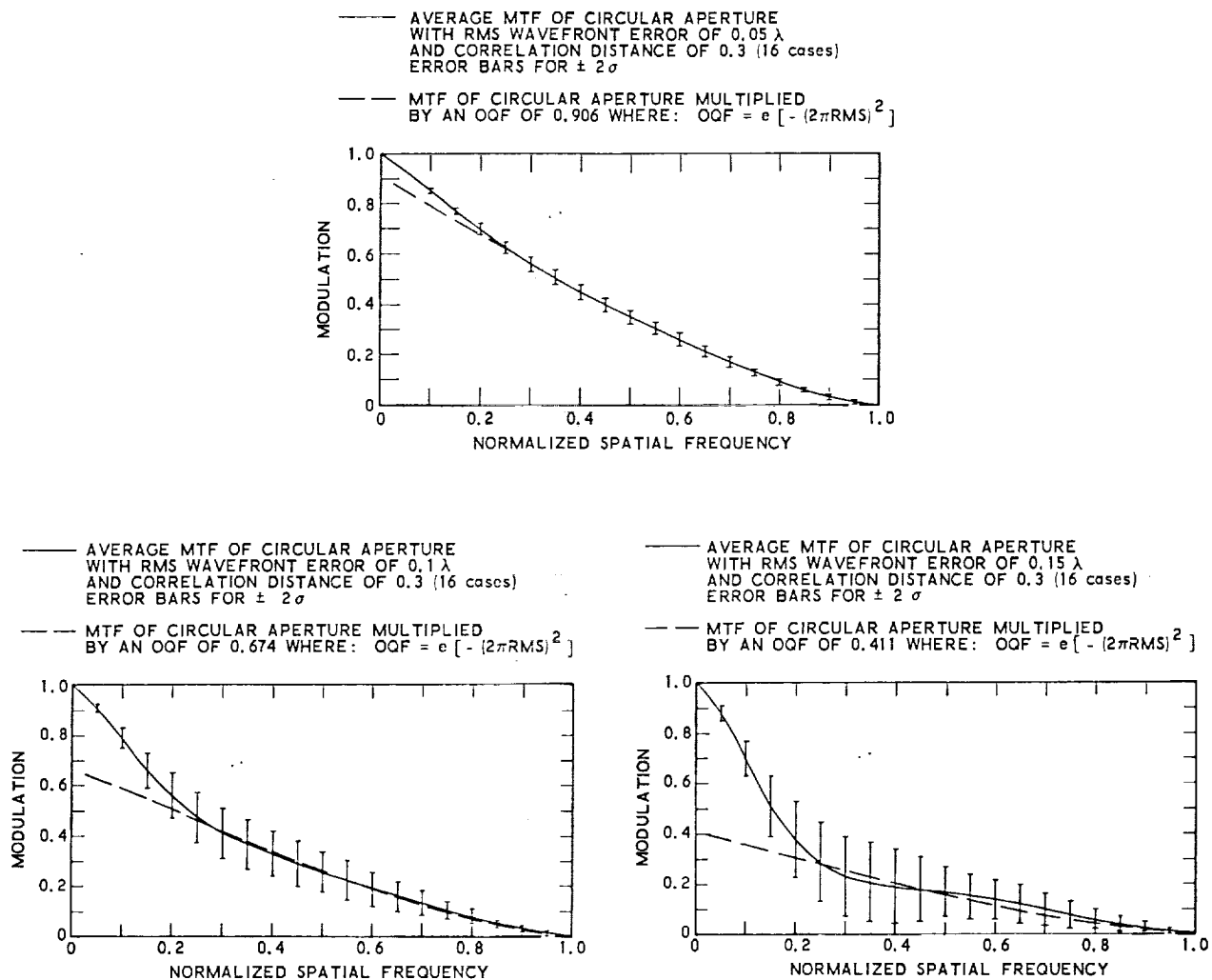


Fig. 4-78 — Variance from the statistical mean in MTF calculations (from Nicholson, ref. no. 14)



## 5. WIDE ANGLE SCATTERING ANALYSIS

Theoretical and experimental analyses of scattering from surfaces have been performed by a great number of workers studying different regions of the electromagnetic spectrum. Wavelengths studied have ranged from microwaves to x rays. The surfaces involved have included not only man-made surfaces, but also the ionosphere, the surface of the ocean, and the surface of the ground. The most prevalent theoretical models derive from radar studies involving the latter three surface types.

Relatively little of the past work has dealt specifically with scatter from highly polished optical surfaces. Recently, however, the needs of space borne astronomy and high energy laser systems have generated interest in such scattering. Until quite recently, workers studying optical surface scattering have adopted the theoretical models developed for radar scattering to explain optical scattering. But these theoretical models face the same problem discussed in Section 4.9: the surface irregularities are assumed to have a Gaussian autocorrelation function. Since this is in fact not the case, the experimental facts do not agree well with the theory. This fact has been disguised in part by the narrow range of angles over which optical scatter is typically measured. The theoretical model might provide a rough fit over, for example, 5 to 20 degrees. Most experimental measurements have tended to concentrate in this range, since experimental difficulties are encountered at smaller angles, and larger angles are frequently not of great interest. More recent measurements extend over a great enough range of angles to show up the errors in the theory. Direct measurements of the autocorrelation function confirm this.

In this section of the report, we will concentrate almost entirely on the more recent experimental results, and on empirical models used to represent them. A brief review of the older theory based on a Gaussian autocorrelation function will be given for purposes of comparison. The two principal sources of direct scatter measurements we will use are the star profiles calculated by Ivan King<sup>15</sup> and John Kormendy<sup>16</sup>, and the scatter coefficient measurements of Roland Shack and Micheal DeBell<sup>17</sup>. Other data will be referenced as cited. We will develop a scatter coefficient model based on the Arizona data and use it to generate a star profile model. This latter will be compared to the King/Kormendy data and will be used as the basis of a computer program to calculate the contribution to the background image irradiance of scattered starlight. Some results of analyses with that program will be included.

### 5.1 BECKMANN MODEL FOR SURFACE SCATTERING

Perhaps the most widely used models for scattering from surfaces are those of Peter Beckmann.<sup>18, 19</sup> Beckmann generally treats the surface as a perfect conductor with surface irregularities which can impose phase errors on wavefronts reflected from it. The surface can then be treated as a spectrum of phase gratings, and the scattered light as a spectrum of plane waves diffracted by them. Beckmann describes a number of models for the phase gratings, including one random model based on Gaussian statistics using a Gaussian autocorrelation function. We will examine this model, using the formulation of Smith and Hering.<sup>20</sup>

Smith and Hering define a bidirectional reflection coefficient which describes both the specular and diffuse reflectivity of the surface.

$$f_{bd}(\theta', \phi'; \theta, \phi) = f_{sp}(\theta')U(\theta', \phi'; \theta, \phi) + f_{sc}(\theta', \phi'; \theta, \phi) \quad (61)$$

where  $\theta', \phi'$  = direction of incident ray in polar and azimuth angles

$\theta, \phi$  = direction of reflected "ray"

$f_{bd}()$  = total bidirectional reflectance

$f_{sp}(\theta')$  = specular component

$f_{sc}()$  = scatter component

$U()$  = 1.0 in specular direction and 0 in all other directions.

The specular component is given by

$$f_{sp}(\theta') = \exp \{-[4\pi(\sigma/\lambda) \cos \theta']^2\} \quad (62)$$

where  $\sigma$  = the rms height of the surface irregularity on the mirror (not on the wavefront).

The diffuse component is given by

$$f_{sc}(\theta', \phi'; \theta, \phi) = \frac{2\pi(\sigma/\lambda)^2 B \exp \{-(\sigma/\lambda)E\}^2}{m^2 \cos \theta \cos \theta'} \times \sum_{M=1}^{\infty} \frac{[(\sigma/\lambda)E]^{2M}}{M(M!)} \exp \left[ \frac{-2\pi^2 (\sigma/\lambda)^2 H}{M m^2} \right] \quad (63)$$

where  $m$  = rms slope =  $\sqrt{2}(\sigma/a)$

$a$  = correlation length

$$B = \frac{1 + \cos \theta \cos \theta' + \sin \theta \sin \theta' \cos (\phi' - \phi)}{\cos \theta + \cos \theta'}$$

$$E = 2\pi(\cos \theta + \cos \theta')$$

$$H = \sin^2 \theta + \sin^2 \theta' + 2 \sin \theta \sin \theta' \cos (\phi' - \phi)$$

For normal incidence,  $B = 1.0$ ,  $E = 2\pi(1 + \cos \theta)$ , and  $H = \sin^2 \theta$ . Eqs. 62 and 63 reduce to

$$f_{sp}(\theta) = \exp[-4\pi(\sigma/\lambda)^2] \quad (64)$$

and

$$f_{sc}(\theta) = \frac{2\pi(\sigma/\lambda)^2 \exp \{-[2\pi(\sigma/\lambda) (1 + \cos \theta)]^2\}}{m^2 \cos \theta} \times \sum_{M=1}^{\infty} \frac{[2\pi(\sigma/\lambda) (1 + \cos \theta)]^{2M}}{M(M!)} \exp \left\{ - \left[ \frac{2\pi^2 (\sigma/\lambda)^2 \sin^2 \theta}{M m^2} \right] \right\} \quad (65)$$



Note that Eq. 64 is one form of approximation for calculating the Strehl definition (see reference 6, page 4-3).

Eq. 65 has been used to compute the scatter coefficients for the case  $\sigma = 20$  Ångstroms and  $a = \lambda/2, \lambda, 2\lambda$ , and  $4\lambda$ . The results are shown in Fig. 5-1, which plots the log of  $f_{sc}(\theta)$  versus  $\log \sin(\theta)$ . Note that all four curves have the same general form, a long flat portion at small angles, plus a strong roll-off at large angles. Changing the correlation length  $a$  increases the scatter coefficient at small angles and shifts the shoulder of the curve toward smaller angles.

It is generally assumed that the correlation length for polished mirror surfaces is in the region of one wavelength. Since such mirrors tend to have scatter coefficients which vary as the inverse square of  $\sin \theta$  in the vicinity of 5 to 10 degrees, than in the absence of measurements outside this range of angles, the Beckmann theory seems to fit the data if  $a = 1$  to 2 wavelengths.

In Fig. 5-1, we have added two curves taken from the next section of this report. Although neither represent scatter measurements over the entire range of angles plotted, each implies that the other can be extrapolated as shown. Neither of these curves can be fit by Eq. 65 for any combination of  $\sigma$  or  $a$ . We must therefore assume the Beckmann theory to be inapplicable to scattering from well polished mirrors.

## 5.2 DATA FROM THE LITERATURE

There is very extensive literature on scattering theory and scatter measurements. Most of it is irrelevant to our purposes and will not be cited. Rather, we will cite only that data which applies to the topics under discussion. This will fall into three categories: first, the King/Kormendy star image profiles, which are unique in giving the effective point spread function for a complete system from the center of the image out to 5 degrees; second, direct measurements of scattering at angles greater than about 1 degree; third, measurements of surface irregularity and its statistics.

### 5.2.1 King and Kormendy Star Profile

In 1971, King<sup>15</sup> published the composite profile of a star image shown in Fig. 5-2. This was taken from microdensitometric tracings of star images on film from a number of separate telescopes, including the 60-inch Cassegrain at Mount Wilson and the 48-inch Schmidt telescope at Mount Palomar. The curves cover data from substantially less than one arc-second to about 5 degrees. The ordinate is surface brightness or effective radiance in magnitudes per square arc-second for a zero magnitude star.

Two aspects of the data are particularly interesting: first, an extensive section of the profile follows an inverse square dependency on angular radius; second, the data from a number of different instruments of different design and different aperture diameter follow roughly the same star profile. The inverse square characteristic eliminates diffraction at the pupil from consideration as the source of the profile, since diffraction at a circular aperture has an inverse cube dependency on angular radius. The fact that the same curve applies to a number of different telescopes indicates that design type and aperture diameter are of secondary importance in defining the star profile.

King made no significant attempt to define the source of this shape, and this is indeed a difficult problem. The complete system involves transmission through the turbulent atmosphere, diffraction by the telescope aperture, scatter at several optical surfaces, and scatter within the film emulsion. The shoulder toward the center of the curve is without doubt due to atmospheric turbulence, but beyond that, explanations are speculative.

Kormendy<sup>16</sup> did a far more detailed analysis of the star image profile for the 48-inch Schmidt telescope at Mount Palomar, with the intent of providing a radiometric calibration for the telescope. His data, shown in Fig. 5-3, plots surface brightness in magnitudes per square

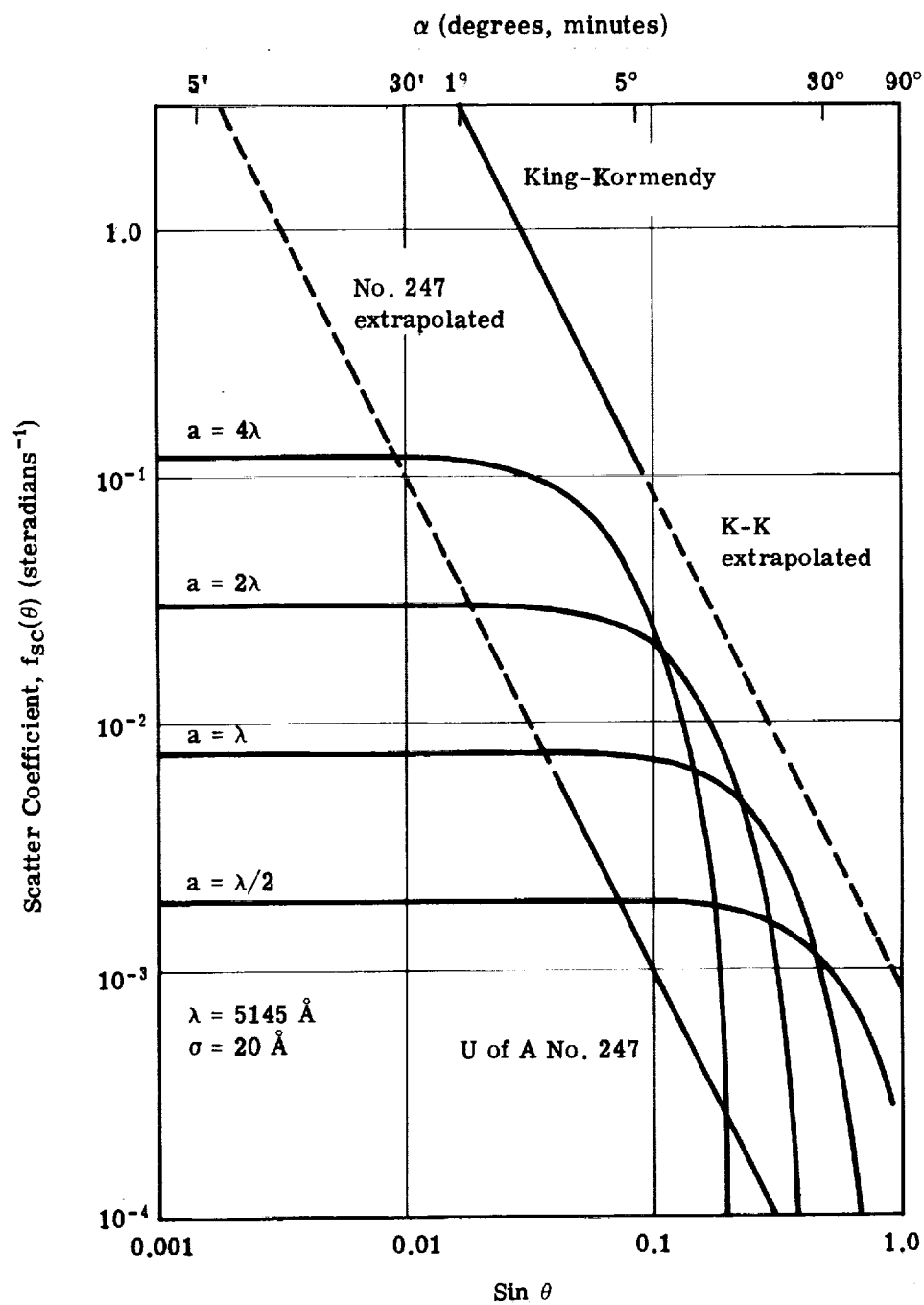


Fig. 5-1 — Beckman theory scatter curves for different correlation lengths, compared to King-Kormendy and University of Arizona data

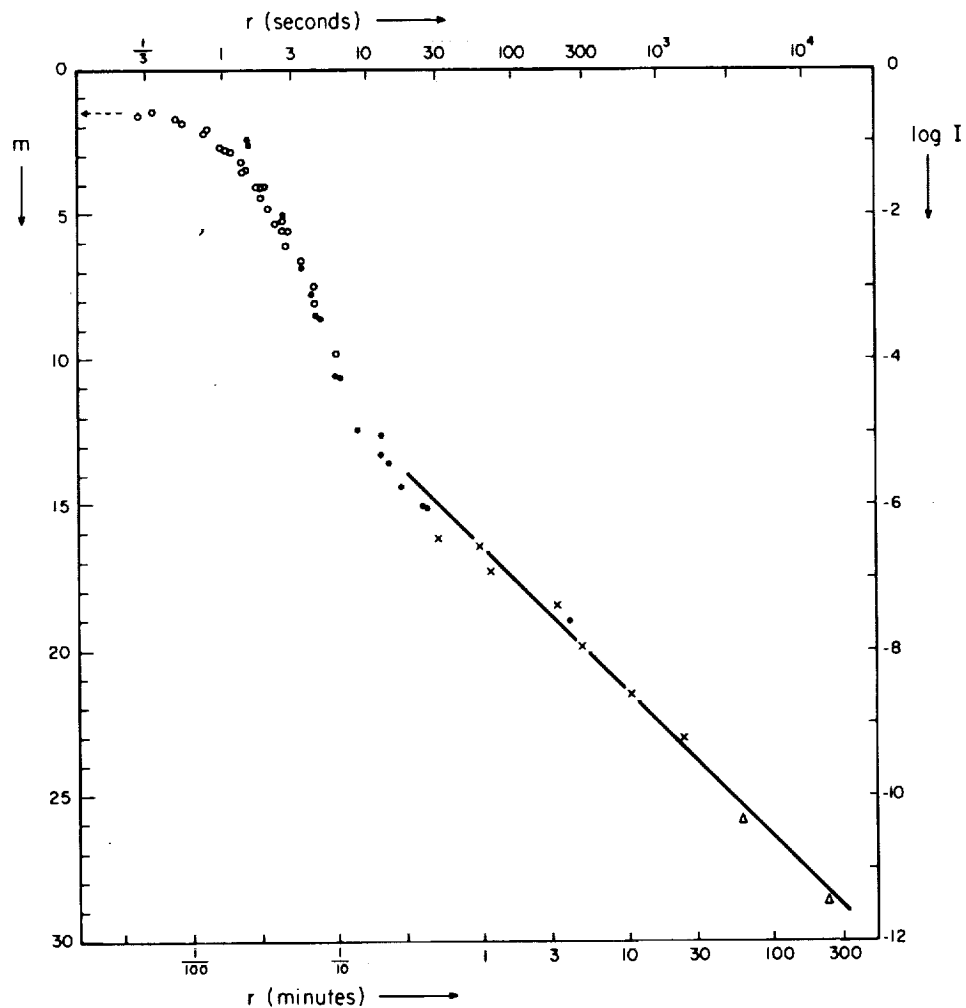


Fig. 5-2 — Surface brightness, in magnitude per square second, in the image of a star of magnitude zero. Open circles are derived from 60-inch Cassegrain images, closed circles from diameters of NPS stars on the Palomar Observatory Sky Survey (POSS), and crosses from other stars on POSS. Straight line is inverse-square law found by de Vancouleurs. Triangles are from sky brightness near the sun (Ref. 15).

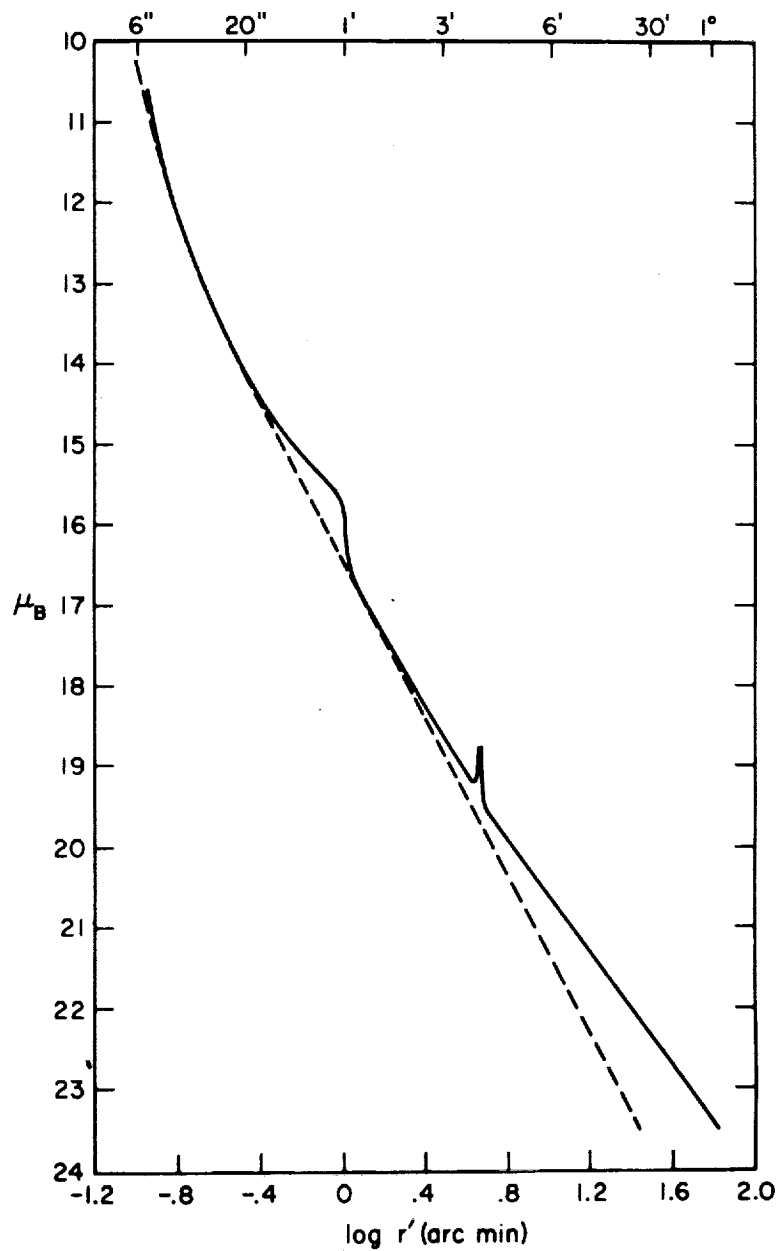


Fig. 5-3 — Brightness profile of a 0-magnitude star. Surface brightness in B magnitudes per square second of arc is plotted against the logarithm of the radius. The dashed curve is due to King (1971) (Ref. 16).

arc-second against the log of the image radius in arc-minutes. The dashed line is from King's data, and the solid line is Kormendy's new curve. There are two anomalies in the latter, one due to a ghost image produced by the Schmidt plate, and the second (at 1 arc-minute) a ghost image produced by a filter in front of the photographic plate. Kormendy's data agrees well with King's data at smaller angles, but shows a lower slope at large angles.

Kormendy makes a more detailed attempt at explaining the shape of the curve. He dismisses diffraction at the aperture as a possible cause, indicating that it will be well below the plotted curves. Scattering in the emulsion of the photographic plate may account for the change in slope inside of 20 arc-seconds, but cannot explain the power-law part of the curve. He also gives reasons for dismissing scattering from atmospheric haze. This leaves scattering from optical surface irregularities and dust in the telescope as the most probable cause. We will return to considering this possibility after we have generated a star profile model based on mirror surface scattering.

### 5.2.2 University of Arizona Scatter Measurements

The data published in reference 17 represents perhaps the most comprehensive attempt to measure scatter from mirror surfaces of differing roughnesses that is presently available. Measurements were made on a number of different samples of glass and fused silica polished by a number of different techniques. Surface finish ranged from ground glass to superpolish. Scatter angle (normal incidence) ranged from roughly 2 degrees out to nearly 90 degrees. (There is some question about the validity of the data below 5 degrees, however, due to some extraneous background contribution.)

Fig. 5-4 is typical of the output of these measurements. The uppermost curves are for ground glass samples. The remaining five curves are for glass and fused silica samples of different surface roughness. Table 5-1 summarizes some of the data about them, including surface roughnesses and scatter coefficient  $\rho_s(\alpha)$  for  $\alpha = 5.74^\circ$  ( $\sin \alpha = 0.10$ ). It should be noted that the surface roughness was estimated visually from FECO interferograms and its accuracy is highly suspect. Note also that this data is for the roughness of the wavefront, not the mirror surface.

This data is used as the basis for the scatter coefficient model developed in Section 5.3, which follows a suggestion on page 30 of reference 17. This data will be discussed further at that time.

Table 5-1 — Scatter Data from University of Arizona Measurements (Reference 17)

Sample	$\sigma_w(\text{\AA})$	$\omega = \sigma_w/\lambda$	$\rho_s(\alpha_1)^*$
EDF 3-11	150	0.0292	$1.43 \times 10^{-2}$
222	120	0.0233	$1.22 \times 10^{-3}$
EDF 3-4	25	0.0049	$8.42 \times 10^{-4}$
247	40	0.0078	$8.42 \times 10^{-4}$
236	10	0.0019	$1.75 \times 10^{-4}$

\*  $\sin \alpha_1 = 0.10$   
 $\lambda_1 = 514.5 \text{ nm}$

### 5.2.3 Michelson Laboratory Data

Bennett's group at Michelson Laboratory, Naval Weapons Center, China Lake, California is one of the most active in studying scattering from mirrors. Although much of their early work tended to be involved with variation in specular reflectivity with roughness<sup>21</sup> or total scatter,

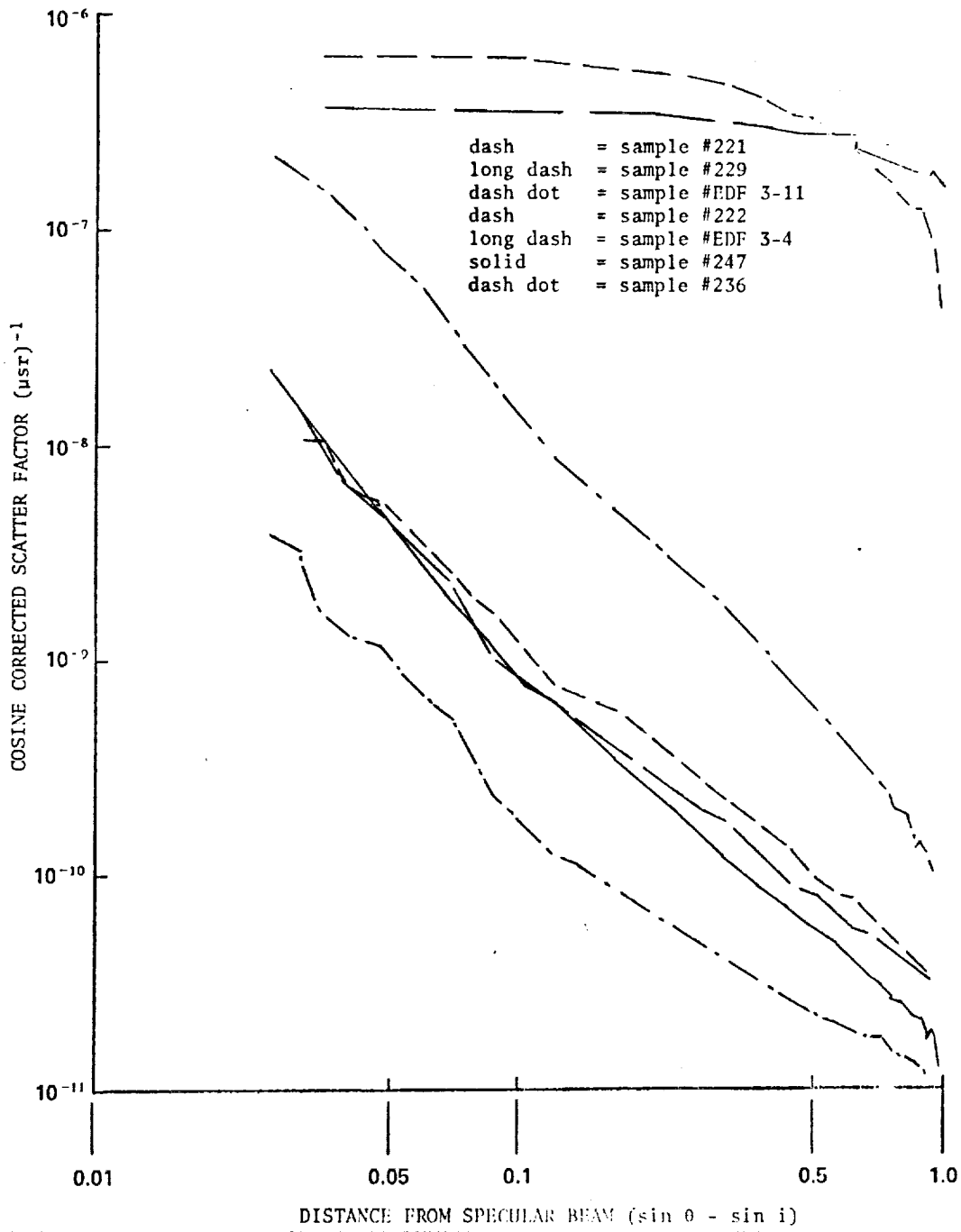


Fig. 5-4 — Scatter as a function of surface roughness normal incidence; corrected for best fit background (University of Arizona)

some of their recent work is of more direct interest to this study. In particular, they have developed a FECO interferometer which they have used to measure the surface microstructure of mirrors, from which they have computed the statistical characteristics of the surface irregularities.<sup>23, 24</sup> Figs. 5-5 to 5-8 represent data taken from these measurements. The important points to note from this data are that both height and slope data are Gaussian, while the autocorrelation function is non-Gaussian. These examples are typical of their other data as well (see references 23 and 24).

It is interesting to compare the autocorrelation function in Fig. 5-5 to Fig. 4-29c. They are rather similar, particularly in terms of their behavior near the origin. In this region, Bennett's data tends to fit a linear exponential curve, although that fit breaks down where the autocorrelation function goes negative. These autocorrelation functions are probably indicative of a very broad spatial frequency distribution in the surface irregularities.

Work is continuing at Michelson Laboratory to attempt to fit a scatter function to this autocorrelation function. No satisfactory solution has been found as of this writing (personal communication from J. Bennett).

#### 5.2.4 Other Data Sources

Three other data sources are worth noting. Smith and Hering<sup>20</sup> also measured surface irregularities and computed the associated autocorrelation functions, with results similar to Jean Bennett's data given above. Their measurements were made mechanically, with a stylus, and therefore are of comparatively poor lateral resolution. Jay Eastman<sup>25</sup> has made measurements of surface roughness with a scanning Fizeau interferometer. He shows the surface irregularities to have an autocorrelation function which is approximately a linear exponential (see Fig. 5-9). It should be noted that no attempt was made to define the correct zero height for this function. The fact that  $C(s)$  in Fig. 5-9 is all positive is an artifact of the normalization technique. Eastman's work is worth noting here primarily because of his development of scanning Fizeau interferometer, which is competitive in performance to the FECO interferometer. (See Section 7.2 and Appendix B for further discussion.)

The third data source of interest is a recent paper by Heinisch<sup>26</sup>, which discusses the effects of dust and surface contaminants on the bidirectional reflectivity of mirrors. His measurements are made at 10.6 micrometers, but the results are indicative of what can be expected at different wavelengths. Fig. 5-10 reproduces his principal figure. Replotting the lower two curves in log-log coordinates shows them to have straight sections varying in slope from about 1.6 to 2.8, which is within the range indicated by Arizona data. The accumulated dust raises the scatter level roughly 50 times and changes the slope of the scatter curve. Removing the dust restores the original level of scatter almost completely.

### 5.3 SCATTER COEFFICIENT MODEL BASED ON EMPIRICAL DATA

The data on star profiles from King and Kormendy and the data from mirror scatter measurements from the University of Arizona suggest that the scatter coefficient follows an inverse power law over a considerable range of scatter angles. Thus a model using an inverse power law seems reasonable. There are two endpoint conditions which deviate from this law, however. At 90 degrees, the scatter coefficient must go to zero via a cosine roll-off. Also, the inverse power law cannot hold at zero scatter angle where it would be infinite. Thus a small angle roll-off is also required. The complete model should have the general form shown in Fig. 5-11 when plotted on log-log paper. This curve can be represented by an equation of the form

$$\rho_s(\alpha) = \frac{C_1 \cos \alpha}{(1 + C_2 \sin^2 \alpha)^{s/2}} \quad (66)$$

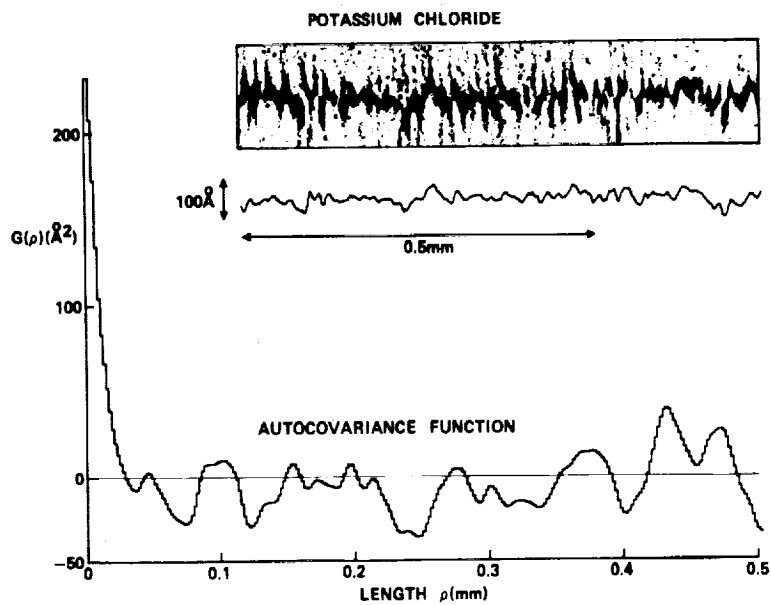


Fig. 5-5 — Photograph, TV scan, and autocovariance function for a 29 Å rms polished potassium chloride surface

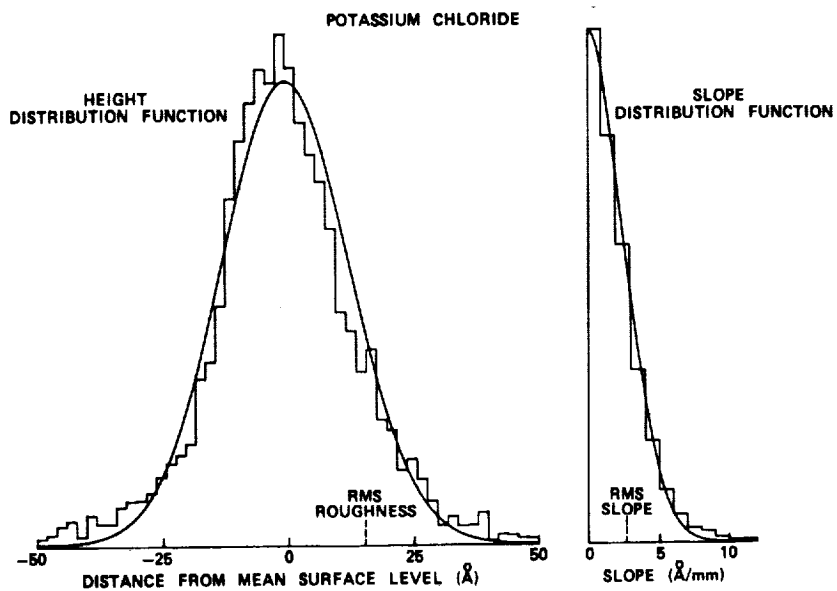


Fig. 5-6 — Height and slope distribution functions for the same potassium chloride surface (after Ref. 23, 24)



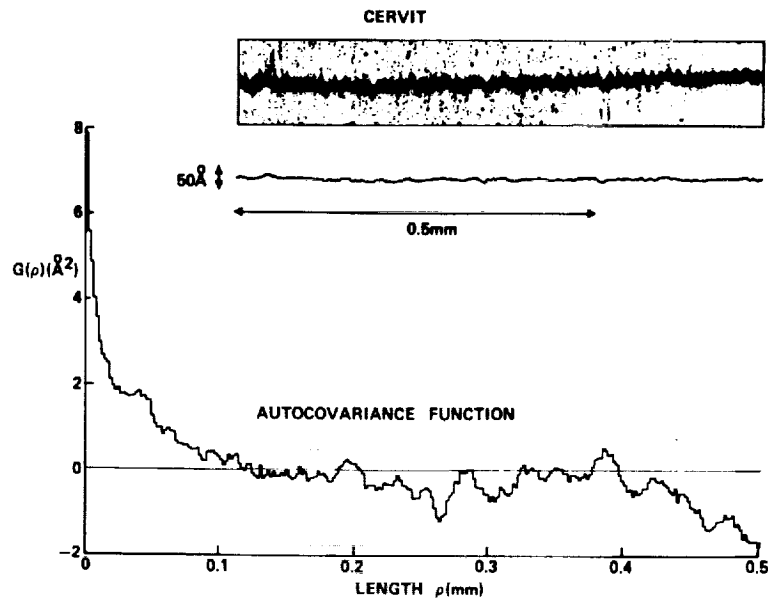


Fig. 5-7 — Photograph of Feko fringe, TV scanning camera trace, and autocovariance function for an 8 Å rms roughness polished Cer-Vit surface

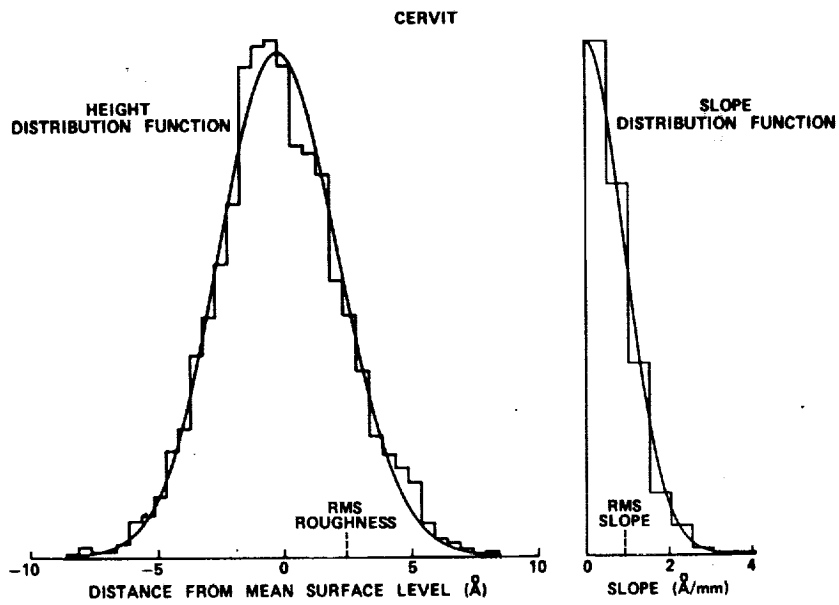


Fig. 5-8 — Height and slope distribution functions for the same Cer-Vit surface; the smooth curves are Gaussians that have the same area under the curves as the measured histograms

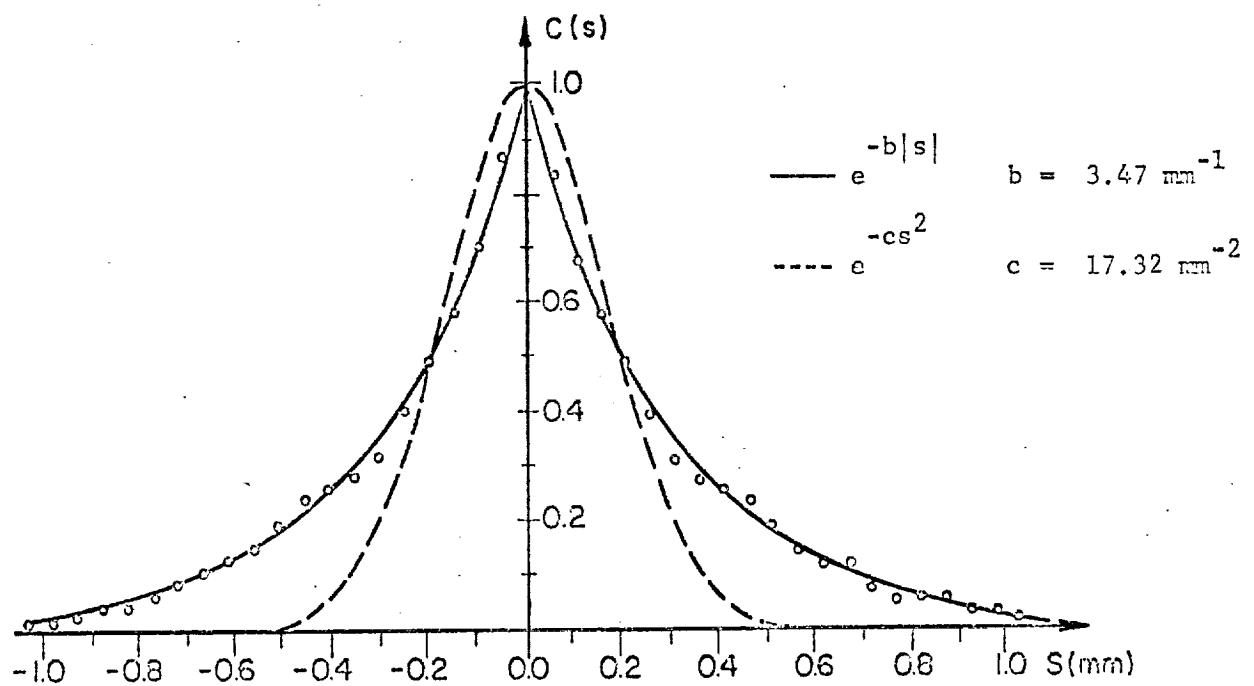


Fig. 5-9 — Autocorrelation data for sample E-1 after Ref. 25

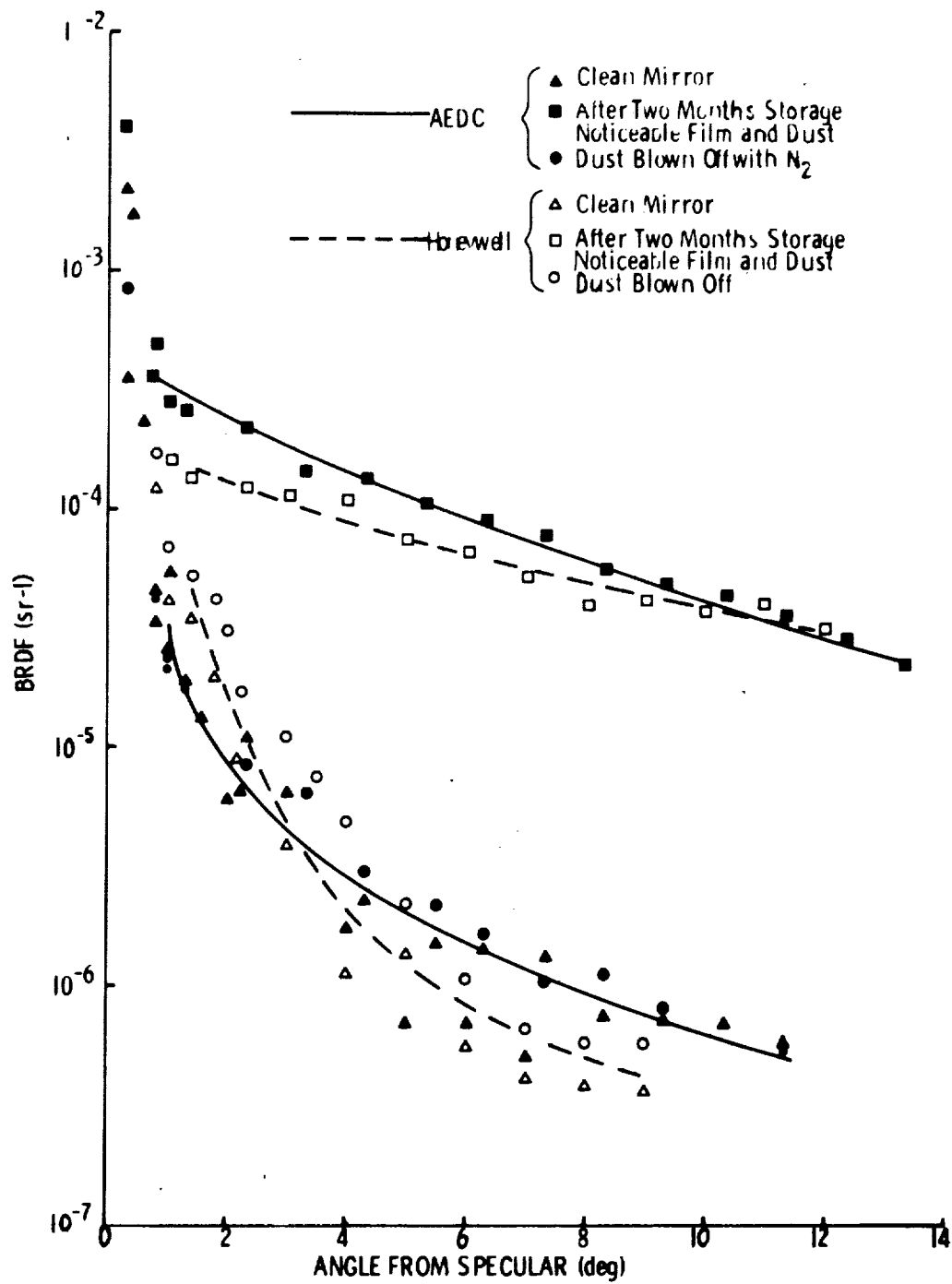


Fig. 5-10 — Effect of dust on BRDF of metal mirror

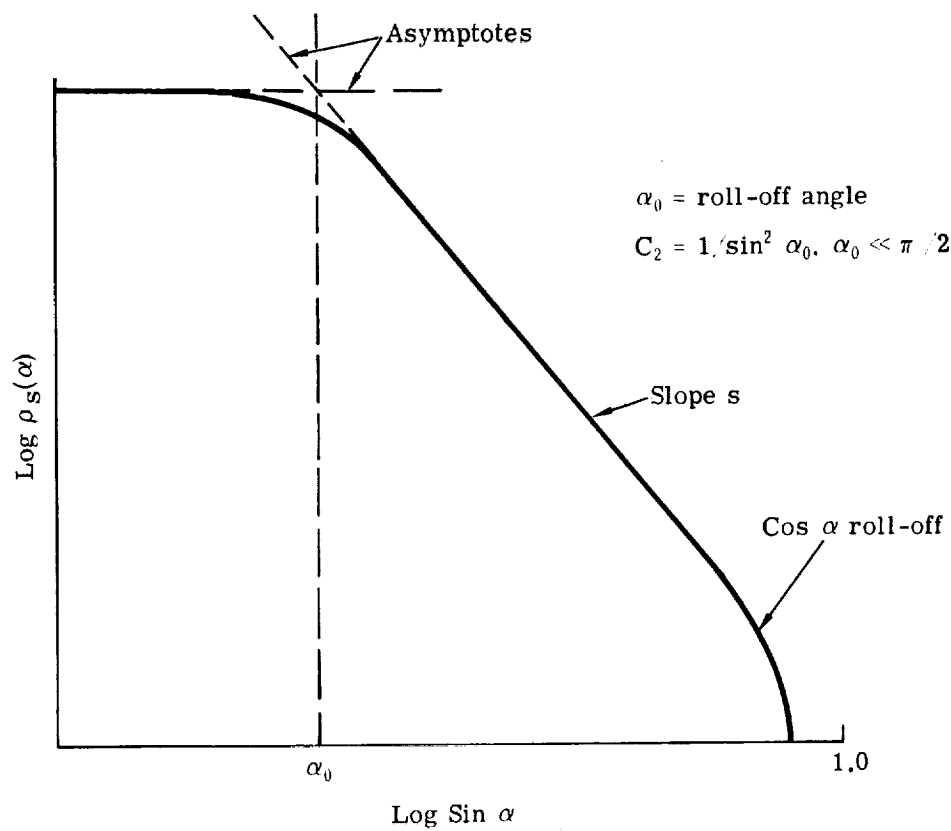


Fig. 5-11 — General form of empirical scatter coefficient  $\rho_S(\alpha)$

The units of  $\rho_s(\alpha)$  are steradians<sup>-1</sup>. Light is assumed to be normally incident. (Note: This model is drawn from reference 17, page 30, equation 67.)

$C_1$  represents the value of the scatter coefficient at very small angles,  $\alpha \ll \alpha_0$ .  $C_2$  is the constant defining where small angle roll-off occurs. Numerically,  $C_2 = 1/\sin^2 \alpha_0$ , where  $\alpha_0$  is the angle at which the asymptotes to the two straight-line portions of the curve cross. We might therefore rewrite Eq. 66 as

$$\rho_s(\alpha) = \frac{C_1 \sin^S \alpha_0 \cos \alpha}{(\sin^2 \alpha_0 + \sin^2 \alpha)^{S/2}} \quad (67)$$

In general, we will not be able to determine  $C_1$  or  $\alpha_0$  very readily. In later analyses, we will assume a value for  $\alpha_0$ , generally an angle smaller than any we will use in practice. But if we have one measured value of the scatter coefficient,  $\rho_s(\alpha_1, \lambda_1)$ , measured at angle  $\alpha_1 \gg \alpha_0$  and wavelength  $\lambda_1$ , and if we know the slope  $S$ , then we can say that

$$C_1 \sin^S \alpha_0 = \rho_s(\alpha_1, \lambda_1) \sin^S \alpha_1 / \cos \alpha_1 \quad (68)$$

Thus

$$\rho_s(\alpha) = \frac{\rho_s(\alpha_1, \lambda_1) \sin^S \alpha_1 \cos \alpha}{\cos \alpha_1 (\sin^2 \alpha_0 + \sin^2 \alpha)^{S/2}} \quad (69)$$

In Section 4.2.4, we discussed how changing wavelengths changed the scatter function due to a spectrum of small phase amplitude phase gratings. The change in scatter was due to two effects, increase in the effective phase amplitude and decrease in the scatter angle for a given spatial frequency phase grating, as wavelength decreases. The net result was the (4-S) scaling law of Eq. 35.

Now consider how these arguments apply to the scatter function model represented by Fig. 5-11. First, as wavelength decreases, points in the straight-line portions should scale upward according to Eq. 35. Second, as wavelength decreases,  $\alpha_0$  will become smaller. Thus if we wish to know  $\rho_s(\alpha, \lambda)$  when we have measured data for  $\rho_s(\alpha_1, \lambda_1)$ , we should rewrite Eq. 69 as:

$$\rho_s(\alpha, \lambda) = \frac{(\lambda/\lambda_1)^{(S-4)} \rho_s(\alpha_1, \lambda_1) \sin^S \alpha_1 \cos \alpha}{\cos \alpha_1 [(\lambda/\lambda_1)^2 \alpha_{01} + \sin^2 \alpha]^{S/2}} \quad (70)$$

We have written  $\alpha_{01}$  to indicate that this is the roll-off angle at  $\lambda_1$ .

It should be emphasized that these wavelength scaling rules are tied to the assumption that the phase amplitudes of the wavefront irregularities remain small through the wavelength region, and to the assumption that the features of the scatter function (slope of the straight-line portions and the small angle roll-off) are a result of the spatial frequency distribution of the wavefront surface irregularities. If the phase amplitudes of the surface irregularities become too large, these assumptions break down due to interactions between different spatial frequency components. The one-to-one relationship between spatial frequency components of the wavefront irregularity function and features of the scatter function break down when sum and differencing of components occurs, and when significant higher order terms show up. (See Figs. 4-56 through 4-59, Section 4.7.4, for examples). Thus, care should be taken in using this equation to scale scatter functions into the far ultraviolet. If the total scattered light is more than a few percent of the light in the point source image, these equations probably do not hold.

Eq. 70 has been used to compute the curves in Figs. 5-12 and 5-13. Fig. 5-12 shows how the choice of roll-off angle affects the scatter function curve. This has obvious implications concerning total scattered light and will be dealt with below. Fig. 5-13 shows how slope  $s$  will affect scaling of the scatter function with wavelength. The constants for the three different scatter functions were selected to make them all equal at  $\sin \alpha_1 = 0.10$  and  $\lambda_1 = 0.60$  micrometers. It will be seen from the way the position of the intersection point for the three curves shifts that the scaling consists of shifting the curves left a distance  $\log (\lambda_2/\lambda_1)$  and upward a distance  $\log (\lambda_1/\lambda_2)^4$ . This follows directly from the change in scatter angle and phase amplitude for each spatial frequency component of the wavefront irregularity function with the consequent scattering of more light into a smaller solid angle, as discussed in Section 4.2.4. At any given scatter angle, however, we see that wavelength scaling is strongly dependant on the scatter function slope  $s$ , with the change being greatest for the smallest slope.

It is interesting to apply the two wavelength scaling rules of the above paragraph to the infrared data from Heinisch<sup>26</sup>. To match the University of Arizona data<sup>17</sup>, we must scale from 10.6 micrometers to 0.5145 micrometer. The data is shifted left in angle space by the scale factor  $(0.5145/10.6) = 0.0485$ , and  $1^\circ$  becomes  $2' 54''$ . (This is a roundabout method for measuring small angle scattering.) The scatter coefficient is scaled upward by a factor  $(10.6/0.5145)^4 = 1.80 \times 10^5$ . The results of this scaling are shown in Fig. 5-14 with some of the University of Arizona data for comparison. A scatter function curve from Eq. 70 has been added. This was given a slope of 2 and fit roughly to the scaled Heinisch data.

The mirror measured by Heinisch is described as a "high quality, low scatter electroless nickel coated aluminum mirror," but no data is given as to the rms deviation of its surface irregularities. Therefore, the most we can say from Fig. 5-14 is that the scaled infrared scatter coefficients are consistent with the University of Arizona data and the scatter function model Eq. 70. This consistency is maintained over assumed slopes ranging from about 1.7 to 2.0, with a slope of 1.8 matching the Heinisch data to sample no. 247.

Eq. 70 is the complete statement of the scatter function model we will use in analyzing wide angle scattering. In most of the actual analysis, we will use somewhat simplified forms of the model for convenience. We will generally assume that  $s = 2$ , except when specifically examining the effects of slope variation, as in Fig. 5-13. In some of the star profile calculations below we ignore the wavelength scaling of  $\alpha_0$  as well.

If we assume that  $s = 2$ , Eq. 66 becomes

$$\rho_s(\alpha) = C_1 \cos \alpha / (1 + C_2 \sin^2 \alpha) \quad (71)$$

We wish to integrate Eq. 71 to determine the total scattered light (TSL) due to the wavefront surface irregularities. Normalizing the integral to give TSL = 1.0 for a perfect Lambertian reflector, for which  $\rho_s(\alpha) = (\cos \alpha)/\pi$ , we obtain

$$\text{TSL} = \frac{2\pi}{\pi-2} C_1 \int_0^{\pi-2} \frac{\alpha \cos \alpha \, d\alpha}{(1 + C_2 \sin^2 \alpha)} \quad (72)$$

Eq. 72 is not an easy integral to solve analytically, but if two simplifications are made, an approximate solution can be found. First, we use the asymptotic form of the scatter function:

$$\begin{aligned} \rho_s(\alpha) &= C_1 \cos \alpha, \alpha \leq \alpha_0 \\ &= \frac{C_1 \cos \alpha}{C_2 \sin^2 \alpha}, \alpha > \alpha_0 \end{aligned} \quad (73)$$

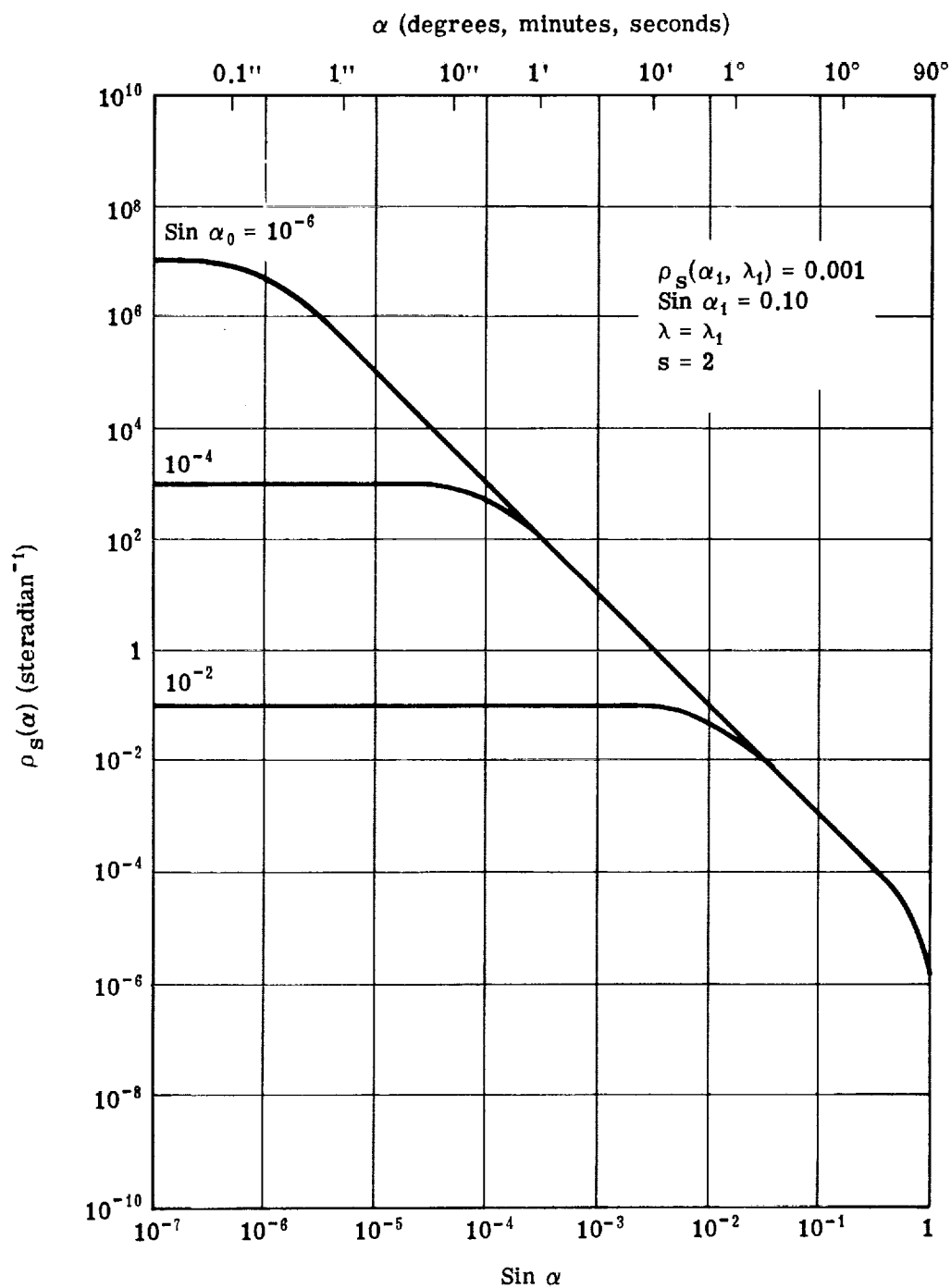


Fig. 5-12 — Variation of  $\rho_S(\alpha)$  with roll-off angle



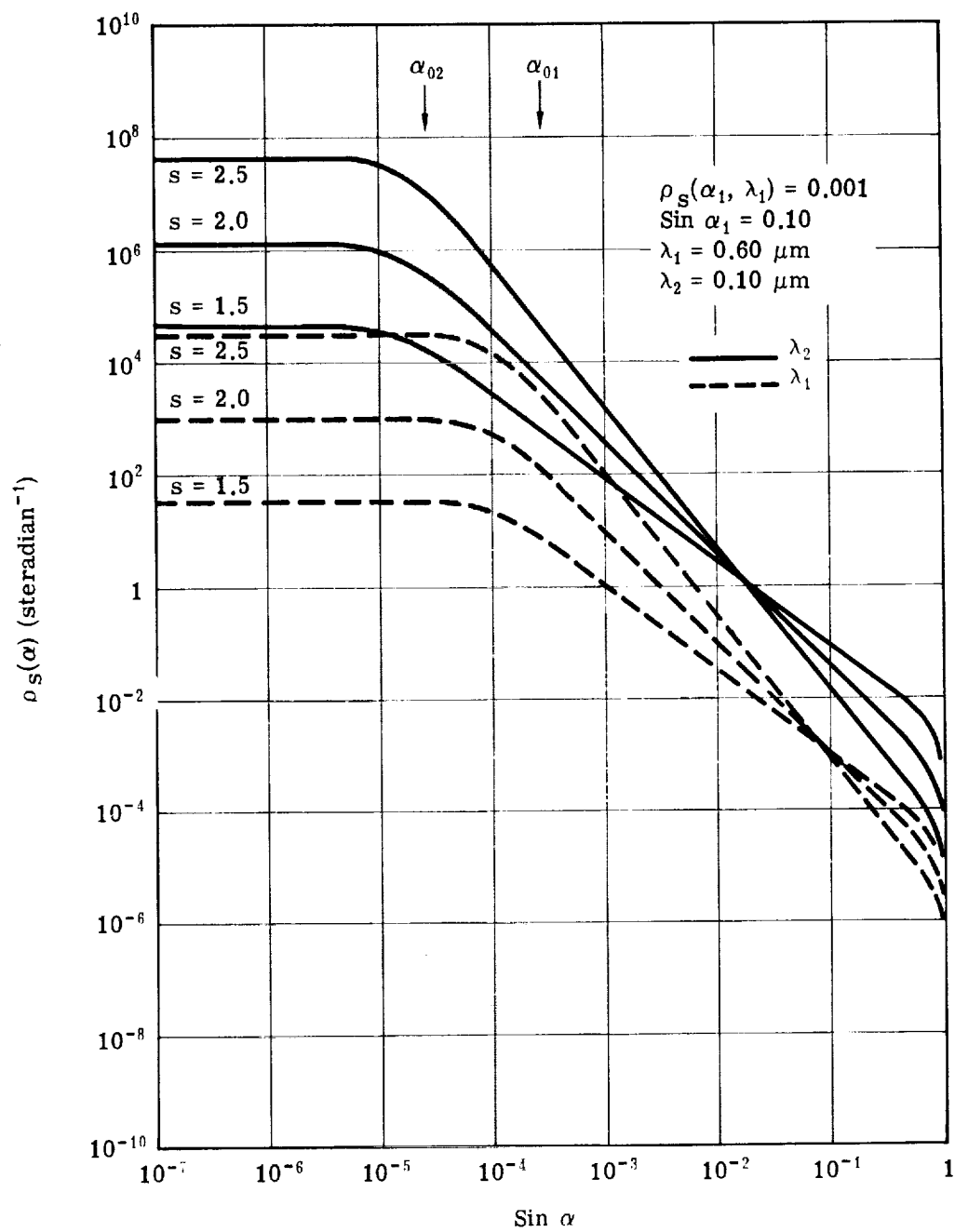


Fig. 5-13 — Variation of  $\rho_S(\alpha)$  with wavelength and slope  $s$

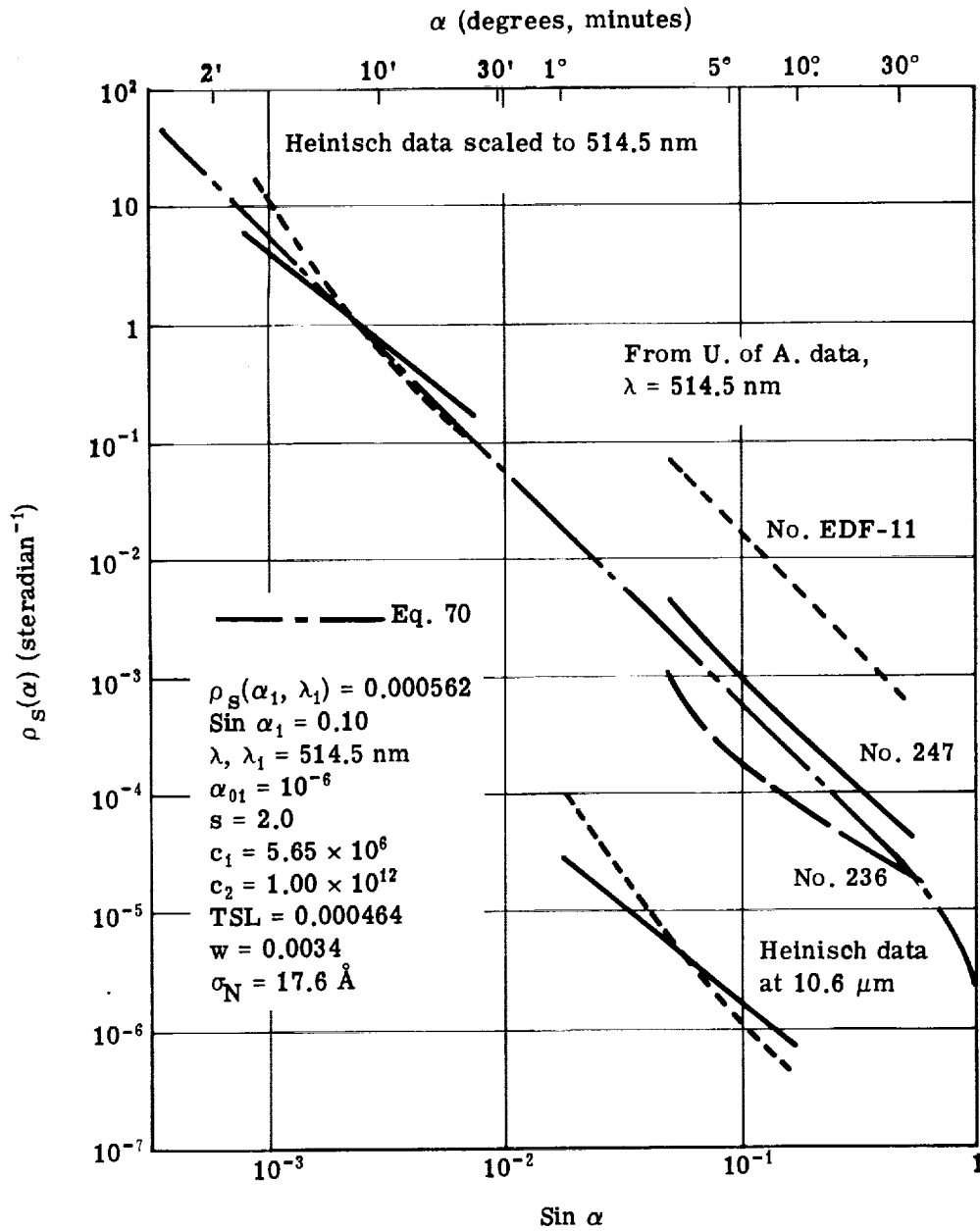


Fig. 5-14 — Heinisch infrared data<sup>28</sup> scaled to 514.5 nm and compared to University of Arizona data<sup>17</sup>

Second, we transform the notation, setting  $x = \sin \alpha$ , and  $x_1 = \sin \alpha_0$ . The integral can then be rewritten

$$\text{TSL} = \frac{2\pi C_1}{\pi-2 C_2} \left[ C_2 \int_0^{x_2} \arcsin x \, dx + \int_{x_1}^1 \frac{\arcsin x \, dx}{x^2} \right], \quad (74)$$

from which we get

$$\begin{aligned} \text{TSL} = \frac{2\pi C_1}{(\pi-2)C_2} & [2\sqrt{C_2} \arcsin(1/\sqrt{C_2}) + \sqrt{C_2} \sqrt{C_2-1} - C_2 \\ & + \frac{\pi}{2} + \ln[\sqrt{C_2} + \sqrt{C_2-1}]] \end{aligned} \quad (75)$$

In general,  $C_2 \gg 1$ . Therefore, Eq. 75 can be simplified to read

$$\text{TSL} = \frac{\pi C_1}{(\pi-2)C_2} [4 - \pi + \ln(4C_2)]. \quad (76)$$

If we wish to rewrite this in the manner of Eq. 70, remembering that we have set  $s = 2$ ,

$$\text{TSL} = \frac{\pi(\lambda_1/\lambda)^2 \rho_s(\alpha_1, \lambda_1) \sin^2 \alpha_1}{(\pi-2) \cos \alpha_1} \{4 - \pi + 2\ln[2(\lambda_1/\lambda)] - 2\ln(\sin \alpha_1)\} \quad (77)$$

Eq. 77 can be used to study the effects of varying wavelength and roll-off angle on the total scattered light. Fig. 5-12 implies that a small roll-off angle will substantially increase the amount of light scattered into the forward hemisphere by the corresponding mirror. Table 5-2 gives numerical data to demonstrate this. Changing the roll-off angle from half a degree to 0.02 arc-second increases total scatter by a factor of 3. (The latter angle corresponds roughly to the middle-ultraviolet Airy disk radius for the large space telescope.) Thus the difference between this model for the scatter function and the Beckmann model can have real physical significance.

Table 5-3 gives the total scattered light for some of the samples run by the University of Arizona<sup>17</sup> for the test wavelength, and for ultraviolet wavelengths of interest to the LST program. A scatter function curve we fit to the square-law portion of the King-Kormendy (K-K) star profiles is also included. The variation of the total scattered light with wavelength and surface roughness is pretty much as expected. Note that the integrated scatter for the K-K example goes above 1.0 at 121.5 nanometers, indicating that the roll-off angle is too small for that case. In fact, it is probable that this scatter function model is significantly erroneous at any wavelength shorter than 325 nanometers for this example, even neglecting that the original telescope from which the data was taken has a refracting corrector plate and may not transmit light of those wavelengths.

The total scattered light is related to the rms wavefront error for the wavefront by the equation

$$\text{TSL} = 1 - \exp [-(2\pi\omega)^2] \quad (78)$$

for small wavefront errors. (The more commonly seen form uses the first term in the series expansion of the exponential.) We can thus estimate the rms wavefront error by inverting Eq. 78

It is interesting to use Eqs. 78 and 77 to examine how the rms wavefront error varies with wavelength. In particular, it is interesting to see how the rms wavefront deviation  $\sigma_w = \omega\lambda$  varies with wavelength, as is shown in Table 5-4.

These results might be dismissed as anomalous, since one normally assumes that the surface irregularities are independent of wavelength. There is a physical explanation, however. The finest detail which can be resolved on the mirror surface is limited by the wavelength of the reflected light. Thus reducing the wavelength allows finer structure to affect the scattering function, i.e., the spatial frequency bandpass is increased. This will increase the rms deviation.

Table 5-2—Variation of Total Scattered Light With Roll-Off  
Angle,  $\alpha_0$  [ $\rho_s(\alpha_1) = 0.085$ ;  $\sin \alpha_1 = 0.10$ ;  $\lambda/\lambda_1 = 1.0$ ]

$\sin \alpha_0$	$\alpha_0$	TSL	Multiplier
$10^{-2}$	34' 23"	0.02693	1.000×
$10^{-3}$	3' 26"	0.03776	1.402×
$10^{-4}$	21"	0.04858	1.804×
$10^{-5}$	2.1"	0.05941	2.206×
$10^{-6}$	0.21"	0.07024	2.608×
$10^{-7}$	0.021"	0.08106	3.010×

Table 5-3 — Variation of Total Scattered Light With Wavelength  
and Surface Roughness ( $\sin \alpha_0 = 10^{-6}$ ;  
 $\sin \alpha_1 = 0.10$ ;  $\lambda_1 = 514.5$  nm)

Sample	236*	247*	EDF 3-11*	K-K†
$\rho_s(\alpha_1, \lambda_1)$	0.00018	0.00084	0.0143	0.085
Wavelength, nm				
514.5	0.000145	0.000694	0.0118	0.0702
325.0	0.000374	0.001793	0.0305	0.181
121.5	0.007843	0.0136	0.232	—

\* From University of Arizona data (reference 17).

† Fitted to inverse square curve of King-Kormendy data.

Table 5-4 — Variation of RMS Deviation of Wavefront,  $\sigma_w$ ,  
With Wavelength (same cases as in Table 5-3.)

Sample	236	247	EDF 3-11	K-K
Wavelength, nm				
514.5	9.84	21.6	89.3	221.0*
325.0	10.0	21.9	91.1	231.4*
121.5	10.3	22.7	99.4	—

\* Effective value, since scatter comes from several surfaces in series, plus dust, etc.

An increase in effective rms deviation due to an increase in the spatial frequency bandpass because of wavelength change is hard to detect with present measurement techniques. Integrated scatter is seldom measured over a full hemisphere from 0 to 90 degrees. Those portions of the

scattered light falling inside 1 degree are seldom considered, and as we have shown, they are of considerable significance in this model. Also, measurements of rms deviation in mirror surfaces are usually done over a very restricted spatial frequency range, due to instrumentation limitations. Even then, measurements are usually made at only one wavelength; so any variation in spatial frequency bandpass of the instrumentation would not be considered.

#### 5.4 IMAGE IRRADIANCE DUE TO SCATTERING

Use of the scatter coefficient  $\rho_s(\alpha)$  allows calculation of the image irradiance due to scattering of light from a point source in a very simple manner. Consider, for example, a parabolic mirror with a point source on its optical axis. Rays from the point source lie parallel to the optic axis, and are focused at the center point of the image plane. Any image point a distance  $h'$  from the center point is associated with object angle  $\alpha$ . A pair of rays traced from any point on the mirror to the point source image and the point at  $h'$  will be separated by the angle  $\alpha$ . Therefore,  $\alpha$  can be identified with the scatter angle, above. Thus, if  $E_a$  is the aperture irradiance due to light from the point source, then the mirror will appear to have a radiance ( $L\alpha$ ) at all points in the mirror, as seen from  $h'$ , which is given by

$$L(\alpha) = \rho_s(\alpha) E_a \quad (79)$$

If  $F$  is the focal ratio of the parabola, the image irradiance  $E_i$  at  $h'$  is given by

$$E_i(\alpha) = \pi L(\alpha)/4F^2 = \pi \rho_s(\alpha) E_a/4F^2 \quad (80)$$

Now consider the Cassegrain telescope shown in Fig. 5-15 and again assume the point source is on axis. We will also assume that both mirrors have the same specular reflectivity  $\rho$  and the same scatter function, i.e.,  $\rho_s(\beta) = \rho_s(\alpha)$  when  $\beta = \alpha$ . Scattering from the primary mirror will follow the same relationship as for the parabola above, except that the scattered light reflects off the secondary before it reaches the image. Thus the contribution from the primary mirror to the irradiance at  $h'$ ,  $E_{ip}(\alpha)$ , will be given by

$$E_{ip}(\alpha) = \pi \rho \rho_s(\alpha) E_a/4F^2 \quad (81)$$

The contribution from the secondary mirror is

$$E_{is}(\beta) = \pi \rho_s(\beta) E_p/4F^2 \quad (82)$$

(We are ignoring the effects of the central obstruction to simplify the equations.)

Simple geometry tells us that

$$E_b = \rho (D_p/D_s)^2 E_a \quad (83)$$

and the optical invariant tells us that

$$\sin \beta = (D_p/D_s) \sin \alpha \quad (84)$$

We will use Eq. 67 to define the scatter coefficient, and make the following simplifying assumptions:

$$\cos \beta \approx \cos \alpha \approx 1.0$$

$$\beta, \alpha \gg \alpha_0$$

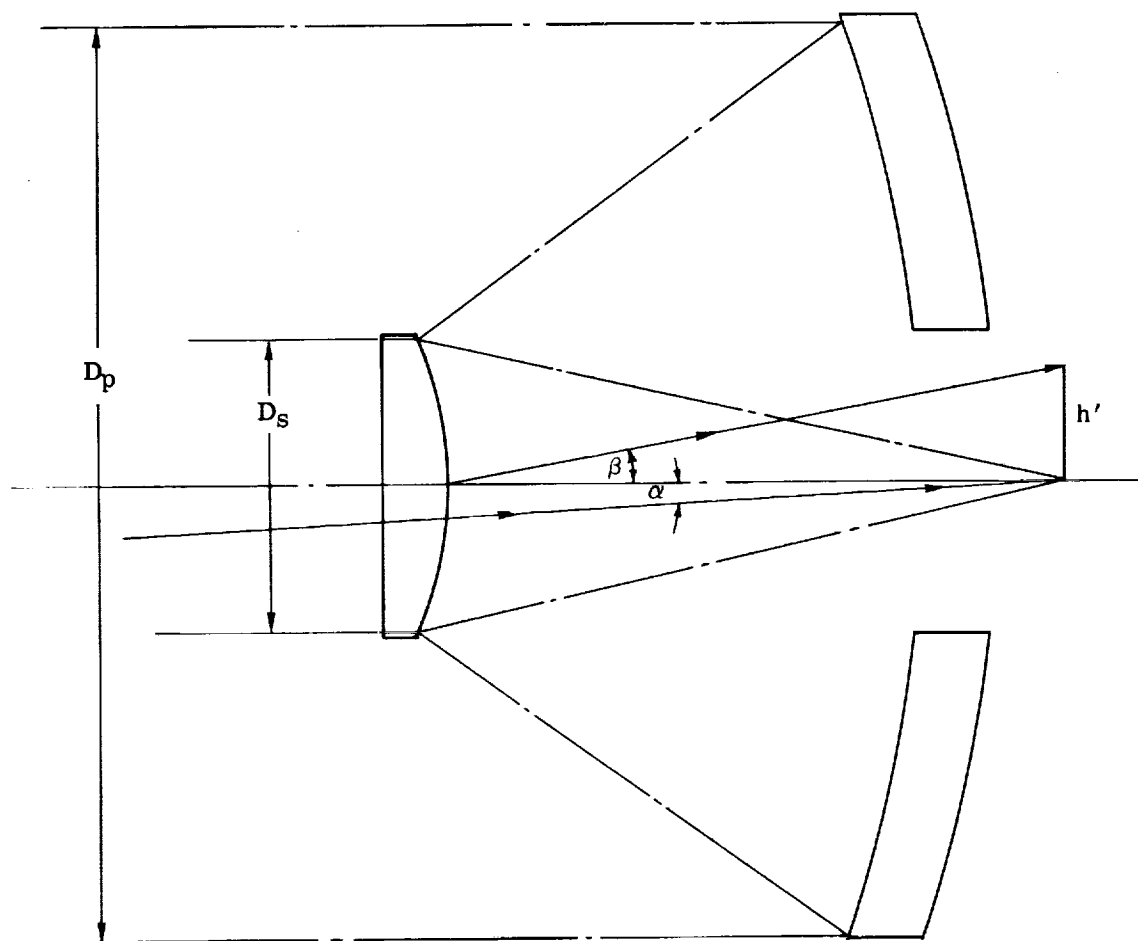


Fig. 5-15 — Cassegrain configuration for scatter calculation

From this, it follows that the scattered light contribution from the secondary is

$$E_{is}(\alpha) = \pi \rho \rho_s(\alpha) E_a (D_p/D_s)^{(2-s)}/4F^2 \quad (85)$$

Note that this differs from Eq. 80 only in the term  $(D_p/D_s)^{2-s}$ , and that if  $s = 2$ , the contributions from the two mirrors are identical. We can generalize this by saying that in an  $n$  mirror optical system, if the slope of the scatter function is 2, then

$$E_i(\alpha) = \pi n \rho^{n-1} \rho_s(\alpha) E_a / 4F^2 \quad (86)$$

If the slope  $s$  differs from 2, then the relative scatter contribution in an  $n$  mirror train depends upon the axial beam diameter at each mirror. If  $s > 2$ , the largest aperture mirrors will dominate, and if  $s < 2$ , the smallest will dominate.

## 5.5 STARLIGHT SCATTERED FROM THE PRIMARY MIRROR

One problem of special concern to astronomers is the degree to which scattered light will raise the background image irradiance. Although the actual field of view of the LST will be fairly small, less than 1 degree including the tracking field, the primary mirror will be illuminated by a much larger portion of the sky. Light from stars well outside the nominal field of view will therefore be scattered and diffracted into the field of view. The question is, will this scattered starlight add enough light to raise the effective background significantly above that due to zodiacal light and unresolved stars?

We will use a very elementary model for estimating the contribution of scattered starlight to the effective sky background. We can build a model for a star image profile similar to those of King and Kormendy using diffraction theory and the scatter model described above. Allen<sup>27</sup> provides tables of star densities according to magnitude and position in the sky. If we assume these stars are distributed on a uniform rectangular grid, we can add their star profiles at a given point to determine the effective background radiance they generate. Star profiles outside the nominal field of view can be multiplied by a vignetting factor to account for shading of the primary mirror by the telescope tube.

We have developed a computer program to do this calculation. It will be described below along with some results computed with it. A copy of this program and a user's manual are being supplied separately. First, we will develop the star profile model and compare it to the King and Kormendy models.

### 5.5.1 Star Profile Model

If the aperture irradiance from a star on the optical axis of the telescope is  $E_a$ , then diffraction theory tells us that the image irradiance at the center of the Airy disk in a perfect lens is

$$E_{ip}(0) = \pi^2 \tau D_p^2 E_a / 16 \lambda^2 F^2 \quad (87)$$

$\tau$  being the optical system transmittance, including central obstruction. (We will ignore the image spread due to the central obstruction.) An object of uniform radiance  $L$  will give an image irradiance

$$E_i = \pi \tau L / 4F^2 \quad (88)$$

By combining Eqs. 87 and 88, we can define an effective sky background radiance  $L_b(0)$  corresponding to the center of the Airy disk:

$$L_b(O) = \pi D_p^2 E_a / 4\lambda^2. \quad (89)$$

In reference 6, we defined conversion constants between  $E_a$  and its source star magnitude  $m_v$ , and between  $M_v$  magnitudes per square arc-second and  $L$ ,

$$E_a = 2.65 \times 10^{-6 + 0.4m_v} \text{ lumens/meter}^2 \quad (90)$$

$$L_p = 1.13 \times 10^{(5 - 0.4M_v)} \text{ lumens/meter}^2\text{-steradian} \quad (91)$$

If these terms are substituted into Eq. 89, the following can be shown:

$$\mathcal{M}_v(O) = 26.837 + m_v - 5 \log D_p + 5 \log \lambda \quad (92)$$

Eq. 92 defines the zero reference point in calculating the star profile model.

The average normalized irradiance in the ring structure of the Airy pattern is given by

$$E_{id}(\alpha)/E_{ip}(O) = 4\lambda^3/\pi^4 D_p^3 \alpha^3 \quad (93)$$

From Eqs. 80 and 87, neglecting  $\tau$ , we obtain

$$E_{is}(\alpha)/E_{ip}(O) = 4\rho_s(\alpha)\lambda^2/\pi D_p^2 \quad (94)$$

The sum of Eqs. 93 and 94 is the ratio of the effective radiance at  $\alpha$  to the effective radiance at the center of the pattern,  $E_i(\alpha)/E_{ip}(O)$ . Subtracting  $2.5\log[E_i(\alpha)/E_{ip}(O)]$  from Eq. 92 will give the total effective radiance at  $\alpha$ .

In completing this model by substituting Eq. 70 for the scatter coefficient, we have used several simplifications: first,  $s = 2$ ; second, we have assumed that  $\cos \alpha = 1.0$ ; third, we have neglected the scaling of  $\alpha_{01}$  with wavelength. (The latter was done inadvertently in computer programming before the wavelength scaling laws were fully analyzed. It has no effect on the results in this section, however, since  $\alpha \gg \alpha_{01}$  for virtually all examples considered, and has not been corrected in the computer program.) Eqs. 70, 93, and 94 combine to give

$$\frac{E_i(\alpha)}{E_{ip}(O)} = \frac{4\lambda^3}{\pi^4 D_p^3 \alpha^3} + \frac{4\lambda_1^2 \rho_s(\alpha_1, \lambda_1) \sin^2 \alpha_1}{\pi \cos \alpha_1 (\alpha_0^2 + \alpha^2) D_p^2} \quad (95)$$

After conversion into log units and combination of Eqs. 92 and 95, the complete star profile model becomes

$$\begin{aligned} \mathcal{M}_v(\alpha) = & 30.303 + m_v + 2.5 \log D_p + 5 \log \lambda + 7.5 \log \alpha + 2.5 \log \cos \alpha_1 \\ & + 2.5 \log (\alpha_0^2 + \alpha^2) - 2.5 \log [\lambda^3 \cos \alpha_1 (\alpha_0^2 + \alpha^2) \\ & + \pi^3 D_p \alpha^3 \lambda_1^2 \rho_s(\alpha_1, \lambda_1) \sin^2 \alpha_1] \end{aligned} \quad (96)$$

It should be pointed out that while we refer to visual magnitudes and to image irradiances in lumens per square meter in Eqs. 90 and 91, the units are cancelled by the equality 89. Thus, any form of magnitude may be used in Eq. 96, as long as  $m_v$  and  $\mathcal{M}_v$  are consistent.

Eq. 96 has been used to generate a star profile model matching that of King at large scatter angles. This is compared to the data of King and Kormendy in Fig. 5-16. King's star profile and the model agree well at angles larger than 12 arc-seconds. Since Kormendy claims that below



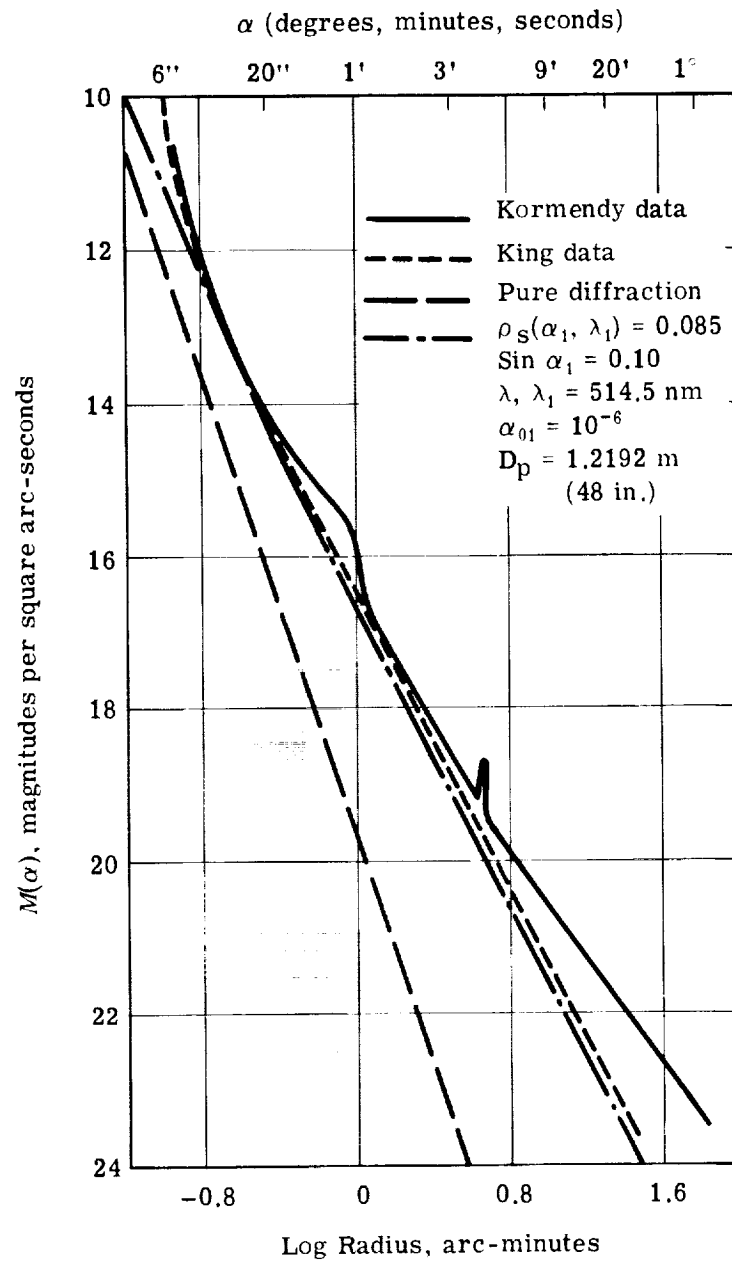


Fig. 5-16 — Star profile model of Eq. 96 compared to King/Kormendy star profiles; pure diffraction curve shown for comparison

20 arc-seconds the curve rolls up due to scattering in the emulsion in which the image is recorded, the mirror scatter model should not match the data below this angle. Eq. 96 assumes a slope of 2. We have made no attempt to match Kormendy's lower slope angle, although that could be done. Since Kormendy's curve shows variation in slope, a more complex scatter function model will be required to match it.

In Table 5-4, we showed that this model corresponds to a single scattering surface with rms deviation (on the wavefront)  $\sigma_w = 221$  Ångstroms. In reality, the Schmidt telescope is implied by Kormendy to have five optical surfaces: the primary mirror, two surfaces on the corrector plate, and at least two surfaces on the spectral filter. (We are not familiar with the telescope ourselves.) If we assume each refracting surface has the same scatter function, then the rms deviation in the wavefront added by each surface is 98 Ångstroms, as calculated through Eq. 78. This would be about 49 Ångstroms rms on a mirror surface, and considerably more than that on the refraction surfaces. This is not out of line with normal mirror finishing practices. Allowing for the presence of some dust on the surfaces, the scatter data must be considered to be of a magnitude consistent with optical surface scatter as its principal source.

We have used Eq. 96 to study the effects of varying the scatter constant  $\rho_s(\alpha_1, \lambda_1)$ , the wavelength, and the number of mirrors in the image forming train on the star profile of a zero magnitude star. The results have been plotted in Figs. 5-17, 5-18, and 5-19.  $\mathcal{M}_v(\alpha)$  is plotted versus  $\log \sin \alpha$  over angles ranging from just under 0.1 arc-second to 30 arc-minutes. All plots are for an aperture diameter of 3.0 meters, and the roll-off angle has been set to  $10^{-6}$  radian. Other parameters are identified on the figures.

Fig. 5-17 shows variation of the star profile as  $\rho_s(\alpha_1, \lambda_1)$  is varied from 0.0001 to 0.1, where  $\lambda_1 = 632.8$  nanometers and  $\sin \alpha_1 = 0.1$ . The smallest value of  $\rho_s(\alpha_1, \lambda_1)$  corresponds to a superpolished surface for which  $\sigma_w \approx 9$  Ångstroms, and the largest corresponds to a very rough surface for which  $\sigma_w \approx 300$  Ångstroms. The intermediate values correspond roughly to the normal range of surface finishes. As can be seen from the plots, the star profile for the superpolished surface differs little from a straight line over its entire length, and is in fact virtually identical to the diffraction limited profile at angles less than 1 arc-minute. The 0.01 curve shows departure from the diffraction limited profile down to under 1 arc-second, but the departures are small. Note that the diffraction limited profile is for the average of the ring structure. In this regard, it is interesting to compare Fig. 5-17 with Fig. 4-65a, which shows the corresponding plot for the simulated LST wavefront. Allowing for the 10-unit scale change in effective radiance due to the difference in  $m_v$ , the two curves do agree reasonably well.

Fig. 5-18 shows variation in the star profile as a function of wavelength. It gives profiles for  $\rho_s(\alpha_1, \lambda_1) = 0.001$  and  $\alpha_1$  and  $\lambda_1$  as before for  $\lambda = 632.8, 325$ , and 121.5 nanometers. Decreasing the wavelength reduces the diffraction profile but increases scatter. Again, it is interesting to compare these results with the simulated LST wavefront data of Section 4.8. The figures corresponding to the two shorter wavelength profiles are Figs. 4-66a and 4-67a. Again allowing for the change in  $m_v$ , we see that in these cases, the effects of ripple are pushing the PSF well above the diffraction-average of our star profile model.

Fig. 5-19 shows the effects of having more than one mirror, where the scatter constant  $\rho_s(\alpha_1, \lambda_1) = 0.01$  for the individual mirrors. These curves in effect assume that the specular reflectivity of all mirrors is 1.0, so that the effective scatter function of  $n$  mirrors is  $n$  times that of one mirror. It is also assumed that the star is in the field of view, so that all  $n$  mirrors are illuminated by it. If some of the mirrors are only partially illuminated by light from this star, the amount of scattered light must be reduced accordingly.

We have considered the effects of reducing the aperture diameter from 3.0 to 2.4 meters, but have not plotted the results. The diffraction limited part of the curve is raised by 0.24 magnitude per square arc-second, and the scatter limited end of the curve is not affected at all.

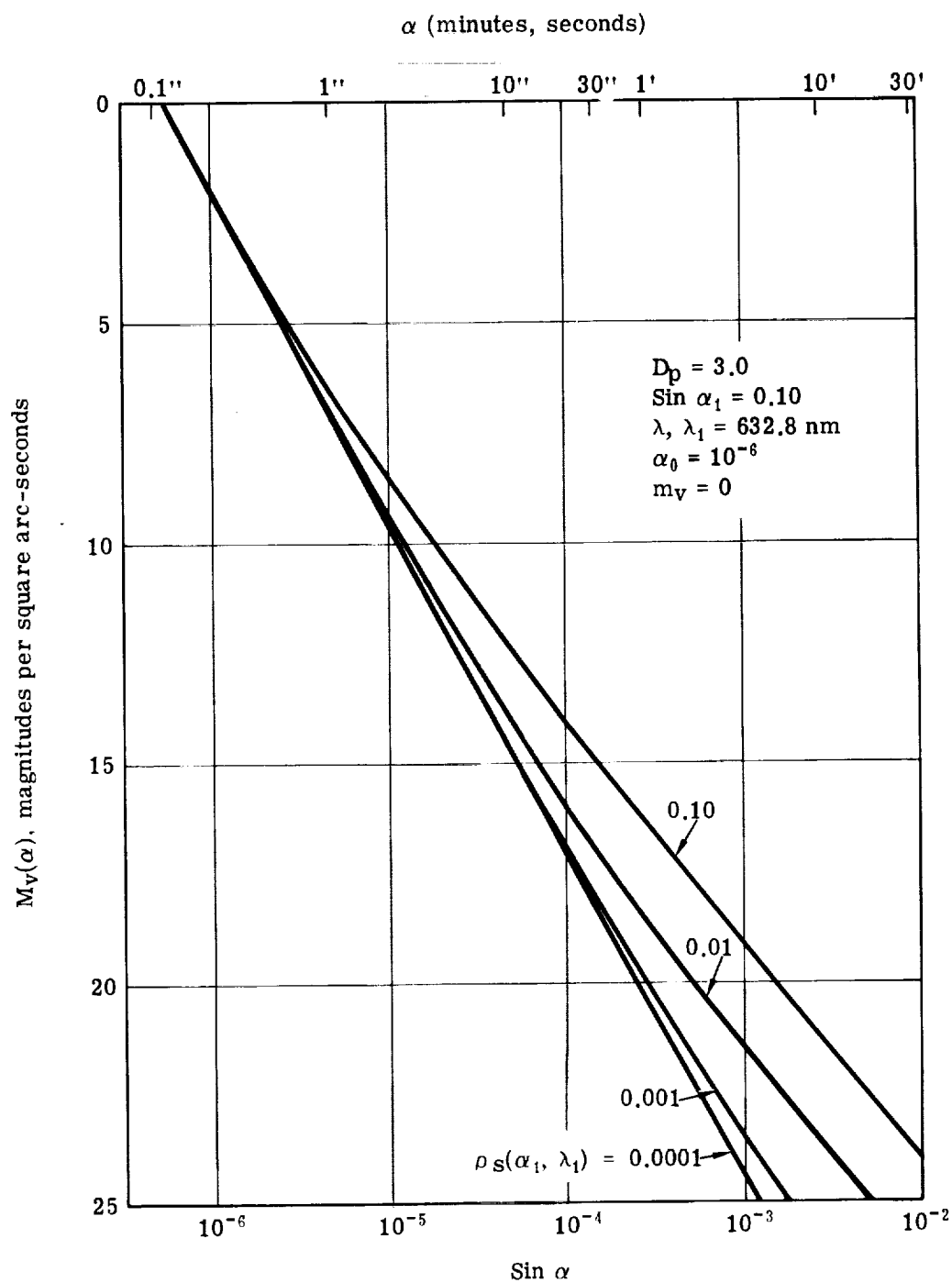


Fig. 5-17 — Variation of star profile as a function of scatter constant

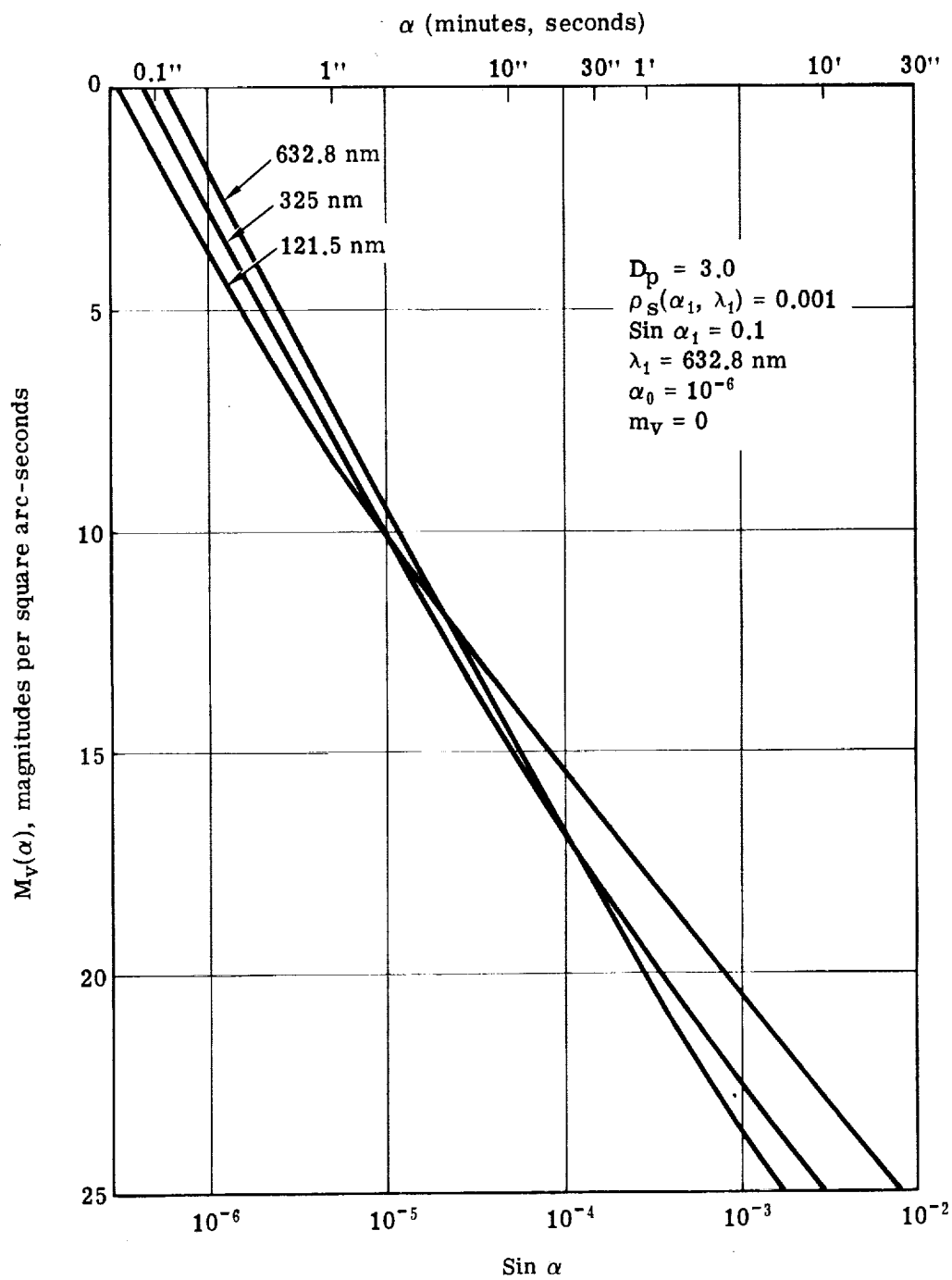


Fig. 5-18 — Variation of star profile as a function of wavelength

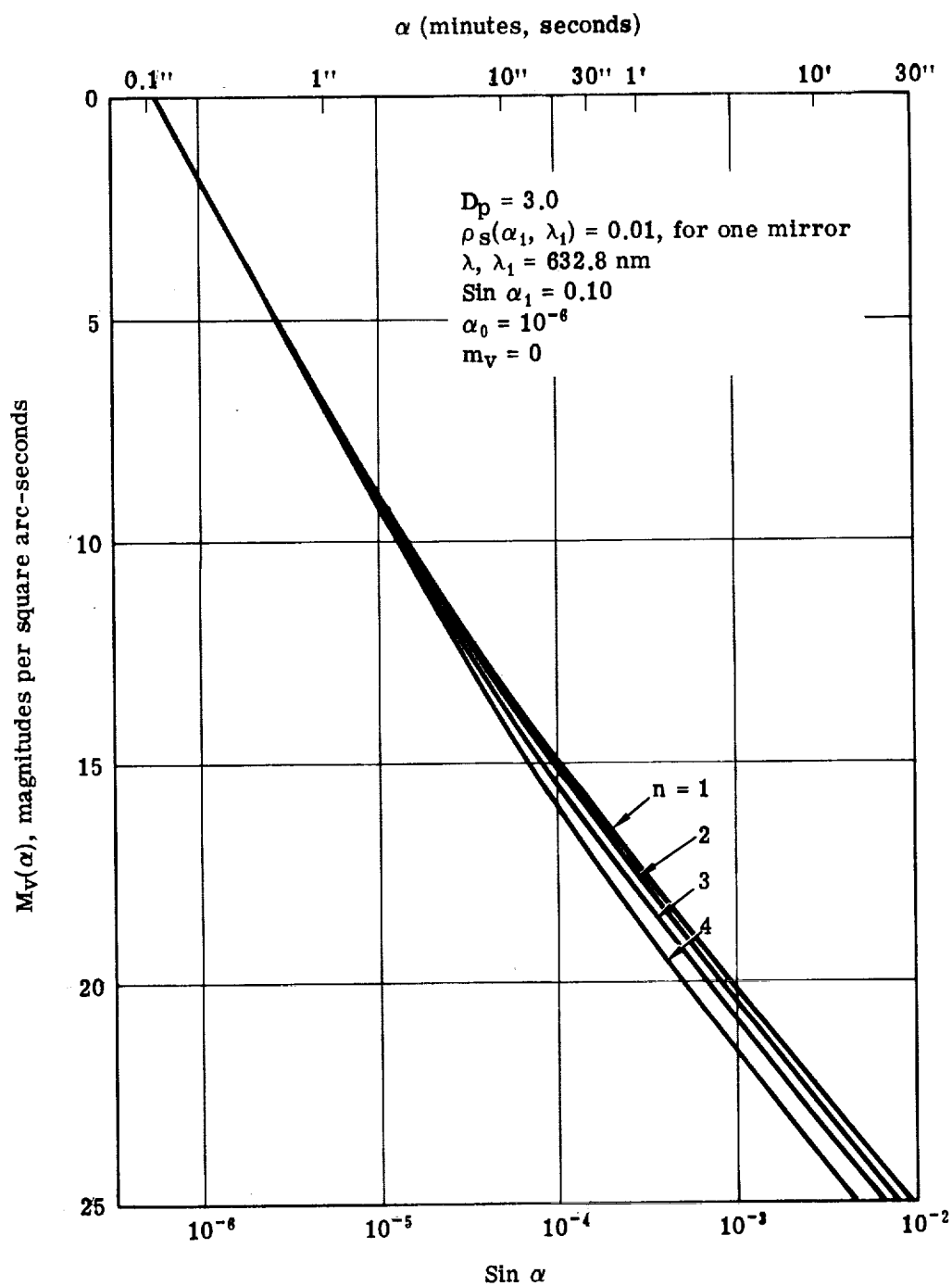


Fig. 5-19 — Variation of star profile with number of mirrors

### 5.5.2 MISCAT Computer Program Model

Eq. 96 represents the effective radiance distribution of a star image as projected back into object space. If we wish to determine the effective background radiance at a point  $(x, y)$  in the sky due to scattered light from a series of stars located at points  $(x_i, y_j)$ , we can use Eq. 96 to define the contribution of each, and sum the contributions. We need only define the angle  $\alpha_{ij}$  between the points  $(x, y)$  and  $(x_i, y_j)$ , and substitute it into Eq. 96 to compute the individual contribution. The average star spacing and number of stars involved can be estimated from tables in Allen<sup>27</sup>. The field of view over which calculations are to be made can be determined from the vignetting characteristics of the LST. We have developed a computer program, MISCAT, which calculates the effective background radiance due to scattered starlight using this model. The computation technique will be described here, and an operating manual is being supplied separately.

Eq. 96 is for an on-axis star, and must be modified to account for vignetting in the telescope for use in MISCAT. Fig. 5-20 is the telescope model used for calculating vignetting, and Fig. 5-21 shows the vignetting diagram. The user supplies the dimensions  $L, S, D_p$ , the central obstruction diameter ratio  $\epsilon$ , and the unvignetted field of view  $\theta$ , in radians. From these, the computer calculates  $D_L = D_p + L\theta$ ,  $D_s = \epsilon D_p$ ,  $d_s = \alpha S$ , and  $d_L = \alpha L$ . The transmitting area  $A$  is computed by standard formulas described in the operating manual. The vignetting factor  $W(\alpha)$  is given by

$$W(\alpha) = 4A(\alpha)/\pi(1 - \epsilon^2)D_p^2 \quad (97)$$

The reduction in the effective radiance of a star at angle  $\alpha_{ij}$ ,  $\mathcal{M}(\alpha_{ij})$ , is given by

$$\mathcal{M}(\alpha_{ij}) = -2.5 \log W(\alpha_{ij}) \quad (98)$$

Adding Eqs. 96 and 98 gives the corrected star contribution,  $\mathcal{M}_{ij}$ . Written out in full, this becomes

$$\begin{aligned} \mathcal{M}_{ij} = & 30.041 + m_v + 7.5 \log D_p + 5 \log \lambda + 2.5 \log(\cos \alpha_1) + 2.5 \log(1 - \epsilon^2) \\ & + 7.5 \log \alpha_{ij} + 2.5 \log(\alpha_0^2 + \alpha_{ij}^2) - 2.5 \log A(\alpha_{ij}) \\ & - 2.5 \log[\lambda^3 \cos \alpha_1 (\alpha_0^2 + \alpha_{ij}^2) + \pi^3 D_p \alpha_{ij}^3 \lambda_1^2 \rho_s(\alpha_1, \lambda_1) \sin \alpha_1] \end{aligned} \quad (99)$$

To compute the total scattered light, we must define the coordinates of each star and the total number of stars. The maximum possible number of stars is limited by the field of view boundary at which  $W(\alpha) = 0$  (or an arbitrarily chosen fraction larger than 0). We can determine the number of stars of a given magnitude lying within this boundary from Allen's tables of star densities at different galactic coordinates.

The model starfield we use is illustrated in Fig. 5-22. The point at which we compute effective scatter radiance is on the axis of the telescope, at coordinates  $(0, 0)$ . The stars are distributed on a rectangular grid with the spacing of  $a$ , in radians. If  $N_k$  is the number of stars per square degree of magnitude  $m_k$ , the spacing is given by

$$a = 0.01745 N_k^{-1/2} \quad (100)$$

then

$$x_i = (i - 0.5)a; y_j = (j - 0.5)a \quad (101)$$

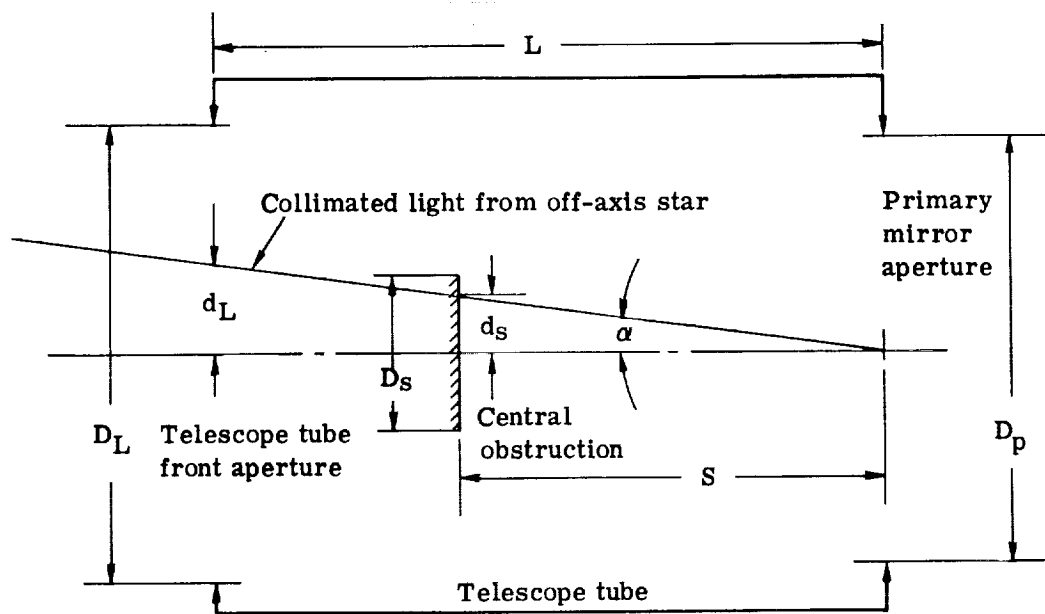


Fig. 5-20 — Telescope model for computing vignetting factor when star is off-axis an angle  $\alpha$

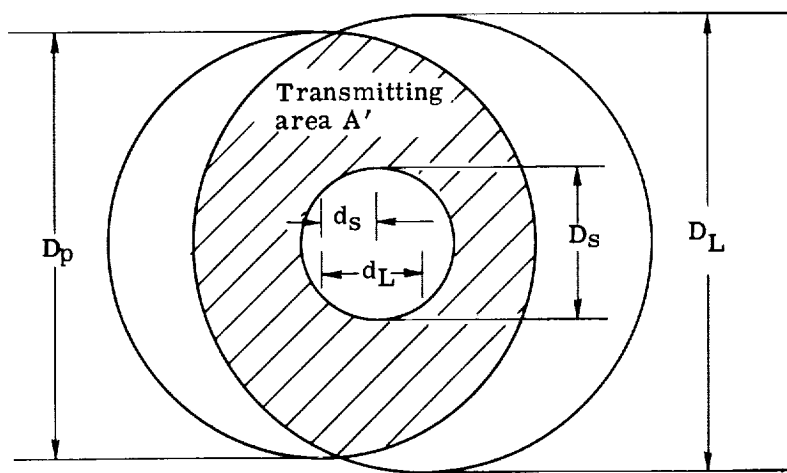


Fig. 5-21 — Vignetting pattern



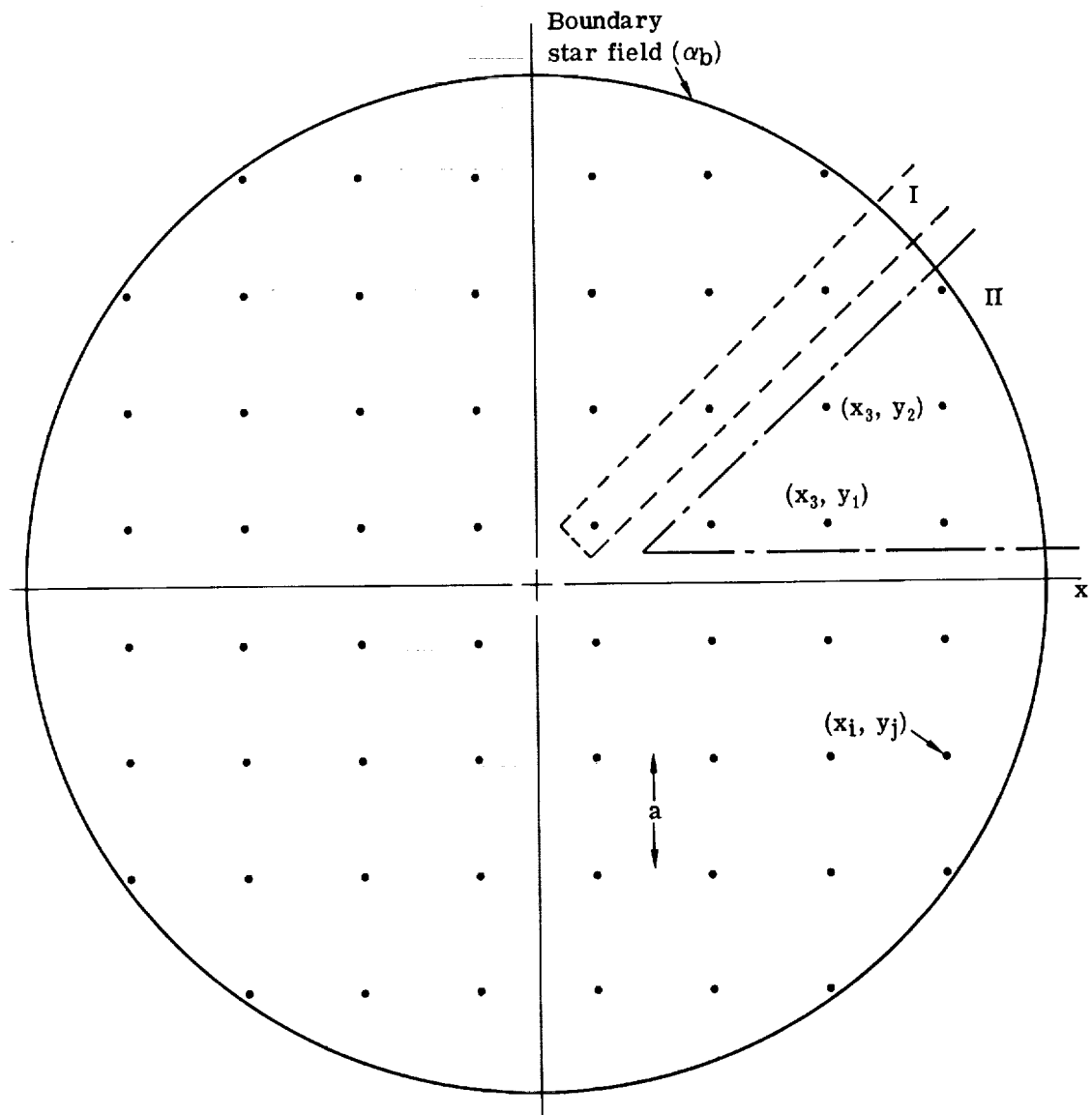


Fig. 5-22 — Star matrix and starfield boundary for calculating contribution of each star to scattered starlight background

and

$$\alpha_{ij} = \sqrt{x_i^2 + y_j^2} \quad (102)$$

These values are substituted into Eq. 99, and the total effective radiance  $\mathcal{M}_T$  is calculated by the summation

$$\mathcal{M}_T = -2.5 \log \left[ \sum_{\alpha_b} 10^{-0.4 \mathcal{M}_{ij}} \right] \quad (103)$$

where  $\alpha_b$  marks the domain of the summation boundary. The number of calculations can be reduced somewhat by taking advantage of symmetry. In Fig. 5-22, note that there are two different star groups: group I repeats itself 4 times, and group II 8 times.

Input to the computer program includes: the telescope parameters defined above, the constants defining the scatter function, the base wavelength at which calculations are to be made, and a table of star magnitudes and population densities. As an output, the user receives a table showing the background contribution for each star magnitude plus the total contribution from all input stars. Further description of the program will be found in the operation manual.

### 5.5.3 MISCAT Results

Several sets of computations have been run with MISCAT to test the program, and to see which design parameters most strongly affect the level of scattered starlight. Table 5-5 gives the stellar population statistics for the galactic equator, which represents the most populous sky background the LST will have to view. This data was used in all MISCAT runs described here. The nominal telescope design parameters used were  $D_p = 3.0$  meters,  $L = 13.2$  meters,  $S = 6.39$  meters,  $\epsilon = 0.32$ , and  $\theta = 0.008$  radian. The nominal scatter function parameters were  $\alpha_1 = 0.1$ ,  $\lambda = \lambda_1 = 514.5$  nanometers,  $\rho_s(\alpha_1, \lambda_1) = 0.01$ , and  $\alpha_0 = 10^{-5}$ . These values should be assumed except where otherwise indicated.

In Table 5-6, we show the effects of varying  $\rho_s(\alpha_1, \lambda_1)$  and  $\alpha_0$ . As expected, varying the scatter coefficient does affect the background contribution significantly, although not as strongly as expected. Thus, a change of 100× in the scatter coefficient has changed the background contribution by roughly 50 to 60×. Change in  $\alpha_0$  has very little effect.

Table 5-7 shows that changing the tube length has little effect on the amount of scattered starlight. This signifies that only the stars nearest the field of view are contributing significant amounts of scattered starlight to the background. (Note that stray sunlight and earthlight scattered off the inside walls of the telescope tube are strongly affected by tube length.)

Table 5-8 shows that changing wavelength strongly affects the amount of scattered starlight. Here one has to be careful of how magnitude is defined. No attempt has been made to consider spectral characteristics of the stars involved in the population data of Table 5-5, only that  $\mathcal{M}_T$  will be consistent with the units of  $m_k$ .

In evaluating these results, it should be noted that the darkest sky background expected from the LST is on the order of  $\mathcal{M}_v = 23.5$  magnitudes per square arc-second. Of all the background contribution values shown here, the only one approaching that is for  $\rho_s(\alpha_1, \lambda_1) = 0.1$ ,  $\lambda = 121.5$ . This is an example which should be far worse than will ever be encountered with the LST. It should be pointed out that the data in Tables 5-6 through 5-8 represents additions to the background, and that  $\mathcal{M}_T = 25$ , for example, will increase the background total from 23.5 to 23.3. This is not a significant increase, however. Thus, this data leads us to conclude that if our scatter function model is correct, scattered starlight from the primary mirror will not be a

significant factor in determining the effective sky background radiance, if the primary mirror has a normally smooth finish. Superpolishing is therefore not necessary for reasons of controlling scattered starlight.

This data indicates that scattered light from stars outside the field of view should not be a problem even in the worst situation, when viewing the Galactic equator. For this reason, we have not completed calculations for the best situation, viewing the Galactic poles.

Table 5-5—Stellar Population Density  
at Galactic Equator (stars per square degree)  
(Allen<sup>27</sup>, page 234)

$m_k$	$N_k$
4	0.0178
5	0.0525
6	0.1514
7	0.4074
8	1.122
9	3.31
10	9.33
11	26.92
12	75.86
13	199.53
14	524.81
15	1,318.
16	2,512.
17	6,760.
18	15,849.
19	31,622.
20	50,119.
21	100,000.

Table 5-6— $\mathcal{M}_T$  as a Function of  $\rho_s$  and  $\alpha_0$   
at Galactic Equator (magnitude per square second)

$\alpha_0$	$\rho_s$		
	0.001	0.01	0.1
0.00001	30.46	28.55	26.14
0.0001	30.49	—	26.20
0.001	30.64	—	26.50
0.01	30.93	—	26.29

Table 5-7— $\mathcal{M}_T$  as a Function of L at Galactic Equator  
(magnitude per square second)

L, meters	10	13.2	15	20
T	28.52	28.55	28.57	28.61

Table 5-8— $\mathcal{M}_T$  as a Function of Wavelength at  
Galactic Equator (magnitude per square second)

$\rho_s$	$\lambda$ , nm		
	514.5	325	121.5
0.01	28.55	27.62	25.51
0.1	26.14	25.15	23.01

## 6. EFFECTS OF MIRROR SURFACE COATINGS

In the LST, the mirror substrates will be coated with a thin layer of aluminum to give high reflectivity over the maximum possible spectral range. This coating will have a thin protective overcoating, probably of magnesium fluoride. It is legitimate to ask whether or not these coatings will contribute significantly to the magnitude of the scatter coefficient. Unfortunately, there is little concrete data from which one can draw quantitative answers to that question.

In general, it is assumed that the aluminum and  $\text{MgF}_2$  coatings will neither add to nor smooth out the surface roughness of the mirror substrate, but will reproduce it substantially intact. We have discussed this subject with Dr. J. Stanford of the Michelson Laboratory, Naval Weapons Center, China Lake, California. He feels that current data supports this theory. Normal scattering theory, therefore, predicts that these coatings will have no significant effect on scattering, provided a competent job has been done in laying down the coatings.

There is one effect which can be attributed to the aluminum film, when coupled with the surface roughness of the mirror substrate, which is not explained by scalar scattering models. At wavelengths in the vicinity of  $1300 \text{ \AA}$ , the reflectivity of roughened aluminum surfaces is reduced by surface plasmon coupling, which causes absorption of the incident radiation. The principal reference of interest is a paper by Endriz and Spicer,<sup>28</sup> who have produced the data shown in Fig. 6-1. This data may indicate that a very smooth surface should be required for the LST mirrors on the basis of system transmittance considerations alone. There is reason to believe that this data is pessimistic, however, and does not apply to polished mirror substrates.

We are not in a position to do detailed research on surface plasmon effects. Our current understanding has been developed through the cited reference and other literature, and through discussions with J. M. Elson and J. Stanford of Michelson Laboratory. Mr. Elson has worked with Ritchie<sup>29</sup> at Oak Ridge, and is one of the leading authorities on surface plasmon effects. He is familiar with the work of Endriz and Spicer cited above, and has explained why it should be considered pessimistic.

The principal reason for suspecting the data to be inapplicable in our case is that the roughened surfaces were not a product of substrate polishing. The aluminum coating was layed down on top of an undercoating made rough by crystallization in the coating process. It is suspected that the spatial frequency distribution of the surface irregularities in this coating is quite different from what can be expected in polished mirrors, and that the differences are such as to make the plasmon coupling more effective. It is believed that the effects shown in Fig. 6-1 may be pessimistic by an order of magnitude, perhaps more.

At present, there are too many unanswered questions to say anything conclusive about surface plasmon coupling and how it will affect ultraviolet performance in the LST. It is known that the surface plasmon coupling is dependent in part on the spatial frequency distribution of the surface

irregularities, but the exact nature of the dependency is not known; nor is there adequate data as to the spatial frequency distribution of surface irregularities in polished glass substrates.

Most of the light absorbed in the surface plasmon coupling is reradiated, but again there is little measured data available. The reradiation pattern will be dependent upon the spatial frequency distribution of the mirror surface irregularities, it is believed. The nature of the pattern is not known, but it is presumed that the distribution will be neither specular nor Lambertian. There is a directional effect in mirrors that are overcoated to give enhanced reflectivity at a wavelength where the plasmon coupling is strong. In this case, there is some peaking (a 50 percent increase) of the reradiation at angles where the coating reflectance is enhanced<sup>22</sup>. This is not expected to be a problem with the LST, where the protective  $\text{MgF}_2$  coating is quite thin. It is expected that the reradiation pattern for the LST mirrors will be more nearly diffuse. If this is indeed the case, it should contribute little to the background image irradiance. This remains to be proven, however.

We expect to see new data on the surface plasmon effect in the near future. Dr. Stanford has begun a new series of ultraviolet reflectance and scattering measurements on platinum and aluminum. He has been associated with modifications to the synchrotron facility at Stanford University. Intense synchrotron radiation is emitted between 350 and 3100 Å, the range over which he is making measurements. This unique light source is free of many of the experimental problems that affect most far-ultraviolet measurements, and should give some of the best data ever obtained for ultraviolet scattering. This should be of considerable help in evaluating the effects of surface plasmon coupling. In addition, surface plasmon theory is advancing rapidly for other applications, so the analysis and interpretation of results should be improved.

In brief, surface plasmon effects will certainly be present in the LST mirrors at certain wavelengths in the ultraviolet. While earlier evidence made this appear to be a particularly severe problem, current thinking has downplayed its significance. Conclusive quantitative data is still lacking, but the area is being studied actively. We recommend that the subject be reanalyzed when better data and better theory become available.

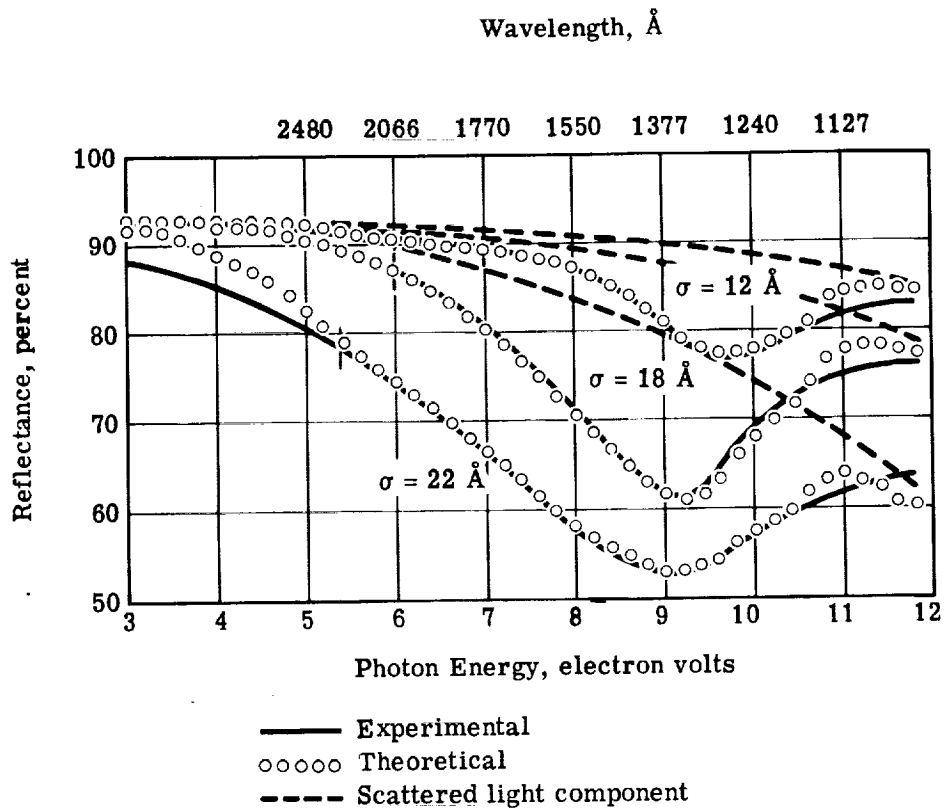


Fig. 6-1 — Effect of surface roughness on aluminum reflectivity (after Endriz and Spicer)





## 7. FUTURE EXPERIMENTAL MEASUREMENTS PROGRAM

All of the foregoing analysis is based on extrapolation of existing measurements of wide angle scattering and on large spatial frequency figure errors in mirror surfaces. Hard data on the shape of the point spread function between a few Airy radii and about 1 degree does not exist, nor does hard data exist on the heights and spatial frequency distribution of mirror surface irregularities associated with scattering at these angles. The King/Kormendy star profiles and wavelength extrapolations of infrared scatter measurements suggest that our wide angle scatter function model is reasonable to a minute of arc or less, but below that no data exists which is directly applicable to LST. There is also little data concerning the scatter contributions we should expect from dust and mirror surface contamination. Further experimental measurements programs are needed in these areas.

Two areas of experimentation are necessary, direct measurement of scattering from astronomical grade mirrors, and measurements of the surface irregularities on those mirrors. Preferably, the same mirrors should be used for both types of experiments so that the distribution of scattered light can be related directly to the spatial frequency distribution of mirror surface irregularities. In this section, we will discuss the requirements for both types of measurements. Emphasis will be placed on the type of data required more than on details of experimental technique, except in certain aspects of the center of curvature scatter experiment.

### 7.1 MEASUREMENT OF SCATTERED LIGHT

Three basic problems make scattering measurements at small angles very difficult. First, and most difficult, is the problem of experimental setup: illuminating a large enough area to cause scattering at the small angles desired, and getting close enough to the specularly reflected beam to measure the scattered light. Second, eliminating other scatter sources from the apparatus. The addition of other optical elements to control the first problem introduces additional scatter surfaces, which must be accounted for in data reduction. Third, the scatter component we wish to measure can be quite low compared to pupil diffraction, as illustrated in Fig. 5-17. Separating scatter from diffraction will therefore be difficult in many types of experiments.

The first two problems can be eliminated by measuring the scatter function for a spherical mirror from its center of curvature, as described below. The spherical mirror is both the scatter source and focusing optics, eliminating all other optical components between the point source pinhole and the sensor aperture. Pupil diffraction can be controlled by apodization, as mentioned in Section 4.5, allowing scattered light to be measured at very small angles. This gain is purchased by a loss in other aspects of the experiment, however. There is no possibility of an A-B comparison of the light beam with and without the scatter surface, since it is an intimate part of the focusing optics. We will discuss these problems in Section 7.1.1.

An alternate approach is suggested by the results plotted in Fig. 5-14: multiple wavelength scatter measurements. We can estimate the scatter of, say, 0.5-micrometer radiation at 3 minutes

of arc by measuring the scatter of 10-micrometer radiation at 1 degree. Such measurements could be done with a number of existing experimental setups, which makes this approach attractive. Some of the advantages and disadvantages of this approach will be discussed in Section 7.1.2.

### 7.1.1 Center of Curvature Scatter Experiment

The basis of the center of curvature scatter experiment is illustrated in Fig. 7-1. A spherical mirror images its center of curvature with perfect fidelity. If we place an illuminated pinhole to one side of the center of curvature of the mirror, it will be reimaged perfectly at a point equidistant from the center of curvature and directly opposite the object pinhole. The image point will be spread out by pupil diffraction plus scattering due to mirror surface irregularities. This pattern can be scanned with a pinhole photometer to measure the diffraction and scatter components. The only optical component between pinhole light source and pinhole photometer besides the spherical mirror is air, and that can be eliminated by running the test in a vacuum chamber if necessary. There is no fundamental limitation on the diameter of the spherical mirror except cost and availability, so scatter measurements could be made at very small angles.

There are two important limitations on the experiment, however. The measurements must be compared to theory, since there is no means of removing the scatter surface without also removing the focusing surface. Secondly, as shown in Fig. 5-17, the scattered light will be masked by diffracted light at small angles for all but the roughest mirror surfaces, if that scatter function model is correct. Thus very careful control of the experimental parameters will be necessary, and data reduction will be complicated.

In Section 4.5, it was shown that changing the pupil illumination pattern from flat to a Gaussian function of the distance from the center of the pupil will suppress pupil diffraction without affecting scatter due to diffraction by wavefront irregularities. Apodization of this type would serve several useful functions in the scatter measurements experiment. First, it would allow measurement of the scatter function to within several Airy radii of the center of the pattern. Second, comparison between measurements with the Gaussian pattern might serve the function of an A-B test, reducing somewhat the difficulties of direct comparison to theory. Third, apodization concentrates all light except the scattered light within the central maximum, to a good approximation. Thus, measuring the amount of light in the central maximum and comparing it to the amount of light striking the mirror will give the total scattered light from a few Airy radii to 90 degrees.

The latter task has some obvious experimental problems as well: it is necessary to map the illumination pattern of the mirror accurately, and to discount absorption by the aluminum coating. If these problems can be overcome, however, the technique should give a far truer measure of the total scattered light than the usual integration sphere measurements, which usually don't measure the scatter component within a degree or so of specular.

The experimental problem now is to generate the Gaussian apodization function in the illumination pattern. Two closely related techniques for doing this have been suggested by Adrian Walther and Roland Shack in personal discussions. Both rely on the filtering technique illustrated in Fig. 7-2. This shows a light distribution filter formed by an absorbing medium sandwiched between a flat glass plate and a convex spherical lens. The transmittance  $\tau(y)$  of the absorbing medium at height  $y$  above the centerline is given by

$$\tau(y) = \exp(-\alpha_c t) \quad (104)$$

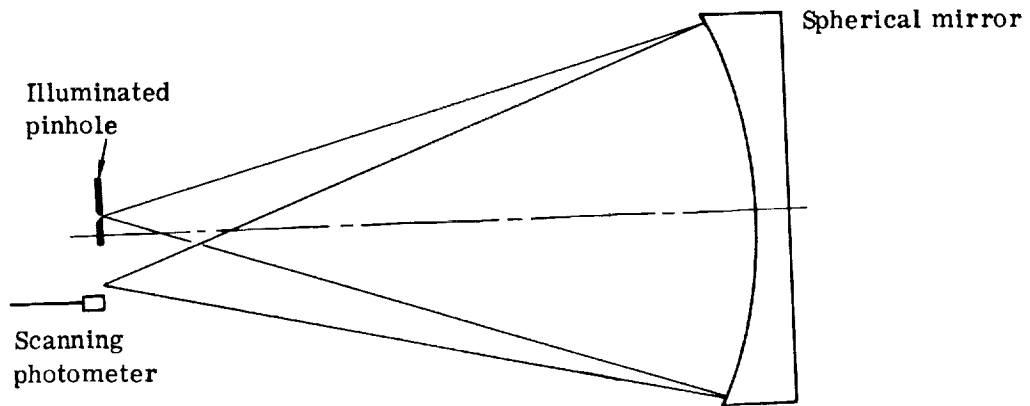


Fig. 7-1 — Basic center of curvature scatter measurement experiment

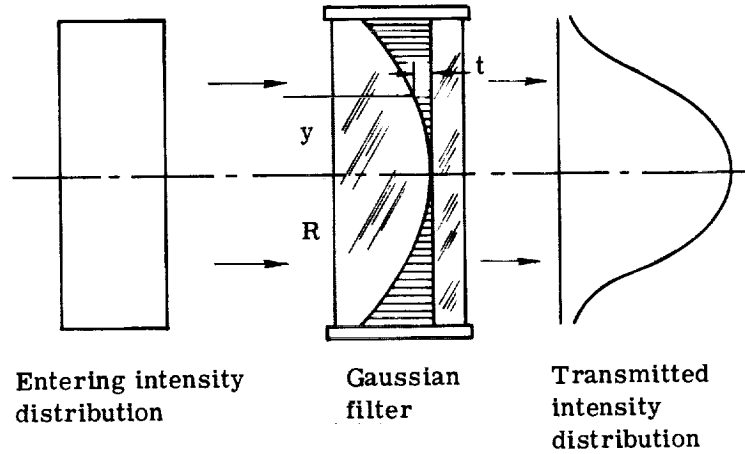


Fig. 7-2 — Filter for producing Gaussian intensity distribution

where  $\alpha_c$  is the absorption constant and  $t$  is the thickness of the absorbing medium. But if the radius of curvature of the spherical surface is  $R \gg y$ , the  $t = y^2/2R$ , to a sufficient approximation. Thus

$$\tau(y) = \exp(-\alpha_c y^2/2R), \quad (105)$$

which is a Gaussian function of  $y$ .

The suggested techniques for incorporating this effect into the center of curvature scatter experiment are illustrated in Fig. 7-3. A. Walther suggests a large cell followed by a focusing lens, with a truncating pinhole being necessary to eliminate any scattering from the lens. R. Shack suggests a Gaussian pinhole formed by a very small sphere sandwiched between two flat glass plates. The absorbing medium could be a solid in the first case, but must be a liquid in the second. The latter is probably preferable in either case, since it might eliminate speckle problems with a laser light source, and since in any case it allows control of the width of the Gaussian profile by diluting the absorbing medium or making it more concentrated.

The center of curvature technique as described here can be applied only to spherical mirrors, if other scattering surfaces are not to be added. It could be used as the basis for an A-B type comparison for a large folding flat. In this case, one would compare the scatter function of the sphere to the combined scatter function of the two mirrors used in double pass. It is also possible to do a center of curvature test on large concave mirrors with the aid of a null lens, if scattering in the null lens can be discounted in data reduction. The fact that the null lens optical surfaces are close to the focus of the system should help. Perhaps one of the more important experiments to be run on spherical mirrors is to insert refracting elements near the focus to test whether scatter measurements can be made on parabolas during fabrication using this technique.

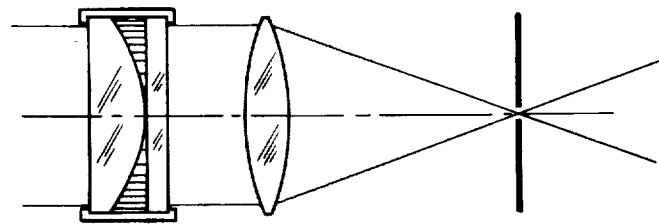
We feel that the center of curvature scatter experiment represents the most powerful technique for measuring scatter at very small angles of any presently suggested. We recommend that it be pursued further.

### 7.1.2 Multiple Wavelength Scatter Measurements

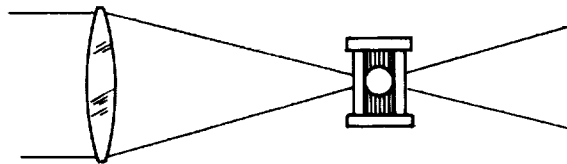
While it is difficult to make scatter measurements at angles well under 1 degree, scatter measurements are routinely made at angles of 1 degree and greater by a number of workers<sup>17,20,22,26</sup> at a variety of wavelengths. We have shown in Fig. 5-14 how scatter measurements of 10.6-micrometer radiation at 1 degree can be scaled to give visible light scatter data at 3 arc-minutes. In principle, then, one can build up narrow angle scatter data at short wavelengths by making wide angle scatter measurements at longer wavelengths.

This approach to narrow angle scatter measurements has several advantages. First, it can be done with equipment which already exists in a number of laboratories. Second, it gives a method of detecting at least some instrumentation difficulties. Most scatter measurements we have seen show the scatter functions measured to roll upward at small angles. In at least one instance,<sup>17</sup> this was a result of instrumentation problems, and not a real effect. A scatter measurement series run with, say, 1.6-micrometer radiation and scaled to 0.5 micrometer would overlap data taken at the latter wavelength, but with the angle scale shifted downward by a factor of  $1/3.2\times$ . This should reveal any angle dependent instrumentation problems and allow data to be corrected for them.

The wavelength scaling rules demonstrated in Fig. 5-14 are an inherent property of the "spectrum of plane waves" scatter model, which attributes scattering to the geometry of the wavefront irregularities introduced by reflection off the mirror. If the scattering process can legitimately be represented as diffraction by a series of cosine phase gratings of different spatial frequency and phase amplitude, these wavelength scaling rules will be valid. Thus if we take



(a) Walther Gaussian pinhole



(b) Shack Gaussian pinhole

Fig. 7-3 — Techniques for producing Gaussian pinholes

scatter data at a series of wavelengths, and find that after scaling there are discrepancies which cannot be explained by instrumentation errors, then this is evidence that other scatter mechanisms are involved.

There are both advantages and disadvantages to the latter aspect of wavelength scaling. The advantage is that it may aid in defining spectral regions where other scatter mechanisms predominate. The disadvantage is that wavelength scaling of this nature may not be applicable in wavelength regions where nonscalar scatter mechanisms are suspected. In particular, it seems likely that this is true in regions of the ultraviolet where surface plasmon coupling changes reflectivity characteristics.

We feel that coordinated scatter measurements at a number of wavelengths with subsequent wavelength scaling of the results would be a useful experiment to perform, both in terms of improving our understanding of the scatter mechanism, and in terms of extending (with relatively little expense) the angular domain over which visible and near ultraviolet scatter coefficients are known. A series of scatter measurements should be made on the same mirror samples at a series of wavelengths. The wavelengths should run from 10.6 micrometers in the infrared to as short a wavelength in the visible and near ultraviolet as possible. The wavelengths should be spaced apart no more than a factor of 2 to 4 in wavelength to maximize overlap of data in angle space. (This would require the addition of measurements somewhere in the range of 3 to 5 micrometers.) The range of angles over which scatter measurements are made at each wavelength should be maximized for the same reason.

## 7.2 SURFACE IRREGULARITY MEASUREMENTS

In discussing surface irregularity measurements here, we will confine ourselves primarily to discussing what should be measured, rather than techniques for making the measurements. Dr. James Wyant of the University of Arizona Optical Sciences Center has prepared a survey of current measurement techniques and their limitations, which we include as Appendix B of this report. (This was prepared under a consulting agreement on NASA contract NAS8-29949. We include it here to avoid any unnecessary duplication of effort in this section.) Dr. Wyant's memo will be referenced where called for.

In our consideration of the relationship between surface irregularities and the scattering they cause, it is clear that there are two areas of study in which data is not available. First, there are no surface height profiles with lateral resolutions in the range of a few micrometers to tens of centimeters. Second, where height profiles have been taken, no attempt has been made (or at least none published) to compute the spatial frequency spectra of the surface irregularities. Instead, rms deviations are measured or estimated, and used in statistical models which assume certain spatial frequency distributions. As we have tried to demonstrate in Section 5, the most commonly used assumption in this regard, which gives the Gaussian autocorrelation function, is wrong.

The lateral resolution problem is best illustrated by Table 7-1. The spectrum of phase gratings model for scattering by surface irregularities shows that the scatter angle  $\alpha$  is related to the period  $d$  of the phase grating by the grating equation

$$\sin \alpha = \pm \lambda/d \quad (106)$$

for normal incidence. Thus, if we are interested in investigating surface irregularities associated with scatter angles from 1 arc-second out to a few degrees at wavelengths in the visible and ultraviolet, we must be able to resolve spatial frequencies with periods in the range indicated in Table 7-1.

Table 7-1 — Period d of Phase Grating Associated  
With Scatter Angle  $\alpha$  and Wavelength  $\lambda$

Scatter Angle, $\alpha$	Wavelength ( $\lambda$ ), nanometers		
	632.8	325.0	121.5
1"	130.52mm	67.04mm	25.06mm
3"	43.51mm	22.35mm	8.35mm
10"	13.05mm	6.70mm	2.51mm
30"	4.35mm	2.24mm	835.4 $\mu$ m
1'	2.18mm	1.12mm	417.7 $\mu$ m
3'	725.1 $\mu$ m	372.4 $\mu$ m	139.2 $\mu$ m
10'	217.5 $\mu$ m	111.7 $\mu$ m	41.77 $\mu$ m
30'	72.51 $\mu$ m	37.24 $\mu$ m	13.92 $\mu$ m
1°	36.26 $\mu$ m	18.62 $\mu$ m	6.96 $\mu$ m
3°	12.09 $\mu$ m	6.21 $\mu$ m	2.32 $\mu$ m
10°	3.64 $\mu$ m	1.87 $\mu$ m	0.700 $\mu$ m
30°	1.27 $\mu$ m	0.650 $\mu$ m	0.243 $\mu$ m
90°	0.633 $\mu$ m	0.325 $\mu$ m	0.122 $\mu$ m

It is clear that the range of resolutions involved is too great to be handled by an single measurement technique. Dr. Wyant has pointed out that most measurement techniques have resolutions which are not much greater than 500 elements across a field of view. For the finest resolutions involved, it is clear that one must sample areas of a mirror rather than measure its entire area, at least for LST size mirrors. We will therefore not recommend pursuit of any specific measurement technique, except to point out that some of the tests, such as the Lyot test, are readily adapted to the type of experimental setup used for the center of curvature scatter experiment. These might therefore be considered to be logical companion experiments.

We feel that three aspects should be stressed in future measurements programs. First, the spatial resolution range should be expanded to include the domain between figure error and surface microstructure. In LST terms, this covers the range from perhaps 15 centimeters down to well below 1 millimeter. Second, Fourier transforms of the surface height distributions should be performed so that spatial frequency distributions can be measured. Third, programs which coordinate scatter measurements with surface irregularity measurements and rms deviation calculations should make sure that the spatial frequency bandpass on the surface measurements include only those spatial frequencies appropriate to the range of angles over which scatter coefficients are being measured.





## 8. REFERENCES

1. Ratcliffe, J. A., "Some Aspects of Diffraction Theory and Their Application to the Ionosphere", Reports on Progress in Physics, XIX, 188 (1956).
2. Barakat, R., and Houston, A., Appl. Opt., 5K1850 (1966).
3. Jaquinot P., and Roizen-Dossier, B., "Progress in Optics", Vol. III, E. Wolf, ed., North-Holland/Wiley, 1964, pp. 31-186.
4. Brown, D. S., J. of Sci. Inst., 32:137 (1955).
5. Brown, D. S., "The Computer Assisted Figuring of Large Mirrors", Proceedings of the ESO/CERN Conference on Large Telescope Design, March 1-5 (1971).
6. Itek Corporation, Large Space Telescope: Image Quality Analysis, Final Report, NASA Contract NASw-2313, rev. 4 Dec 1973.
7. O'Neill, E. L., "Introduction to Statistical Optics", Addison-Wesley, Reading, Mass., 1963.
8. Schwesinger, G., Optik, 34:553 (1972) (See Appendix A for translation).
9. Lee, Y. W., "Statistical Theory of Communication", John Wiley & Sons, New York, 1960, p. 39 (Eqs. 153 and 154).
10. Fried, D. L., and Cloud, J. D., J. Opt. Soc. Am., 56:1667 (1966).
11. Whalen, A. D., "Detection of Signals in Noise", Academic Press, Chapter 2, 1971.
12. Barakat, R., Optica Acta, 18:683 (1971).
13. Barakat, R., and Blackman, E., Optica Acta, 20:901 (1973).
14. Nicholson, D. S., "Estimating Optical System Performance from a Statistical Description of Its Probable Manufacturing Errors", delivered at SPIE Annual Meeting, Aug. 1974, and to appear in a "Proceedings" volume.
15. King, I. R., Pub. Astron. Soc. Pac., 83:199 (1971).
16. Kormendy, J., Astron. J., 78:255 (1973).
17. Shack, R., and DeBell, M., Surface Scatter Study, Final Report, Contract no. FO4701-72-C-0181, University of Arizona Optical Sciences Center.
18. Beckmann, P., and Spizzichino, A., "The Scattering of Electromagnetic Waves from Rough Surfaces", Pergamon Press, New York, 1963.
19. Beckmann, P., "Progress in Optics", Vol. VI, E. Wolf, ed. John Wiley & Sons, New York, 1967, p. 55.
20. Smith, T. F., and Hering, R. G., Surface Roughness Effects on Bidirectional Reflectance, Final Report on Contract No. 951661 from Jet Propulsion Laboratories, California Institute of Technology. Technical Report No. ME-TR-661-2, University of Illinois at Urbana, June 1972.
21. Bennett, H. E., and Porteus, J. O., J. Opt. Soc. Am., 51:123 (1961).
22. Bennett, H. E., et. al., "Scattering from Mirror Surfaces used in Space Applications", in Space Optics, edited by B. J. Thompson and R. R. Shannon, National Academy of Sciences, Washington, D. C., 1974.
23. Bennett, J. M., Surface Roughness Measurements using a FECO Scanning Interferometer, in High Energy Laser Mirrors and Windows, semi-annual report No. 4, Sept. 1973-March 1974, Naval Weapons Center, China Lake, California.

24. Bennett, J. M., "Statistical Characterization of Mirrors and Window Surfaces" Presented at the Optical Society of America Meeting, Oct. 1974 (copy obtained from the author).
25. Eastman, J. M., and Baumeister, P. W., Measurements of the Microtopography of Optical Surfaces Using a Scanning Fizeau Interferometer, presented at the Optical Society of America, Oct. 1974 (copy obtained from the author).
26. Heinisch, R. P., and Young, R. P., Opt. Eng., 13:327 (1974).
27. Allen, C. W., "Astrophysical Quantities", 2nd. ed., Athlone Press, London, 1963.
28. Endriz, J. G., and Spicer, W. E., Phys. Rev. B, 4:4,144 (1971).
29. Elson, J. M., and Ritchie, R. H., Phys. Stat. Sol. (b), 62:461 (1974).

## Appendix A

### TRANSLATION OF SCHWESINGER'S PAPER

The following is a translation from German of the article "Illuminance Distribution in the Diffraction Image of Telescope Mirrors with Random Surface Irregularities," by G. Schwesinger, from OPTIK, vol. 34, 1972.



# ILLUMINANCE DISTRIBUTION IN THE DIFFRACTION IMAGE OF TELESCOPE MIRRORS WITH RANDOM SURFACE IRREGULARITIES\*

by G. SCHWESINGER

CARL ZEISS, OBERKOCHEN

Translated by Serge Kunica and William B. Wetherell

## ABSTRACT

In the literature, the possibility has been discussed of achieving diffraction limited performance even with large telescope mirrors and despite atmospheric scintillation. The present article investigates whether certain assumptions made in this connection are really permissible. In particular, it is concerned with the problem of suitable correlation or covariance functions for describing random wave departures by statistical surface errors. It is shown that the surface undulations of actually fabricated mirrors are characterized by correlation functions strongly departing from the published assumptions. This leads to a different distribution of illuminance in the point image. For practical application in instrument design, values are computed for the encircled energy. Some arguments also indicate a different shape for the covariance functions associated with scintillation effects.

## 1. INTRODUCTION

Wavefronts having random statistical variations in amplitude and phase are examined in the theory of wave propagation in the turbulent atmosphere. In recent years, many articles have appeared which are addressed to this problem, and which also deal with the difficult question regarding the form of the correlation function or covariance function of these statistical variations. The knowledge of these functions is important, among other things, for the determination of the illuminance distribution in the diffraction images formed by lenses and mirrors. Chernov<sup>1</sup> was the first to deal with these questions in general terms, apparently. Scheffler<sup>2,3</sup> has built upon Chernov's analysis and theoretical results in an attempt to show that it should be possible, under certain postulated conditions, to drive the optical performance of large telescopes, as represented by the effective star-disk image diameter, up to nearly the limit set by diffraction, even when taking into consideration the image degradation due to atmospheric scintillation. This would require the

---

\* This article first appeared in OPTIK, vol. 34, pp 553-572, 1972.

The research upon which this article is based was part of a technology study funded by the Federal Ministry for Education and Science. Responsibility for its contents lies entirely with the author.

optical surface to meet surface irregularity tolerances which have not yet quite been realized, at least not in very large instruments. The practical application of the technique would therefore not be conceivable without the dedicated effort of the instrument manufacturers to build a mirror which is substantially better than has ever been built. If one realizes that the present state-of-the-art is attained only with considerable difficulties and enormous fabrication effort, one can imagine that the required accuracy will necessitate considerable advances in related technology, and large amounts of money.

The latter concern should by no means be taken to have been the principal reason for voicing objections to Scheffler's results, however. In the main, the justification for the doubts expressed above was based on observational astronomy, which, until recently, has given no valid indication that diffraction limited imagery is attainable, even with the best of seeing conditions, i.e., an effective star-disk diameter of 0.3 arc seconds or less. (Various reasons have been advanced for this.) However, such objections would only become valid if the theory were itself simultaneously disproved, because otherwise the seemingly irrefutable argument that such a precision mirror as is required by Scheffler does not exist, or can exist only as the rarest of exceptions, may be challenged. One earlier observation which has been reported<sup>4</sup> could possibly be taken as an example of such an exception. According to this report, an 82-inch telescope was used under the best seeing conditions to resolve a double star whose components are separated by only 0.10 arc second. This report is cited here without comment, to illustrate that where so fundamental a question is concerned, considerable differences of opinion exist.

The difficulty of the problem is further increased, owing to the fact that two image degrading effects, atmospheric scintillation and fabrication errors of the telescope mirror, work in concert: therefore, both must be accounted for simultaneously by one general theory, if conclusions are to be drawn with certainty regarding their optical effects. The work of Scheffler should have been a point of departure for this, in that it attempted to treat both error sources through the same statistical theory, and to draw quantitative conclusions. A statistical theory lends itself readily to the treatment of scintillation, particularly since in most instances the effects of scintillation are recorded as a temporal average.

The analysis of irregularities in the mirror surfaces on a statistical basis also offers a considerable advantage, since one can normally assume that a carefully executed fabrication process will greatly reduce or completely eliminate systematic figure errors such as zonal aberrations, astigmatism, etc., so that in the end there remains a wavefront with small irregular deviations, whose configuration is not easily described analytically, and whose effect on the diffraction image depends on the coincidences of a given case. With a statistical treatment, however, one abstracts from these coincidences and ascertains expectation values, which have a more general significance, and which allow fundamental questions to be answered. It is evident, however, that when evaluating image quality for a real system, measuring the actual surface irregularities remains desirable.

The scope of the present study is to explore how random mirror errors can be analyzed from a statistical viewpoint, when one discards the special simplifying assumptions which Scheffler has used in order to make the problem more easily manageable mathematically. An assessment will therefore be made as to whether one or another of these quite plausible assumptions has not led to questionable results with regard to the necessary surface quality of the mirrors. The question as to whether Scheffler's equation for the assessment of scintillation is admissible or not will be treated as a side issue. In oral discussions, it was variously surmised that the theory cannot be satisfied in some regards: however, that lacks final clarification.

## 2. THE SIGNIFICANT RESULTS OF SCHEFFLER'S TREATMENT

To begin with, we will review briefly the main steps in the mathematical analysis used by Scheffler, which originated with Chernov.<sup>1</sup>

A telescope of focal length  $F$ , and having a circular pupil, is assumed. Points in the pupil are represented by the coordinates  $(y_1, z_1)$ , defined so that their origin lies on the optical axis. The complex amplitude function due to a point source at infinity, located on the optical axis, will be evaluated at the paraxial point  $(y, z)$  in the focal plane. This complex amplitude function will be influenced by the aberrations of the optical system which originate in the random surface deformations of the primary mirror. These deformations shall be of a statistical nature,

and are so defined that their arithmetic average is zero. The corresponding phase disturbance  $S(y_1, z_1)$  in the pupil is  $2k$  times the height of the surface deformation, where the wave number  $k = 2\pi/\lambda$ , and  $\lambda$  is the wavelength. The variance of the phase disturbance is  $\sigma^2$ . The complex amplitude function  $u$  at the point  $(y, z)$  in the focal plane is given by the well known relationship<sup>5</sup>

$$u(y, z) = \iint_A e^{i[S(y_1, z_1) + (k/F)(yy_1 + zz_1)]} dy_1 dz_1. \quad (1)$$

The domain of integration is the pupil area  $A$ . A complex constant in front of the integral sign is immaterial for the problem at hand, and has therefore been omitted. If  $u^*$  is the complex conjugate of the integral, then the irradiance  $H(y, z)$  is given by the product  $uu^*$ . Formally, this can be written

$$H(y, z) = \iint_A dy_1 dz_1 \iint_A dy_2 dz_2 e^{i[S(y_1, z_1) - S(y_2, z_2)]} \times e^{i(k/F)[y(y_1 - y_2) + z(z_1 - z_2)]} \quad (2)$$

The evaluation of this quadruple integral for the phase deviations  $S$  for a given individual case would yield for this case the corresponding point spread function in the image plane. One could, of course, obtain it more easily from equation (1) by forming the product  $uu^*$ . Here, however, we are only interested in the statistical expectation value of this integral, which is the average over all possible distributions of phase deviations having the same variance  $\sigma^2$  and the same waveform characteristics. The latter is described by a normalized correlation function, which is defined as follows;

$$K(y_1, z_1; y_2, z_2) = K(r) = \langle S(y_1, z_1) S(y_2, z_2) \rangle / \sigma^2, \quad (3)$$

where

$$r = [(y_1 - y_2)^2 + (z_1 - z_2)^2]^{1/2}. \quad (4)$$

$\langle \rangle$  signifies the average over the area of the pupil. Since the mean value of  $S$  is vanishingly small, the definition (3) is also the normalized covariance function. With a correlation function of this form, it was shown previously by Keller,<sup>6</sup> and more strictly confirmed by Chernov,<sup>1</sup>



that the following relationship is valid:\*

$$\langle e^{i[S(y_1, z_1) - S(y_2, z_2)]} \rangle = e^{-\sigma^2[1 - K(r)]}. \quad (5)$$

From this, one obtains as the median irradiance distribution,

$$\begin{aligned} \bar{H}(y, z) = & \iint_A dy_1 dz_1 \iint_A dy_2 dz_2 e^{-\sigma^2[1 - K(y_1 z_1; y_2 z_2)]} \\ & \times e^{i(k/F)[y(y_1 - y_2) + z(z_1 - z_2)]}. \end{aligned} \quad (6)$$

This integral cannot be separated into two double integrals, making its evaluation considerably more difficult.

From this so far rigorous theory, Scheffler derived quantitative results. For the correlation function, he assumed a Gaussian distribution function with a correlation length  $\ell$ , thus

$$K(r) = e^{-(r/\ell)^2}. \quad (7)$$

Scheffler used this function not only to describe the surface irregularities of the mirrors, but also the phase variations caused by scintillation. The function  $K(r)$  of equation (7) has the required endpoint characteristics that  $K(0) = 1$  and  $K(\infty) = 0$ . It is, despite this, unsuitable for the problem under consideration, as will be demonstrated in section 3.

For the purpose of comparison with later numerical results, only Scheffler's final equations, which were derived from equation (6) with the aid of some approximations, are presented here. They read as follows, where  $R$  is the radius of the pupil and  $\alpha$  is the angular distance of the point  $(y, z)$  from the optical axis,

$$\alpha = (y^2 + z^2)^{1/2}/F. \quad (8)$$

Therefore,

$$\bar{H}(\alpha) = 4e^{-\sigma^2} \left[ \frac{J_1(kR\alpha)}{kR\alpha} \right]^2 + (1 - e^{-\sigma^2})(\ell/R)^2 e^{-(1/4)(k\ell\alpha)^2}, \quad \sigma \leq 1, \quad (9a)$$

$$= 4e^{-\sigma^2} \left[ \frac{J_1(kR\alpha)}{kR\alpha} \right]^2 + (1 - e^{-\sigma^2})(\ell/\sigma R)^2 e^{-(1/4)(k\ell\alpha/\sigma)^2}, \quad \sigma \geq 1. \quad (9b)$$

$\bar{H}(\alpha)$  is so normalized that for a perfect mirror, ( $\sigma = 0$ ), the irradiance

\* See the Appendix

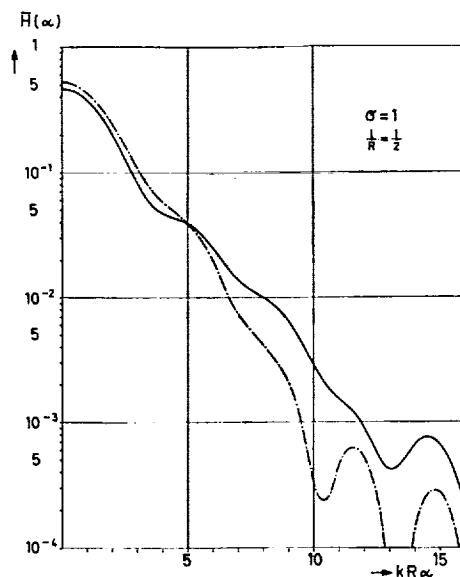


Figure 1 Intensity distribution  $\bar{H}$  in the diffraction image for a Gaussian correlation function with correlation length  $\ell = R/2$ . The broken curve is from equation (9), and the solid curve from equations (31), (33).

is 1.0 at the axial point  $\alpha = 0$ . Scheffler limits the validity of these equations to the domain  $(\ell/R)^2 \ll 1$ , and considers this assumption consistent with the measured surface irregularities of telescope mirrors. This assumption will be investigated more closely later. However, a further question arises in connection with the derivation of equation (9), with regard to the validity of several decisive mathematical simplifications Scheffler introduced in order to solve the integral (6) using the function  $K(r)$  in the form of equation (7). A computational example gives a partial answer. In figure 1, the broken curve represents the evaluation of equation (9) for the case  $\sigma = 1$  and  $\ell/R = 1/2$ . The solid curve represents a considerably more accurate solution to the integrals which was derived using the method of computation described in section 5. As a criterion of accuracy, it can be shown that the above technique gives a value of 0.4645 for  $\bar{H}(0)$ , as compared to 0.5259 from equation (9). For the special case of the axial point, the integral will yield an analytically exact solution, giving a value of 0.4581. Although the assumption that  $(\ell/R)^2 \ll 1$  is not completely satisfied, Scheffler's solution follows the basic characteristics quite well, even though it is somewhat optimistic with regard to the

sharpness of the energy concentration. For smaller values of  $(\ell/R)$ , the errors will probably be somewhat lower.

From equation (9), which states the core of his theory, Scheffler has concluded that large reflecting optics having random surface irregularities can, under certain circumstances, achieve a high definition image approaching the angular resolution possible with perfect optics, when observing through the turbulent atmosphere. The smaller the correlation length  $\ell$  and the variance  $\sigma^2$  of the surface deviations, the greater the achievable resolution. Scheffler estimates that the value of  $\ell$  should be less than 1/5th to 1/10th of the pupil radius  $R$ , and that the value of  $\sigma$  for the combination of both sources of phase disturbances should probably be less than 1. In actuality, as is shown by equation (9), the fraction of energy represented by the second term is distributed very evenly because of the small value of  $\ell^2$  in the exponential and in the factor in front of the exponential. In the vicinity of the optical axis, therefore, the reduction in intensity is due entirely to the factor  $\exp(-\sigma^2)$  by which the perfect lens diffraction pattern is multiplied. When one judges only in terms of a resolution criterion such as Rayleigh's criterion, this diminution in intensity will not result in a reduction in resolution.

The significance of this situation can be assessed approximately by inspecting integral (6) without resorting to calculations. When  $K(r)$  falls rapidly to zero at small radii, then the first term in the integrand is of almost constant value  $\exp(-\sigma^2)$ , disregarding the effects of the area elements, which correlate with each other only for extremely small values of  $r$ . The number of occurrences of such correlations over very short distances is, however, very small compared to the number of remaining cases. At both ends of the range  $0 \leq r \leq 2R$ , the number of occurrences of correlative connections reduces to zero (see section 3.) One can state, under these presumed conditions, that in the vicinity of the optical axis, at least,  $\bar{H}$  is approximated by the aberration free diffraction pattern, as reduced by the factor  $\exp(-\sigma^2)$ , since the aberration free pattern is governed by the second term of the integrand. It can further be expected that the missing energy will be found in a broader overlay. Conversely, one can therefore state that the correlation functions which fall off less

steeply than surmised above, or which show significant variations over a significant portion of the  $r$ -domain, can so modify the condition of  $\bar{H}$  that Scheffler's conclusions are no longer permissible. This question shall now be pursued.

### 3. THE SURFACE IRREGULARITY STRUCTURE OF ACTUALLY FABRICATED TELESCOPE MIRRORS

The correlation function defined by equation (3) can be determined numerically, if the surface irregularities of the mirror in question are well enough known. One can then divide the pupil into the finest possible matrix of  $M$  area elements, e.g., in equal sized squares, and perform the summation of the product  $S(y_1, z_1)S(y_2, z_2)$  over all the area elements whose centroids are separated by between  $r - \frac{1}{2}\Delta r$  and  $r + \frac{1}{2}\Delta r$ . Let  $P_\epsilon(r)$  be such a partial summation for the mean separation  $r$  with an incremental width  $\Delta r = \epsilon$ . Let the associated number of individual terms in the summation  $P_\epsilon(r)$  be  $n_\epsilon(r)$ . The quotient  $P_\epsilon/n_\epsilon$  represents the average value  $\langle S(y_1, z_1)S(y_2, z_2) \rangle$ . The correlation value to be formed in correspondence with equation (3) thus becomes

$$K_\epsilon(r) = \frac{P_\epsilon(r)}{\sigma^2 n_\epsilon(r)} = \frac{n_\epsilon(0)}{n_\epsilon(r)} \cdot \frac{P_\epsilon(r)}{P_\epsilon(0)} . \quad (10)$$

In figure 2, correlation functions computed by this process are shown for three actual telescope mirrors.\* Unfortunately, reliable numerical data about the surface irregularities of large telescope mirrors is very seldom available, and is not usually accurate enough to allow structural peculiarities to be assessed in detail. As a case in point, consider the well known article on the surface figure accuracy of the Lick 120-inch mirror.<sup>7</sup> Scheffler inferred from the surface contour map published in that article that his postulated value of  $R/3$  for the correlation length  $\ell$  of equation (7) is compatible with the surface irregularity structure of the Lick mirror. Figure 2 shows, however, that the actual correlation function of the Lick mirror is not even approximately Gaussian. The most prominent

---

\* Contrary to appearances, the slope of these curves is zero at  $r = 0$ . As Chernov has noted, this is always valid, if the variable quantity to be described, in this case the surface irregularities, is free of discontinuities.

C-3

C-2

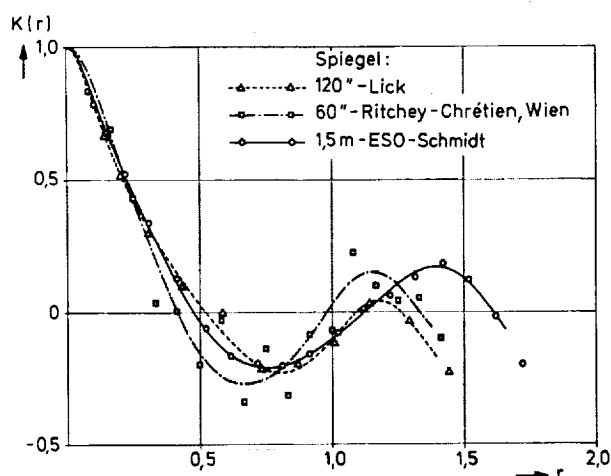


Figure 2 Correlation functions of the surface irregularities of three actually fabricated telescope mirrors.

difference is the pronounced oscillation, which extends over a wide range of  $r$ .

Similar oscillations are exhibited by the correlation functions of two newer mirrors of medium size which have been finished by the firm of Carl Zeiss, Oberkochen. Both have clear apertures of a little over 1.5 meters. Figure 2 shows the condition of the primary mirror of the 60-inch Ritchey-Chrétien telescope of the Leopold-Figl Observatory for Astrophysics in Vienna. The regrettably large dispersion of the data points was due to the simplified data reduction technique used, but it does not obscure the existence and approximate amplitude of the oscillations. A more careful evaluation, using a finer matrix of sample points, eliminates the large dispersion of values, as figure 2 shows for the spherical primary mirror of the Schmidt telescope of E.S.O. In this case, the oscillations are particularly pronounced.

The fundamental similarity of the correlation curves for these three mirrors is remarkable, almost astonishing, when one considers the manifold differences in the manufacturing technology. This is implied in part through the varying characteristics of their surface cross sections.\* As you know, the laps for the final polishing of spherical and aspheric mirror surfaces have somewhat different configurations, and the polishing

\* Parabolic, hyperbolic and spherical, respectively. [Translators' note.]

machines are also adjusted to different kinematic parameters during operation. Also, the construction of the polishing machine on which the Lick mirror was finished differs considerably from the configuration of the machine which was used with both of the other mirrors. Finally, the form of the Lick mirror substrate, and therefore its elastic behavior, is quite different from both of the smaller solid mirrors, since the Lick mirror is thinner and has a ribbed back surface. The level of accuracy with which they were figured also differs. For the Lick mirror,  $\sigma$  is about 2, and for the other two mirrors,  $\sigma$  is 0.43 and 0.7, respectively.

The similar nature of the correlation curves is probably attributable to the circumstance that the required optical precision can be attained only through the use of large area laps, approaching the size of the mirror, at least during the early stages of fine polishing. In fact, when one determines the spatial frequency spectrum of the correlation curve, through Fourier transformation, one finds a distinct maximum at wavelengths which are even somewhat longer than the mirror radius. This is in contradiction to Scheffler's assumptions.

The appearance of negative correlation values, which also contradicts Scheffler's assumptions, can be explained theoretically. To begin with, it can be stated that the sum of all the previously mentioned partial sums  $P_\epsilon$ , which are found by numerical analysis of  $K_\epsilon$  in the domain  $0 \leq r \leq 2R$ , vanishes, since, according to previous assumptions,  $S$  is a statistical function with a vanishing average value. From this it follows, with reference to equation (10), that

$$K_\epsilon(r)n_\epsilon(r) = \frac{n_\epsilon(0)}{P_\epsilon(0)} \sum P_\epsilon(r) = 0. \quad (11)$$

If one imagines that the incremental width  $\Delta r$  is made smaller and smaller by increasing the number of area elements, then in the limit as  $M \rightarrow \infty$ , one can define a continuous distribution function,  $\phi(r)$ , which indicates the relative frequency with which pairs of area elements can be found in the plane of the pupil whose mutual separation lies between  $r$  and  $r + dr$ . Obviously it follows that

$$dn(r) = \text{const } \phi(r)dr, \quad (12)$$

and the sum (11) becomes the integral

$$\int_r K(r) dr = 0 . \quad (13)$$

In the following,  $r$  is expressed as a multiple of the pupil radius  $R$ . From (12) and (13), it follows that

$$\int_r K(r) \phi(r) dr = 0 . \quad (14)$$

Since  $\phi(r)$  is always positive, the possible correlation functions  $K(r)$  are therefore subject to the limiting constraint that in the value domain  $r$ , both positive and negative values of the function must occur.

For the computation of the irradiance distribution  $\bar{H}$ , it is therefore essential to employ a correlation function which fulfills the constraint (14), and which conforms to the characteristics of the empirically measured function. The frequency distribution  $\phi(r)$  required for that purpose falls from a maximum in the middle of the  $r$ -domain to zero at both ends of that domain. One can recognize this intuitively, through the fact that the separation vector  $\vec{r}$  may have several degrees of freedom to vary vector length within the area of the pupil, e.g., displacement parallel to the longitudinal or transverse axes, as well as rotation. These degrees of freedom are restricted for  $r = 0$  and  $r = 2$ , however. In the former case, rotation is meaningless, while in the latter, no translations are possible except rotation about the center of the pupil. The relative number of occurrences  $\phi(r)$  of the possible attitude variations of the vectors  $\vec{r}$ , or in other words the probability  $\phi(r)dr$  that two points within the pupil lie separated by a distance in the range  $r$  to  $r + dr$ , can be shown to be as we state here without proof:

$$\phi(r) = Cr \left\{ \frac{\pi}{2}(1-r)^2 + \int_{1-r}^1 \arccos[(r^2 + \rho^2 - 1)/2r\rho] \rho d\rho \right\}, \quad r \leq 1, \quad (15a)$$

$$\phi(r) = Cr \int_{r-1}^1 \arccos[(r^2 + \rho^2 - 1)/2r\rho] \rho d\rho, \quad r \geq 1. \quad (15b)$$

The constant  $C = 1.2731$ .

The theoretical shape of  $\phi(r)$  is shown in figure 3. Additional points have been introduced representing two of the numerical evaluations of  $K(r)$  described above, specifically having the number of sample points  $M = 144$  and  $M = 305$ , respectively. The number of sample points is obviously still much too small to achieve a smooth frequency distribution in this empirical fashion.

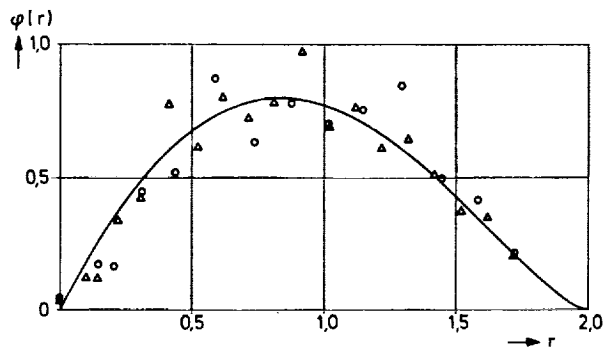


Figure 3 Frequency distribution  $\phi(r)$  for the point separation  $r$  with a circular pupil of radius 1.0.

#### 4. CHARACTERISTICS OF THE COVARIANCE FUNCTION FOR ATMOSPHERIC SCINTILLATION

Since the use of a function  $K(r)$  of the form (7) to describe the mirror surface irregularities is of doubtful validity, the question remains as to what the covariance functions of the variations in index of refraction, amplitude and phase due to atmospheric turbulence look like. The problem of defining these is very difficult and has not as yet been resolved satisfactorily. Even though the definitive answer to the postulated question must be reserved for later investigation, it is still possible to say with certainty that the effects of scintillation on image formation by a telescope cannot be described by a covariance function which is always positive. When one considers a plane wave of infinite transverse extent which has been transmitted through the atmosphere, it can be seen on the basis of elementary considerations that the frequency distribution  $\phi(r)$  is proportional to  $r$ . The constraint (14) reduces to

$$\int_0^{\infty} K(r) r dr = 0 .$$

This constraint was previously used by Fried<sup>8</sup> as a control for the covariance function he derived, and he also noted that the appearance of negative covariance values should be expected, in principle, with two dimensional distributions. In one special case, that of intensity scintillations, it has already been shown on the grounds of energy conservation that the transverse covariance function must have negative values over a substantial domain. This has been pointed out by Burke<sup>9</sup>.



Shack<sup>10</sup> also used the integral constraint cited above. The Gaussian distribution (7) used by Scheffler does not appertain at all to covariance functions which satisfy this constraint. The Gaussian Distribution (7) therefore cannot be used without reservations for the assessment of the effects of turbulence.

The above considerations for a wavefront of infinite extent must be modified for image formation in a telescope, since the pupil transmits only a finite region of the wave. However, this does not alter the fact that negative values of the covariance function will appear.

Heidbreder and Mitchell<sup>11</sup> have shown quantitatively that for small phase disturbances, the principal effect of scintillation is a reduction in intensity at the center of the diffraction image and a reduction in resolution in comparison to the diffraction limit, even if the transverse linear displacements, i.e., the "dancing" of the stars, could be completely compensated for through a servo control device. Without compensation of the directional scintillation, however, the resolution degradation will increase significantly, as can be seen from the sample calculations in the cited publication.\*

## 5. THE EFFECT OF RANDOM SURFACE IRREGULARITIES ON THE DISTRIBUTION OF IRRADIANCE IN THE DIFFRACTION IMAGE

With the realistic description of the surface irregularity characteristics of telescope mirrors we have derived, it is possible to deduce reliable expectation values for the structure of the point spread function. Even if one has to forgo assessment of the scintillation effects while its theoretical basis is still uncertain, the prediction and evaluation of the expected image quality due to the mirror alone is of the greatest importance for instrument definition, mirror technology and testing methodology. The following derivation points in this direction.

To begin with, the integral (6) from which we start is rewritten in polar coordinates,  $(\rho_1, \phi_1)$ ,  $(\rho_2, \phi_2)$  and  $(\rho, \phi)$ , where

$$y_j = R\rho_j \cos \phi_j ; \quad z_j = R\rho_j \sin \phi_j ; \quad j = 1, 2 ,$$

and there are corresponding formulas for  $y$  and  $z$ . The radii  $\rho_1$ ,  $\rho_2$  and  $\rho$  are normalized to the value of  $R$ , as was  $r$ . It is also established that

\* In this regard, see also references 10 and 12.

$$\phi_j = \phi_j - \phi ; \quad j = 1, 2 .$$

A simple transformation results in

$$\begin{aligned} y(y_1 - y_2) + z(z_1 - z_2) &= R^2 [\rho \rho_1 \cos (\phi_1 - \phi) - \rho \rho_2 \cos (\phi_2 - \phi)] \\ &= R^2 \rho (\rho_1 \cos \phi_1 - \rho_2 \cos \phi_2) . \end{aligned}$$

With the new variables,

$$\zeta = \frac{k}{F} r^2 \rho = kR\alpha , \quad (16)$$

the integral assumes the following form, which is independent of  $\phi$ , i.e., rotationally symmetric:

$$\begin{aligned} \bar{H}(\zeta) &= \int_0^{2\pi} \int_0^{2\pi} \int_0^1 \int_0^1 e^{-\sigma^2 [1-K(r)]} e^{i\zeta(\rho_1 \cos \phi_1 - \rho_2 \cos \phi_2)} \\ &\quad \times \rho_1 \rho_2 d\rho_1 d\rho_2 d\phi_1 d\phi_2 , \end{aligned} \quad (17)$$

where

$$r = [\rho_1^2 + \rho_2^2 - 2\rho_1 \rho_2 \cos (\phi_2 - \phi_1)]^{1/2} , \quad (18)$$

This integral generally cannot be solved for an arbitrarily chosen function  $K(r)$ . If one realizes that the first exponential in the integrand can be represented by a polynomial in even powers of  $r$ , then through

$$e^{-\sigma^2 [1 - K(r)]} = \sum_{m=0}^{\mu} b_m r^{2m} , \quad (19)$$

the powers of  $\cos (\phi_2 - \phi_1)$ , which appear because of equation (18), can be represented by the cosine sums of the multiple arguments, and one obtains  $\bar{H}(\zeta)$  as a sum of partial integrals

$$\begin{aligned} \bar{H}_{ms}(\zeta) &= \int_0^{2\pi} \int_0^{2\pi} \int_0^1 \int_0^1 \cos n(\phi_2 - \phi_1) e^{i\zeta(\rho_1 \cos \phi_1 - \rho_2 \cos \phi_2)} \\ &\quad \times \rho_1^{s_1} \rho_2^{s_2} d\rho_1 d\rho_2 d\phi_1 d\phi_2 , \end{aligned} \quad (20)$$

$$\text{where} \quad s_1 = 2(m - s) - n + 1 , \quad (21)$$

$$s_2 = 2s + n + 1 , \quad (22)$$

$$n \leq m \leq \mu , \quad (23)$$

$$\text{and} \quad 0 \leq s \leq m - n . \quad (24)$$

The latter integrals can be solved now utilizing the integral representation of the Bessel function  $J_n(x)$ , which is

$$\int_0^{2\pi} e^{in\phi} e^{ix \cos \phi} d\phi = 2\pi i^n J_n(x) . \quad (25)$$

Both integrations with respect to  $\Phi_1$  and  $\Phi_2$  lead to

$$\begin{aligned} \int_0^{2\pi} \int_0^{2\pi} & \left[ \frac{1}{2} e^{in(\Phi_2 - \Phi_1)} + \frac{1}{2} e^{-in(\Phi_2 - \Phi_1)} \right] e^{i\zeta(\rho_1 \cos \Phi_1 - \rho_2 \cos \Phi_2)} d\Phi_1 d\Phi_2 \\ &= 2\pi^2 [i^n J_n(-\zeta\rho_2) \cdot i^{-n} J_{-n}(\zeta\rho_1) + i^{-n} J_{-n}(-\zeta\rho_2) \cdot i^n J_n(\zeta\rho_1)] \\ &= 4\pi^2 J_n(\zeta\rho_1) J_n(\zeta\rho_2). \end{aligned}$$

If one changes the integrating variables from  $\zeta\rho_j$  to  $v_j$ , then

$$\begin{aligned} \bar{H}_{mns}(\zeta) &= 4\pi^2 \int_0^1 J_n(\zeta\rho_1) \rho_1^{s_1} d\rho_1 \int_0^1 J_n(\zeta\rho_2) \rho_2^{s_2} d\rho_2 \\ &= \frac{4\pi^2}{\zeta^{(s_1+s_2+2)}} \int_0^\zeta J_n(v_1) v_1^{s_1} dv_1 \int_0^\zeta J_n(v_2) v_2^{s_2} dv_2. \end{aligned} \quad (26)$$

In both integrations with respect to  $v_1$  and  $v_2$ , use can be made of the recursion formula

$$\int J_n(v) v^{n+p} dv = J_{n+1}(v) v^{n+p} - (p-1) \int J_{n+1}(v) v^{n+1+(p-2)} dv. \quad (27)$$

With respect to equations (20), (21) and (22), therefore, one can set

$$p = s_1 - n = 2(m - n - s) + 1, \quad (28)$$

$$p' = s_2 - n = 2s + 1. \quad (29)$$

Noting that  $p$  and  $p'$  are odd numbers,  $p$  can accordingly be represented by the number  $2N + 1$ . The successive applications of the recursion formula (27) yields

$$\begin{aligned} \int J_n(v) v^{n+p} dv &= J_{n+1}(v) v^{n+p} - (p-1) J_{n+2}(v) v^{n+p-1} \\ &+ (p-1)(p-3) J_{n+3}(v) v^{n+p-2} - (p-1)(p-3)(p-5) J_{n+4}(v) v^{n+p-3} \\ &+ \dots + (-2)^N N! J_{n+N+1}(v) v^{n+N+1}. \end{aligned} \quad (30)$$

If one defines the function  $Q(\zeta)$  according to

$$\begin{aligned} Q_{mns}(\zeta) &= \zeta^{-(n+p+1)} \int_0^\zeta J_n(v) v^{n+p} dv \\ &= \frac{1}{\zeta} J_{n+1}(\zeta) - \frac{p-1}{\zeta^2} J_{n+2}(\zeta) + \frac{(p-1)(p-3)}{\zeta^3} J_{n+3}(\zeta) \\ &- \frac{(p-1)(p-3)(p-5)}{\zeta^4} J_{n+4}(\zeta) + \dots + \frac{(-2)^N N!}{\zeta^{N+1}} J_{n+N+1}(\zeta), \end{aligned} \quad (31)$$

and a related function  $Q'(\zeta)$ , in which  $p'$  replaces  $p$  and  $N' = s$  replaces  $N$ , then one obtains, because of the relationships (28) and (29),

$$Q_{mns}(\zeta) Q'_{mns}(\zeta) = \zeta^{-(2m+4)} \int_0^\zeta J_n(v) v^{n+p} dv \int_0^\zeta J_n(v) v^{n+p'} dv,$$

and

$$\bar{H}_{mns}(\zeta) = 4\pi^2 Q_{mns}(\zeta) Q'_{mns}(\zeta). \quad (32)$$

$\bar{H}$  shall be normalized such that it will have a value of 1.0 on axis for an aberration-free image. With  $m = n = s = 0$ ,  $p = p' = 1$ , (32) becomes

$$\bar{H}_{000}(\zeta) = 4\pi^2 Q_{000}^2(\zeta) = \pi^2 [2J_1(\zeta)/\zeta]^2.$$

The required normalization  $\bar{H}_{000}(0) = 1$  is thus obtained by eliminating the factor  $\pi^2$ . Finally, the total irradiance  $\bar{H}(\zeta)$  is given as a sum of all the individual contributions of the polynomial set

$$\bar{H}(\zeta) = 4 \sum_{m=0}^{\mu} \sum_{n=0}^m \sum_{s=0}^{m-n} b_n a_{mns} Q_{mns}(\zeta) Q'_{mns}(\zeta). \quad (33)$$

$a_{mns}$  denotes a coefficient which results from a binomial development of  $r^{2m}$  and the transformation of the powers of the cosine terms into trigonometric sums.

We forgo presentation of the complete equation for the triple summation, which would be quite involved, since the number of terms increases rapidly with  $\mu$ . On the other hand, a value of  $\mu$  of about 6 to 8 is needed in approximating an oscillating correlation curve of the form shown in figure 2. Figure 4 shows the results of a polynomial representation with  $\mu = 8$ , which should reproduce the average characteristics of the described correlation curves. The curve  $K(r)$  shown in figure 4 was obtained by inverting the approximation to the exponential (19), for the case\*  $\sigma = 0.24\pi = 0.7540$ . This function, furthermore, satisfies the constraint of equation (14). For other values of  $\sigma$ , the polynomial coefficients  $b_m$  vary accordingly, and it can be seen that the correlation curves determined by inverting equation (19) are no longer exactly identical. On the whole, the quality of the polynomial fit decreases with increasing values of  $\sigma$ .

---

\* This corresponds to the smallest value treated in reference 2.

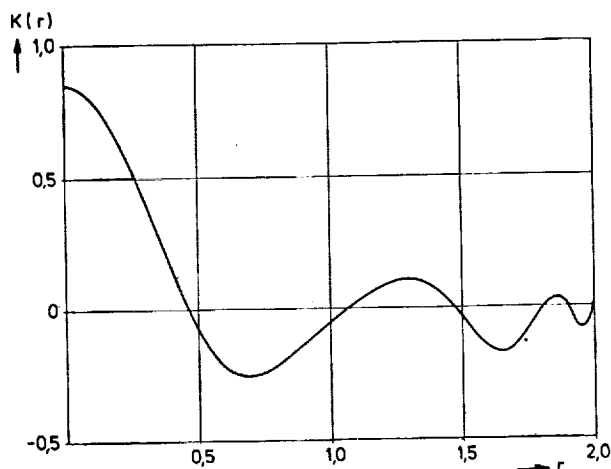


Figure 4 Polynomial approximation of a correlation function of the type shown in figure 2.

It can be recognised from figure 4 that difficulties are encountered in reproducing the beginning portion of the empirical curve, with the rapid variation of curvature and steep slope in the vicinity of  $r = 0$ ; this means that a many-termed polynomial is required. Similarly, the short oscillations at the end of the curve probably do not entirely correspond with reality; however, this region cannot be evaluated experimentally with any degree of reliability. Neither of the identified deviations are considered to be of grave significance, since in the regions of poor approximation, the frequency distribution  $\phi(r)$ , as has been shown, falls to zero, so that the value of the integral  $\bar{H}(\zeta)$  is not seriously falsified. This is further supported by the accuracy comparison in connection with figure 1, which is based on similar circumstances, although in somewhat milder form.

Irradiance distributions were calculated for various values of  $\sigma$ , using correlation functions of the described forms. The results are presented in figures 5 - 9. For comparison, the results calculated from equations (7) and (9) of Scheffler are presented for the value  $R/l = 5$ , which Scheffler used in his own work, along with  $R/l = 10$ . The latter value would have led to even greater differences from the new results. Since for  $\sigma = 0$  the results are identical, the discrepancies become increasingly more pronounced as the value of  $\sigma$  increases. To be sure, the correlation function illustrated in figure 4 still leads to an irradiance distribution with characteristics which are typical of random wavefronts, as has been

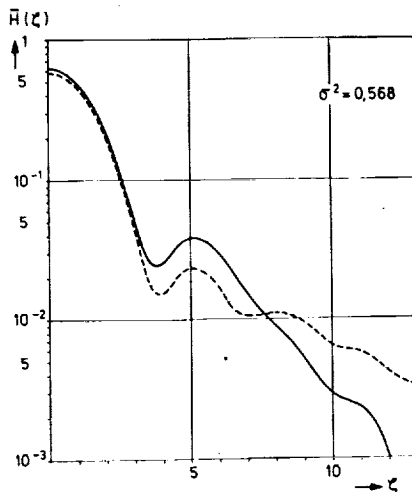


Fig. 5

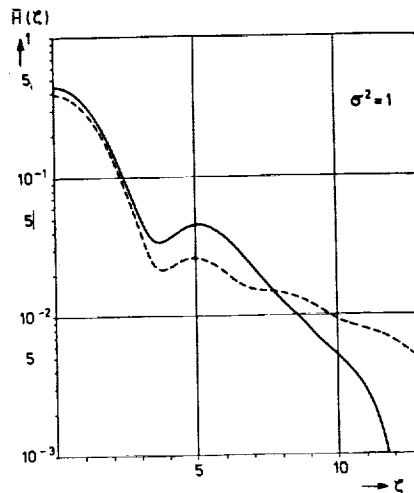


Fig. 6

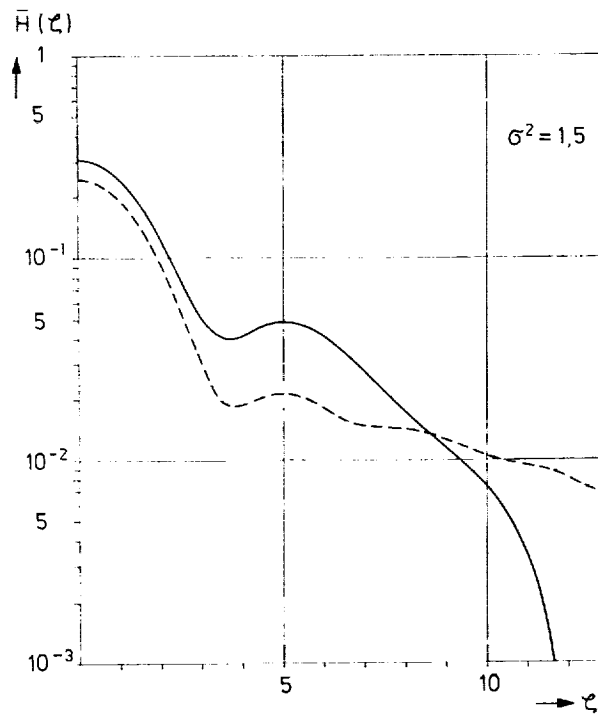


Fig. 7

Figures 5-9 Normalized irradiance distribution  $\bar{H}$  in the diffraction image. Solid curves are for a correlation function of the form of figure 4. Dashed curves correspond to equation (9), with  $\ell = R/5$ .

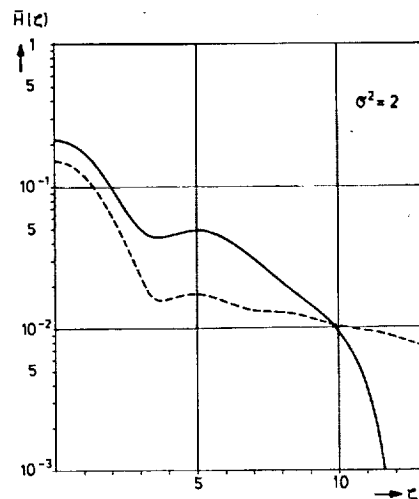


Fig. 8

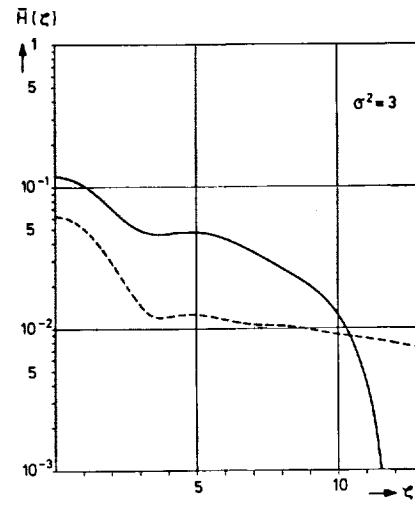


Fig. 9

published frequently,<sup>6,2,10</sup> i.e., an attenuated diffraction distribution and a superimposed flat supplementary distribution. However, this characteristic is now clearly less pronounced. There is found, namely, a flattening of the diffraction core, while of the diffraction minima, essentially only an indication of the first minimum remains. Beyond the weak secondary maximum, the irradiance drops more rapidly than for the Gaussian correlation function. There is therefore less energy spread out, which results in the central maximum remaining higher. The total energy within a given circle is thus increased, and this is especially important for photography of stars and related tasks. The effect on the achievable angular resolution is less clear. A theoretical criterion for the spread of the image, such as the radius  $\zeta$  at which the irradiance has dropped to a given fraction of the maximum value, would indicate a worse angular resolution. However, such a criterion is hardly sufficient, if the maximum irradiance at the axis has been reduced as far below that of the aberration free image as in the cases with larger values of  $\sigma$ .

For evaluating the quality of telescope mirrors, it has proven useful to consider the percentage fraction of the energy which is concentrated by the mirror inside a circular area with a specified radius  $\zeta$ . The specification of requirements on the instrument manufacturer, then, will usually have prescribed the encircled energy values for various radii which correspond to specified angular diameters of star images. This leads to an

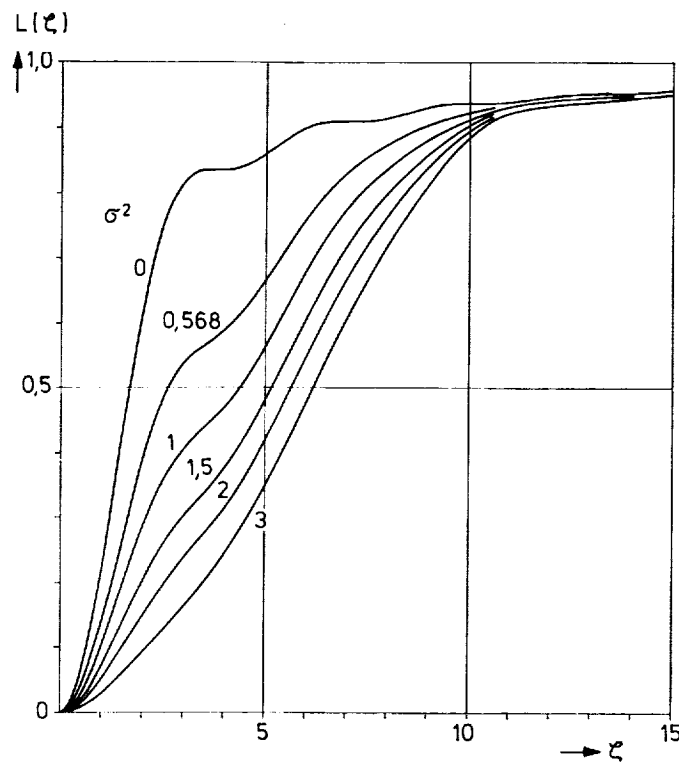


Figure 10 Encircled energy  $L$  in the diffraction image for the correlation function of figure 4.

overspecification, however, since if one can assume, as has been shown here, that the empirical correlation functions of the surface irregularities lead only to slight differences, then the functional development of the average expectation value of the encircled energy  $L(\zeta)$  as a function of  $\zeta$  is already fixed through the single parameter  $\sigma$ . It would therefore be more realistic to orient specifications of the kind mentioned above toward well-founded encircled energy curves. Such curves are shown in figure 10, and are the results of integration by zones of the irradiance curves given earlier. These encircled energy curves should be especially useful for practical applications. They show a bulge in the region where otherwise the undisturbed first diffraction minimum would occur; the bulge is especially pronounced for small values of  $\sigma$ , and indicates that there is already a significant image degradation. Since the encircled energy requirements established for astronomical purposes start with lower limits which are never under 50 percent, but on the contrary usually lie above that value, this bulge is of grave significance with regard to quality requirements.



Comparison of the curves  $L(\zeta)$  with results which have been published for the familiar axially symmetric aberrations shows clear differences not only in the general shape of the curves, but also in the average quality of the encircled energy. Using the same parametric values of  $\sigma$  for comparison, the results of Focke<sup>14</sup> and Barakat<sup>15</sup> for zonal spherical aberration, and of the latter also for simple spherical aberration, show more favorable encircled energy values, while Wolf's investigation<sup>16</sup> of the deviation from best focus, viewed roughly in the average, show a tendency to somewhat degraded encircled energy with increasing  $\sigma$ . With such comparisons, however, it should be noted that with large values of  $\sigma$ , the curves  $L(\zeta)$  calculated here become somewhat uncertain, due to the reduced quality of the polynomial fit of equation (19). Presumably the correct values of  $L$  are somewhat lower, especially in the upper region. Other interesting results and opportunities for comparison are proffered by the work of Barakat,<sup>17</sup> Shannon<sup>18</sup> and Tschunko<sup>19</sup>. The latter work, though, treats artificially generated surface irregularities, which bear no direct comparison to those postulated here.

At this point, I would like to express my appreciation to Mr. K. P. Zimmer and Mr. E. D. Knohl for the development of the computer programs and for performing the computations. I would also like to thank Mr. C. H. Kühne and Dr. R. Wilson for their useful discussions.

#### APPENDIX: WITH REGARD TO THE VALIDITY OF EQUATION (5)

The relationship (5) is rigorously valid only for a Gaussian distribution of the phase disturbance  $S$ . For other distributions it represents a very good approximation, so long as the deviations from a Gaussian distribution are not large. Even gross deviations produce only moderate errors, as is shown by the example of a symmetrical triangular distribution (Simpson's distribution) for the same variance  $\sigma^2$ . In this case, the right side of equation (5) is replaced by

$$\frac{1 - \cos \{ \sigma [12(1 - K)]^{1/2} \}}{6\sigma^2(1 - K)}$$

The following table shows that despite the drastic difference between

the two distributions, the average functions under consideration diverge noticeably only for large values of  $\sigma^2(1 - K)$ .

TABLE  
THE AVERAGE VALUES OF THE COINCIDENCE MAGNITUDE  
 $\exp \{i[S(y_1, z_1) - S(y_2, z_2)]\}$

$\sigma^2(1 - K)$	0.25	0.50	1.00	1.50
Gaussian Distribution	0.77880	0.60653	0.36788	0.22313
Triangular distribution	0.77370	0.58997	0.32474	0.16141

#### REFERENCES

1. L. A. Chernov, *Wave Propagation in a Random Medium*, translated by R. A. Silverman, McGraw-Hill Book Co., New York 1960.
2. H. Scheffler, *Z. Astrophysik* 55 (1962) 1.
3. H. Scheffler, *Optik* 19 (1962) 478.
4. G. van Biesbroeck, *Astron. J.* 52 (1946) 34.
5. M. Born and E. Wolf, *Principles of Optics*, 2nd ed., Pergamon Press 1964, p. 436, 460.
6. G. Keller, *Astron. J.* 58 (1953) 113.
7. N. U. Mayall and S. Vasilevskis, *Lick Obs. Bull. Nr. 567* (1960) 304.
8. D. L. Fried and J. D. Cloud, *J. Opt. Soc. Amer.* 56 (1966) 1667.
9. J. J. Burke, *Opt. Sciences Center Newsletter* 1 (1967) No. 5, p. 18, Univ. of Ariz.
10. R. V. Shack, *Optical Sciences Tech. Report No. 19*, Univ. of Ariz. 1967
11. G. R. Heidbreder and R. L. Mitchell, *J. Opt. Soc. Amer.* 56 (1966) 1677
12. D. L. Fried, *J. Opt. Soc. Amer.* 55 (1965) 1427.
13. E. Jahnke and F. Emde, *Funktionentafeln*, Dover Pub. New York, 1945
14. J. Focke, *Opt. Acta* 3 (1956) 110.
15. R. Barakat, *J. Opt. Soc. Amer.* 51 (1961) 152.
16. E. Wolf, *Proc. Roy. Soc. A* 204 (1951) 533.
17. R. Barakat, *Opt. Acta* 18 (1971) 683.
18. R. R. Shannon, *Opt. Sciences Center Newsletter* 5 (1971) No. 1, p. 16, Univ. of Ariz.
19. H. F. A. Tschunko, *Appl. Opt.* 10 (1971) 2423.

## Appendix B

### SURFACE ROUGHNESS MEASUREMENTS TECHNIQUES

This memorandum was prepared by Dr. James C. Wyant of the University of Arizona Optical Sciences Center under a consulting agreement to Itek for NASA contract No. NAS8-29949. The latter is the LST phase B study, and Dr. Wyant's memo was written in connection with the S.R. & T. task concerning specific surface measurement techniques. Since it also serves the purposes of the present study, we include a copy here. Both contracts are with the same customer.



Memo to: W. Wetherell

From: J. C. Wyant

Subject: Surface Roughness Measurement Techniques

Date: October 27, 1974

In this memo I describe and compare eight surface roughness measurement techniques. The eight techniques are: 1. LUPI, 2. A.C. LUPI, 3. Multiple beam interferometer, 4. Fringes of equal chromatic order (FECO), 5. Lyot test (sometimes called Zernike phase contrast test), 6. Central dark ground method (CDGM), 7. A. C. Fizeau interferometer (the system described by Jay Eastman at the last OSA meeting), and 8. A. C. differential interferometers. As I understand, you are interested in surface roughness amplitudes and periods which vary by two orders of magnitude from  $500 \text{ \AA}^0$  P-V to  $5 \text{ \AA}^0$  P-V and 100 mm to about 1 mm, respectively. I believe there is more than one method available which has the capability of making these measurements. The measurement problem is simplified somewhat since you are interested mostly in the surface statistics rather than a detailed surface contour map. My recommendations are given in the conclusion section at the end of this memo.

PRECEDING PAGE BLANK NOT FILMED

~~PRECEDING PAGE BLANK NOT FILMED~~

B-3

## LUPI

Since the LUPI is well known to you I will not go into its operation, and I will only comment on its surface roughness amplitude and frequency measurement capability.

I believe that under good conditions, namely vibration isolation and probably in a vacuum tank, a LUPI has a P-V surface measurement capability of approximately  $200 \text{ \AA}^0$ , which corresponds to approximately 1/15 fringe. Samples can be taken either along a line perpendicular to the fringes, or preferably along one fringe. The reason it is preferred that samples be taken along a fringe is that if data is taken along a line perpendicular to the fringes only one dimensional resolution is being utilized for measuring both sample position and surface contour, while if data is taken along a fringe the positional resolution is in the direction of the fringe and surface contour is obtained from resolution perpendicular to the fringe. Since two dimensional resolution is utilized, in practice more sample points can be obtained across the sample. Naturally the average distance between fringes has to be measured in order to calculate the surface height variations. I suspect that from 100 up to perhaps 500 data points could be taken along a fringe.

In order to obtain the  $200 \text{ \AA}^0$  surface measurement capability the wavefront deformation introduced by the interferometer must be subtracted by using a technique such as the one developed at Itek consisting of analyzing data obtained by rotating and translating the surface under test.

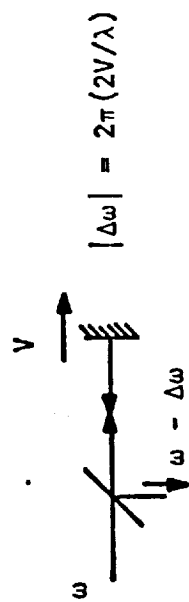
The  $200 \text{ \AA}^0$  P-V surface measurement capability is probably determined

by the vibrations in the system. In the testing of a short radius of curvature mirror it may be possible to reduce the 200 A<sup>0</sup> P-V error by a factor of two. One method of increasing the measurement accuracy and perhaps also the number of samples would be to use an AC LUPI.

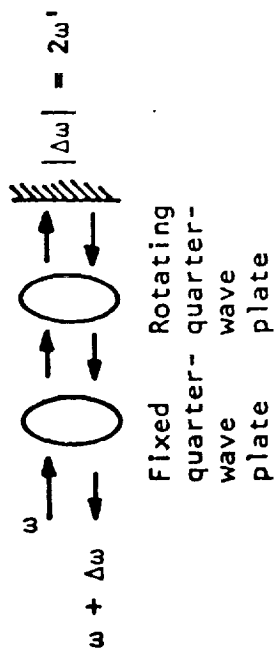
The basic difference between a conventional interferometer and an AC or heterodyne interferometer is that in an AC interferometer the two interfering beams have slightly different optical frequencies. Possible methods of obtaining two coherent beams having different optical frequencies are illustrated in Figure 1 and include reflecting one of the beams off a moving mirror, transmitting a beam twice thru a rotating  $\frac{1}{4}$  wave plate (or once thru a rotating  $\frac{1}{2}$  wave plate), using a Zeeman laser which emits two beams having different frequencies, or using a moving grating or a Bragg cell which doppler shifts the light in the diffracted order. Regardless of how the two beams having different optical frequencies are produced, when the two beams are interfered, the irradiance of the resulting interferogram varies sinusoidally with time. By using either an array of detectors in the interference plane, or one stationary detector and one scanning detector, electronic phase measuring techniques can be used to measure the relative phase differences in the interferogram plane. This technique offers a major improvement over a conventional LUPI in that better phase measurement accuracy can be obtained and additionally many measurements can be taken in a short period of time and processed electronically to average out the effect of vibration and turbulence and thus increase the accuracy of the measurement even in a less than ideal environment. An additionally good feature is that surface departure information is no longer extracted from the fringe deviation from straightness. Thus, if N samples are to be taken across a pupil, the scanner used to move the detector around needs to have only N one-dimensional resolution points.



• Moving mirror

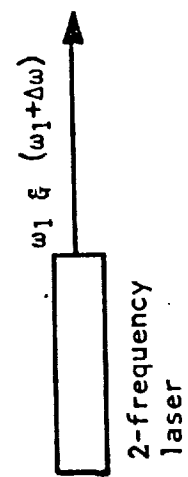


• Rotating quarter-wave plate

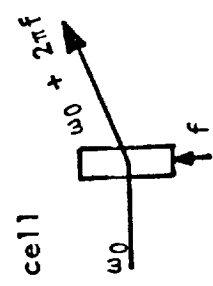


$\omega' =$  angular rotation speed

• Zeeman laser



• Bragg cell



• Moving grating

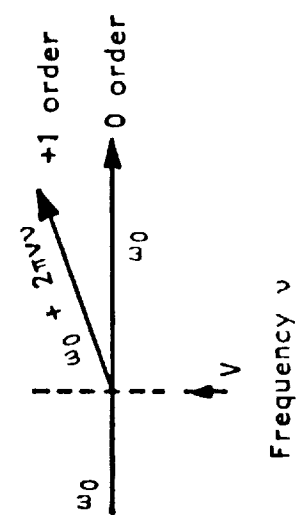


Figure 1. Possible methods of producing a frequency shift.

Many methods of making an AC LUPI exist. One possible method is shown in Figure 2. In this setup the light exiting a conventional LUPI is incident upon a Bragg cell. The angle between the reference beam and the test beam is selected such that the zero order of the test beam and the first order of the reference beam leave the Bragg cell at the same angle. Since the zero order of the test beam is not doppler shifted and the first diffracted order of the reference beam is doppler shifted an amount  $f$ , the drive frequency of the Bragg cell, the two interfering beams have different optical frequencies and electronic phase detection can be used. One of the detectors would be stationary and the second detector would scan the image of the test surface in the desired fashion. Other beams leave the Bragg cell, but they all leave at an angle different from the desired two beams and can be eliminated by placing a small aperture in the appropriate position in the focal plane of the lens after the Bragg cell such that the aperture transmits only the two beams of interest. The diverger in the LUPI could of course be removed for the testing of plane mirrors.

I think that with an AC LUPI it would be possible to obtain up to 500 samples across an aperture and a measurement accuracy of at least  $50 \text{ \AA}$ , probably even better. To obtain these results the errors in the interferometer must first be calibrated and subtracted from the test results.

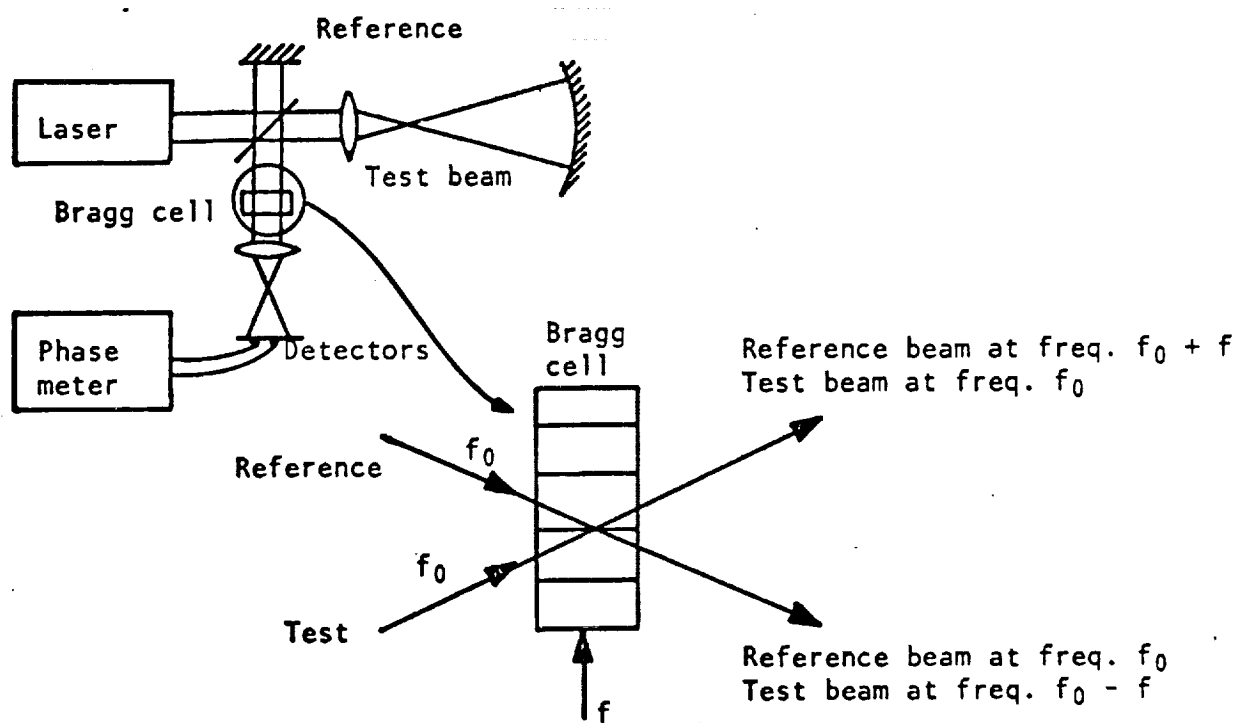


Figure 2. One possible AC LUPI.

## Multiple Beam Interferometry

Multiple beam interferometry is characterized by its very sharp fringes. If fringe position data is obtained with the naked eye I think that a multiple beam interferometer has a distinct advantage over a two beam interferometer. However, if a more sophisticated way of measuring fringe position, such as a scanning microdensitometer, is used, I do not believe the sharp fringes obtained using a multiple beam interferometer offer any appreciable advantage. This is partially borne out by the fact that while Perkin Elmer uses multiple beam interferometry almost exclusively, and Itek uses two beam interferometry, both companies appear to have essentially the same measurement accuracy. Multiple beam interferometry has the disadvantage that the surfaces under test must be coated.

Two types of multiple beam interferometers are the Fizeau and the P.E. SWIM.<sup>1</sup> I think the SWIM and LUPI give similar accuracy, while the Fizeau, whether multiple beam or not, might give better results by a factor of 2 or more since effects of vibration and turbulence are eliminated. The Fizeau does offer the problem that surfaces up to only 12 inches or so in diameter can be measured.

## FECO Test

A FECO interferometer is basically a multiple beam interferometer in which the test sample is focused on the entrance slit of a spectrograph. The output of the spectrograph gives the surface profile. A schematic diagram of a FECO interferometer is shown in Figure 3. A white light source from a point source Z is collimated by lens  $L_1$  and reflected to the reference surface and the test surface (i.e. multiple beam interferometer, I) by beam splitter B. Both the reference surface and the test surface are coated to have a reflectance of about 90%. The light reflected from the reference and test surfaces passes thru the beam splitter, and lens  $L_2$  focuses an image of I on entrance slit S of a spectrograph. The white light is dispersed by the spectrograph and a spectrum containing interference fringes is formed in the focal plane F which is conjugate to I. Each fringe shown in F gives the profile of a line, or actually a slit, of the difference between the test piece and the reference surface. The profile line in the output of the spectrograph can be converted to the departure of the test surface from the reference surface by using the technique described in reference 2.

There is one major difference between a Fizeau multiple beam interferometer and a FECO interferometer. The difference being that in a multiple beam interferometer each fringe is a contour line, i.e. the loci of points for which the difference between the test surface and the reference surface is a constant number of wavelengths and the only way information can be obtained about the surfaces for points between fringes in a

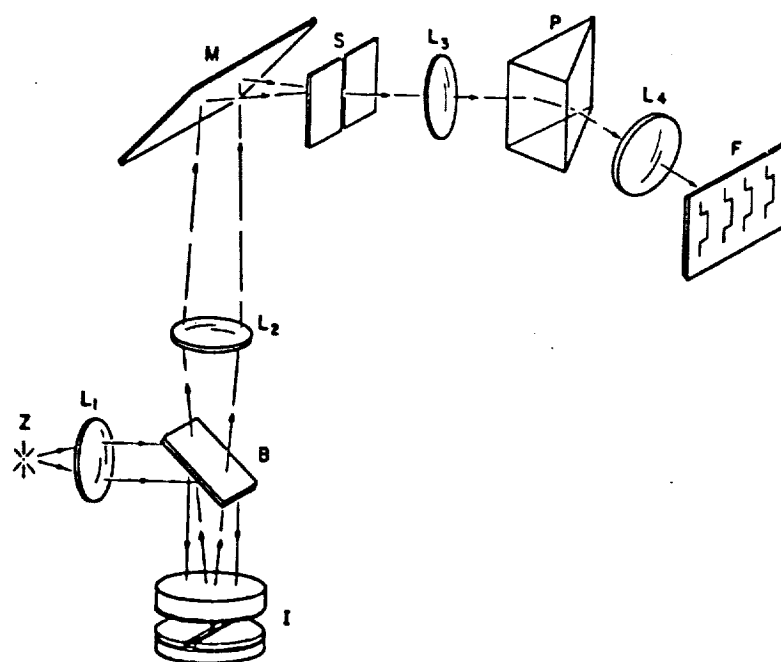


Figure 3. FECO interferometer.

multiple beam interferogram is to move the fringes around by either changing the distance between the test surface and the reference surface or by changing the wavelength. With the FECO interferometer the portion of the surface for which the profile is obtained can be easily selected, i.e. the profile is obtained for the portion of the surface which is focused on the spectrograph slit.

As you know, the Bennetts have been using the FECO interferometer for measuring surface roughness and they described some of their work at the latest OSA meeting. I am sorry that at the time I am writing this memo I do not have access to their latest work. They are sending me information, but I have not received it yet.

As Jean Bennett described at the last OSA meeting, they have developed a FECO interferometer that can resolve height differences of under  $5 \text{ \AA}$  with a lateral resolution limit of about 2 microns. Wavelengths are measured at 512 equally spaced points along the length of an interference fringe which corresponds to a total distance of 1 mm on the test surface. They appear to be ahead of everyone else on their measurement techniques.

The Bennetts can look at a total sample distance of only 1 mm since they want a lateral resolution of only a few microns. Since you do not have this lateral resolution requirement you can look at much larger samples up to 1, 10, or perhaps even 30 cm. You would simply set up a normal multiple beam interferometer using a small white light source and image the sample onto the entrance slit of the spectrograph.

My main complaint about the FECO test is that the sample must be coated.

Perhaps for the spatial frequencies you are interested in this is not a critical factor, but I am not 100% convinced that at the small amplitude variations it can always be assumed that the coating follows the surface sufficiently closely.



## Lyot Test and Central Dark Ground Method

Both the Lyot test (often called Zernike test) and the central dark ground method provide means of measuring the surface roughness of polished surfaces. The Lyot test gives a linear relationship between irradiance and height variation of the surface under test. The central dark ground method (CDGM), in which a small stop is used to block the zero order spectral component, can give both the point by point surface height variations and with a single measurement the rms surface height variations. The Lyot test and the CDGM test are similar and can be analyzed as follows:

Let the amplitude of the light reflected by the test surface be given by

$$t(x,y) = t_0 \exp[i\phi(x,y)]. \quad (1)$$

If  $Z(x,y)$  is the height variations of the surface being looked at in reflection, then

$$\phi(x,y) = \frac{2\pi}{\lambda} [2Z(x,y)]. \quad (2)$$

In the following it is assumed that the magnification is unity and that the imaging optics is large enough to collect all the diffracted rays that carry any appreciable energy.

In the Lyot test the light reflected from the element under test is brought to focus and a mask is placed at the focus as shown in Figure 4. The mask which covers the central portion of the Airy disk transmits an amount  $a$  of the undiffracted light and retards the phase of the undiffracted light by either  $\frac{1}{4}$  wave (positive phase contrast) or  $\frac{3}{4}$  wave (negative phase contrast) relative to the phase retardation of the diffracted light. For positive phase contrast the irradiance as a function of  $x$  and  $y$  in

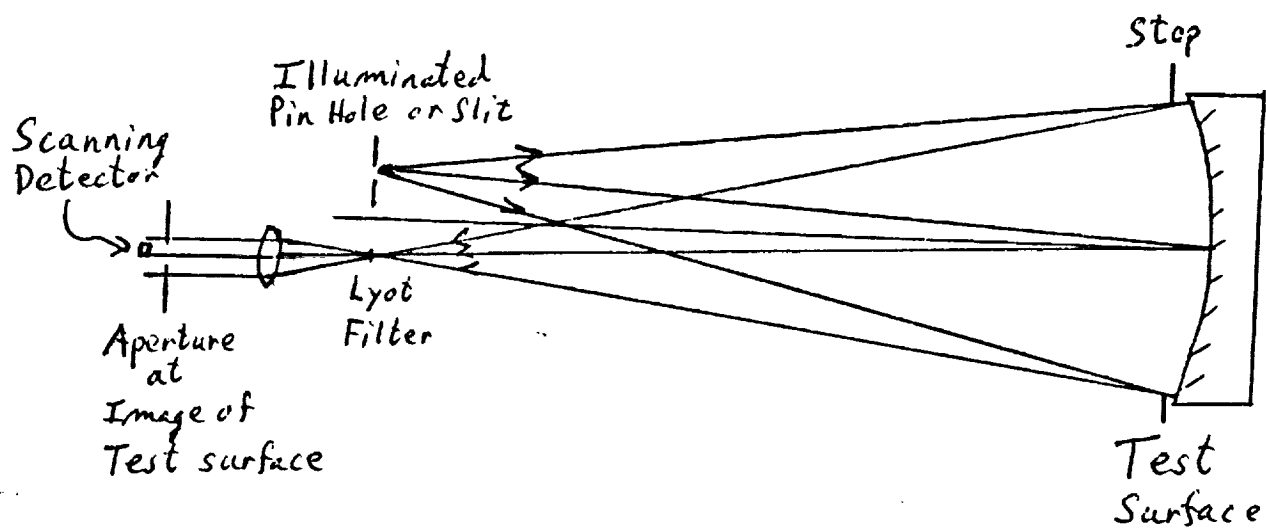


Figure 4. Surface roughness measurement by Lyot test.

the image plane is given by

$$\begin{aligned}
 I(x,y) &= \left| \exp i\phi(x,y) - 1 + a \exp(i\pi/2) \right|^2 t_0^2 \\
 &= [2 + a^2 - 2 \cos \phi(x,y) + 2a \sin \phi(x,y)] t_0^2 \\
 &\approx t_0^2 [a^2 + 2a\phi(x,y)]
 \end{aligned}
 \tag{3}$$

The  $t_0^2$  in the above equation corresponds to the strong wave component that is reflected from the sample without change, while the  $a \exp(i\pi/2)$  is the portion of this undiffracted light that is transmitted with a  $90^\circ$  phase change.

As long as  $\phi \ll a$ , the observed irradiance is linearly related to the height variations of the surface. If  $I=I_0$  when  $\phi=0$ , then

$$\frac{I(x,y)}{I_0} = 1 + \frac{2\phi(x,y)}{a}
 \tag{5}$$

or

$$\phi(x,y) = \left[ \frac{I(x,y)}{I_0} - 1 \right] \frac{a}{2}
 \tag{6}$$

So as long as  $a$ , the zero order amplitude transmission of the mask is known,  $\phi(x,y)$  can be determined.

If  $\phi \not\ll a$  there is not a linear relationship between observed irradiance and the height variations of the surface. In this case the relationship between  $\phi$  and  $I$  can in most cases of interest be approximated as

$$\frac{I(x,y)}{I_0} = \left[ \frac{\phi(x,y)}{a} + 1 \right]^2 \quad (7)$$

or

$$\phi(x,y) = \left[ \sqrt{\frac{I(x,y)}{I_0}} - 1 \right] a \quad (8)$$

Table I shows different values of irradiance ratios  $I(x,y)/I_0$  obtained for different values of  $\phi$  and  $a$ . Eq. (7) was used for all the calculations. For the irradiance ratios below the horizontal lines in the table there is a linear relationship between irradiance and height variations and Eq(5) could have been used for the calculations. The relationship between  $a$  and optical density  $D$  shown in the table is  $D = \log (1/a^2)$ .

It should be noted that in Figure 4 the light diffracted at the edge of the test piece was eliminated by placing at the image of the test piece an aperture smaller than the image. From the analysis you recently performed it appears that this mask is not needed if the test sample is illuminated with a suitably apodized wavefront, instead of a wavefront having uniform intensity as is generally used.

Recently a modification in the Lyot mask was introduced which extends the linear operating range by about a factor of 3 or 4.<sup>3</sup> In the modified Lyot test the undiffracted light is phase shifted by  $45^\circ$  and is unattenuated, while the diffracted light is attenuated by a factor of  $\sqrt{2}$ . Under these conditions the irradiance in the image plane is given by

TABLE I: IRRADIANCE RATIOS FOR LYOT TEST

Surface Height Variation Z(x,y)	$\phi(x,y)$ for reflection off surface	Irradiance ratio for reflection measurement					
		$\alpha = 1$	.56	.32	.18	.1	.056
		D = 0	.5	1	1.5	2	2.5
200 A°	0.5	2.25	3.58	6.57	14.27	36	98.6
100 A°	0.25	1.56	2.09	3.17	5.71	12.3	29.9
50 A°	0.125	1.26	1.50	1.93	2.87	5.06	10.5
25 A°	0.0625	1.13	1.24	1.43	1.82	2.64	4.48
10 A°	0.025	1.05	1.09	1.16	1.30	1.56	2.09
5 A°	0.0125	1.03	1.05	1.08	1.14	1.27	1.50
1 A°	0.0025	1.005	1.01	1.02	1.03	1.05	1.09

$$D = \text{Density} = \log (1/a^2)$$

$$\text{Irradiance Ratio} = \left( \frac{\phi(x,y)}{a} + 1 \right)^2$$

=  $\frac{\text{observed irradiance}}{\text{irradiance for no surface height variation}}$

$$\begin{aligned}
 I(x,y) &= \left| (\exp i \phi(x,y) - 1) / \sqrt{2} + \exp i \pi/4 \right|^2 t_o^2 \\
 &= [1 + \sin \phi(x,y)] t_o^2
 \end{aligned} \tag{9}$$

Then

$$\frac{I(x,y)}{I_o} = 1 + \sin \phi(x,y) \approx 1 + \phi(x,y) \tag{10}$$

Although the modified Lyot test has a slightly larger linear operating range than the regular Lyot test, the  $\sqrt{2}$  amplitude attenuation of the diffracted light means that a given change in the surface height variations changes the irradiance ratio by only half as much as in the case of the unattenuated regular Lyot test.

The CDGM test is the same as the Lyot test except now the mask transmits none of the undiffracted light. Thus, the irradiance in the image plane is given by

$$\begin{aligned}
 I(x,y) &= \left| \exp i \phi(x,y) - 1 \right|^2 t_o^2 \\
 &= [2 - 2 \cos \phi(x,y)] t_o^2 \\
 &\approx t_o^2 \phi^2(x,y).
 \end{aligned} \tag{11}$$

The observed irradiance is no longer linearly related to the height variations of the surface, however there is a known relationship. If the mask is removed the irradiance,  $I_0$ , in the image plane is  $t_0^2$ . The ratio of irradiance with mask to irradiance without mask is given by

$$\frac{I(x,y) \text{ with mask}}{I \text{ without mask}} = \phi^2(x,y) \quad (12)$$

So by measuring  $I(x,y)$ , one obtains  $\phi(x,y)$ . Table II gives irradiance ratios as a function of  $Z(x,y)$  and  $\phi(x,y)$ .

Instead of measuring the height variations of the sample point by point, the CDGM test can be used to measure the rms height variation,  $Z(x,y)$ . The total amount of flux,  $F$ , in the image plane is given by

$$\begin{aligned} F &= \int I(x,y) \, dx \, dy \\ &= \int_{t_0^2}^2 \phi^2(x,y) \, dx \, dy \end{aligned} \quad (13)$$

If the mask is removed the flux in the image plane is  $\int_{t_0^2}^2 dx \, dy$ . The ratio of flux with mask to flux without mask is

$$\frac{F \text{ with mask}}{F \text{ without mask}} = \frac{\int_{t_0^2}^2 \phi^2(x,y) \, dx \, dy}{\int_{t_0^2}^2 dx \, dy} = (\phi_{\text{rms}})^2 \quad (14)$$

To obtain an accurate measurement of  $\phi_{\text{rms}}$  it is necessary to block out the light diffracted by the edge of the sample. This is easily accomplished by reimaging the sample onto an aperture smaller than the image of the sample, as shown in Figure 5. Your recent results indicate that if the sample is illuminated with an appropriately apodized beam essentially the same results are obtained without the mask.

Table II which gave the irradiance ratios as a function of  $Z(x,y)$  also gives the flux ratios as a function of  $Z_{\text{rms}}$ . For example, if  $Z_{\text{rms}}$  is  $50 \text{ \AA}^0$ , then the flux ratios for a reflection test would be 0.016 i.e., 1.6% of the light is diffracted (scattered) out of the direct beam. The ratios are small for small rms surface variations and would be hard to measure in practice. However, in a sense, this is good. The flux ratio is a measure of the Strehl ratio. For small surface errors the Strehl ratio differs from the ideal value of unity by an amount equal to  $(\phi_{\text{rms}})^2$ .



TABLE II: IRRADIANCE RATIOS FOR CDGM TEST

Surface Height variation $Z(x,y)$	$\phi(x,y)$ for reflection off surface	CDGM Test Irradiance Ratio
200 A°	0.5	0.25
100 A°	0.25	0.063
50 A°	0.125	0.016
25 A°	0.0625	0.0036
10 A°	0.025	0.0006
5 A°	0.0125	0.0002
1 A°	0.0025	0.000006

$$\text{Irradiance Ratio} = \phi^2(x,y)$$

$$= \frac{\text{IRRADIANCE WITH CDGM MASK}}{\text{IRRADIANCE WITHOUT CDGM MASK}}$$

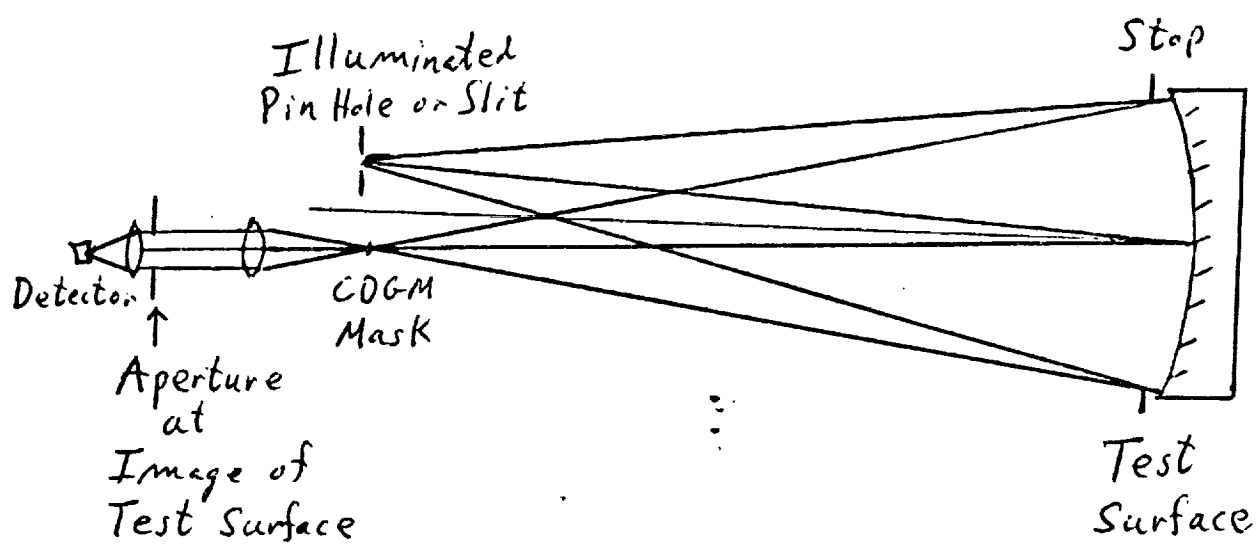


Figure 5. Surface roughness measurement by central dark ground method.

## AC Fizeau Interferometer

At the last OSA meeting Jay Eastman described a scanning Fizeau interferometer. Figure 6 shows one possible configuration. The instrument is similar to conventional Fizeau interferometers except the reference surface is oscillated by a piezoelectric transducer, which causes the light reflected by the reference surface to be doppler shifted in frequency. Therefore, the two interfering beams have different optical frequency and the irradiance of the interferogram varies sinusoidally with time. Hence, AC heterodyne phase detection can be used in the manner described in the section above on the AC LUPI. In the instrument built by Eastman rms surface roughness of  $20 \text{ \AA}$  could be measured for a 1 mm strip of the surface. By sacraficing lateral resolution, the sample size could probably be increased to 1 cm. For larger surfaces it might be hard to control the oscillation of the reference surface.

The surfaces would not need to be coated. The light source could be selected such that the coherence length is short enough that the only interference present would be between light reflected by one surface of the reference piece and light reflected by the test surface. Light reflected by other surfaces would not effect the results.

The AC Fizeau has the advantage over the AC LUPI that setup vibration and turbulence would produce much less effect, just as in a conventional Fizeau. The AC Fizeau does have the problem that only relatively small samples could be tested.

My main complaint about the AC Fizeau interferometer is the problem in oscillating the reference surface without distorting its shape. One way of getting around this problem would be to use an AC differential interferometer.

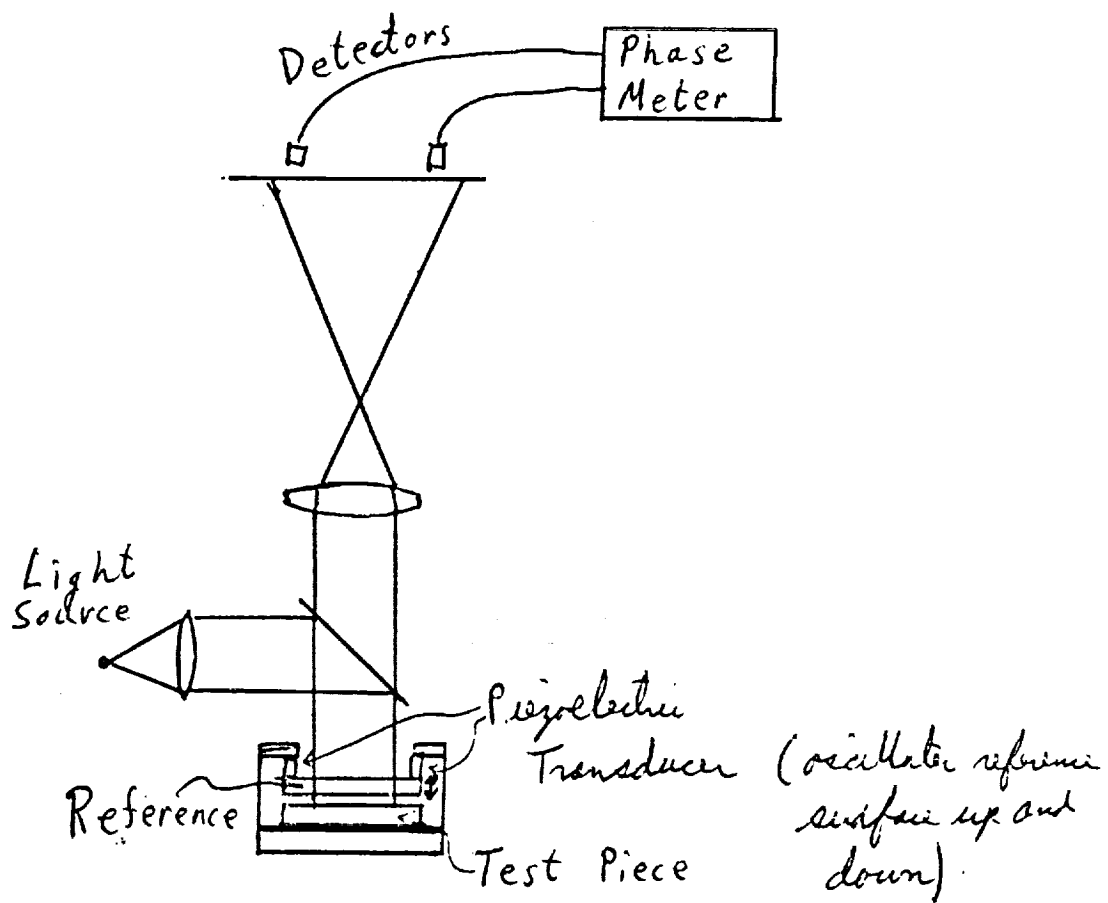


Figure 6. AC Fizeau Interferometer.

## AC Differential Interferometers

The data obtained from a differential interferometer is slightly different from that obtained from a Fizeau. The AC Fizeau gives the contour difference between the test surface and the reference surface, while the AC differential interferometer is a lateral shear interferometer and gives the height difference between points on the test surface separated the shear distance. If the shear is large compared to the largest period surface structure being looked at, the surface statistics measured by the two interferometers are essentially the same.

Several types of AC differential interferometers exist. One type is the AC polarization interferometer shown in Figure 7. In the figure S is the light source, which would probably be a Hg lamp,  $L_1$  is a collimating lens, and  $P_1$  and  $S_1$  are a polarizer and Savart plate, respectively. The Savart plate has the property that an incident ray is sheared in two: an ordinary ray and an extraordinary ray. Thus, if it is illuminated with a beam of light, two laterally displaced beams will exit the plate. The two sheared beams have orthogonal polarization.  $P_1$  and  $S_1$  can be eliminated if a slit source is used instead of an extended source.

$P_2$  and  $S_2$  are another polarizer and Savart plate.  $S_2$  converts the beam reflected by the sample into two beams laterally displaced a distance  $\Delta S$ . The two displaced beams have orthogonal polarization. Let one polarization be in the x direction and the other in the y direction. Furthermore, let  $\phi(x,y)$  be the phase difference between the two beams. If  $Z(x,y)$  is the height variations of the sample then

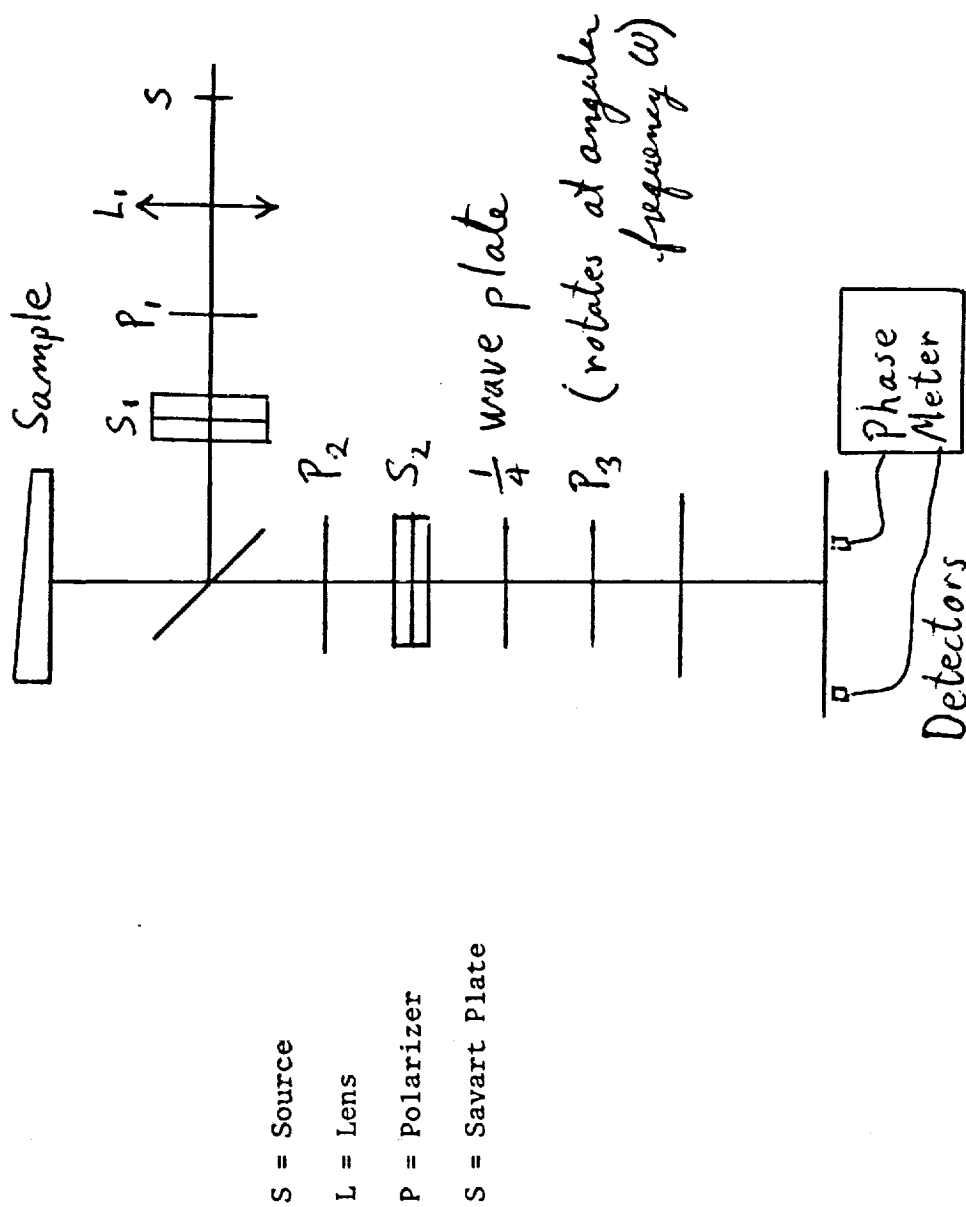


Figure 7. Polarization AC Differential Interferometer.

$$\phi(x,y) = \frac{2\pi}{\lambda} \left\{ 2[Z(x+\delta s, y) - Z(x, y)] \right\}$$

It can be shown that if a  $\frac{1}{4}$  wave plate is placed after the Savart plate and the slow axis of the plate makes an angle of  $45^\circ$  with respect to the x axis, the light leaving the  $\frac{1}{4}$  wave plate will be linearly polarized at an angle  $\phi(x,y)/2$  from the slow axis of the  $\frac{1}{4}$  wave plate. If the polarizer placed after the  $\frac{1}{4}$  wave plate is rotated at angular frequency  $\omega$ , the photodetector sees a signal proportional to

$$\begin{aligned} & \cos^2[2\omega t + \phi(x,y)/2] \\ &= \frac{1}{2} [1 + \cos[4\omega t + \phi(x,y)]] \end{aligned}$$

Thus, AC phase detection can be used to measure  $\phi(x,y)$ .

A second AC differential interferometer is illustrated in Figure 8 and described more fully in reference 4. In this interferometer both the shear and modulation are obtained by using two acousto optic Bragg cells which are driven at different frequencies.

AC differential interferometers show a lot of potential for measuring surface roughness. The sample would not have to be coated. The back surface of the sample could have the appropriate shape to throw light reflected off the back surface out of the interferometer. Almost any size sample could be tested by placing the required expanding optics ( a diverger for large spherical surfaces, a microscope for small surfaces, etc) between the shearing device (Savart plate or Bragg cell) and the surface under test. Although the optics should be good they do not have to be

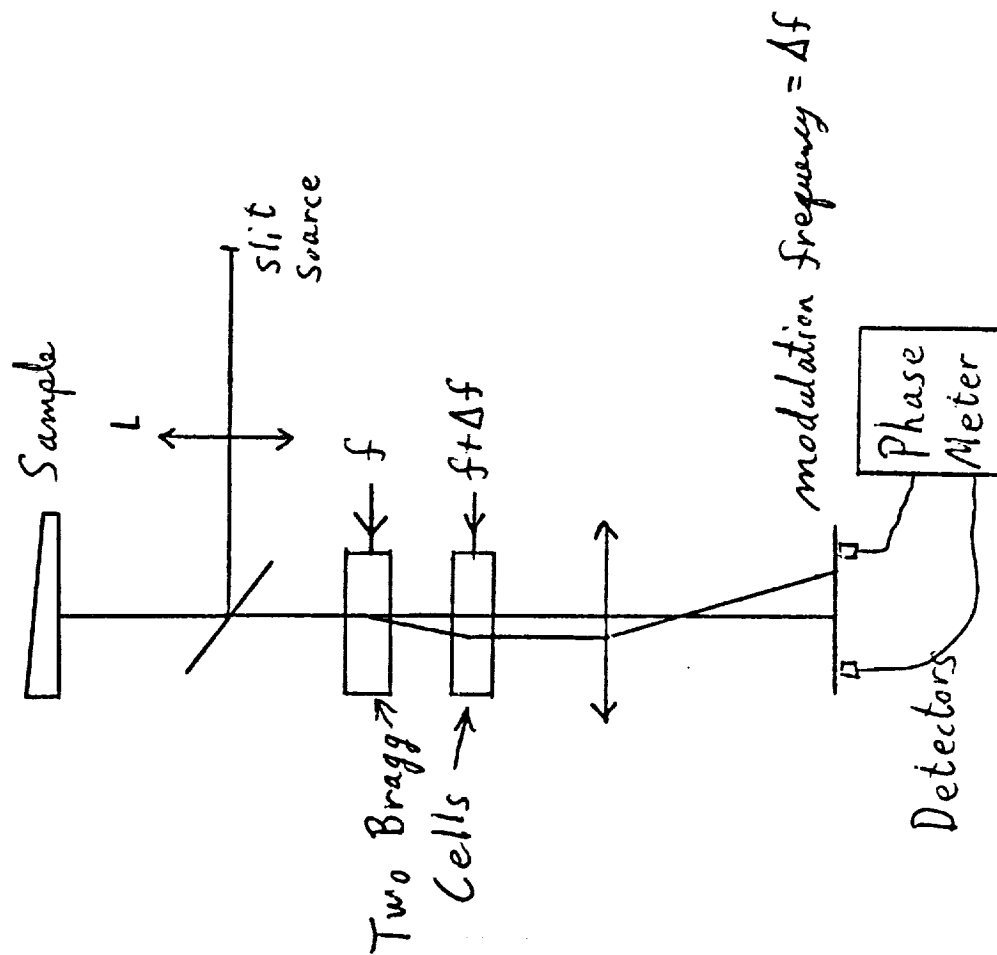


Figure 8. Bragg Cell AC Differential Interferometer.



unreasonably good since an extended, or at least a slit source, is being used. The phase measurement is made in a plane conjugate to the sample, and due to the source's finite size, aberrations in the instrument which occur in a plane different from either the sample plane or a plane conjugate to the sample plane are smeared across the sample and the biggest effect is to reduce the lateral resolution capability of the system. (What I say above can be seen to be true by observing the fact that dust in interferometers have less effect on test results as the source size increases.) The above results suggest that turbulence has less effect on the results for a differential interferometer test than for a LUPI test.

Perhaps the largest source of error in AC differential interferometers is produced by non uniform frequency modulation of the output signal. I do not know how uniform a signal can be produced using a rotating analyzer to generate the signal. I do know that Bragg cells have shown a uniformity of at least 1/100 wave with time, but I do not know if the phase gradient across the diffracted beam is this good (i.e. are the grating planes in the Bragg cell equally spaced to within 1%).

## Conclusions

The LUPI is probably good for measuring surface variations up to 1/15 fringe or  $200\text{\AA}$ . Probably a minimum of 100 sample points across the aperture can be obtained. To obtain these results errors in the interferometer would have to be subtracted from the test results and vibration isolation and a vacuum chamber would be required.

An AC LUPI is a good way of improving the measurement accuracy and perhaps increasing the number of sample points which could be obtained across the sample. A measurement accuracy of  $50\text{\AA}$  or better P-V could be obtained for perhaps as many as 500 samples across the aperture. Again to obtain these results errors in the interferometer would have to be calibrated and subtracted from the test results.

Fizeau multiple beam interferometry could probably yield a P-V accuracy of 50 to  $100\text{\AA}$  for 100 or more sample points across the aperture. However, the aperture size would be limited to about 12 inches diameter. A SWIM interferometer could increase the maximum allowable aperture, however this would increase vibration and turbulence problems which would reduce the accuracy to a point similar to that obtained using a LUPI.

FECO interferometry has been used extensively by the Bennetts and its performance for measuring small period structure is known. Probably 5 to  $10\text{\AA}$  measurement accuracy can be obtained for 500 sample points across an aperture for apertures up to 12 inches diameter. My main complaint about the FECO test, which is a complaint about multiple beam tests in general, is that the sample must be coated.

The Lyot test looks promising for being able to test large diameter surfaces with an accuracy of  $5 \text{ \AA}^0$  for 500 or so sample points across the sample. Vibration isolation and a vacuum chamber would probably be required for testing large diameter surfaces. The sample would not have to be coated if the second surface was made such as to reflect the beam out of the system.

The CDGM is interesting only because it can provide the rms surface structure with a single measurement, however it does not have sufficient sensitivity for the measurements you want.

An AC Fizeau interferometer would probably give surface roughness measurements good to  $20 \text{ \AA}^0$  or better for 500 sample points across the aperture. The interferometer works well with uncoated surfaces. The largest problem with the interferometer is that only small pieces, maybe up to 1 cm diameter, can be tested. I am worried about being able to oscillate the reference mirror without distorting its shape.

AC differential interferometers appear promising. As long as the lateral shear is greater than the largest period of surface roughness of interest, surface statistics should be the same as obtained using a Fizeau interferometer where two surfaces having similar statistics are compared. I think  $5 \text{ \AA}^0$  sensitivity can be obtained. Both small and large surfaces could be tested. Perhaps for the larger pieces vibration isolation and a vacuum chamber would improve the results. 500 samples could be obtained across the aperture. Although the interferometer optics should be good, if an extended source, or at least a slit source, is used the interferometer optics would not have to have super quality. The sample

also does not need to be coated.

I think that for the measurements you want, where you do not need to know exactly where the surface deformation is, but are only concerned with the statistics, the AC differential interferometer has all the good characteristics of the AC LUPI, and some better features in that effects of turbulence, vibration, and optical imperfections in the interferometer are reduced. In my slightly biased opinion, I think the AC differential interferometer is the most promising technique for making measurements across the wide range of amplitude and period of surface structure you are interested in and could even look at higher frequency structure than what you are interested in. Even micron type ripple could be measured by using a microscope to image the sample on the detector plane.

## References

- 1) L.R. Heintze, H.D. Polster, and J. Vrabel, Appl. Opt. 6 1924 (1967).
- 2) G. Hass and R.E. Than (editors), Physics of Thin Films (Academic Press, New York, 1967) p. 31.
- 3) H.B. Henning, Electro-Optical Systems Design, 30 (June, 1974).
- 4) J.F. Ebersole and J.C. Wyant, Appl. Opt. 13 1004 (1974).



## Appendix C

### PERFECT LENS PSF OVERLAYS

The attached transparencies show the PSF's for a perfect lens, both obstructed and unobstructed. The obstructed lens has a central obstruction diameter ratio of 0.324, matching the A.A.T. primary. The other two PSF's are plotted on a radius scale of 100 and 50 Airy radii, matching the two scales most commonly used in the text.

These transparencies can be layed on top of the figures in Section 4 to show how the PSF is modified by the form of wavefront error under discussion. Two sets of the overlays are provided; the reader may wish to cut the individual charts apart for convenience.

